CHEMICAL REVIEWS

Review

pubs.acs.org/CR

Simulating Coherent Multidimensional Spectroscopy of Nonadiabatic Molecular Processes: From the Infrared to the X-ray Regime

Markus Kowalewski,*[,†,‡] Benjamin P. Fingerhut,*[,§,‡] Konstantin E. Dorfman,*[,⊥] Kochise Bennett,[†] and Shaul Mukamel*[,†]

[†]Department of Chemistry and Department of Physics and Astronomy, University of California, Irvine, California 92697-2025, United States

[§]Max-Born-Institut für Nichtlineare Optik und Kurzzeitspektroskopie, D-12489 Berlin, Germany

[⊥]State Key Laboratory of Precision Spectroscopy, East China Normal University, Shanghai 200062, China

ABSTRACT: Crossings of electronic potential energy surfaces in nuclear configuration space, known as conical intersections, determine the rates and outcomes of a large class of photochemical molecular processes. Much theoretical progress has been made in computing strongly coupled electronic and nuclear motions at different levels, but how to incorporate them in different spectroscopic signals and the approximations involved are less established. This will be the focus of the present review. We survey a wide range of time-resolved spectroscopic techniques which span from the infrared to the X-ray regimes and can be used for probing the nonadiabatic dynamics in the vicinity of conical intersections. Transient electronic and vibrational probes and their theoretical signal calculations are classified by their information content. This includes transient vibrational spectroscopic methods (transient infrared and femtosecond off-resonant stimulated Raman), resonant electronic probes (transient absorption and photoelectron spectroscopy), and novel stimulated X-ray Raman techniques. Along with the precise definition of what to calculate for predicting the various signals, we outline a toolbox of protocols for their simulation.

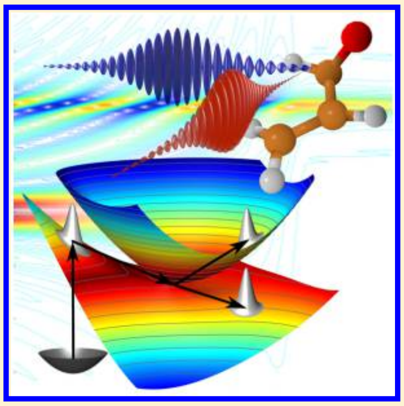

CONTENTS

Received: February 6, 2017
Published: September 26, 2017

DOI: 10.1021/acs.chemrev.7b00081
Chem. Rev. 2017, 117, 12165−12226

1. INTRODUCTION

It has been widely believed that electronic states of the same symmetry cannot cross. Hund, von Neumann, and Wigner first realized[1,2] that the strict noncrossing rule for potential energy surfaces (PESs) of the same symmetry only holds for systems with one vibrational degree of freedom. Teller described these degenerate points as double cones[3] and coined the term conical intersection (CoIn). CoIns in crossings are possible if there are two or more vibrational modes. It was thought that such electronic degenerate points between two PESs are very rare and special cases. With the advent of modern quantum chemistry methods and the computer age, it is now established that CoIns can be found in almost any molecule.[4] They are the rule rather than the exception and play an essential role in photochemistry, photophysics, and nature. CoIns enable ultrafast, sub-100 fs nonradiative relaxation pathways, which control product yields and rates of a large class of photochemical processes (for a general review of CoIns see ref 5). At a CoIn, electronic and nuclear frequencies are comparable and become strongly coupled since the Born−Oppenheimer approximation,[6] which normally allows their separation, breaks down.

The celebrated Woodward−Hofman rules[7] in organic chemistry relate the stereochemistry of pericyclic reactions to orbital symmetry. The photoinduced reaction pathway involves CoIns, as has been shown on, e.g., cyclohexadiene.[8−15] Artificially designed molecular systems like optical switches[10,16] rely on CoIns as a basic functional principle. Many important light-induced biological processes, like the photosynthesis of Vitamin D,[17] the main event of vision in retinal,[18] photodamage of deoxyribonucleic acid (DNA),[19] and DNA repair,[20−22] are decided by CoIns. This review surveys the spectroscopic techniques that can be employed for the monitoring of CoIns and outlines protocols for their simulation.

The strong mixing of the nuclear and the electronic degrees of freedoms in the vicinity of a CoIn affects vibrational and electronic properties. Two strategies are possible for their spectroscopic detection: One can either use transient vibrational spectroscopy or probe properties which are attributed to electronic states. Vibrational techniques rely mainly on the fact that the shape of the potential energy is heavily affected by the CoIn, which results in a temporal variation of vibrational mode frequencies of spectator modes. This can be probed by, e.g., femtosecond stimulated Raman spectroscopy (FSRS), coherent anti-Stokes Raman spectroscopy (CARS), or transient infrared (IR). More subtle vibrational properties are the temporal change of intermode couplings, which require multidimensional vibrational probe schemes, such as transient 2D-IR, to observe. Changes in the vibrational frequency, intensity of a vibrational transition, or intermode couplings during the time evolution of an excited state wavepacket can serve as signatures for a CoIn. The second major class of spectroscopic techniques detect properties attributed to electronic states. As the system passes through a CoIn, population is transferred between the electronic states involved in the surface crossing. The character of the adiabatic electronic wave function changes rapidly, as do properties such as transition dipole moments. The energy gap between the electronic states varies strongly down to degeneracy of both curves at the CoIn. These changes can be probed by addressing the electronic degrees of freedom either by resonant transient absorption with visual/ultraviolet (UV) light, in a Raman process with extreme ultraviolet (XUV) of X-ray light, or tracked by time-resolved photoelectron spectroscopy. Moreover, the branching of the nuclear wavepacket creates a short-lived electronic coherence that can be probed by sufficiently short pulses. In a landmark femtosecond experiment, the population dynamics of electronic states was spectroscopically observed by Zewail[23−25] in sodium iodide molecules and theoretically described by means of wave packet dynamics.[26,27] Since this system only has a single vibrational degree of freedom, it constitutes an avoided crossing[28,29] rather than a CoIn.

Commercial ultrafast laser sources with sub-100 fs pulse lengths cover the IR to the near UV regime. More recent developments[30] pushed the limits further toward the attosecond

X-ray regime. The high-harmonic generation (HHG) technique creates table-top light sources[31] that can produce pulses as short as 70 as,[32,33] while free electron lasers (FELs) provide ultrashort subfemtosecond pulses[34−36] up a to a few keV in photon energy with high photon fluxes that can cover the full range of all relevant time scales from vibrational IR, vibrational Raman spectroscopy over electronic UV−visual (VIS) spectroscopy to X-ray electronic Raman techniques to time-resolved X-ray diffraction. HHG can provide a versatile light source for the pump, the probe,[37−39] or both.[40]

In this review, we review ultrafast time-resolved spectroscopic techniques that can be used to detect the excited state nonadiabatic dynamics in molecules. We will focus on the detection of the dynamics in the vicinity of CoIns, the theoretical description, and simulation protocols for these signals. Technological advancements and state-of-the-art experiments will be surveyed. For a more general review on the spectroscopy of reaction intermediates see ref 41. The influence of CoIns on photoinduced chemical dynamics has been reviewed in refs 42 and 43. An earlier theoretical review of femtosecond spectroscopy and nonadiabatic processes can be found in ref 44. We will introduce the general theoretical description of the spectroscopic signals perturbative in the external field in terms of the loop diagram formalism, along with a brief overview of the basic simulation protocols for the signals. In the next sections, we give a more detailed survey of different types of vibrational (sections 2 and 3) and electronic (section 4) spectroscopic probes. While most transient vibrational detection techniques and transient absorption spectroscopy have become well established during the past decade, electronic detection techniques based on XUV and X-ray pulses (section 5) are more recent and have yet to be established as standard experimental techniques.

1.1. Conical Intersections and Their Theoretical Description

We first briefly introduce the theoretical description of CoIns in terms of the diabatic and adiabatic electronic states. Atomic units are used in the following ($\hbar = m_e = 4\pi\epsilon_0 = 1$). The Born−Oppenheimer approximation, which allows for the separation of nuclear and electronic degrees of freedom, breaks down in the vicinity of a CoIn where electronic and vibrational frequencies are not well separated (see Figure 1). A common approach to account for coupled nuclear and electronic degrees of freedom begins with the adiabatic electronic states. The total wave function can be expanded as a sum of products of the nuclear wave function $\psi_k(q)$ and the electronic wave function $\phi_k(r; q)$

$$\Psi_k(q, r) = \psi_k(q)\phi_k(r; q) \tag{1}$$

where $q \equiv (q_1,...,q_M)$ denotes the set of nuclear coordinates, $r \equiv (r_1,...,r_N)$ are the electronic coordinates, and the index k runs over all electronic states. The adiabatic electronic wave function $\phi_k(r; q)$ is obtained by solving the electronic Schrödinger equation for fixed nuclear geometries (e.g., by means of common electronic structure methods like post-Hartree−Fock or time-dependent density functional theory methods, etc.[45,46]). This results in the adiabatic potential energy surfaces $\hat{V}_k = \langle\phi_k|H_{\mathrm{el}}|\phi_k\rangle$, which are the eigenvalues of the electronic Hamiltonian H_{el} ($\hat{V}$ indicates that $V(q)$ is an operator with respect to the nuclear coordinates q). Note that the matrix of potential energies is diagonal in this representation. The off-diagonal nonadiabatic couplings between the adiabatic states arise from the nuclear kinetic energy operator[5,47,48]

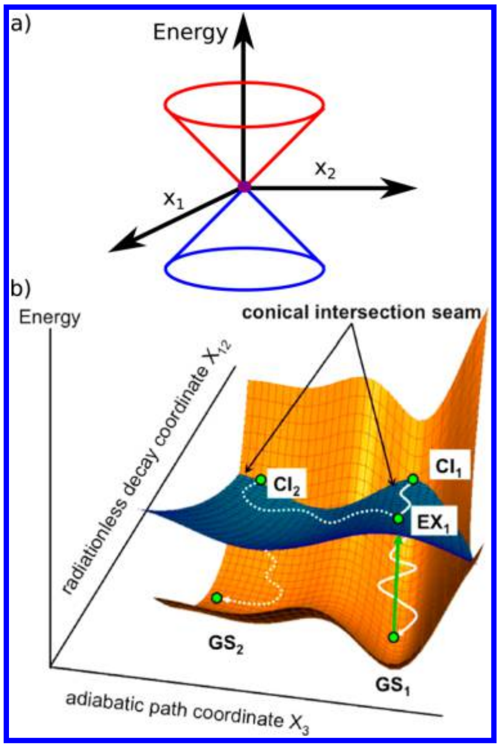

Figure 1. Schematic representation of a CoIn in the adiabatic representation: (a) Potential energy surface (PES) in the branching space x_1/x_2 spawned by the gradient difference vector and the derivative coupling vector. Any motion along x_1 or x_2 lifts the degeneracy and generates the cone shape. (b) Space of the radiationless decay coordinate x_{12}, which is part of the branching space, and the adiabatic path coordinate x_3, which is part of the seam space. Adapted with permission from ref 4. Copyright 2014 Elsevier.

$$\hat{T} = -\sum_i \frac{1}{2m_i}\frac{\partial^2}{\partial q_i^2} \tag{2}$$

where m_i is the mass of the ith nucleus. In the next step, the matrix elements

$$\hat{H}_{kl}^{(\mathrm{ad})} = \langle\Psi_k(q, r)|\hat{T} + \hat{H}_{\mathrm{el}}|\Psi_l(q, r)\rangle_r \tag{3}$$

are calculated by integrating over the electronic coordinates r. Letting $\hat{T}$ act on the nuclear−electronic product wave function $\Psi_l(q, r)$ creates new terms due to the product rule of differentiation. The matrix elements of the adiabatic electronic states then read

$$\hat{H}_{kl}^{(\mathrm{ad})} = \delta_{kl}\hat{T} + \delta_{kl}\hat{V}_k + \sum_i \frac{1}{m_i}\left(\hat{f}_{kl}^{(i)}\frac{\partial}{\partial q_i} + \frac{1}{2}\hat{h}_{kl}^{(i)}\right) \tag{4}$$

where $\hat{f}$ and $\hat{h}$ are the derivative coupling term and the scalar coupling, respectively

$$\hat{f}_{kl}^{(i)}(q) = \langle\phi_k(q)|\partial_{q_i}|\phi_l(q)\rangle_r \tag{5}$$

$$\hat{h}_{kl}^{(i)}(q) = \langle\phi_k(q)|\partial_{q_i^2}^2|\phi_l(q)\rangle_r \tag{6}$$

Here, $\langle\rangle_r$ denotes integration over the electronic coordinates. The scalar term $\hat{h}_{kl}^{(i)}$ is usually dropped and approximated by taking a Hermitian average

$$\hat{H}^{(\mathrm{ad})} = \frac{1}{2}(\hat{H}^{(\mathrm{ad})\dagger} + \hat{H}^{(\mathrm{ad})}) \tag{7}$$

which leads to the approximate Hermitian Hamiltonian[47]

$$\hat{H}^{(\mathrm{ad})}_{kl} = \delta_{kl}\hat{T} + \delta_{kl}\hat{V}_{kl} + \sum_i \frac{1}{2m_i}\left(2f^{(i)}_{kl}\frac{\partial}{\partial q_i} + \frac{\partial}{\partial q_i}f^{(i)}_{kl}\right) \tag{8}$$

The adiabatic description is characterized by a diagonal potential energy operator and electronic states, which change their electronic character abruptly as the nuclear coordinate is varied in the vicinity of a CoIn. This is a convenient representation since more than two electronic states can be readily handled and the coupling between electronic states is highly localized. One difficulty is that the nonadiabatic coupling matrix elements diverge at degenerate points.

The diabatic representation is an alternative description in which the PES are allowed to cross. For a system with a CoIn between two adiabatic electronic states ψ_i the diabatic states χ_i are obtained by a rotation

$$\begin{pmatrix} \chi_1(q,t) \\ \chi_2(q,t) \end{pmatrix} = \begin{pmatrix} \cos(\theta(q)) & \sin(\theta(q)) \\ -\sin(\theta(q)) & \cos(\theta(q)) \end{pmatrix} \begin{pmatrix} \psi_1(q,t) \\ \psi_2(q,t) \end{pmatrix} \tag{9}$$

where the mixing angle $\theta(q)$ is obtained by requiring the derivative coupling $\hat{f}_{kl}$ to vanish

$$\langle \phi_k(q)|\frac{\partial}{\partial q_i}|\phi_l(q)\rangle_r - \frac{\partial}{\partial q_i}\theta(q_i) = 0 \tag{10}$$

and $\chi_k(q,t)$ are the diabatic nuclear wave functions. Applying the rotation eq 9 to the adiabatic PESs yields the diabatic PESs $\hat{S}_1$, $\hat{S}_2$ along with the diabatic couplings $\hat{S}_{12}$ (note that $\hat{S}_{ij} \equiv S_{ij}(q)$)

$$\begin{pmatrix} \hat{S}_1 & \hat{S}_{12} \\ \hat{S}_{12} & \hat{S}_2 \end{pmatrix} = \begin{pmatrix} \cos(\theta(q)) & \sin(\theta(q)) \\ -\sin(\theta(q)) & \cos(\theta(q)) \end{pmatrix} \begin{pmatrix} \hat{V}_1 & 0 \\ 0 & \hat{V}_2 \end{pmatrix} \tag{11}$$

The molecular Hamiltonian in the diabatic basis then reads

$$\hat{H}^{(\mathrm{dia})} = \mathbf{1}\hat{T} + \begin{pmatrix} S_1(q) & S_{12}(q) \\ S_{12}(q) & S_2(q) \end{pmatrix} \tag{12}$$

The potential energy matrix now has smooth off-diagonal elements and is free of the derivative couplings. In contrast to the adiabatic representation, the couplings are now significantly delocalized. Note that, in general, eq 10 is only guaranteed to have a solution for two electronic states,[49] whereas the adiabatic representation can be easily used with more than two states. In practice, the conditions in eq 10 are approximated to yield a quasi-diabatization.[5,50] The choice of the mixing angle is then not unique and depends of the employed method. For a selection of possible quasi-diabatization methods see refs 5 and 51−55. A system where the electronic populations follow the adiabatic states during the time evolution is commonly labeled adiabatic, while a system that preserves its electronic character by following a single diabatic state is called diabatic.

The reduced electronic density matrix in the adiabatic basis is obtained by integrating over the nuclear degrees of freedom q

$$\rho_{\mathrm{el}} = \mathrm{Tr}_{\mathrm{nuc}}(\rho) = \begin{pmatrix} \langle\psi_1|\psi_1\rangle & \langle\psi_1|\psi_2\rangle \\ \langle\psi_2|\psi_1\rangle & \langle\psi_2|\psi_2\rangle \end{pmatrix} \tag{13}$$

where $\rho_{ii} = \langle\psi_i|\psi_i\rangle$ is the population of the ith electronic state and $\rho_{12} = \rho^*_{21} = \langle\psi_1|\psi_2\rangle$, i.e., the nuclear wavepacket overlap, is the electronic coherence between the two states. The wave functions $\psi_{1/2} \equiv \psi_{1/2}(q)$ are the nuclear wave packets on the adiabatic PESs 1 and 2, respectively (see eq 1). From eq 13, it becomes clear that the electronic coherence depends on the overlap of the nuclear wavepackets in different electronic states. Note that the reduced density matrix elements depend on the choice of basis, i.e., they will differ in the adiabatic and diabatic representations. A proper description of electronic coherences (off-diagonal elements) is important to properly reproduce the dynamics of the system. For the simulation of spectra, which involve broad-band XUV or X-ray pulses, electronic coherences and their proper description may also be important for accurate reproduction of the signal. If the probe pulse has a sufficiently broad bandwidth to cover several electronic states, electronic coherences ρ_{12} can be utilized for the detection of CoIns (see section 5.2).

1.2. Nuclear Dynamics Simulation Protocols

The simulation of transient spectra requires one to calculate the time evolution of the electronic and nuclear degrees of freedom after photoexciation. Two basic routes are available for the simulation: Semiclassical methods, which treat the nuclei classically, and wavepacket dynamics, which provide a fully quantum description of the nuclear degrees of freedom. A prominent example of semiclassical methods, which is used to simulate the excited state dynamics in systems with CoIns, is Tully's fewest switching surface hopping (FSSH) algorithm.[56,57] The basic idea is that the dynamics of the nuclei is described by classical mechanics coupled to the electronic degrees of freedom, which in turn are described quantum mechanically as a multilevel system (see refs 58 and 59 for recent reviews). A swarm of classical trajectories is launched on the adiabatic electronic surfaces, requiring only local information, such as single-point energies and nuclear gradients. When a trajectory reaches a region of nonzero nonadiabatic coupling, it may jump to another electronic state and continue its time evolution there. This method is computationally very efficient and allows one to include all nuclear degrees of freedom. However, special care has to be taken to account for the electronic coherences and its consequences for the hopping dynamics. Modern extensions of this algorithm address this problem by, e.g., introducing phases between different trajectories.[60] An alternative semiclassical approach is ab initio multiple spawning (AIMS).[61] Here, the nuclei are described by frozen Gaussian wavepackets whose equations of motion are also dictated by locally derived quantities (i.e., single-point energies and nuclear gradients). When a wavepacket reaches a region of nonzero nonadiabatic coupling, it spawns a new wavepacket on the approaching surface, intrinsically describing the electronic coherence properly.

The second strategy for obtaining the molecular dynamics is a full quantum description of the nuclear and electronic degrees of freedom. Since the size of the nuclear wave function grows exponentially with the number of vibrational modes, this method is limited to small molecules or a subset of reactive coordinates.[47,62−64] This requires evaluation of the global PES, either by fits to analytical functions,[65] in terms of a vibronic coupling Hamiltonian,[50] or explicitly. The coupled nuclear−electronic wavepacket dynamics can be then obtained by solution of the time-dependent Schrödinger equation on, e.g., spatial grids,[64] or multiconfiguration time-dependent Hartree (MCTDH).[66] The methods address the problem of the

DOI: 10.1021/acs.chemrev.7b00081
Chem. Rev. 2017, 117, 12165−12226

electronic coherences with high accuracy and further include quantum effects of the vibrational motion.

In the following sections, we survey a broad range of possible spectroscopic techniques and their numerical simulation. Starting with vibrational techniques in sections 2 and 3 that rely on detection schemes with short IR and optical pulses, we continue with optical valence electronic techniques (section 4). Finally, we describe cutting edge electronic Raman techniques performed with X-ray pulses (section 5) that carry higher levels of information[67−69] through the use of core electron excitations. While the vibrational techniques monitor the vibrational frequency shifts during the nonadiabatic dynamics, the optical detection of electronic degrees of freedom offers a different window into the nonadiabatic dynamics in the vicinity of CoIns. This inherently benefits from the large pulse bandwidth and temporal resolution down to the attosecond time scale. The theoretical formalism of electronic probe techniques is closely related to the vibrational (IR or Raman) probe techniques. For example, the X-ray Raman scheme is conceptually closely related to a vibrational Raman scheme but differs in the participating intermediate states (Figure 2). Core excited states rather than low-lying valence excited states serve as intermediates. For clarity, we present below the various simulation protocols for infrared signals and comment when appropriate about how they can be adapted to other signals.

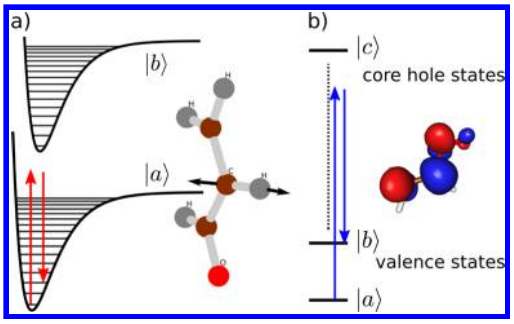

Figure 2. Schematic of vibrational (optical) Raman spectroscopy (a) vs electronic (X-ray) Raman spectroscopy (b).

2. SIMULATION PROTOCOLS FOR UV−VIS PUMP AND BROAD-BAND IR PROBE (UV/IR) SIGNALS

We start by discussing theoretical aspects of nonlinear optical signals that can be employed for capturing nonadiabatic processes. Various simulation protocols are presented for the simplest and most intuitive UV−vis pump IR probe (UV/IR) signal. The different protocols offer a hierarchy of approximations that start from a quantum treatment of electronic and nuclear degrees of freedom, moving on to semiclassical models where only a few degrees of freedom treated quantum mechanically are modulated by a classical reaction coordinate, to incoherent averaging over contributions arising from different product states. We note that the formalism is applicable to a variety of vibrational detection modes, like stimulated Raman spectroscopy (SRS) probe signals, covered in detail in section 3 where the initial preparation by an actinic pulse and the genuine time-frequency resolution of these measurements are addressed. Our analysis is based on a perturbative expansion in the external fields in which the signals are expressed in terms of response functions. A different and powerful approach is based on a nonperturbative propagation of the driven system[70] which will not be reviewed here. It has been widely and successfully employed to FSRS[71] and 2D-UVvis[72−74] techniques. An in-depth discussion of the different possible detection modes and their formal theoretical description can be found in ref 75.

The formalism outlined in this section allows one to consider the entire detection process, including the actinic pump pulse and the IR or Raman probe sequence, as a single four-wave or six-wave mixing event, respectively. In general, the actinic pump can impulsively create coherences in the vibrational state manifold. In that case, the preparation process due to the actinic pump pulse has to be explicitly considered in the description of the *n*-wave mixing process. If, in contrast, the actinic pulse is short enough to impulsively trigger bath dynamics but long compared to the vibrational periods, the limited bandwidth can only create populations but not coherences in the relevant vibrational modes. We can then exclude the actinic pump from the description of the optical process, and the process can be viewed as a four-wave-mixing (FWM) experiment from a nonstationary state created by the actinic pump and characterized by a generalized susceptibility. This simpler, widely used approach only holds in a limited parameter regime. If no dynamics is launched and the prepared state is stationary then the pulsed experiment can be viewed as many stationary IR or Raman experiments done in parallel and the pulse duration becomes immaterial.

2.1. Loop Diagram Representation of Frequency-Dispersed Transmission Signals

Stimulated optical signals are defined as the energy change of the detected electromagnetic field. The radiation−matter interaction Hamiltonian is

$$H'(t) = V^{\dagger}(t)\mathcal{E}(t) + V(t)\mathcal{E}^{\dagger}(t) \tag{14}$$

where $\tilde{V}(t) = V(t) + V^{\dagger}(t)$ is a dipole operator in the Heisenberg picture and $E(t) = \mathcal{E}(t) + \mathcal{E}^{\dagger}(t)$ is the electric field operator. Both $\tilde{V}$ and E are separated into positive $(V^{\dagger}(t)\mathcal{E}(t))$ and negative $(V(t)\mathcal{E}^{\dagger}(t))$ frequency components (annihilation and creation photon operators, respectively). The dipole operator is further given by the sum of the electronic and nuclear dipole moments $V(t) = V_{\mathrm{e}}(t) + V_{\mathrm{n}}(t)$. Various optical signals can be defined as the change of the energy of the electromagnetic field

$$S = \int_{-\infty}^{\infty} \frac{\mathrm{d}}{\mathrm{d}t}\langle \mathcal{E}^{\dagger}(t)\mathcal{E}(t)\rangle \mathrm{d}t \tag{15}$$

The Heisenberg equation of motion for the field operator

$$\frac{\mathrm{d}}{\mathrm{d}t}\mathcal{E}(t) = \frac{i}{\hbar}[H, \mathcal{E}(t)] + \left(\frac{\partial A}{\partial t}\right)_{H} \tag{16}$$

then gives for the above integrated signal

$$\begin{aligned} S(\Gamma) &= \frac{2}{\hbar}\int_{-\infty}^{\infty} \mathrm{d}t' \mathcal{I} P(t')\mathcal{E}^{*}(t') \\ &= \frac{2}{\hbar}\int_{-\infty}^{\infty} \frac{\mathrm{d}\omega'}{2\pi} \mathcal{I} P(\omega')\mathcal{E}^{*}(\omega') \end{aligned} \tag{17}$$

where we replaced the field operators with their classical envelopes after evaluating the commutator in eq 16, Γ collectively denotes a set of parameters that characterize the various laser pulses, $\mathcal{I}$ denotes the imaginary part, and

$$P(\omega) = \int_{-\infty}^{\infty} \mathrm{d}t P(t) e^{i\omega t} \tag{18}$$

where $P(t) = \langle V(t)\rangle$ is the nonlinear polarization that arises from the interaction with the pump and the probe pulses. The angular brackets denote $\langle\ldots\rangle = \mathrm{Tr}[\rho(t)\ldots]$ with the density operator $\rho(t)$ defined in the joint field–matter space of the entire system. In practice, the temporal or spectral range of the integrations in eq 17 is restricted by the response function of the detector. If the detector contains a narrow time gate with nearly δ function response $\delta(t' - t)$, eq 17 yields

$$S_{\mathrm{TG}}(t;\,\Gamma) = \frac{2}{\hbar}\mathcal{I}P(t)\mathcal{E}^*(t) \tag{19}$$

Similarly, if the detector consists of a spectrometer with narrow frequency response $\delta(\omega' - \omega)$, we obtain the frequency-gated signal

$$S_{\mathrm{FG}}(\omega;\,\Gamma) = \frac{2}{\hbar}\mathcal{I}P(\omega)\mathcal{E}^*(\omega) \tag{20}$$

Note that the two signals of eqs 19 and 20 are different and are not related by a simple Fourier transform. A Wigner spectrogram representation[77−79] with arbitrary temporal and spectral gates was developed in ref 80 for the integrated pump−probe signals eq 17.

We shall use loop diagrams[81] to describe the more detailed time- or frequency-gated signals, eqs 19 and 20, respectively. For clarity, we focus on the frequency-gated expressions in the following. The corresponding time-gated signals are given in the Appendix, Time-Gated Signals. We start with the UV/IR signal as sketched in Figure 3. Considering frequency dispersed infrared detection (FDIR), the pump pulse centered at time $\tau_3 = 0$ promotes the system from its ground electronic state g to the vibrational state a of an excited electronic state and launches the vibrational dynamics. The IR probe pulse centered around $\tau_3 = T$ can then either stimulate emission that couples the vibrational state a and lower vibrational state d (cf. level scheme (i) in Figure 3a) or an absorption to higher vibrational state c (level scheme (ii)). The transient absorption (TA) signal is defined as the change in probe intensity and is either time gated, eq 19, or frequency gated, eq 20. Both can be represented by the loop diagrams shown in Figure 3b which contain four field−matter interactions—two with each pulse—and are thus somewhat simpler than SRS (see section 3.3) that involves six radiation−matter interactions. Loop diagrams are pictorial representations of Hilbert-space expectation values $\langle\Psi(t)|\hat{V}(t)|\Psi(t)\rangle$. They differ from the Feynman ladder diagrams (which are representations of the Liouville-space expectation value $\langle\langle \mathbf{1}|\rho(t)\rangle\rangle$) in that field−matter interactions on the ket and bra are no longer relatively time ordered. This is easily understood since both ket and bra are then just copies of the same perturbatively expanded state $|\Psi(t)\rangle$ and allows signals of nondissipative systems to be represented more compactly. Diagram rules are given in ref 81. Note that the signals given by eqs 19 and 20 are expressed in terms of $\mathcal{E}^*$, which makes the arrow corresponding the last interaction pointing to the left. We further choose the last interaction to occur on the left branch, which corresponds to the ket part of the density matrix. This arbitrary choice removes any ambiguity in the diagram rules without loss of generality.

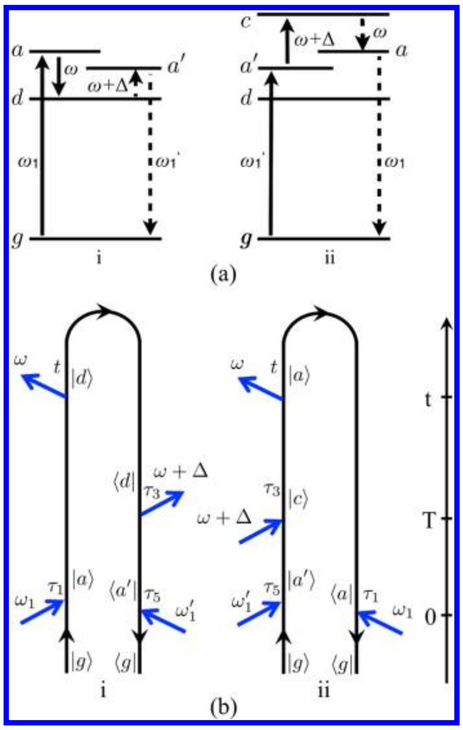

Figure 3. UV/IR signal with FDIR detection: (a) Level scheme indicating the excitation pathways on the ket side (solid arrows) and the bra side (dashed arrows). (b) Loop diagrams describing the UV/IR technique; for details see text. Reproduced with permission from ref 76. Copyright 2013 Royal Society of Chemistry.

The electric field consists of the pump field 1 and a probe field 2

$$\mathcal{E}(t) = \mathcal{E}_1(t) + \mathcal{E}_2(t - T) \tag{21}$$

where T represents the delay of the probe pulse relative to the pump. The signal is given by the two loop diagrams shown in Figure 3b, plus their complex conjugates. These give for the frequency-gated signal eq 20

$$S_{\mathrm{IR}}(\omega,\,T) = \mathcal{I}\int_{-\infty}^{\infty}\frac{\mathrm{d}\Delta}{2\pi}\mathcal{E}_2^*(\omega)\mathcal{E}_2(\omega+\Delta)\tilde{S}_{\mathrm{IR}}(\omega,\,T;\,\Delta) \tag{22}$$

where the auxiliary Δ-dispersed signal is given by the two diagrams $\tilde{S}_{\mathrm{IR}}(\omega,\,T;\,\Delta) = \tilde{S}_{\mathrm{IR}}^{(i)}(\omega, T;\,\Delta) + \tilde{S}_{\mathrm{IR}}^{(ii)}(\omega,\,T;\,\Delta)$

$$\begin{aligned}\tilde{S}_{\mathrm{IR}}^{(i)}(\omega,\,T;\,\Delta) = {}&\frac{2}{\hbar}\int_{-\infty}^{\infty}\mathrm{d}t\int_{-\infty}^{t}\mathrm{d}\tau_1\int_{-\infty}^{t}\mathrm{d}\tau_3\int_{-\infty}^{\tau_3}\mathrm{d}\tau_5\\ &\times\mathcal{E}_1^*(\tau_5)\mathcal{E}_1(\tau_1)e^{i\omega(t-\tau_3)-i\Delta(\tau_3-T)}\\ &\times\langle V_{\mathrm{e}}G^\dagger(\tau_3,\,\tau_5)V_{\mathrm{n}}^\dagger G^\dagger(t,\,\tau_3)V_{\mathrm{n}}G(t,\,\tau_1)V_{\mathrm{e}}^\dagger\rangle\end{aligned} \tag{23}$$

$$\begin{aligned}\tilde{S}_{\mathrm{IR}}^{(ii)}(\omega,\,T;\,\Delta) = {}&\frac{2}{\hbar}\int_{-\infty}^{\infty}\mathrm{d}t\int_{-\infty}^{t}\mathrm{d}\tau_1\int_{-\infty}^{t}\mathrm{d}\tau_3\int_{-\infty}^{\tau_3}\mathrm{d}\tau_5\\ &\times\mathcal{E}_1(\tau_5)\mathcal{E}_1^*(\tau_1)e^{i\omega(t-\tau_3)-i\Delta(\tau_3-T)}\\ &\times\langle V_{\mathrm{e}}G^\dagger(t,\,\tau_1)V_{\mathrm{n}}G(t,\,\tau_3)V_{\mathrm{n}}^\dagger G(\tau_3,\,\tau_5)V_{\mathrm{e}}^\dagger\rangle\end{aligned} \tag{24}$$

Note that in eqs 23 and 24 the Δ-dispersed signal $\tilde{S}(\omega,T;\,\Delta)$ accounts for the interaction with the pump pulse $\mathcal{E}_1$ while the observable UV/IR signal $S_{\mathrm{IR}}(\omega,T)$, involves two additional interactions with $\mathcal{E}_2$. $\tilde{S}(\omega,T;\,\Delta)$ represents the contribution of the ω and $\omega + \Delta$ frequency components of $\mathcal{E}_2$ to the signal, where ω is the detected frequency. $\tilde{S}(\omega,T;\,\Delta)$ contains more information than the experimental observable signal and demonstrates the conjugate time−frequency resolution inherent to the UV/IR experiment, in detail analyzed in sections 2.3 and 3.3.1. The observable signal is obtained by integration over Δ. $G(t_1,t_2) = (-i/\hbar)\theta(t_1 - t_2)\mathrm{e}^{-iH(t_1-t_2)}$ denotes the retarded

Green's function. Even though this Green's function only depends on the difference of its two time arguments, we retain both arguments and write $G(t_1,t_2)$ rather than $G(t_1 - t_2)$. This is done since in the reduced (semiclassical) description developed below (cf. section 2.2.2) if the system is coupled to some stochastic bath degrees of freedom, time-translational invariance is lost and G then depends on both time arguments rather than on their difference. The corresponding time-gated signal (eq 19) is given in the Appendix (eqs 86 and 87). Equations 23 and 24 may be simplified further under the condition of an impulsive pump. We can then set $\mathcal{E}_1(\tau) = \mathcal{E}_1\delta(\tau)$, and the τ_1 and τ_5 integrations can be eliminated.

Diagram (*i*) (eq 23) represents a forward and backward time-evolving vibrational wavepacket. First, the pulse $\mathcal{E}_1$ electronically excites the molecule via $V_e^\dagger$. The wave function then propagates forward in time from τ_1 to t. Then the IR probe pulse $\mathcal{E}_2$ de-excites the vibrational transition to the lower vibrational level via V_n, which then propagates backward in time from t to τ_3. Pulse $\mathcal{E}_2$ excites the vibration via $V_n^\dagger$, and the wave function propagates backward in time from τ_3 to τ_5. The final de-excitation by pulse $\mathcal{E}_1$ returns the system to its initial state by acting with V_e. Diagram (*ii*) (eq 24) can be interpreted similarly: following initial electronic excitation the wave function propagates forward in time from τ_5 to τ_3. At this point a vibrational excitation promotes it to the higher vibrational state and the wave function propagates forward in time from τ_3 to t. After vibrational de-excitation it then propagates backward from t to τ_1 where an electronic excitation brings the system back into its initial ground state.

2.2. Simulation Toolbox for Nonlinear Optical Signals with Broad-Band Probe Pulses

We now present a general analysis of the central microscopic matter quantity, i.e., the 4-point matter correlation function of eqs 23 and 24, and derive closed expressions that can be used for microscopic quantum simulations of UV/IR signals. In section 3 we adopt the same techniques to Raman probe signals. Three representations for these correlation functions, each suggesting a different simulation strategy, will be presented.

2.2.1. First Simulation Protocol: Numerical Propagation of the Wave Function.

The first protocol includes all relevant electronic and nuclear (including bath) degrees of freedom explicitly and involves the numerical propagation of the wave function. This is the most general, expensive, and accurate method.[82,83] The central molecular quantity for microscopic simulations of UV/IR signals, eqs 22−24 (and, as will be demonstrated in section 3.3, for the SRS technique as well), is the 4-point matter correlation function given in the time domain

$$F_i^{\mathrm{IR}}(\tau_1, t, \tau_3, \tau_5) = \langle V_e G^\dagger(\tau_3, \tau_5) V_n^\dagger G^\dagger(t, \tau_3) V_n G(t, \tau_1) V_e^\dagger \rangle \tag{25}$$

$$F_{ii}^{\mathrm{IR}}(\tau_1, t, \tau_3, \tau_5) = \langle V_e G^\dagger(t, \tau_1) V_n G(t, \tau_3) V_n^\dagger G(\tau_3, \tau_5) V_e^\dagger \rangle \tag{26}$$

The frequency domain form is given in the Appendix, eqs 95 and 96. The observable UV/IR signal can be obtained from eqs 25 and 26 by a convolution with respective pump $\mathcal{E}_1$ and probe fields $\mathcal{E}_2$ at the interaction times τ_1, τ_3, and τ_5, respectively (cf. eqs 22−24). Equations 25 and 26 can be understood using a forward (G) and backward ($G^\dagger$) time-evolving vibrational wavepacket. The free-evolution periods can be directly read from the diagrams and are separated by interactions with the laser pulses, mediated by respective dipole operators $V_{n/e}$. For illustration, let us describe eq 25 and diagram (*i*) of the UV/IR technique (Figure 3 b): First, the UV−vis pump pulse $\mathcal{E}_p(\omega_1)$ brings the molecule via $V_e^\dagger$ to an electronic excited, vibrational state $|a\rangle$, followed by forward propagation of the wave function in time from τ_1 to t. The resonant IR probe pulse $\mathcal{E}_2$ then de-excites the system to a different vibrational level $|d\rangle$ via V_n, which then propagates backward in time from t to τ_3 on the other branch of the loop. Pulse $\mathcal{E}_2$ further excites the vibrational mode via $V_n^\dagger$ to $|a'\rangle$, followed by the third free-evolution period backward in time (τ_3 to τ_5). Finally, interaction with the optical pulse $\mathcal{E}_1$ via V_e returns the system to the final state. Diagram (*ii*) can be interpreted similarly (eq 26) but corresponds to IR absorption and excitation to a higher vibrational state vibrational level $|c\rangle$ with two forward evolution periods on the left branch of the loop.

The simulation protocol based on these equations involves both the forward (G) and the backward ($G^\dagger$) propagation of the entire wave function in the space of all electronic and nuclear degrees of freedom. This task can be carried out by numerically exact propagation techniques, based on the split-operator Fourier transform, the short iterative Lanczos method, or a Chebyshev expansion,[82,84] where the wave function is commonly expanded in the set of orthogonal eigenstates of H. Nonadiabatic effects can be accounted for either in a diabatic or in adiabatic basis of the participating electronic states.[64] The major drawback of this numerically exact treatment is that the computational effort and storage requirements grow exponentially with the number of degrees of freedom, which limits their application to molecular systems composed of only a few degrees of freedom. The change to a nonorthogonal representation of the time-dependent wave function allows one to evaluate the Trotter expansion analytically, avoiding the unfavorable scaling behavior, which is accordingly not an intrinsic property of the powerful propagators.[83,85] The approximate MCTDH method[86] formally still scales exponentially, but superior scaling and low memory requirements compared to the exact propagation methods can be achieved if the number of degrees of freedom and contraction coefficients is large. A major drawback of all propagation methods is that the global multidimensional PES has to be known a priori. Approximate direct quantum dynamical approaches like, e.g., the variational multiconfiguration Gaussian wavepacket method[87−89] or AIMS,[90−92] which rely on Gaussian functions as a basis set, circumvent this shortcoming as the PES is only sampled on-the-fly in the part of space where it is actually required.

In some applications, it may be desirable to only consider a few vibrational modes explicitly and treat the remaining ones classically. Even in this case, we may use the Green's functions expressions, eqs 23 and 24, propagated forward and backward along the loop under an effective time-dependent Hamiltonian.[93] This method is a compromise between a full quantum and a classical dynamical description. Its numerical implementation was developed in ref 94 and demonstrated for the calculation of FSRS spectra of acrolein subject to nonadiabatic relaxation. A few spectator, e.g., C−H stretch modes are chosen as marker bands, which are then treated by direct propagation under the influence of a time-dependent potential. First, the molecular dynamics is calculated semiclassically within the framework of surface-hopping methods.[56,59] Each trajectory is then used to provide an effective potential for the marker bands. The global subspace potential in the active marker bands is calculated explicitly for each time step of the trajectory. The inclusion of anharmonicities and intermode couplings is then straightforward.

The separation into quantum and classical subsystems, where the classical subsystem imposes time-dependent fluctuations of the Hamiltonian along a collective bath coordinate, provides a microscopic way for incorporating non-Gaussian fluctuations and respective line shapes. It is commonly employed for the simulation of 2D spectroscopic signals in the IR spectral region by direct propagation of a time-dependent Hamiltonian along the configurations imposed by a classical trajectory.[93,95,96] For electronic excited states, limitations arise from the absence of back coupling between the quantum system and the classical system. Thus, nuclear relaxation effects like the dynamic Stokes shift are not accounted for. Moreover, thermal equilibration of the branching of populations, i.e., the detailed balance limit between reaction channels, is not guaranteed. Section 4.2 provides an overview of recent efforts to address these limitations by combining Tully's surface-hopping methodology with direct propagation algorithms of a time-dependent Hamiltonian along classical trajectory configurations.

2.2.2. Second Simulation Protocol: Snapshot Limit; Sum Over States (SOS) Approximation. An alternative simulation protocol is based on an expansion of matter correlation functions (eqs 25 and 26) in the eigenstates of the total system. If all bath degrees of freedom are included explicitly, the approach is formally equivalent to the numerical propagation of the wave function described in section 2.2.1. Again, in this approach bath degrees of freedom cannot be eliminated and must be included explicitly. The resulting sum over states (SOS) expansion of the signal then requires diagonalization of the total vibrational Hamiltonian. Starting with eqs 23 and 24, the frequency-gated UV/IR signal can be expressed

$$S_{\mathrm{IR}}^{(i)}(\omega,\, T) = -\mathcal{I}\frac{2i}{\hbar^4}\sum_{a,a',d}\frac{\mu_{ga'}\mu_{ag}^{*}\mu_{a'd}^{*}\mu_{ad}e^{-(i\omega_{aa'}+\gamma_{aa'})T}}{\omega-\omega_{ad}+i\gamma_{ad}}$$
$$\times\,\mathcal{E}_2^{*}(\omega)\mathcal{E}_2(\omega-\omega_{aa'}+i\gamma_{aa'})\mathcal{E}_1^{*}(\omega_{a'}+i\gamma_{a'})\mathcal{E}_1(\omega_a-i\gamma_a) \tag{27}$$

$$S_{\mathrm{IR}}^{(ii)}(\omega,\, T) = -\mathcal{I}\frac{2i}{\hbar^4}\sum_{a,a',c}\frac{\mu_{ga'}\mu_{ag}^{*}\mu_{a'c}^{*}\mu_{ac}e^{-(i\omega_{a'a}+\gamma_{a'a})T}}{\omega-\omega_{a'c}+i\gamma_{a'c}}$$
$$\times\,\mathcal{E}_2^{*}(\omega)\mathcal{E}_2(\omega-\omega_{a'a}+i\gamma_{a'a})\mathcal{E}_1^{*}(\omega_{a'}+i\gamma_{a'})\mathcal{E}_1(\omega_a-i\gamma_a) \tag{28}$$

The corresponding time-gated signals are given in the Appendix, eqs 90 and 91. The frequency-dispersed UV/IR signal, eqs 27 and 28, depends on the product $\mathcal{E}_2^{*}(\omega)\mathcal{E}_2(\omega-\omega_{a'a}+i\gamma_{a'a})$. This creates an uncertainty during the interaction time with the probe pulse which is governed by the inverse time scale of vibrational dynamics (i.e., the spectral width of $\omega_{a'a}$) and bath dephasing rate $\gamma_{a'a}$. The quantum pathways selected by the dynamics yield therefore the effective bandwidth of the probe pulse that interacts with the system. This introduces uncertainty to the interaction time τ_3 (cf. Figure 3b) stemming from the finite bath's dynamics time scale. The corresponding measurement cannot be viewed as a stroboscopic snapshot of the system but is determined by the vibrational dynamics represented by the coherence between a and a'. The bandwidth of the pump pulse which prepares the vibrational coherence of the system is crucial. The energy spread of $\omega_{aa'}$ is controlled by the pump bandwidth and is also a measure of the inverse time scale of the matter dynamics initiated by the pump. If a single state is selected ($a = a'$) then there is no dynamics and the same signal can be generated by a continuous wave (CW) pump tuned generally to level a, and the pump duration then becomes immaterial. A broad distribution of vibrational states will result in a fast dynamics that is affected by the pump duration. The broad-band technique amounts to multiple CW experiments in parallel, which is experimentally convenient since it does not require one to scan the frequency but reveals no additional information beyond the two-mode experiment. With initiation by an actinic pump pulse, which prepares a wavepacket with different a, a' pairs, the technique may be viewed as many FWM experiments done in parallel, it is essentially a broad-band FWM which only has three modes (note that CARS is a four-mode process).

In the SOS protocol, the basis set expansion has to cover the complete vibrational dynamics under investigation, which can be tedious or even impossible for complex reactive systems or nonadiabatic relaxation via multiple electronic states. Diagonalization of the resulting Hamiltonian is a nontrivial task. Model Hamiltonians may be used to reduce the system size and provide an affordable simulation. For example, exciton Hamiltonians are commonly used to describe multiple excitations in chromophore aggregates.[97] Here, the resulting SOS expansion of the signal only requires the diagonalization of an effective vibrational Hamiltonian. This offers a numerically more tractable algorithm when it is possible to truncate the relevant phase space and provides useful insights and a convenient computational algorithm. Once the eigenstates in the reduced dimensional model space are obtained, this protocol allows the straightforward interpretation of the signals. We note that this highly intuitive snapshot limit simplifies the calculation but is not always satisfied when we have continuously evolving states (e.g., the modulation of a vibrational mode along a reaction coordinate, cf. section 2.2.3). We can then define distinct evolution and detection segments where, during the latter, the system eigenstates are assumed to be frozen. Employing an X-ray Raman detection mode that monitors the electronic degrees of freedom, this protocol was successfully applied to investigate the nonadiabatic ring-opening dynamics of furan (cf. section 5.1).

2.2.3. Third Simulation Protocol: Frequency Modulation Induced by Coupling to a Classical Bath. An alternative simple and intuitive description can be developed by treating some (bath) degrees of freedom as classical and assuming that they modulate the vibrational frequencies of interest. We start with the UV/IR signal employed to detect excited vibronic states. Starting from eqs 23 and 24 and assuming that the pump pulse $\mathcal{E}_1$ is impulsive, the semiclassical Δ-dispersed (eq 24) signal reads

$$\tilde{S}_{\mathrm{IR}}(\omega,\, T;\, \Delta) = -\frac{2i}{\hbar^4}\int_{-\infty}^{\infty}\mathrm{d}\tau_3\int_{\tau_3}^{\infty}\mathrm{d}t$$
$$\times\,|\mathcal{E}_1|^2\mathrm{e}^{i\omega(t-T)}\mathrm{e}^{-i(\omega+\Delta)(\tau_3-T)}\sum_a|\mu_{ag}|^2e^{-2\gamma_a t}$$
$$\times\left[\sum_c|\mu_{ac}|^2\mathrm{e}^{-i\int_{\tau_3}^{t}\omega_{ac}(t')\mathrm{d}t'}+\sum_d|\mu_{ad}|^2\mathrm{e}^{i\int_{\tau_3}^{t}\omega_{ad}(t')\mathrm{d}t'}\right] \tag{29}$$

where $\omega_{\alpha\beta} \equiv |\omega_\alpha - \omega_\beta|$. Ensemble averaging $\langle ... \rangle_e$ over the classical set of trajectories is performed at the signal level $S_{\mathrm{IR}}(\omega,T)$. Similarly, one can derive the corresponding SRS result when the extra Raman pump pulse is a narrow band and can be approximated as $\mathcal{E}_3(t) = \mathcal{E}_3\mathrm{e}^{-i\omega_3(t-T)}$ (cf. section 3.3). Equation 29 involves a path integral over the stochastic vibrational frequencies $\omega_{ac}(t)$ and $\omega_{ad}(t)$. The signal depends not only on the initial and final value of the vibrational frequency $\omega_{\nu\nu'}$ but also on the entire pathway from time T to the time when the polarization decays to zero. In the semiclassical protocol of eq 29, the system is partitioned into a classical bath while retaining the quantum character of only a few vibrational modes ($\omega_{ac}(t)$ and $\omega_{ad}(t)$). The time-dependent frequency $\omega_{\nu,\nu'}(t)$ in eq 29 can be calculated by running classical molecular dynamics trajectories. For nonreactive systems (i.e., no chemical bonds are broken or formed) evolving on a single adiabatic PES (i.e., the Born–Oppenheimer approximation remains valid), common molecular dynamics simulations can be used which scale by N^2 if all pairwise electrostatic and van der Waals interactions are explicitly accounted for. The computational cost can be further reduced to linear scaling by suitable cutoffs. The quantum character of the vibrations under investigation can be retained by collective solvent coordinates which allow one to map the classical dynamics onto ab initio-derived electrostatic maps.[98−100]

If the process under investigation is characterized by ultrafast relaxation in the vicinity of a conical intersection, as commonly observed in photoreactions, the breakdown of the Born–Oppenheimer approximation requires that one treats the system by nonadiabatic on-the-fly molecular dynamics.[101] On the basis of the independent trajectory approximation, the nuclear wavepacket is approximated by a swarm of independently evolving trajectories where, within the framework of Tully's fewest switches trajectory surface hopping,[56,57] relaxation between different electronic states is induced by the nonadiabatic couplings. Here, the numerical effort of the dynamics is shifted to the calculation of excited state gradients and nonadiabatic couplings. The construction of global PESs is avoided as only the relevant configuration space is explored during the dynamics. The quantum character of the vibrations is reconstructed by evaluating the excited state Hessian. The restriction to a few vibrational degrees of freedom allows for an efficient algorithm for the calculation of the semiclassical signal which is based on a mode-tracking procedure[102] where only the desired frequencies and normal mode vectors are obtained. As the construction of the complete Hessian matrix is avoided, linear scaling with the number of considered vibrational modes can be achieved.[103] Employing C═O and C−H stretch vibrations as spectator modes this protocol was successfully applied to investigate UV/IR and FSRS signals of nonadiabatic relaxation of the ribonucleic acid (RNA) base uracil (cf. sections 2.4 and 3.3).

2.2.4. Fourth Simulation Protocol: Stochastic Liouville Equation (SLE) for Vibronic Line Shapes. The three protocols presented so far target the wave function and operate in Hilbert space. Reduced descriptions that eliminate bath degrees of freedom can often be more conveniently described in terms of the density matrix in Liouville space. Here we develop such a semiclassical protocol that assumes some fluctuating Hamiltonian parameters due to coupling to a bath described by collective coordinates. Unlike the Hilbert space protocol (section 2.2.3) in which a frequency trajectory is inserted into the wave function description of the signal and the bath degrees of freedom are not explicitly included, the SLE acts in the joint system-plus-bath Liouville (rather than Hilbert) space.[104−106] It assumes that the system is affected by the bath but the bath undergoes an independent stochastic dynamics that is not affected by the system, and system/bath entanglement is thus neglected. If the bath is harmonic and only modulates the transition frequencies, one can solve the dynamics analytically using the cumulant expansion,[107] since the fluctuations are Gaussian, and avoid the SLE. The SLE can describe a broader class of models with continuous or discrete collective coordinates which may be coupled to arbitrary Hamiltonian parameters (not just the frequencies). Adding the bath makes the calculation more expensive but still less demanding than the complete microscopic simulation involving all relevant degrees of freedom. The SLE, originally developed by Kubo and Anderson in nuclear magnetic resonance,[104−106] thus provides an affordable and practical level for modeling complex line shapes.

The SLE assumes that the bath dynamics is described by a Markovian master equation and the joint dynamics of the system-plus-bath density matrix ρ is given by

$$\frac{\mathrm{d}\rho}{\mathrm{d}t} = \hat{\mathcal{L}}\rho(t) = -\frac{i}{\hbar}[H, \rho(t)] + \hat{L}\rho(t) \tag{30}$$

Here, the superoperator $\hat{L}$ describes the stochastic Markovian dynamics of the bath, H is the system Hamiltonian that depends parametrically on the bath, and the Liouville operator $\hat{\mathcal{L}}$ is diagonal in the vibrational space.

We shall apply the SLE to the two-state jump (TSJ) model, which is the simplest stochastic model for line shapes. In this model, the bath has two states that, adopting spin terminology, are denoted "up" + and "down" −. The system has two vibrational states a and c with ω_{ac} being the vibrational frequency unperturbed by the bath. The TSJ coupling to the vibrations is introduced by assuming that the vibrational frequency depends on the bath states: $\omega_+ \equiv \omega_{ac} + \delta$ for + and $\omega_- \equiv \omega_{ac} - \delta$ for −. The TSJ model is a special case of the semiclassical expressions given earlier. It yields simple closed expressions for the Green's functions. We first note from eq 30 that, unlike the UV/IR signal (eqs 22−24) that has been written using loop diagrams in Hilbert space, the TSJ model requires a fully time-ordered description in Liouville space. Each of the loop diagrams in Figure 3b should be split into several ladder diagrams.[108] However, in the case of an impulsive actinic pulse $\mathcal{E}_\mathrm{p}(t) = \mathcal{E}_\mathrm{p}\delta(t)$, each loop diagram corresponds to a single ladder diagram and the total number of diagrams will remain the same. Second, in Liouville space the signal may be recast using the matter quantity given by eqs 25 and 26, where we assume that excitation by the actinic pulse prepares the state u.

The generalization to n states (multistage jump model)[109,110] and after evaluating the time integrals in eq 153 (cf. Appendix), we obtain

$$\tilde{S}^{(i)}_{\mathrm{IR}}(\omega, T; \Delta) = \frac{-2i}{\hbar^2}|\mathcal{E}_1|^2 \sum_{a,c} \mu_{ac}^2 |V_{ag}|^2 \mathrm{e}^{i\Delta T} \times \langle\langle \mathbf{1}|\mathcal{G}_{ac,ac}(\omega)\mathcal{G}_{aa,aa}(-\Delta)|\rho_0\rangle\rangle_S \tag{31}$$

Following eq 144 (cf. Appendix), we introduce the population of state a after interaction with the UV−vis pump pulse

$$\rho_{aa}^{(s)}(t) = |\mathcal{E}_1|^2 |V_{ag}|^2 \mathcal{G}_{aa,aa}(t)|\rho_0\rangle\rangle_S \tag{32}$$

Substituting eq 32 into the signal expression eq 152 and eq 153 gives

$$S_{\mathrm{IR}}(\omega, T) = \mathcal{I}\frac{-2i}{\hbar^2}\mathcal{E}_2^*(\omega) \sum_{a,c} \mu_{ac}^2 \sum_s \mathcal{G}_{ac,ac,s}(\omega) \times \int_{-\infty}^{\infty} \frac{\mathrm{d}\Delta}{2\pi} \mathcal{E}_2(\omega + \Delta)\mathrm{e}^{i\Delta T} \rho_{aa}^{(s)}(-\Delta) \tag{33}$$

where $\rho_{aa}(-\Delta)$ is the Fourier transform of the population time evolution of state a, $\mathcal{G}_{ac,ac}(\omega)$ is a frequency-domain Green's function, and $\sum_s$ represents the sum over bath states. It follows from eq 33 that the Δ integration represents an integral over the bandwidth corresponding to the inverse dephasing time scale. This integral is generally a complex number. Therefore, the signal (eq 33) is governed by both real and imaginary parts of the coherence Green's function $\mathcal{G}_{ac,ac}(\omega)$ and thus contains both absorptive and dispersive spectral features. Dispersive features observed in SRS[110−113] can arise when the dynamics under investigation proceeds on a comparable time scale to the vibrational dephasing. We note that the electronically off-resonant SRS signal, discussed in detail in section 3.3, is formally analogous to the UV/IR signal. Even though these signals represent different physical processes and even involve different numbers of field−matter interactions, they can be described using very similar diagrams. By substitutions of operators $V_n \to \alpha_n$ and the infrared detection frequency ω by the Raman shift $\omega - \omega_3$, the 4-point matter correlation function expression of the UV/IR signal (eqs 22−24) can be transformed to the respective correlation function of the SRS technique (cf. eqs 48−50).

When fluctuations are slow one can neglect the jump dynamics during the dephasing time. We can then replace $\mathcal{E}_2(\omega + \Delta) \simeq \mathcal{E}_2(\omega)$, the integral over Δ yields $\rho_{aa}(T)$, and we obtain the static averaged signal

$$S_{\rm IR}(\omega, T) = \sum_a \sum_s S^{(s)}_{{\rm IR},a}(\omega)\rho^{(s)}_{aa}(T) \tag{34}$$

with

$$S^{(s)}_{{\rm IR},a}(\omega) = -\mathcal{R}\frac{2}{\hbar^2}|\mathcal{E}_2(\omega)|^2|\mathcal{E}_1|^2 \sum_c \mu^2_{ac}\mathcal{G}_{ac,ac,s}(\omega) \tag{35}$$

where $\mathcal{R}$ denotes the real part. Unlike the general UV/IR signal, eq 33, the static averaging limit, eq 34, only describes absorptive line shapes since the bath dynamics is neglected during the dephasing time. Furthermore, the time evolution in this case is governed by a snapshot of the populations of the excited states. Therefore, eqs 33 and 34 are expected to be different at short times and to become more similar at longer time. This was demonstrated for the FSRS signal in refs 109 and 110. Note that since the signal (eq 33) is written in terms of Green's functions expanded in SOS, it can be applied to complex systems with multiple vibrations and various baths coupled to these vibrations. In a typical chemical reaction, such as isomerization, very few collective coordinates are involved. These degrees of freedom are typically treated explicitly, while the remaining vibrational and bath degrees of freedom can be approximated as harmonic vibrations.

2.3. Interplay of Temporal and Spectral Resolution in UV/IR Signals

The picture emerging from the loop diagrammatic representation (Figure 3b and eqs 22−24) is that the effective temporal and spectral resolution of the UV/IR technique is affected by but not solely controlled by experimental knobs. This holds for any broad-band probe detection,[80] such as the Raman-based schemes discussed in section 3.3. Formally, the uncertainties ΔT and $\Delta\omega$ associated with the delay time (i.e., pulse duration) and the frequency resolution of a spectrometer can be independently controlled. This suggests that there is no lower bound to the product $\Delta\omega\Delta T$; the measurement can apparently be interpreted in terms of instantaneous snapshots with high spectral resolution. This apparently contradicts the uncertainty for the Fourier conjugate variables for, e.g., Gaussian pulses $\Delta\omega\Delta T > 15\,000$ cm^{-1} fs.[114] However, this argument is false for the following reason. Achieving ultrafast resolution requires the active involvement of the entire probe bandwidth. This is eroded when a narrower slice of the pulse is selected by the system.

We now discuss how the Fourier uncertainty relation between spectral and temporal resolution appears in the signal. Nonlinear multidimensional spectroscopy signals depend on several time intervals, and there is no problem in having simultaneous high temporal and spectral resolutions in different independent dimensions.[107,115] This is not the case when both dimensions are associated with the same probe pulse. The combined spectral and temporal resolution of the UV/IR technique stems from two interactions with the same probe pulse. The issue was addressed for Raman detection in ref 112 using a semiclassical treatment of bath degrees of freedom.

To pinpoint the factors that determine the genuine resolution, we note that in the most general form the UV/IR signal is given by the two loop diagrams presented in Figure 3b where a sum over paths spans both branches of the loop. Naively, one can argue that a short pulse must interact impulsively with the system at a sharply defined time. However, this is not necessarily the case for the following reason: a pulse is a superposition of modes with well-defined phases. The broader the bandwidth, the shorter the pulse can be. Equations 23 and 24 show that the relevant range of frequencies that actually contribute to a given signal is given by the variable Δ associated with the τ_3 integration ($\Delta = 0$ implies a CW probe). Thus, when only a fraction of the probe modes contributes to a given signal, the full bandwidth of the pulse becomes immaterial and the effective relevant pulse is longer than the actual pulse. The number of contributing modes is governed by the width of the relevant spectral features of the system and can be easily rationalized by the selection of the relevant pathways in the joint field-plus-matter space. Therefore, the resolution in eqs 23 and 24 is controlled by a combination of the pulse, the measuring device, and the system itself that determines Δ. In both diagrams (*i*) and (*ii*), the probe is frequency dispersed by the detection (spectrometer). If only a single mode is selected for detection, one may wonder why does the probe duration matter at all? This is apparent from the diagrams, which show that the signal involves two interactions with the probe. Frequency-dispersed detection only selects the frequency of the last interaction $\mathcal{E}_2^*(\omega)$, whereas the other interaction $\mathcal{E}_2(\omega + \Delta)$ can still involve other modes, making the signal depend on the probe bandwidth. The temporal resolution is eroded if the second interaction also selects a single mode so that $\Delta = 0$.

To better illustrate this important point, we examine the Δ-dispersed, time domain UV/IR signal dressed by the probe pulse

$$\bar{S}(t, T; \Delta) = \int_{-\infty}^{\infty} d\tau \mathcal{E}_2(\tau - T)\tilde{S}(t, T; \tau)e^{i(\omega+\Delta)\tau} \tag{36}$$

(cf. Appendix, eq 85). We reiterate that this is not an observable but serves as an auxiliary quantity used to compute the signal. For clarity, we omit the subscript for τ_3 in the following. Note that in contrast to the τ-dispersed signal $\tilde{S}(t,T;\tau)$, $\bar{S}(t,T;\Delta)$ depends on the probe pulse envelope $\mathcal{E}_2$. As discussed above, Δ may be broadened due to finite time scale of the bath dynamics. The respective frequency-domain signal, eq 22, can be calculated using eq 36

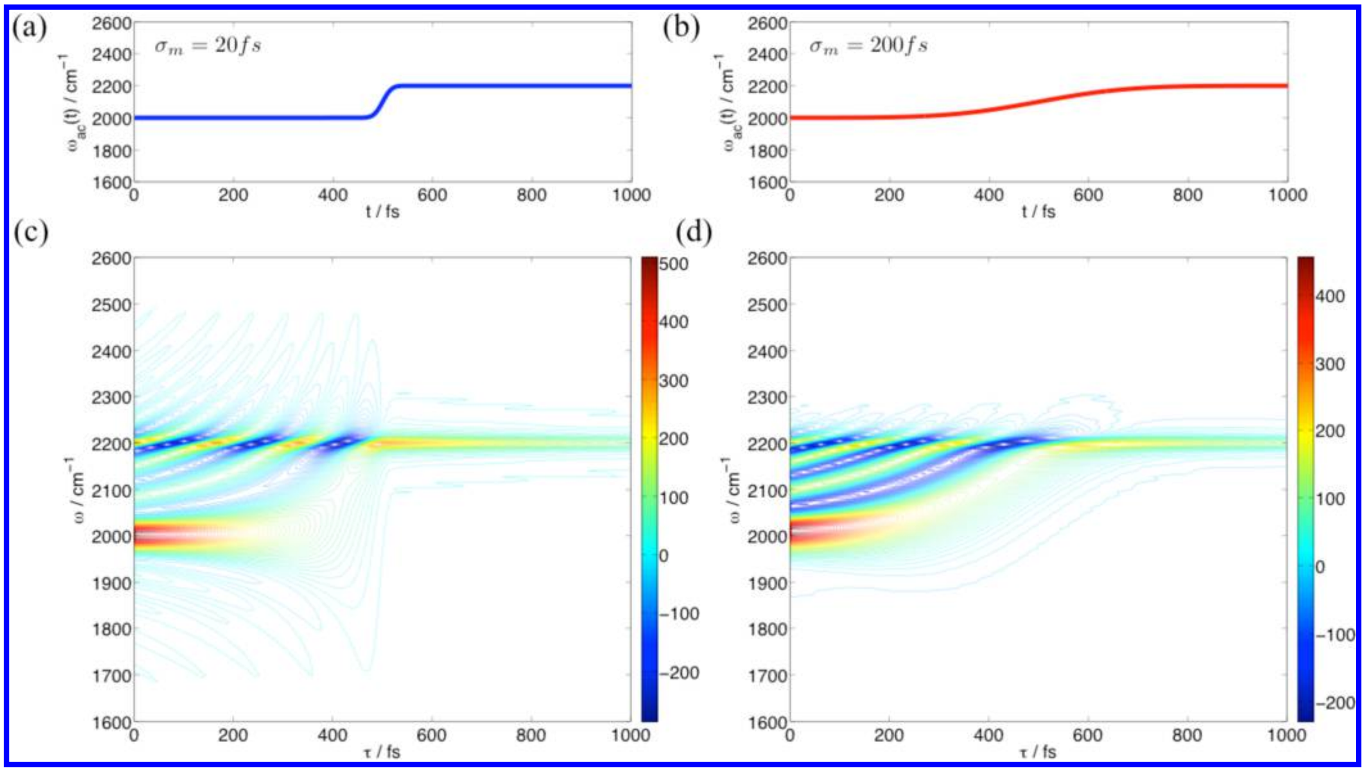

Figure 4. (a) Continuous, nonexponential switch of transition frequency (eq 41) and (c) corresponding 2D representation of the Fourier transform $\tilde{S}(\omega, T = 500\text{ fs}, \tau)$ of the Δ-dispersed signal (eq 42) for $\omega_{ac}^{(0)} = 2000$ cm^{-1}, $\alpha = 200$ cm^{-1}, and $\sigma_{\rm m} = 20$ fs. (b and d) Same as a and c, respectively, with $\sigma_{\rm m} = 200$ fs. Reproduced with permission from ref 76. Copyright 2013 Royal Society of Chemistry.

$$S_{\rm IR}(\omega, T) = \mathcal{I}\int_{-\infty}^{\infty}\frac{{\rm d}\Delta}{2\pi}\int_{-\infty}^{\infty}{\rm d}\tau\int_0^{\infty}{\rm d}t e^{i\omega(t-T)-i\Delta\tau} \times \mathcal{E}_2^*(\omega)\bar{S}(t+\tau, T;\Delta) \tag{37}$$

2.3.1. Linear Matter Chirp. We first consider the simplest example for the bath effect by assuming that it causes a linear time variation of the matter transition frequency (linear "matter" chirp: $\omega_{ac}(t) = \omega_{ac}^{(0)} + \alpha t$ where α is the chirp rate). Even though the linear matter chirp model is not realistic since the transition frequency is changing in an unbounded fashion, this example provides basic insight from an analytical treatment. A more realistic situation with continuously switching transition frequency will be described in section 2.3.2. We shall calculate the effective bandwidth Δ within a semiclassical approximation (cf. section 2.2.2). Taking eq 29 into account and assuming a harmonic potential with states a, c, and d such that $\omega_{ac} = \omega_{ad}$ and setting $\mu_{ad} = \mu_{ac}$, we obtain

$$\bar{S}(t, T; \Delta) = \theta(t)\int_0^t \mathcal{E}_2(\tau - T){\rm e}^{i\Delta\tau-\gamma_a(t+\tau)} \times |\mu_{ag}|^2|\mu_{ac}|^2|\mathcal{E}_1|^2[e^{i\omega_{ac}^{(0)}(t-\tau)+i/2\alpha(t^2-\tau^2)} + c.\ c.\ ] \tag{38}$$

Assuming a Gaussian probe pulse centered at T

$$\mathcal{E}_2(\tau - T) = \mathcal{E}_2{\rm e}^{-(\tau-T)^2/2\sigma_{\rm pr}^2 - i\omega_0\tau} \tag{39}$$

where ω_0 is the central frequency and $\sigma_{\rm pr}$ is the duration of the pulse, we obtain

$$\bar{S}(t, T; \Delta) \approx {\rm e}^{-(\Delta-\Delta_0)^2/2\sigma_{\rm eff}^2} \tag{40}$$

Here, the effective bandwidth is affected by $\Delta_0 = \omega_0 - \omega_{ac}^{(0)} + \alpha(T - \sigma_{\rm pr}^2\gamma_a)$ and $\sigma_{\rm eff}^2 = \sigma_{\rm pr}^{-2} + \alpha^2\sigma_{\rm pr}^2$. Note that Δ_0 is determined by two factors, the inverse of pulse duration $\sigma_{\rm pr}$ and the characteristic time scale α of the matter dynamics. This effect is similar to the broadening of a chirped pulse compared to the transform-limited pulse with the chirp attributed to the matter instead.

We wish to capture the matter dynamics on a given time scale α^{-1}. For a long pulse, the dominant contribution to $\sigma_{\rm eff}$ comes from the matter which ensures high-frequency resolution. In the limit of resonant CW excitation ($\omega_0 = \omega_{ac}^{(0)}$), eq 40 gives $\delta(\Delta)$. The latter implies that the original Δ-dispersed signal (eqs 23 and 24) has no time resolution with respect to τ. Furthermore, this result is independent of the probe time delay T. In the opposite limit, when the pulse is short, the leading contribution comes from the pulse and $\sigma_{\rm eff} \simeq \sigma_{\rm pr}^{-1}$. Therefore, high temporal resolution must be accompanied by low spectral resolution and vice versa. In both limits, the time and frequency resolutions are not independent, since they are not solely controlled by the external manipulation of pulse parameters. Rather, they are governed by a combination of pulse and matter parameters.

2.3.2. Continuous Frequency Switch. We next turn to a different model where the transition frequency varies continuously between two values during a finite time interval (Figure 4a and 4b). This model can represent, e.g., a spectator mode modified by passage through a CoIn or photochemical reaction with nonexponential, ballistic dynamics.[43] We assume

$$\omega_{ac}(t) = \omega_{ac}^{(0)} + \frac{1}{2}\alpha\left[\mathcal{F}\left(\frac{t_0}{\sigma_{\rm m}}\right) - \mathcal{F}\left(\frac{t_0 - t}{\sigma_{\rm m}}\right)\right] \tag{41}$$

where $\mathcal{F}(t) = \frac{2}{\sqrt{\pi}}\int_0^t {\rm d}x{\rm e}^{-x^2}$ is the error function. The transition frequency switches from its initial value $\omega_{ac}^{(0)}$ to its final value $\omega_{ac}^{(0)}$

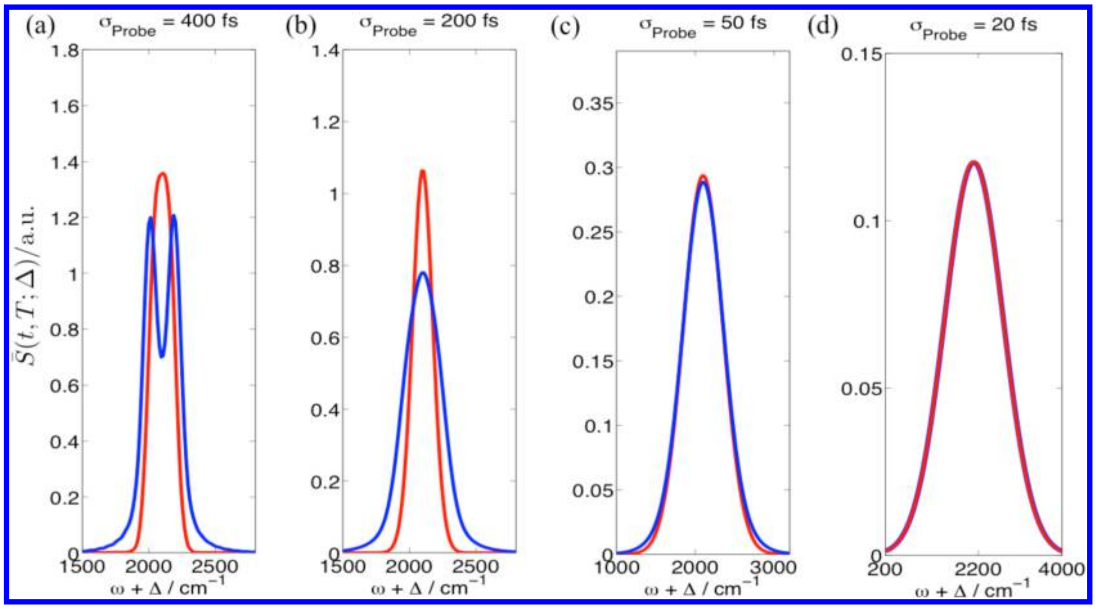

Figure 5. Δ-Dispersed signal (eq 36) for fast (σ_m = 20 fs, blue) and slow (σ_m = 200 fs, red) switchover of the vibrational frequency as depicted in Figure 4a and 4b, respectively. We assume resonant excitation $\omega_0 = \omega_{ac}^{(0)}$. Various panels represent different values of the pulse duration σ_pr = 400 (a), 200 (b), 50 (c), and 20 fs (d). Reproduced with permission from ref 76. Copyright 2013 Royal Society of Chemistry.

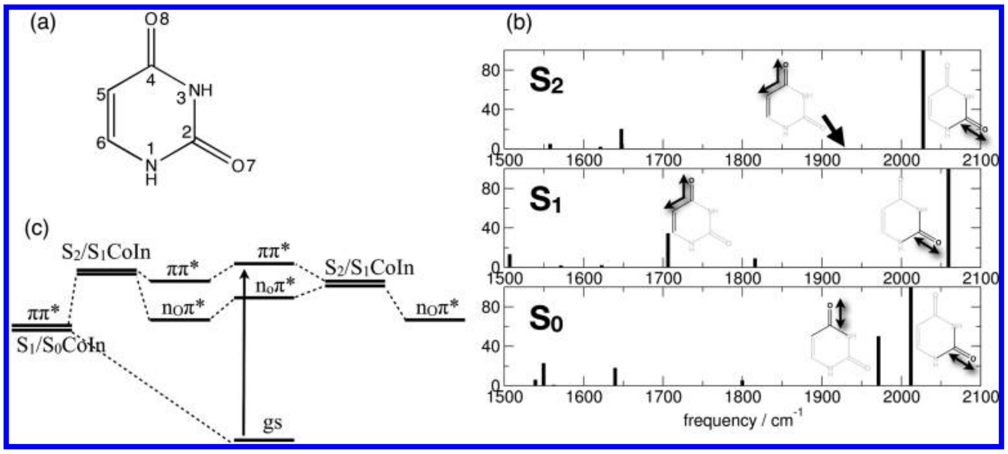

Figure 6. Schematic of UV/IR detection of uracil employing carbonyl C═O marker bands: (a) Chemical structure of uracil. (b) Frequencies and relative intensities of C═O marker bands calculated on the CASSCF(14/10)/6-31G* level of theory in the electronic ground state S_0 ($\tilde{\nu}_{\text{C=O}_7}$ = 2012 cm^{-1}, $\tilde{\nu}_{\text{C=O}_8}$ = 1971 cm^{-1}), the excited states S_1 ($n_{\text{O}_8}\pi^*$; $\tilde{\nu}_{\text{C=O}_7}$ = 2059 cm^{-1}, $\tilde{\nu}_{\text{C=O}_8}$ = 1706 cm^{-1}) and S_2 ($\pi_\text{O}\pi^*$; $\tilde{\nu}_{\text{C=O}_7}$ = 2028 cm^{-1}, $\tilde{\nu}_{\text{C=O}_8}$ = 1929 cm^{-1}). (c) Schematic of the electronic states involved in the femtosecond excited state relaxation of uracil: direct $\pi\pi^* \to$ gs channel (left) leads to ultrafast repopulation of the electronic ground state, while indirect $\pi\pi^* \to n_\text{O}\pi^*$ channel (right) involves an optical dark $n_\text{O}\pi^*$ intermediate state. Reproduced with permission from ref 103. Copyright 2013 American Chemical Society.

+ α during time interval σ_m = 20 fs around t_0 (cf. Figure 4a). Employing the semiclassical simulation protocol (section 2.2.2) the Fourier transform of the Δ-dispersed signal is depicted in Figure 4c as two-dimensional plot of ω vs τ:

$$\tilde{S}(\omega,\, T;\, \tau) = \int_{-\infty}^{\infty} \frac{\mathrm{d}\Delta}{2\pi} \tilde{S}(\omega,\, T;\, \Delta)\mathrm{e}^{-i(\omega+\Delta)\tau} \tag{42}$$

At T = 500 fs, the pattern evolves with dominating emission peak at initial frequency $\omega_{ac}^{(0)}$ = 2000 cm^{-1} for short times τ < 500 fs, turning into the final frequency $\omega_{ac}^{(0)} + \alpha$ = 2200 cm^{-1} for longer times τ > 500 fs. For times shorter than γ_a^{-1} = 1 ps the oscillatory region of the plot shows frequency beating and matter chirp. At longer times, the signal decays exponentially $\sim\mathrm{e}^{-\gamma_a\tau}$. For slower dynamics, σ_m = 200 fs (see Figure 4b) the Δ-dispersed signal (eq 42) is plotted in Figure 4 d, which is similar to Figure 4c but stretched according to the longer time scale σ_m.

To determine the joint temporal and spectral resolution for the system dynamics given by eq 41 with σ_m = 20 fs and σ_m = 200 fs, we examine the Δ-dispersed, time domain signal (eq 36) for different values of the probe pulse duration σ_pr (cf. Figure 5a–d). For long probe pulses (σ_pr = 400 fs, Figure 5a), the slow matter dynamics appears as a single peak at the final frequency $\omega + \Delta = \omega_{ac}^{(0)} + \alpha$, whereas fast dynamics gives two peaks which correspond to the initial and final frequencies (red line), which demonstrates that high-frequency resolution is accompanied by poor time resolution in this case. For a shorter pulse (σ_pr = 200 fs, Figure 5b), both fast and slow dynamics give a single emission peak centered at final frequency $\omega_{ac}^{(0)} + \alpha$. However, fast dynamics yields a larger bandwidth due to combined pulse and matter bandwidths. Further decrease of the pulse duration (σ_pr = 50–20 fs, Figure 5c and 5d) shows that the fast dynamics converges and becomes indistinguishable from the slow dynamics. In this case the frequency resolution is eroded and the spectrum does not carry any matter information. It simply gives the Fourier transform of the probe pulse. Therefore, for a long probe pulse, the spectrum has a perfect frequency but a poor time resolution. This corresponds to a CW experiment in which the actinic pulse prepares the system in an equilibrium population state described by ρ_{aa}. In this case, time translation invariance via eq 94 yields $\omega_1 = \omega_1'$ (see Appendix, Frequency-Domain UV/IR Signal Expression) and consequently $\omega = \omega'$. In the opposite, short pulse limit, the high time resolution is accompanied by poor frequency resolution. The resulting spectrum will not contain any relevant matter information and will be given by a Fourier transform of the probe pulse. In both limits the temporal and spectral resolutions are not independent and are governed by a combination of matter and field parameters.

2.4. Frequency-Dispersed Infrared Detection of Nonadiabatic Relaxation

In the following, we survey several techniques that employ an IR probe pulse for monitoring the vibrational degrees of freedom and their frequency shifts during the nonadiabatic dynamics. We start with the UV/IR setup in section 2.4.1. Nonadiabatic simulations of the RNA base uracil will serve to demonstrate the information content of the vibrational detection scheme. The numerical example is followed by a brief review of transient two-dimensional infrared spectroscopy (T-2DIR) (section 2.4.2), a nonlinear detection technique with the ability to reveal additional information, and a novel two-dimensional electronic−vibrational spectroscopy (2DEV) technique (section 2.4.3).

2.4.1. UV−vis Pump IR Probe (UV/IR). The time-resolved UV/IR technique (see Figure 3) is widely employed due to its ability to derive structural specific information about rearrangement of atoms in excited states. Recent applications of the technique have been reported in refs 116−127. Unique marker bands (e.g., the IR-intense carbonyl C═O stretch vibrations of the nucleobases, cf. Figure 6) serve as fingerprint of the excited state photoreaction. This allows one to obtain structural information about transient reaction intermediates[128−132] and ultimately reveal reaction mechanisms.[116,118,133−135]

Unraveling the excited state dynamics of DNA and RNA nucleobases has attracted considerable attention.[136−141] UV irradiation of the isolated nucleobases leads to population of an electronic excited state with $\pi\pi^*$ character. The nucleobases have been engineered by nature to be photostable with respect to UV irradiation.[142,143] At the core of this self-protection mechanism are femto- to picosecond excited state deactivation paths mediated by CoIns[143−145] where the electronic energy is efficiently converted into nuclear motion. The excited state deactivation of pyrimidine bases involves several interconnected excited state decay pathways, e.g., a direct $\pi\pi^* \rightarrow$ gs channel leads to ultrafast repopulation of the electronic ground state, while an indirect $\pi\pi^* \rightarrow n_O\pi^*$ channel involves an optical dark $n_O\pi^*$ intermediate state (cf. Figure 6c). Due to their subpicosecond deactivation dynamics the nucleobases serve as ideal experimental and theoretical test cases for CoIn-mediated processes (see also Summary and Conclusions, section 6). We note that a direct transfer of UV photoprotection mechanisms from isolated nucleobases to DNA as a carrier of genetic information should be considered with some caution. Even though ultrafast photochemical dimerization has been reported in DNA,[116] additional long-lived relaxation channels,[126] involving reactive charge transfer states,[123] can eventually lead to harmful DNA photolesions on slower time scales.[19,118,146]

We apply the semiclassical simulation protocol[76] outlined in section 2.2.3 to investigate nonadiabatic relaxation of the RNA base uracil by means of quantum-classical on-the-fly trajectory simulations that provide an assignment of spectroscopic signatures of the distinct deactivation pathways.[103] The vibrational subsystem of carbonyl C═O fingerprint modes is treated quantum mechanically, with their time-dependent Hamiltonian modulated by a classical bath during nonadiabatic relaxation. To avoid the costly calculation of the entire excited state Hessian matrix, a mode-tracking procedure[102] was employed to reconstruct the time-dependent Hamiltonian of C═O modes on-the-fly by block diagonalization. This numerical algorithm decouples the numerical effort from system size, making simulations of time-resolved UV/IR signals in electronic excited states for medium-sized molecules feasible.

Simulations of vibrational motions of C═O fingerprint modes in the electronically excited states reveal clear signatures of different relaxation pathways on a hundreds of femtoseconds time scale, which arise from the ultrafast branching of population in the excited state (Figure 6). Notably, dynamic simulations based on the CASSCF(14/10)/6-31G* level of theory predicted a stable population of the $n_O\pi^*$ state via the $\pi\pi^* \rightarrow n_O\pi^*$ channel on the picosecond time scale that is not subject to relaxation to the electronic ground state, in agreement with very recent findings from time-resolved near-edge X-ray absorption fine structure (NEXAFS) spectroscopy on the deactivation mechanism of thymine.[139] The sensitivity of the UV/IR technique allows one to assign structural information to transient features in the time-resolved UV/IR signal. The high-energy C═O$_7$ mode preserves its localized character and shows a blue shift of ~40 cm^{-1} due to slight bond contraction in the $n_O\pi^*$ state compared to the S$_0$ state (Figures 6b and 7). Accordingly, a spectral signature of $\pi\pi^* \rightarrow n_O\pi^*$ could be identified that appears as a blue shift of the intense intense C═O$_7$ mode. The C═O$_8$ in contrast is elongated upon population of the $n_O\pi^*$ state and shows a pronounced red shift with substantially reduced intensity due to the delocalized character of the modes. We note that the absolute C═O modes frequencies evaluated on the CASSCF(14/10)/6-31G* level of theory are of limited accuracy (and sometimes corrected by empirical correction factors) as dynamic electron correlation and anharmonic effects have been neglected. Nevertheless, the derived frequency shifts in the electronic excited states provide trends for experimental detection that have been successfully employed in the real-time UV/IR detection of DNA photolesions.[135]

This study further demonstrates that the inherent temporal and spectral resolution of the technique is not purely instrumental but depends on the vibrational fluctuation time scale as well. The system dynamics time scale imposes a lower bound on the probe pulse and defines the actual time resolution that can be observed in the experiment. The requirements for IR probe pulses are predicted to be t_{fwhm} = 100−200 fs, readily available with current pulse technology,[147−149] as the best compromise of temporal and spectral resolution, which allows one to resolve spectral features characteristic for the individual relaxation mechanisms. There are two fundamental reasons why the UV/IR signal (eq 29) may not be simply interpreted as stroboscopic snapshots of the instantaneous vibrational frequency: (1) the uncertainty in τ_3 around T restricts the ability to initiate the probe process at a precisely defined instant of time; (2) the UV/IR signal at the delay time T is governed by a

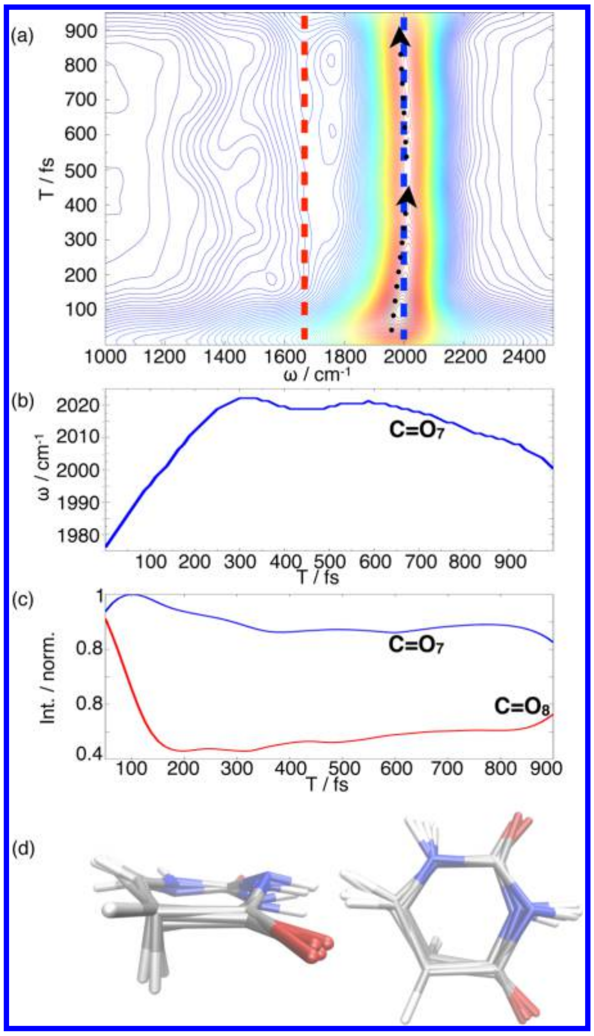

Figure 7. (a) UV/IR signal of C═O_7 and C═O_8 modes of uracil excited state dynamics averaged over 44 trajectories (CASSCF(14/10)/6-31G* level of theory, $\mathcal{E}_2$ pulse parameters: t_{fwhm} = 175 fs, ω_0 = 2000 cm^{-1}; increments of ΔT = 25 fs). (b) Peak shift of C═O_7 vibrational frequency as indicated by black dots in a. (c) Time evolution of C═O_7 and C═O_8 vibrational intensity. (d) Overlay of S_1/S_0 CoIn structures reached during the dynamics. Reproduced with permission from ref 103. Copyright 2013 American Chemical Society.

time integral over the frequency trajectory rather than the snapshot value at one time. Both effects generally hinder the simple interpretation of the signal by inspection. However, for delay times beyond the dephasing time, the snapshot picture increasingly becomes more accurate.

The relaxation mechanism of pyrimidine bases uracil and thymine is an ongoing matter of debate.[137−141,150−153] A comprehensive and quantitative theoretical description of the DNA and RNA base excited state dynamics in solution is challenging and has to account for static and dynamic electron correlation on the highest level,[154,155] the influence of the solvent environment that can lead to a reordering of electronic states compared to the gas phase,[156] as well as the contribution of dark triplet states[157,158] to time-resolved spectra.

2.4.2. Transient Two-Dimensional Infrared Spectroscopy (T-2DIR). The UV/IR technique provides information about the structural dynamics under investigation by monitoring transient intermediates. Similar to infrared absorption experiments performed in the electronic ground state, information about intermode couplings and environment fluctuation dynamics is not directly accessible by this linear detection.[159] Some of these limitations can be eliminated by augmenting UV/IR detection by a quadratic detection mode[75] that allows one to spread the information content in two dimensions. The respective technique, T-2DIR, was first realized in 2003 by the Hamm group.[160−164] Comprehensive reviews on recent technical developments of the T-2DIR technique are given in refs 165−167. Difficulties in performing such experiments arise from the increased optical complexity inherent in a fifth-order method and from the differential absorption of already small nonlinear spectroscopic signals which poses strict requirements on signal-to-noise. By referencing to a characterized ground state species, the quasi-equilibrium dynamics of excited electronic states has been demonstrated by T-2DIR.[168] Recent studies revealed the potential of T-2DIR to characterize excited state intermediates, thereby providing a way to correlate nuclear and electronic degrees of freedom.[169−173]

2.4.3. Two-Dimensional Electronic−Vibrational Spectroscopy (2DEV). A coherent extension of UV/IR, termed 2DEV,[174] developed recently correlates the optical excitation pulse with infrared detection. The line shapes and temporal evolution of the 2DEV signals contain additional information on the coupling between the electronic degrees of freedom and the vibrational manifold. The experimental realization relied on a pump−probe setup,[175−178] thus self-heterodyning the nonlinear signal followed by phase cycling. Recent technological advances involve octave-spanning broad-band mid-IR pulses to improve the detection window.[179] Conceptually, 2DEV is closely related to the two-dimensional UV−vis (2D-UV/vis) signals discussed in section 4.2 and can be regarded as an extreme two-color 2D experiment.[180] In 2DEV, the first interaction with the optical pulse $\mathbf{k}_1$ creates a coherence between ground and excited electronic states that, after coherence time, is converted into a population state (either ground or excited state) by the second interaction with an optical pulse $\mathbf{k}_2$. After a waiting time T, the IR probe pulse $\mathbf{k}_3$ addresses the vibrational manifold from which emission of the signal $\mathbf{k}_{\mathrm{sig}}$ occurs. Details of the line shape evolution, especially for CoIn-mediated processes, requires further theoretical investigations. A first step in this direction was taken for model systems in refs181−183. Note that for nonreactive systems the response function formalism developed in ref 107 can be employed for the description of the third-order 2DEV signal. Recent variants of the 2DEV technique reported the correlation of the ground state vibrational degrees of freedom with electronic degrees of freedom, as proposed in ref 184, termed two-dimensional vibrational-electronic spectroscopy (2DVE), thereby inverting the correlation plot of the 2DEV technique.[180]

The 2DEV technique's ability to correlate electronic and vibrational degrees of freedom was applied to investigate the carotenoid β-apo-8′-carotenal (bapo),[185] a class of molecules where strong vibronic coupling has been reported.[186] The correlation between excited state C═C stretching modes and electronic degrees of freedom persisted longer than the sub-300 fs S_2 lifetime, which suggests evidence for the involvement of a conical intersection linking the S_2 and S_1 states of bapo.[185]

An interesting application of 2DEV to monitor the transfer of electronic excitation energy among pigments in the light-harvesting complex II (LHCII) has been reported.[187] By exploiting the inherent structural sensitivity of IR signals to the local protein environment of chlorophyll (Chl) a and b vibrational modes[188] the localized vibrations were employed as

Table 1. Summary of off-Resonant Stimulated Raman Techniques[a]

signal	$S^{(\mathrm{fd})}$	$S^{(E)}$
S_{LB}	eq 69: oscillatory gain/loss pattern may show Stokes/anti-Stokes oscillations as a function of the delay T	zero spectral resolution due to ω integration; may visualize weak transitions due to weighting factors ω
S_{LH}	eq 80: high spectral resolution compared to S_{LB}; each peak oscillates at it is own frequency and with it is own phase, making it a background-free technique for coherence (phase retrieval) measurements	does not carry new information compared to $S^{(fd)}$
S_{QB}	eq 22 for IR probe and eqs 63 and 65 for Raman probe: signal is always dominated by Stokes contributions due to prominence of populations (which do not contribute to lower order linear signals)	transition spectra can be achieved by Fourier transform over T
S_{QH}	eqs 49, 50, and 60 for FSRS and eq 77 for attosecond stimulated Raman spectroscopy (ASRS): spectral and temporal resolutions are higher than S_{LH} (not conjugated), but retrieval of frequencies and phases is more complicated due to population-dominated (phase insensitive) contributions	Fourier transform over T can visualize weak transitions

[a] Note that signals $S^{(N)}$ vanish for both linear and quadratic detection protocols, so they have been omitted.

structural reporters within the protein complex. Compared to the 2D-UV/vis signals (discussed in section 4.2), which are often broad and congested,[189] 2DEV offers the advantage that specific molecular marker bands can be assigned to the spatial position of a molecular species. The predictive power of the approach strongly depends on the assignments of excited state vibrational bands that are subject to frequency shifts induced by the local electrostatic environment. With current quantum chemistry methods such assignments are prohibitively expensive, calling for further development of current computational techniques.

Thanks to the structural sensitivity of IR signals, the UV/IR technique, multidimensional variants, or 2DEV should allow for sensitive detection of nuclear rearrangements that accompany nonadiabatic relaxation dynamics. Nevertheless, limitations arise because of the following. (i) Due to commonly employed pulses ≈ 100 fs with some hundred (∼200−300) cm^{-1} bandwidth.[147] Substantial effort has been made to extend the bandwidth of mid-IR pulses[179,190−198] by using novel pulse generation technologies. (ii) Due to the available spectral range of IR laser pulses: typical probe pulses cover the mid-IR spectral range, but for the molecular fingerprint region, i.e., low-frequency modes (<1000 cm^{-1}), pulse technology is not yet fully developed. Recent developments provided access to phosphate stretch and DNA backbone modes in nonlinear IR experiments,[199−201] and advances in THz pulse generation[202,203] are encouraging to close the gap to lower frequencies. (iii) Pronounced cooling signals[118,204] observed in aqueous solutions obscure the time resolution for early delay times (<few picoseconds).

3. ELECTRONICALLY OFF-RESONANT STIMULATED RAMAN SPECTROSCOPY (SRS)

Frequency-dispersed Raman (section 3.3) is an alternative detection mode for vibrations, which complements the UV/IR technique. Nonadiabatic simulations on the RNA base uracil will serve to demonstrate the information content of the vibrational detection schemes. Section 3.3.1 presents the interplay of temporal and spectral resolution in stimulated Raman spectroscopy (SRS) along with a discussion of several off-resonant Raman detection schemes in sections 3.3.2 and 3.3.3. These techniques all provide 2D signals when displayed vs one time delay variable and a second frequency variable and depend on the same matter correlation functions that carry the relevant information.

3.1. Simulation Protocols

Using an intuitive diagrammatic approach, we derive expressions for the following three detection protocols of electronic Raman signals: (*i*) the change in number of photons $S^{(N)}$, (*ii*) the change in the transmitted probe energy $S^{(E)}$, and (*iii*) the frequency-dispersed probe transmission $S^{(\mathrm{fd})}$. In addition, signals may be either linear or quadratic in the probe intensity and may utilize broad-band or hybrid-shaped (a combination of broad and narrow bandwidths) probes as well as resonant or off-resonant with material transitions. The energy exchange between field and matter is discussed. In the case of an off-resonant probe, the number of photons is conserved and $S^{(N)} = 0$. For a hybrid pulse composed of a narrow-band and a broad-band component, we see oscillations between Stokes/anti-Stokes components[205] with the delay T, whereas for a single broad-band pulse the entire pulse envelope oscillates, smearing out the spectral features of the hybrid signal.[206]

We present a classification scheme for multidimensional stimulated Raman spectroscopies applicable when the preparation of some nonstationary state, the nature or dynamics of which is the object of study, is temporally well separated from the detection process. Many conventional spectroscopic techniques (e.g., pump−probe) are carried out under these conditions.[207−209] We take the initial state as given and classify signals by their dependence on detection parameters, which control which features of the nonstationary state are observable and how they manifest. In particular, we examine different choices of the field (whether it is resonant or off-resonant with respect to the material transitions), the intensity scaling with the detecting field (linear or quadratic), the spectral shape of the detecting field (broad band or hybrid broad−narrow band). These are only a few of the possible combinations of parameters that could be used for spectroscopic detection of a time-evolving state. Similar ideas apply to off-resonant X-ray scattering (diffraction)[210,211] and to spontaneous emission following impulsive X-ray Raman excitation.[212] These will be described in section 5.

We examine different simulation protocols and derive expressions that may be used for the direct numerical propagation of the wave function in Hilbert space, when all degrees of freedom are included explicitly, or the density matrix in Liouville space,[113] which gives a simplified picture of bath effects and allows for a reduced description via the SLE.[109,110,213]

The off-resonant signals are explored first, and expressions for each of the three detection protocols for signals linear and quadratic in the field intensity are derived. In the off-resonant regime the field−matter interaction Hamiltonian is the product of field intensity and a molecular polarizability. We then calculate these signals for a simple model system and discuss the properties of each signal and what information it reveals. This analysis is then repeated for the resonant signals from the same model. Here, the field−matter interaction Hamiltonian is the dot product of field amplitude and molecular transition dipole. We conclude with a comparison of off-resonant versus resonant signals and a general discussion of the utility of this signal classification scheme. While off-resonant Raman signals are simpler to analyze, resonant pulses are more selective to a given chromophore and provide additional specific information about molecules.[214] A specific example of resonant Raman detection is given for X-ray detection (section 5.1).

3.2. Detection Schemes for off-Resonant Raman Signals

We will investigate stimulated Raman signals from a molecular model system with a band of valence states. We assume that the system is prepared at time τ_0 in a superposition of valence states ψ_i and is monitored by interaction with a broad-band probe pulse centered at time t_0. The different detection protocols for linear and quadratic signals and their most striking features in the off-resonant case are summarized in Table 1.

For an off-resonant Raman process, the field−matter interaction Hamiltonian in the interaction picture is given by

$$H'(t) = \alpha^{(0)}(t)|\mathcal{E}(t)|^2 \tag{43}$$

where $\alpha^{(0)}$ represents the off-resonant polarizability, which is a Hermitian operator in the space of the valence states ($\alpha^{(0)}$ is real). In the following, we assume that the electric field $\mathcal{E}(t) = \int_{-\infty}^{\infty} \frac{d\omega}{2\pi}\mathcal{E}(\omega)e^{-i\omega t}$ consists of short pulses which are temporally well separated from the preparation process. This ideal scheme simplifies the interpretation of signals. We start with the frequency-dispersed (fd) transmission of the probe pulse (heterodyne-detected, frequency-dispersed photon-number change governed by eq 20)

$$S^{(\mathrm{fd})}(\omega, t_0, \tau_0) = \frac{2}{\hbar}\mathcal{I}\int_{-\infty}^{\infty} dt\, e^{i\omega(t-t_0)}\mathcal{E}^*(\omega)\mathcal{E}(t-t_0) \times \mathrm{Tr}[\alpha_{\mathrm{L}}^{(0)}(t)e^{-i/\hbar \int H'_{-}(\tau)d\tau}\rho_i(\tau_0)] \tag{44}$$

where $\rho_i = |\psi_i\rangle\langle\psi_i|$ is the initial density matrix (immediately following the state preparation process). We adopt a superoperator notation that provides a convenient book-keeping of time-ordered Green's functions. An ordinary operator A is associated with two superoperators[213] defined by their action on the operator $A_{\mathrm{L}} \equiv AX$ (action from the left) and $A_{\mathrm{R}} \equiv XA$ (action from the right). We further define the symmetric and antisymmetric combinations $A_+ = (A_{\mathrm{L}} + A_{\mathrm{R}})$, $A_- = (A_{\mathrm{L}} - A_{\mathrm{R}})$.

Note that we recast the dipole interactions into polarizabilities. This allows one to recast (see Appendix, Mapping of off-Resonant Interactions to Effective Polarizabilities) a four-point correlation function as it appears in the quadratic detection scheme to a two-point correlation function.

The H'_- exponential represents evolution of the matter with the probe field (since the preparation processes have ceased) until the final interaction with the probe. We can then expand the signal perturbatively in H'_- to obtain signals with the desired field scaling (linear or quadratic in intensity are considered here).

Alternatively, one can detect the total change in the photon number which is given by the zeroth spectral moment of $S^{(\mathrm{fd})}$ (given by eq 15)

$$S^{(N)}(t_0, \tau_0) = \int_{-\infty}^{\infty}\frac{d\omega}{2\pi}S^{(\mathrm{fd})}(\omega, t_0, \tau_0) \tag{45}$$

A third type of signal is given by the total change in the energy of the transmitted pulse which is the first spectral moment of $S^{(\mathrm{fd})}$

$$S^{(E)}(t_0, \tau_0) = \int_{-\infty}^{\infty}\frac{d\omega}{2\pi}\hbar\omega S^{(\mathrm{fd})}(\omega, t_0, \tau_0) \tag{46}$$

$S^{(\mathrm{fd})}$ is the most detailed measurement, whereas $S^{(N)}$ and $S^{(E)}$ are its zeroth and first spectral moments. The latter two techniques are simpler to implement experimentally since they do not require frequency-selective detectors or spectrometers.

3.2.1. Signals Linear in the Probe. This technique is essentially a stimulated Raman pump−probe and is the off-resonant analogue of transient absorption. It can be obtained from the zeroth-order expansion of the exponent in eq 44. Here, the photons undergo a redistribution among field modes rather than being absorbed.

3.2.1.1. Linear Broad-Band (LB) Probe. The frequency-dispersed signal oscillates between Stokes (positive red-shifted and negative blue-shifted features) and anti-Stokes (negative red-shifted and positive blue-shifted features). It is worth noting that initial populations only give rise to elastic scattering that does not affect the field energy and thus do not contribute to the off-resonant linear broad-band signal. These signals therefore provide a background-free detection of the electronic coherences. An example of a frequency-dispersed linear broad-band signal is transient absorption given by eq 69.

3.2.1.2. Linear Hybrid (LH) Probe. A hybrid probe is a shaped pulse consisting of a broad-band femtosecond pulse $\mathcal{E}(\omega) = |\mathcal{E}_0(\omega)|e^{i\phi_0}$ and a narrow-band picosecond pulse $\mathcal{E}_1(t) = |\mathcal{E}_1|e^{-i\omega_1 t + i\phi_1}$ centered at ω_1. Due to their dependence on the relative phase of the pulses $\phi_0 - \phi_1$, observation of the linear hybrid signals requires phase control (averaging over random ϕ_0, ϕ_1 causes the signal to vanish). Such signals can reveal the phase of coherences from the oscillations of the separate peaks. This information is not available in the *LB* signal. The photon number signal is slightly more complex: because the hybrid pulse contains both broad- and narrow-band components we need to take into account the contribution to the signal where the last interaction is with the narrow-band component. The total change in photon number vanishes in both broad-band and hybrid cases. The transmitted energy change of the shaped pulse similarly contains both narrow-band and broad-band components, and the total energy change of the shaped pulse is given by the redistribution of the photons between different modes. Energy conservation implies that the pulse energy changes and the molecular energy change must have equal magnitude and opposite sign. An example of a linear hybrid signal is transient redistribution of ultrafast electronic coherences in attosecond Raman signals (TRUECARS) given by eq 80 (see ref 215).

3.2.2. Signals Quadratic in the Probe. The quadratic (i.e., second-order in probe intensity) signal is obtained by expanding the exponent in eqs 44−46 to first order in field−matter interactions.

3.2.2.1. Quadratic Broad-Band (QB) Probe. The quadratic signal oscillates with a phase that depends on states other than the initial state after preparation. This yields the resonance frequency and involves the phases of the polarizability $\alpha^{(0)}$. Comparing this to the corresponding linear signal shows a $\pi/2$ phase shift. As a result, the contributions from populations no longer vanish, and they form a time-dependent background to the quadratic signals. Because the initial excitation by the actinic pump is assumed to be weak (so that the ground state dominates the populations), the contribution of populations is primarily Stokes type. At the same time, the oscillating coherences are too weak to overcome the strong population contributions, so the overall process is Stokes type at all times T. An example of the frequency-dispersed quadratic broad-band signal is illustrated by eq 22 for IR probe and eqs 63 and 65 for Raman probe.

3.2.2.2. Quadratic Hybrid (QH) Probe. As in the linear signal, the narrow-band pulse allows one to clearly resolve the transition peaks. However, unlike the linear signal, the quadratic hybrid signal is independent of the phases of the narrow-band and broad-band pulses ϕ_1 and ϕ_0 and therefore does not require phase-controlled pulses. Just as in the broad-band case, the signal is sensitive to populations, which contribute a static Stokes signal. The example of a frequency-dispersed quadratic hybrid signal is discussed for FSRS in eqs 49, 50, and 60 as well as its attosecond counterpart, ASRS, in eq 77.

In summary, $S^{(\mathrm{fd})}$ shows an oscillatory pattern of gain and loss features in the red-shifted and blue-shifted spectral regions that depends on the initial phase of the coherence created upon excitation. This information is integrated out in $S^{(E)}$ where the entire probe pulse envelope exhibits periodic Stokes (loss) or anti-Stokes (gain) shifts.[206] The broad-band signals do not possess a sufficient spectral resolution to directly observe the transition spectra and only allow one to access it through the Fourier transforms of the energy signals $S^{(E)}(T)$. Utilizing a hybrid broad−narrow pulse combined with frequency-dispersed detection provides high spectral and temporal resolution, thus allowing spectral snapshots to be taken that clearly resolve all transitions and therefore permit extraction of the phases from the oscillation patterns. In linear signals this requires control of the relative pulse phases (which cancel out in the quadratic case). The quadratic and linear signals generally carry the same information about coherences, but this is accessed background free only for linear signals. One important caveat to this is that the magnitudes of the various transition peaks can be enhanced or suppressed by the interference of different pathways.

3.3. Loop Diagram Representation of Raman Signals

Off-resonant Raman signals are formally identical to their IR counterparts and only require replacing some dipole μ with the polarizability α. The electronically off-resonant SRS signal shown in Figure 8a and 8b has some merits compared to UV/IR due to the inherent broad-band detection offered by optical pulses. In SRS, an actinic pump pulse initiates the excited electronic state vibrational dynamics. Pulse 3 and the probe then induce the Raman process (see Figure 8a). The relevant diagrams are shown in Figure 8b (plus their complex conjugates). An electronically off-resonant Raman process induced by pulses 2 and 3 is instantaneous since, by Heisenberg uncertainty, the system can only spend a very short time in the intermediate state. The Raman process can thus be described by an effective field−matter interaction Hamiltonian

$$H'(t) = \alpha_n \mathcal{E}_2^\dagger(t)\mathcal{E}_3(t) + \mathcal{E}_1^\dagger(t)V_e(t) + H.\,c. \tag{47}$$

where α_n is the excited state polarizability that couples fields 2 and 3 parametrically via a Raman process. It is a symmetric (real) operator. Assuming that pulse 3 is narrow band (picosecond), we set $\mathcal{E}_3(t-T) = \mathcal{E}_3 e^{-i\omega_3(t-T)}$. We obtain the frequency-gated Raman analogues of eqs 22−24 that can be read directly from diagrams (i) and (ii) in Figure 8

$$S_{\mathrm{SRS}}(\omega-\omega_3, T) = \mathcal{I}\int_{-\infty}^{\infty}\frac{\mathrm{d}\Delta}{2\pi} \times \mathcal{E}_2^*(\omega)\mathcal{E}_2(\omega+\Delta)\tilde{S}_{\mathrm{SRS}}(\omega-\omega_3, T;\Delta) \tag{48}$$

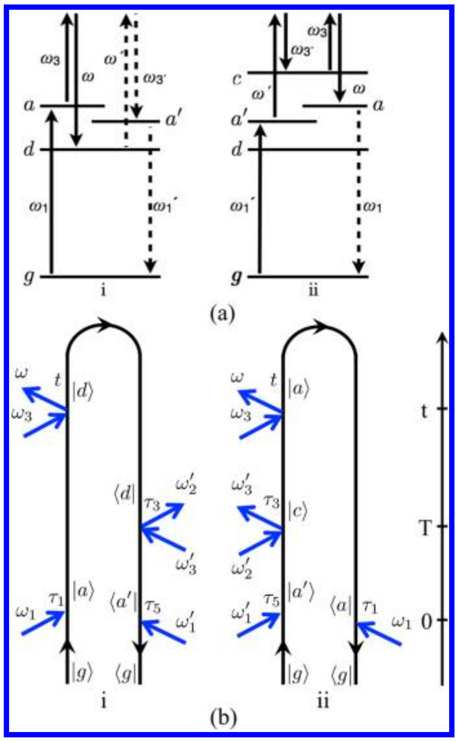

Figure 8. SRS technique: (a) Level schemes indicating the excitation pathways on the ket side (solid arrows) and the bra side (dashed arrows) in analogy to Figure 3a but for off-resonant Raman interactions. (b) Corresponding loop diagrams describing the SRS technique (analog to Figure 3b); for details see text. Reproduced with permission from ref 76. Copyright 2013 Royal Society of Chemistry.

$$\begin{aligned}\tilde{S}_{\mathrm{SRS}}^{(i)}&(\omega-\omega_3, T;\Delta)\\ &= \frac{2}{\hbar}\int_{-\infty}^{\infty}\mathrm{d}t\int_{-\infty}^{t}\mathrm{d}\tau_1\int_{-\infty}^{t}\mathrm{d}\tau_3\int_{-\infty}^{\tau_3}\mathrm{d}\tau_5\\ &\times |\mathcal{E}_3|^2\mathcal{E}_1^*(\tau_5)\mathcal{E}_1(\tau_1)e^{i(\omega-\omega_3)(t-\tau_3)-i\Delta(\tau_3-T)}\\ &\times \langle V_e G^\dagger(\tau_3,\tau_5)\alpha_n G^\dagger(t,\tau_3)\alpha_n G(t,\tau_1)V_e^\dagger\rangle\end{aligned} \tag{49}$$

$$\begin{aligned}\tilde{S}_{\mathrm{SRS}}^{(ii)}&(\omega-\omega_3, T;\Delta)\\ &= \frac{2}{\hbar}\int_{-\infty}^{\infty}\mathrm{d}t\int_{-\infty}^{t}\mathrm{d}\tau_1\int_{-\infty}^{t}\mathrm{d}\tau_3\int_{-\infty}^{\tau_3}\mathrm{d}\tau_5\\ &\times |\mathcal{E}_3|^2\mathcal{E}_1(\tau_5)\mathcal{E}_1^*(\tau_1)e^{i(\omega-\omega_3)(t-\tau_3)-i\Delta(\tau_3-T)}\\ &\times \langle V_e G^\dagger(t,\tau_1)\alpha_n G(t,\tau_3)\alpha_n G(\tau_3,\tau_5)V_e^\dagger\rangle\end{aligned} \tag{50}$$

Corresponding time-gated signals are given in the Appendix (eqs 88 and 89). Note that we express the SRS signal, in analogy to UV/IR, in the Δ-dispersed form and have not yet specified the $\mathcal{E}_2$ probe. The electronically off-resonant SRS signal shown in Figure 8a and 8b is completely analogous to the UV/IR signal. Even though these signals represent different physical processes and even involve different numbers of field−matter interactions, they can be described using very similar diagrams. By substitutions of operators $V_n \rightarrow \alpha_n$ and infrared frequency ω by Raman shift $\omega-\omega_3$, the 4-point matter correlation function expression of the UV/IR signal can be transformed to the respective correlation function of the SRS technique (cf. eqs 23 and 24 and eqs 49 and 50). Assuming that pulse 2 is broad band, the FSRS signal is finally given by eq 48, where the Δ-dispersed signal is given by the two diagrams $\tilde{S}_{\mathrm{SRS}}(\omega-\omega_3,T;\Delta) = \tilde{S}_{\mathrm{SRS}}^{(i)}(\omega-$

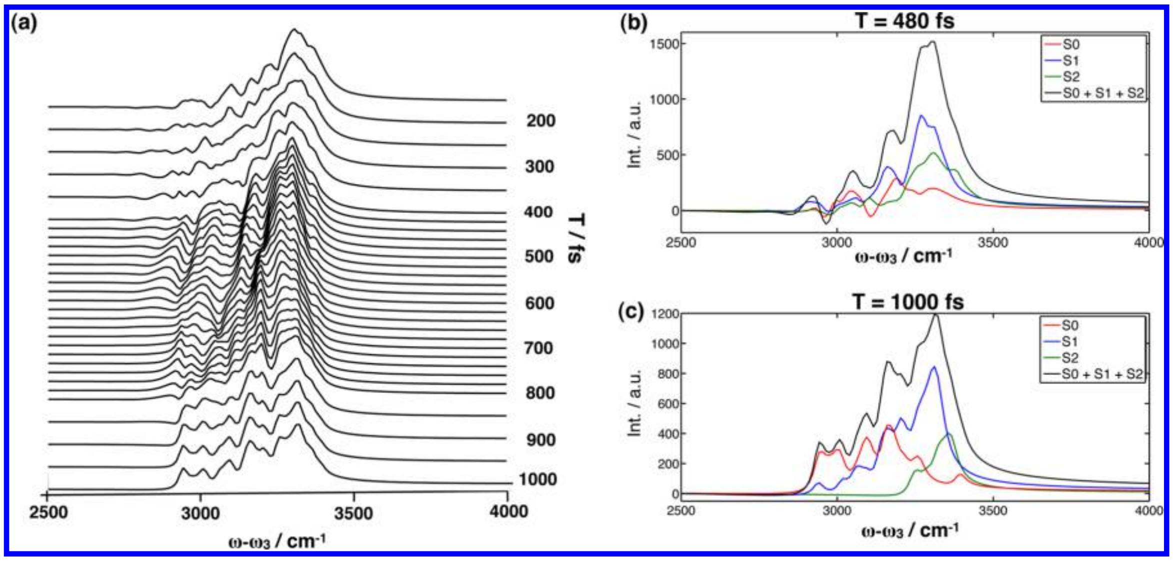

Figure 9. SRS signal (eqs 48 and 51) of the nonadiabatic relaxation of uracil: (a) SRS signal of C−H stretch vibrations averaged over 32 trajectories. (b and c) Contributions of different electronic states at T = 480 and 1000 fs, respectively. Reproduced with permission from ref 113. Copyright 2014 American Chemical Society.

$\omega_3, T; \Delta) + \tilde{S}^{(ii)}_{\mathrm{SRS}}(\omega - \omega_3, T; \Delta)$ (eqs 49 and 50). Following the classification scheme introduced in section 3.2, the FSRS signal employs a quadratic hybrid probe ($S_{\mathrm{QH}}^{(\mathrm{fd})}$) and is frequency dispersed.

Similarly to UV/IR, one can derive the semiclassical SRS signal when the extra pump $\mathcal{E}_3$ pulse is narrow band and can be approximated as monochromatic, $\mathcal{E}_3(t) = \mathcal{E}_3 e^{-i\omega_3(t-T)}$. The Δ-dispersed signal (eqs 49 and 50) then reads

$$\tilde{S}_{\mathrm{SRS}}(\omega - \omega_3,\, T;\, \Delta) = -\frac{2i}{\hbar^4}\int_{-\infty}^{\infty} \mathrm{d}\tau_3 \int_{\tau_3}^{\infty} \mathrm{d}t \times |\mathcal{E}_1|^2 |\mathcal{E}_3|^2 e^{i(\omega-\omega_3)(t-T)} e^{-i(\omega+\Delta)(\tau_3-T)} \sum_a |\mu_{ag}|^2 e^{-2\gamma_a t} \times \left[\sum_c \alpha_{ac}^2 e^{-i\int_{\tau_3}^{t}\omega_{ac}(t')\mathrm{d}t'} + \sum_d \alpha_{ad}^2 e^{i\int_{\tau_3}^{t}\omega_{ad}(t')\mathrm{d}t'}\right] \tag{51}$$

where we added phenomenological dephasing rate γ_a to account for the physical line shapes. On the basis of the loop diagrams,[81] the semiclassical signal expression satisfies the time/frequency resolution limits imposed by the Fourier uncertainty.

We now apply the semiclassical simulation protocol (eqs 48 and 51)[76] to the nonadiabatic relaxation of the RNA base uracil. Quantum-classical on-the-fly trajectory simulations are used to trace the SRS spectroscopic signatures of ultrafast deactivation pathways.[113] The SRS signal of high-frequency C−H and N−H stretch vibrations has been used to study the photophysical photoprotection mechanism of the RNA base uracil. The reaction coordinate for the direct $\pi\pi^* \rightarrow$ gs relaxation mechanism has been characterized as out-of-plane deformation of the $\pi\pi^*$ state, primarily due to twisting of a C═C double bond.[145] The employed semiclassical simulation protocol outlined in section 2.2.3 allows one to derive the system dynamics directly from ab initio on-the-fly simulations and tracks the system dynamics over nonadiabatic relaxation events in the vicinity of CoIns. The overlay of relevant CoIn structures given in Figure 7d demonstrates the pronounced out-of-plane deformation of the aromatic pyrimidine ring. C−H stretch vibrations were used as a local probe of the ring planarity (Figure 9) due to their instantaneous response to distortions required to reach the CoIn structures. At early delay times (T = 100 fs), a single broad band (fwhm ≈ 200 cm^{-1}) centered at $\omega - \omega_3 = 3323$ cm^{-1} can be identified. However, it does not resolve the individual C−H modes, as commonly observed for high-frequency C−H and N−H vibrations.[216] With increased delay time T = [100; 300] fs, the band shows a red shift along the detection axis $\Delta\omega - \omega_3$, which can be assigned to ultrafast $S_2 \rightarrow S_1$ population transfer. At longer T (300−700 fs) we notice the buildup of a pronounced shoulder at the red wing of the band of C−H modes just below 3000 cm^{-1} and shows a characteristic dispersive peak shape of nonexponential CoIn-induced dynamics. This transient modulation reflects the required out-of-plane deformations of the ring π system required to reach CoIn structures and in particular S_1/S_0 CoIn structures (see Figure 7d). The comparison of experimental C−H vibrational spectra of ethylene and ethane[217,218] as prototype sp^2 and sp^3 species, respectively, reveals a red shift of C−H modes of ∼120 cm^{-1}, in agreement with the red shift of transient signatures. The SRS signal of C−H modes thus provides a sensitive local probe of out-of-plane deformations and the local hybridization state of carbon atoms, even in the averaged signal. Further increase in T (700−1000 fs) leads to a decay of the dispersive signatures and absorptive features due to band narrowing can be identified.

In Figure 9b and 9c, the SRS signal is decomposed into the contributions of the individual electronic states for T = 480 and 1000 fs, respectively. Strong spectral overlap is observed of the different product channels (cf. Figure 6) at both delay times. The dispersive line shapes at T = 480 fs around $\omega - \omega_3 \approx 3000$ cm^{-1} predominantly arise from S_0. Note that due to the integral over frequency trajectory in eq 51, trajectories eventually relaxing into S_0 but still in S_1 or S_2 at T = 480 fs have dispersive contributions prior to their hopping event and reflect the S_1 and S_2 contributions to this spectral feature. The results demonstrate that C−H modes offer a valuable local structural probe of out-of-plane deformations of the π system and the local hybridization state of their adjacent carbon atoms.

The semiclassical protocol described in section 2.2.3 is particularly suited for high-frequency spectator modes where the excited state Hessian is reconstructed for the desired modes

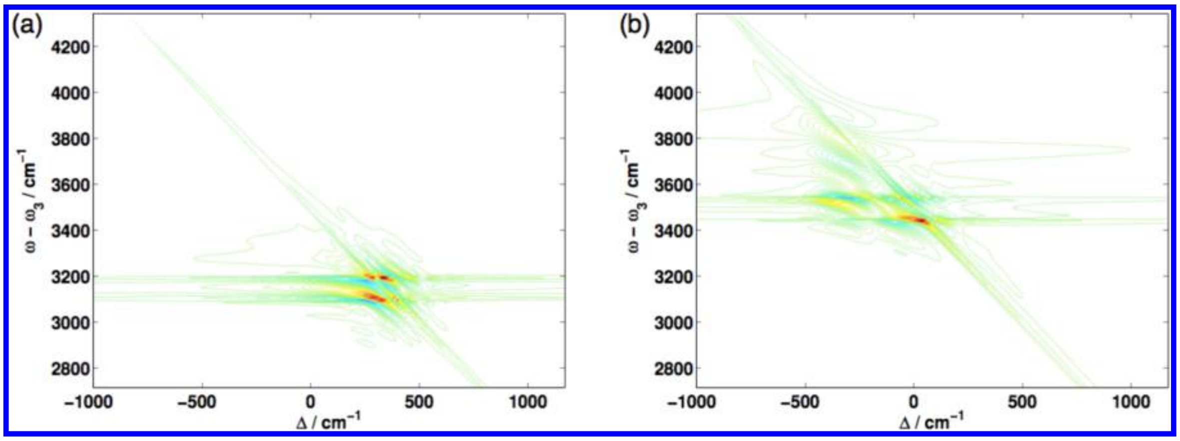

Figure 10. Δ-Dispersed signal (eq 51) of the nonadiabtatic relaxation of uracil via the diabatic pathway $\pi\pi^*_{S_2} \rightarrow \pi\pi^*_{S_1} \rightarrow$ gs: (a) Δ-dispersed signal of C−H− stretch vibrations for T = 580 fs; (b) Δ-dispersed signal of N−H− stretch vibrations for T = 580 fs. Reproduced with permission from ref 113. Copyright 2014 American Chemical Society.

in a mode-tracking procedure. This allows one to decouple the numerical effort from system size and enables ab initio simulations of excited state vibrational dynamics of medium-sized molecules. Nevertheless, for low-frequency modes where the vibrational mode character is modified substantially along the reaction coordinate, the elaborate protocol of section 2.2.1 that relies on the numerical propagation of the wave function is required. As a compromise between fully quantum and semiclassical descriptions, the application of the numerical propagation of the wave function was demonstrated for the calculation of FSRS spectra of acrolein subject to nonadiabatic relaxation.[94] Few spectator modes are selected as marker bands, which are then treated by direct propagation under the influence of a time-dependent potential imposed by semiclassical dynamics along the reaction coordinate. In this scheme the multidimensional potential energy function in the subspace of active marker bands must be calculated explicitly. This accounts for anharmonicities and intermode couplings.

3.3.1. Interplay of Temporal and Spectral Resolution.

The semiclassical signal, eq 48 and eq 51, is derived microscopically from the respective loop diagrams and fully accounts for the time/frequency resolution limits imposed by the Fourier uncertainty. The delay time T and the frequency of the detection axis $\omega - \omega_3$ are independent experimental knobs, and we can formally assign uncertainties ΔT and $\Delta\omega$ associated with the pulse duration and the frequency resolution of a spectrometer. This might suggest that there is no lower bound to the product $\Delta\omega\Delta T$; the measurement can apparently be interpreted in terms of stroboscopic snapshots with high spectral resolution. Typical experiments[111,219] allow for <50 fs pulses and spectral resolution (<10 cm^{-1}) such that $\Delta\omega\Delta T \approx 0.5$ ps cm^{-1},[114,220] which is an order of magnitude smaller than the Fourier uncertainty for Gaussian pulses. Note that the combination of pulses of different length was shown to increase spectral resolution in Raman signals already in the 1980s.[221,222] By providing a proper definition of $\Delta\omega$ and Δt, the formalism of section 3.3 demonstrates that both quantities are not purely instrumental but depend on the system as well. We find that the SRS signal at time T does not represent a snapshot of the system dynamics. Matter dynamics induces a chirp in the SRS signal which directly shows up in the evolving width of the resonances and induces dispersive line shapes in the SRS signals. Analysis of the Δ-dispersed signals demonstrates these matter−chirp contributions to the signal and allows one to estimate the optimal laser pulse bandwidth in SRS experiments.

Although the Δ-dispersed signal (eq 51) is not a measurable observable, it contains more information than the experimental signal and demonstrates the conjugate time−frequency resolution inherent to SRS experiments. The observable SRS signal is given by integration over the Δ axis (eq 48). Along the detection axis $(\omega - \omega_3)$, the resonances of the SRS signal at the observation time T can be identified. Note that due to the integration over the instantaneous frequency trajectory $\omega(t)$, the resonances along $\omega - \omega_3$ do not represent a snapshot of the system dynamics but all frequency components contributing to a single mode in $\omega - \omega_3$ are revealed along the Δ axis. As the instantaneous frequencies $\omega(t)$ of the C_6−H and C_5−H mode are shifted in the course of the nonadiabatic dynamics, both positive and negative frequency components enter along the Δ axis and the Δ-dispersed signal and a matter-induced chirp contributes to the SRS signal. The Δ-dispersed signal of both the C−H and the N−H vibrations of the trajectory of *diabatic* $\pi\pi^*_{S_2} \rightarrow \pi\pi^*_{S_1} \rightarrow$ gs relaxation appears asymmetric along the diagonal, as the evolution of instantaneous frequencies is dominated by a red shift subsequent to the hopping event.

The 2D representation of the Δ-dispersed signal (Figure 10) reveals that SRS signals are indeed limited by the Fourier uncertainty in their respective conjugate variables. Even though high-frequency resolution can be obtained along the detection axis $\omega - \omega_3$, the high temporal resolution affects the signal along the not directly observable Δ axis, where the bandwidth of the femtosecond probe pulse selects the contributing frequency components. Both the $\omega - \omega_3$ axis and the Δ axis are controlled by independent experimental knobs. The inherent matter chirp contribution determines the required bandwidth of the probe ω_3. As the probe pulse bandwidth is increased, only limited frequency components of the pulse contribute to the signal and the probe bandwidth becomes irrelevant. On the other hand, the full probe bandwidth has to cover the bandwidth spanned by the matter dynamics. Inspection of Figure 10 reveals that the dynamics of C−H stretch vibrations covers a bandwidth of ~300−500 cm^{-1} along the Δ axis. For such dynamics, optimal probe pulses with a corresponding duration on the order of 25 fs are readily available in the optical regime. The longer pulse would spoil the temporal resolution, whereas a shorter pulse will result in poor spectral resolution.

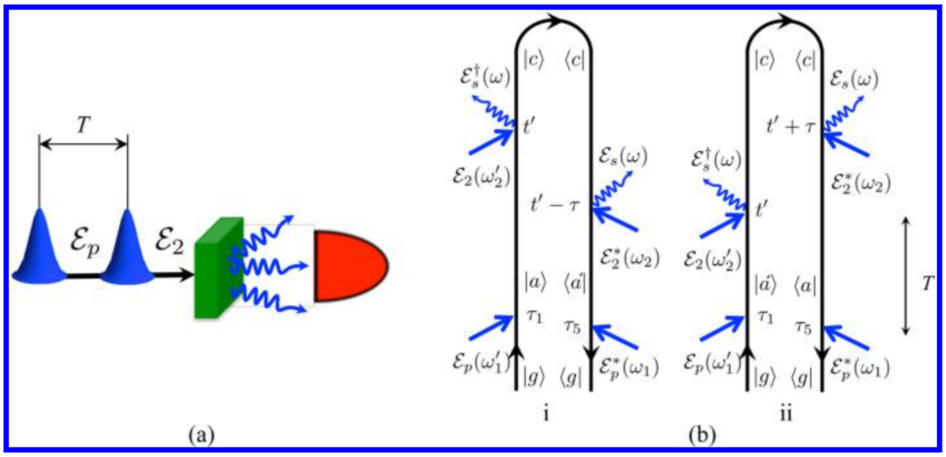

Figure 11. FR-SPRS signal (eq 56): (a) schematic layout and (b) loop diagrams. Time-translational invariance yields $\omega_1'+\omega_2' - \omega + \omega - \omega_2 - \omega_1 = 0$. Note that, in contrast with the stimulated techniques where the last interaction is with the bra, here the last interaction may be either with the bra (diagram *i*, $\tau > 0$) or with the ket (diagram *ii*, $\tau < 0$). Reproduced with permission from ref 213. Copyright 2013 AIP Publishing LLC.

3.3.2. Additional Variants of the SRS Technique.

We next consider several configurations of the SRS technique and address various factors that control the temporal and spectral resolutions. We compare four Raman probe techniques: the homodyne-detected frequency-resolved spontaneous Raman spectroscopy (FR-SPRS),[223−225] the FSRS,[114,219,226−230] the heterodyne-detected transient grating impulsive stimulated Raman spectroscopy (TG-ISRS),[231−234] and the time-resolved impulsive stimulated Raman spectroscopy (TR-ISRS) signal.[235,236] All provide 2D signals when displayed vs one time delay variable and a second frequency variable that reveals the Raman resonances. The schematics of the signals along with the corresponding loop diagrams are shown in Figures 11−14. It follows from the diagrams that all four signals depend on two matter quantities

$$F_i(t_1, t_2, t_3) = \langle VG^\dagger(t_1)\alpha G^\dagger(t_2)\alpha G(t_3)V^\dagger\rangle \tag{52}$$

$$F_{ii}(t_1, t_2, t_3) = \langle VG^\dagger(t_1)\alpha G(t_2)\alpha G(t_3)V^\dagger\rangle \tag{53}$$

where $G(t) = (-i/\hbar)\theta(t)e^{-iHt}$ is the retarded Green's function that represents forward time evolution with the free-molecule Hamiltonian H. $G^\dagger$ represents backward evolution. F_i involves one forward and two backward evolution periods of a vibrational wavepacket. F_{ii} contains two forward followed by one backward propagation. Note that eqs 25 and 26 of the UV/IR technique contain the same free evolution periods where both time arguments ($t = \tau_2 - \tau_1$) were retained for the definition of Green's functions, intended for a semiclassical description. One can express the relevant matter correlation functions (eqs 52 and 53) in the frequency domain

$$F_i(\omega_1, \omega_2, \omega_3) = \langle VG^\dagger(\omega_1)\alpha G^\dagger(\omega_2)\alpha G(\omega_3)V^\dagger\rangle \tag{54}$$

$$F_{ii}(\omega_1, \omega_2, \omega_3) = \langle VG^\dagger(\omega_1)\alpha G(\omega_2)\alpha G(\omega_3)V^\dagger\rangle \tag{55}$$

where $G(\omega) = h^{-1}/[\omega + \omega_g - H/\hbar + i\epsilon]$ and $\hbar\omega_g$ is the ground state energy. Equations 52 and 53 are convenient for microscopic wavepacket simulations (cf. section 2.2.1).[76] Equations 54 and 55 will be used in the six-wave-mixing frequency-domain representation of the signals.

3.3.2.1. *Frequency-Resolved Spontaneous Raman Signal (FR-SPRS).*

The spontaneous Raman signal is measured with homodyne detection. In the FR-SPRS technique (Figure 11) the actinic pulse $\mathcal{E}_p$ first launches the excited state dynamics. After a delay period T, an off-resonant excitation by the Raman pump $\mathcal{E}_2$ is followed by a spontaneous emission of the Raman shifted photon. As shown in the Appendix (Figure 30) this photon may be detected by a time- and frequency-gated detector according to eq 102, and the signal is given by an overlap of the detector and bare signal Wigner spectrograms. For a more direct comparison with the stimulated Raman techniques we shall focus on the simpler frequency gating.

The diagram rules[81] allow one to write the expressions directly from the diagrams. To illustrate how this works let us examine diagram (*i*) (Figure 11b), which represents a forward and backward time-evolving vibrational wavepacket. First, the actinic pulse $\mathcal{E}_p(\omega_1')$ electronically excites the molecule via $V^\dagger$ to state $|a'\rangle$. The wave function then propagates forward in time from τ_1 to t'. Then the off-resonant pump pulse $\mathcal{E}_2(\omega_2{}')$ excites and the instantaneous spontaneously emitted photon $\mathcal{E}_s^\dagger(\omega)$ de-excites the electronic transition to a different vibrational level $|c\rangle$ via α which then propagates backward in time from t' to $t' - \tau$. The spontaneous photon $\mathcal{E}_s(\omega)$ de-excites and pump pulse $\mathcal{E}_2^*(\omega_2)$ excites the electronic transition from state $\langle c|$ to $\langle a|$ via α and the wave function propagates backward in time from $t' - \tau$ to τ_5. The final de-excitation by $\mathcal{E}_p^*(\omega_1)$ brings the system to its initial state by acting with V. Diagram (*ii*) can be interpreted similarly. Note that in diagram (*i*) the chronologically last interaction occurs with the ket, whereas in diagram (*ii*) it is with the bra. The diagram rules, which follow from time translational invariance, imply that the sum of the six frequencies of the various fields must be zero $\omega_1' + \omega_2' - \omega + \omega - \omega_2 - \omega_1 = 0$. For an ideal frequency-resolved detection $F_f(\omega,\bar{\omega}) = \delta(\omega - \bar{\omega})$ and eqs 114 and 115 yield

$$\begin{aligned} S_{\text{FR-SPRS}}(\bar{\omega}, T) = {} & -i\hbar \int_{-\infty}^{\infty} \frac{d\omega_1}{2\pi}\frac{d\omega_1'}{2\pi}\frac{d\omega_2}{2\pi} \\ & \times \mathcal{D}^2(\bar{\omega})\mathcal{E}_2^*(\omega_2)\mathcal{E}_2(\omega_1 - \omega_1' + \omega_2)\mathcal{E}_p^*(\omega_1)\mathcal{E}_p(\omega_1')e^{i(\omega_1-\omega_1')T} \\ & \times [F_i(\omega_1, \omega_1 + \omega_2 - \bar{\omega}, \omega_1') - F_{ii}(\omega_1, \omega_1 + \omega_2 - \bar{\omega}, \omega_1')] \end{aligned} \tag{56}$$

where $\mathcal{D}(\omega) = \omega^3/(2\pi^2c^3)$ is the density of states of radiation modes. $\mathcal{D}(\omega)$ has taken the place of the probe pulse in the stimulated techniques. Equation 56 can be alternatively recast in time domain (cf. Appendix, Frequency-Resolved Spontaneous Raman Signal (FR-SPRS)).

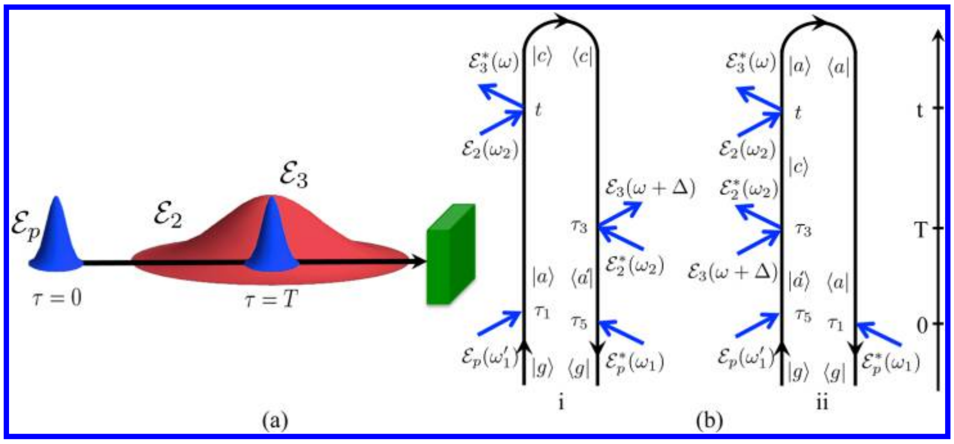

Figure 12. FSRS signal (eq 60): (a) schematic layout and (b) loop diagrams. Time translational invariance yields $\omega_1' + \omega_2 - \omega + (\omega + \Delta) - \omega_2 - \omega_1 = 0$. Reproduced with permission from ref 213. Copyright 2013 AIP Publishing LLC.

We consider the entire process, including the actinic pulse, the Raman pump pulse, and spontaneous emission, as a single six-wave mixing event. In general, the actinic pump pulse can be impulsive, thereby creating coherences in the vibrational state manifold. In this case, the preparation by the actinic pump pulse has to be explicitly considered in the description of the six-wave mixing process. If, in contrast, the actinic pulse is short enough to impulsively trigger bath dynamics but long compared to the vibrational periods, the limited bandwidth can only create populations ρ_{aa} but not coherences $\rho_{aa'}$ in the relevant modes. In this limit, we can omit the actinic pump from the description of the optical process and the process can be viewed as a FWM experiment from a nonstationary state created by the actinic pump. This is a simpler, widely used picture, but it only holds in a limited parameter regime. If no dynamics is initiated and the state ρ_{aa} is stationary then the pulsed experiment can be viewed as many stationary Raman experiments done in parallel and the pulse duration becomes immaterial. Note that the above argument holds for both spontaneous and stimulated signals discussed below.

A simplified physical picture is obtained by a semiclassical model of the bath which assumes that it simply modulates the vibrational frequencies in time. Expanding the matter correlation function (Figure 11b) in system eigenstates, the Green's function for the initially prepared excited state is $G_a(t_1,t_2) = (-i/\hbar)\theta(t_1 - t_2)\mathrm{e}^{-(i\omega_a+\gamma_a)\,(t_1 - t_2)}$, and for the final Raman-shifted excited vibrational state,[76,103] we have

$$G_c^\dagger(t,\, \tau_3) = (-i/\hbar)\theta(t - \tau_3)\mathrm{e}^{i\omega_a(t-\tau_3)}\exp_{-}\left[i\int_{\tau_3}^{t} \mathrm{d}\tau\omega_{\mathrm{ac}}(\tau)\right]$$

where $\omega_{ac}(\tau)$ is the vibrational frequency evolving with classical trajectories. Assuming an impulsive actinic pulse $\mathcal{E}_\mathrm{p}(t) \simeq \mathcal{E}_\mathrm{p}\delta(t)$ we obtain

$$\begin{aligned} S_{\mathrm{FR-SPRS}}(\omega,\, T) &= \mathcal{R}\frac{\mathcal{D}^2(\omega)}{\hbar^2}|\mathcal{E}_\mathrm{p}|^2 \sum_{a,c} |\mu_{ag}|^2\alpha_{ac}^2 \\ &\times \int_{-\infty}^{\infty} \frac{\mathrm{d}\omega_2}{2\pi}\frac{\mathrm{d}\Delta}{2\pi}\mathcal{E}_2^*(\omega_2)\mathcal{E}_2(\omega_2 + \Delta)\mathrm{e}^{i\Delta T} \\ &\times \int_{-\infty}^{\infty} \mathrm{d}t \int_{-\infty}^{t} \mathrm{d}\tau_3\mathrm{e}^{-\gamma_a(t+\tau_3)}\mathrm{e}^{i(\omega-\omega_2)(t-\tau_3)-i\Delta\tau_3} \\ &\times \exp[-i\int_{\tau_3}^{t} \omega_{ac}(\tau)\mathrm{d}\tau] \end{aligned} \tag{57}$$

where $\mathcal{R}$ denotes the real part and $\Delta = \omega_1 - \omega_1'$ represents the spectral bandwidth of the pump pulse, which translates into the spectral bandwidth of the relevant matter degrees of freedom.

The FR-SPRS signal (eq 57) can be recast as a sum of modulus squares of transition amplitudes, which represent pairs of vibrational states a and c

$$S_{\mathrm{FR-SPRS}}(\omega,\, T) = \sum_{a,c} |T_{ca}(\omega,\, T)|^2 \tag{58}$$

where

$$\begin{aligned} T_{ca}(\omega,\, T) &= \frac{\mathcal{D}(\omega)}{\hbar}\mu_{ag}^*\alpha_{ac}\mathcal{E}_\mathrm{p} \int_{-\infty}^{\infty} \mathrm{d}t\frac{\mathrm{d}\omega_2}{2\pi}\mathcal{E}_2(\omega_2) \\ &\times e^{[i(\omega-\omega_2)-\gamma_a]t+i\omega_2 T}\exp[i\int_{0}^{t} \omega_{ac}(\tau)\mathrm{d}\tau] \end{aligned} \tag{59}$$

In the limit of an ideal frequency gate, the detection modes enter as frequency-independent functions. Equations 58 and 59 follow straightforwardly from the more general expressions eqs 106 and 107 (see Appendix). They demonstrate that the FR-SPRS signal is guaranteed to be positive and consists of purely absorptive peaks.

3.3.2.2. *Femtosecond Stimulated Raman Signal (FSRS).*

The FSRS signal employs a quadratic hybrid probe ($S_{\mathrm{QH}}^{(\mathrm{fd})}$) and can be read off the diagrams depicted in Figure 12 as demonstrated above for FR-SPRS; a detailed derivation is given in the Appendix, Stimulated Signals. Following the actinic pulse $\mathcal{E}_\mathrm{p}$, after a delay T, pulse 2 and probe 3 induce the Raman process. The signal is defined as the frequency-dispersed probe transmission $\mathcal{E}_3(\omega)$. Diagram (i) of the FSRS technique can be described similarly to FR-SPRS by replacing the spontaneously generated field $\mathcal{E}_\mathrm{s}$ by a broad-band probe pulse $\mathcal{E}_3$. Diagram (ii) is different. Following the initial electronic excitation by the

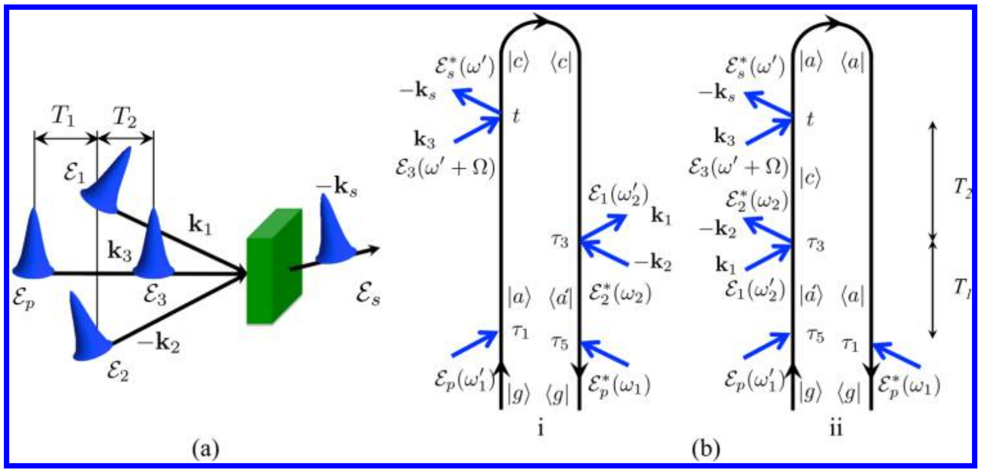

Figure 13. TG-ISRS signal (eqs 62 and 63): (a) schematic layout and (b) loop diagrams. Time translational invariance yields $\omega_1' + (\omega' + \Omega) - \omega' + \omega_2' - \omega_2 - \omega_1 = 0$. Reproduced with permission from ref 213. Copyright 2013 AIP Publishing LLC.

actinic pulse $\mathcal{E}_p(\omega_1')$, the wave function $|a'\rangle$ propagates forward in time from τ_5 to τ_3. At this point, a Raman process involving the pump $\mathcal{E}_2^*(\omega_2)$ and the probe $\mathcal{E}_3(\omega + \Delta)$ promotes the system to the vibrational state $|c\rangle$ and the wave function propagates forward in time from τ_3 to t. After Raman de-excitation governed by $\mathcal{E}_2(\omega_2)\mathcal{E}_3^*(\omega)$ it then propagates backward from t to τ_1 in $\langle a|$ where an electronic excitation via the actinic pulse $\mathcal{E}_p^*(\omega_1)$ brings the system back in its initial ground state. Assuming that pulse 2 is spectrally narrow, we set $\mathcal{E}_2(t - T) = \mathcal{E}_2 e^{-i\omega_2(t-T)}$ and the FSRS signal for the Raman shift $\Omega = \omega - \omega_2$ reads[213]

$$S_{\mathrm{FSRS}}(\Omega, T) = \mathcal{I}\frac{4\pi}{\hbar}\int_{-\infty}^{\infty}\frac{\mathrm{d}\Delta}{2\pi}\frac{\mathrm{d}\omega_1}{2\pi}\frac{\mathrm{d}\omega_1'}{2\pi}\delta(\omega_1 - \omega_1' - \Delta) \times \mathcal{E}_3^*(\Omega + \omega_2)\mathcal{E}_3(\Omega + \omega_2 + \Delta)|\mathcal{E}_2|^2\mathcal{E}_p^*(\omega_1)\mathcal{E}_p(\omega_1')e^{i\Delta T} \times [F_i(\omega_1, \omega_1' - \Omega, \omega_1') + F_{ii}(\omega_1, \omega_1 + \Omega, \omega_1')] \tag{60}$$

where $\mathcal{I}$ denotes the imaginary part. In the Appendix, Stimulated Signals, eq 60 is recast in the time domain. In contrast to FR-SPRS where the gating enters as modulus square of transition amplitudes, in FSRS the symmetry between both loop branches is broken and the FSRS signal cannot be recast as an amplitude square. While the narrow-band picosecond component corresponds to $\mathcal{E}_2$ and enters as an amplitude square, the femtosecond probe field $\mathcal{E}_3{}^*$ enters as $\mathcal{E}_3{}^*(\omega)\mathcal{E}_3(\omega + \Delta)$. Time translational invariance implies $\omega_1' + \omega_2 - \omega + (\omega + \Delta) - \omega_2 - \omega_1 = 0$. In contrast to FR-SPRS, FSRS can contain dispersive spectral features. The reason for this difference is that the spontaneous signal is dissipative from a population state at the end of the detection process. In FSRS, in contrast, it follows from the diagrams in Figure 12 that the system can be detected in a coherence state.[205] The asymmetry is caused by the frequency-dispersed detection of the probe pulse which occurs only at the ket side of the diagram, while the bra side interacts with all frequency components of the probe field controlled by $\mathcal{E}_3(\omega + \Delta)$. For a discussion of the resolution limit in the case of overlapping pulses see ref 237.

Using our semiclassical model of frequency modulation by the bath, the FSRS signal reads

$$S_{\mathrm{FSRS}}(\omega - \omega_2, T) = -\mathcal{I}\frac{4}{\hbar^4}|\mathcal{E}_p|^2|\mathcal{E}_2|^2\sum_{a,c}|\mu_{ag}|^2\alpha_{ac}^2 \times \int_{-\infty}^{\infty}\frac{\mathrm{d}\Delta}{2\pi}\mathcal{E}_3^*(\omega)\mathcal{E}_3(\omega + \Delta)\mathrm{e}^{i\Delta T} \times \int_{-\infty}^{\infty}\mathrm{d}t\int_{-\infty}^{t}\mathrm{d}\tau_3\mathrm{e}^{-\gamma_a(t+\tau_3)+i(\omega-\omega_2)(t-\tau_3)-i\Delta\tau_3} \times \sin\left[\int_{\tau_3}^{t}\omega_{ac}(\tau)\mathrm{d}\tau\right] \tag{61}$$

Here, an integral over the stochastic vibrational frequency trajectory $\omega_{ac}(t)$ determines the matter contribution to the signal.

Stimulated Raman signals such as FSRS may be recorded under resonance conditions allowing for chromophore selectivity,[238] and improved signal-to-noise ratios. Electronically resonant Raman signals may also be described by the loop diagrams but require six-point rather than four-point matter correlation functions since the up and down Raman transitions are no longer simultaneous. Instead of two time variables corresponding to interaction times with the Raman probe, two additional time variables will enter the expression for the signals, since the electronic dephasing is typically very short. The essential part of the formalism remains intact except for the electronic state specific information that is excited resonantly and enters the summation currently hidden in the polarizability. The corresponding expressions can be read off the same diagrams shown in Figures 11−14.

Even though FSRS is a quite recent technique,[111,219,239,240] the scope of applications is widespread. Recent reviews covering technological advances and applications are given in refs 114, 241, and 242. Investigations, performed either in resonant or in off-resonant detection mode, cover the excited state relaxation dynamics of carotenoids[173,238,243−247] and flavins,[248] energy redistribution in myoglobin,[249] excited state proton transfer dynamics in green fluorescent proteins (GFP)[250] and native water environment,[251−253] ultrafast structural evolution in photoactive yellow protein (PYP),[228,254] and hydrogen bond reorganization dynamics subsequent to electronic excitation.[255] Charge and energy transfer dynamics has been investigated by the FSRS technique in transition metal complexes,[256] in dye-sensitized solar cells,[257] for intramolecular charge translocation in 4-(dimethylamino)benzonitrile[226,258] and betaine-30,[247] as well as investigations on polaron formation[259] and exciton

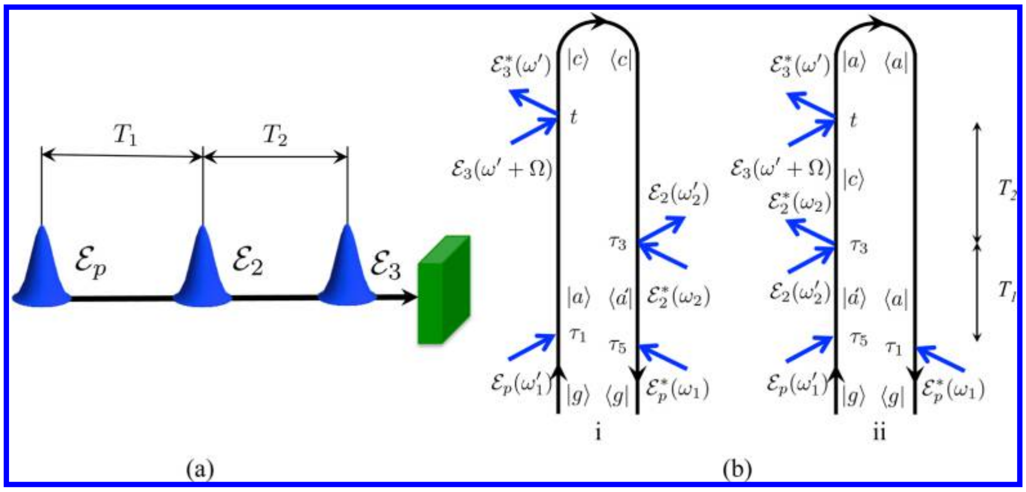

Figure 14. TR-ISRS signal (eqs 64 and 65): (a) schematic layout and (b) loop diagrams. Time translational invariance yields $\omega_1' + (\omega' + \Omega) - \omega' + \omega_2' - \omega_2 - \omega_1 = 0$. Reproduced with permission from ref 213. Copyright 2013 AIP Publishing LLC.

mobility[260] in photoexcited conjugated materials.[261] The relaxation dynamics of molecular switches[229,262,263] was investigated, and intermediates[264] and nonadiabatic relaxation pathways[265] upon photoexcitation could be clarified. Recent technological developments allowed for the implementation of numerous FSRS variants, like two-dimensional FSRS (2D-FSRS),[220,266,267] surface-enhanced FSRS,[268] and six-wave mixing FSRS,[269] discussed in detail in ref 114.

3.3.2.3. Heterodyne-Detected TG-ISRS Signal and TR-ISRS Signal.

In the TG-ISRS signal, two coincident short pulses with wave vectors $\mathbf{k}_1$ and $\mathbf{k}_2$ interact with the system after delay time T_1 from actinic pulse and form an interference pattern with wave vector $\mathbf{k}_1 - \mathbf{k}_2$. After a second delay period T_2, a third beam with wave vector $\mathbf{k}_3$ is scattered off the grating to generate the signal with wave vector $\mathbf{k}_s = \mathbf{k}_1 - \mathbf{k}_2 + \mathbf{k}_3$, which can be recorded in amplitude and phase by heterodyne detection. TG-ISRS signals have been measured by homodyne detection. In the heterodyne-detected TR-ISRS signals, the field is mixed with the transmitted probe field. The homodyne detection scheme of TR-ISRS signals is subject to limitations such as an artificial enhancement of modulation decay and broadened bandwidths in the Fourier spectra due to cross terms from different scattering processes.[236] These limitations are usually eliminated by introducing an external local oscillator,[270,271] which can be conveniently generated in situ by additional molecules in the same solution. Since such a molecular local oscillator contains some dynamics, the response of a combined system is not the same as from a pure optical local oscillator. The heterodyne transient grating (het-TG) signals have been introduced to remedy some of the limitations of the homodyne detection.[236] In the following, we compare both heterodyne-detected TG-ISRS and TR-ISRS signals. Following the classification scheme in section 3.2, both signals employ a quadratic broad-band probe and are recorded frequency dispersed ($S_{\mathrm{QB}}^{(\mathrm{fd})}$).

Fourier transforming the signal with respect to T_2 yields the vibrational spectra for different values of the first delay T_1. Using two loop diagrams as shown in Figure 13b the TG-ISRS is given by

$$S_{\mathrm{TG-ISRS}}(\Omega, T_1) = \mathcal{I}\tilde{S}_{\mathrm{TG-ISRS}}(\Omega, T_1) \times \int_{-\infty}^{\infty} \frac{\mathrm{d}\omega'}{2\pi} \mathcal{E}_s^*(\omega')\mathcal{E}_3(\omega' - \Omega) \tag{62}$$

where Ω is the frequency conjugated to T_2 and

$$\begin{aligned}\tilde{S}_{\mathrm{TG-ISRS}}(\Omega, T_1) = \frac{2}{\hbar}\int_{-\infty}^{\infty} \frac{\mathrm{d}\omega_1}{2\pi}\frac{\mathrm{d}\omega_1'}{2\pi}\frac{\mathrm{d}\omega_2}{2\pi}\mathcal{E}_\mathrm{p}^*(\omega_1)\mathcal{E}_\mathrm{p}(\omega_1') \\ \times \mathcal{E}_2^*(\omega_2)\mathcal{E}_1(\omega_1 - \omega_1' + \omega_2 + \Omega)\mathrm{e}^{i(\omega_1 - \omega_1')T_1} \\ \times [F_i(\omega_1, \omega_1' - \Omega, \omega_1') + F_{ii}(\omega_1, \omega_1 + \Omega, \omega_1')]\end{aligned} \tag{63}$$

The same correlation functions F_i and F_{ii} of FR-SPRS and FSRS fully determine the matter response. Despite the fact that eq 63 closely resembles eq 60 of FSRS, the different detection can become crucial. In contrast to FSRS, which records the frequency-dispersed transmission of the probe pulse $\mathcal{E}_3$, the TG-ISRS signal is measured in the time domain vs two delays T_1, T_2. T_1 controls the time resolution, whereas T_2 governs the spectral resolution. Furthermore, the narrow-band pump $\mathcal{E}_2$ in FSRS enters as a modulus square $|\mathcal{E}_2|^2$, whereas the broad-band fields $\mathcal{E}_1$ and $\mathcal{E}_2$ enter as $\mathcal{E}_2^*(\omega_2)\mathcal{E}_1(\omega_1 - \omega_1' + \omega_2 + \Omega)$. Instead of a single probe $\mathcal{E}_3$, in FSRS a probe pulse $\mathcal{E}_3$ is scattered off the grating and gives rise to a field $\mathcal{E}_s$. Therefore, the four fields in TG-ISRS provide more control parameters for manipulating the signal compared to FSRS/FR-SPRS.

The TR-ISRS signal uses a collinear pump/probe geometry and measures the probe transmission. This signal is a special case of the TG-ISRS with a single pump pulse $\mathcal{E}_1 = \mathcal{E}_2$ and $\mathcal{E}_s = \mathcal{E}_3$ is a probe pulse (see Figure 14a)

$$S_{\mathrm{TR-ISRS}}(\Omega, T_1) = \mathcal{I}\tilde{S}_{\mathrm{TR-ISRS}}(\Omega, T_1) \times \int_{-\infty}^{\infty} \frac{\mathrm{d}\omega'}{2\pi} \mathcal{E}_3^*(\omega')\mathcal{E}_3(\omega' - \Omega) \tag{64}$$

where

$$\begin{aligned}\tilde{S}_{\mathrm{TR-ISRS}}(\Omega, T_1) = \frac{2}{\hbar}\int_{-\infty}^{\infty} \frac{\mathrm{d}\omega_1}{2\pi}\frac{\mathrm{d}\omega_1'}{2\pi}\frac{\mathrm{d}\omega_2}{2\pi}\mathcal{E}_\mathrm{p}^*(\omega_1)\mathcal{E}_\mathrm{p}(\omega_1') \\ \times \mathcal{E}_2^*(\omega_2)\mathcal{E}_2(\omega_1 - \omega_1' + \omega_2 + \Omega)e^{i(\omega_1 - \omega_1')T_1} \\ \times [F_i(\omega_1, \omega_1' - \Omega, \omega_1') + F_{ii}(\omega_1, \omega_1 + \Omega, \omega_1')]\end{aligned} \tag{65}$$

In the Appendix, TG-ISRS and TR-ISRS, eqs 63 and 65 are recast in the time domain.

Even though TR-ISRS and TG-ISRS use a very different experimental setup, they carry the same matter information. TG-

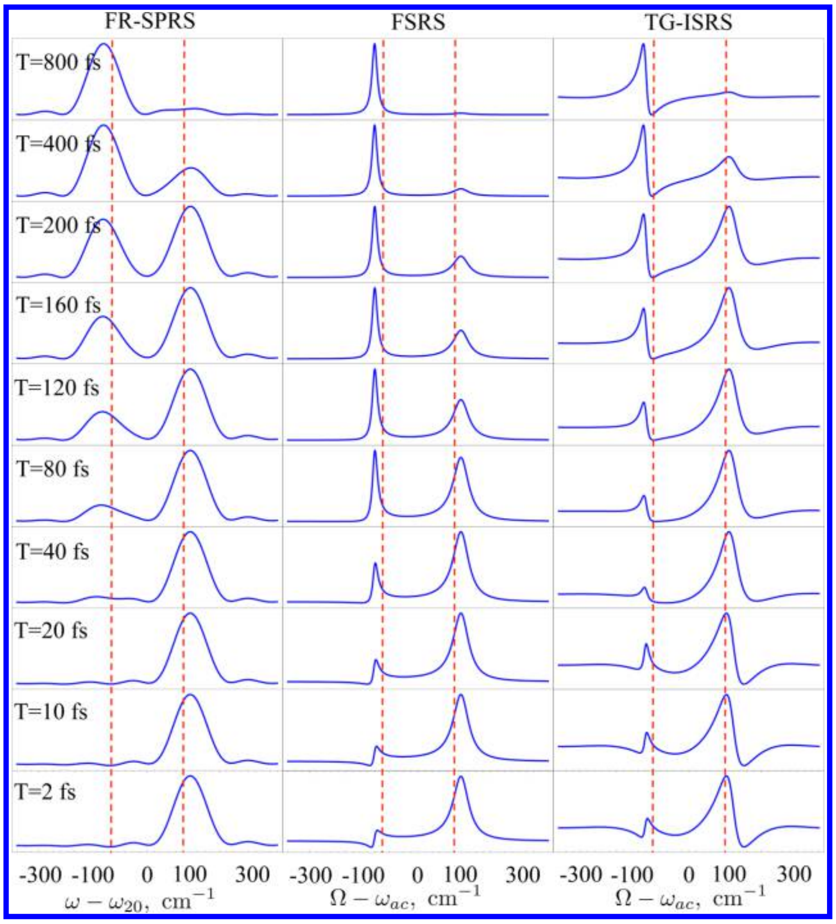

Figure 15. Spontaneous FR-SPRS signal (eq 156, left), stimulated Raman signals FSRS (eq 157, middle), and TG-ISRS (eq 158, $\mathcal{E}_2 = \mathcal{E}_1$ and $\mathcal{E}_s = \mathcal{E}_3$, right) for the two-state jump consisting of a single vibrational mode (TSJ) model (eqs 156−158): signals are shown for for interpulse delay T (2 fs < T < 800 fs) corresponding to the jump dynamics. Model parameters: 150 fs pump $\mathcal{E}_2$ with central frequency of the pump ω_{20} for the FR-SPRS and TG-ISRS, 10 ps pump for FSRS and 5 fs probe $\mathcal{E}_3$ are centered around 800 nm wavelength; unperturbed vibrational frequency ω_{ac} = 1000 cm^{-1}, splitting magnitude δ = 100 cm^{-1}, inverse jump rate k^{-1} = 300 fs, and inverse vibrational dephasing γ_a^{-1} = 620 fs. Red dashed vertical lines correspond to $\pm\delta$. If the pump pulse $\mathcal{E}_2$ in the het-TG technique is shortened to 5 fs, TG-ISRS coincides with FSRS. Reproduced with permission from ref 213. Copyright 2013 AIP Publishing LLC.

ISRS allows for spatial selection and manipulation of the field envelopes and phases, whereas TR-ISRS depends on $|\mathcal{E}_2|^2$ and is independent of the phase of the pump field. Furthermore, if we compare TR-ISRS to the FSRS, we note that the main difference is that the pump pulse $\mathcal{E}_2$ in FSRS is narrow band and thus enters the signal (eq 60) as $|\mathcal{E}_2|^2\delta(\omega_1 - \omega_1' - \Delta)$ which is independent of its phase, whereas in the case of TR-ISRS the broad-band pump yields a phase-dependent contribution to eq 65 $\mathcal{E}_2^*(\omega_2)\mathcal{E}_2(\omega_1 - \omega_1' + \omega_2 + \Omega)$. Similar to FSRS and in contrast to FR-SPRS, TR-ISRS and TG-ISRS can contain dispersive spectral features due to the ability to report on interstate coherences (cf. diagrams in Figures 13b and 14b). The asymmetry between modes in both impulsive stimulated Raman signals arises since the signal is defined as a transmission of a single field, whereas the dissipative signal will require measuring the transmission of all fields.

Treating the bath semiclassically, eqs 62−65 yield

$$\begin{aligned} S_{\text{TG}-\text{ISRS}}(\Omega,\, T_1) = \\ -\mathcal{I}\frac{4}{\hbar^4}|\mathcal{E}_{\text{p}}|^2 \sum_{a,c} |\mu_{ag}|^2\alpha_{ac}^2 \int_{-\infty}^{\infty} \frac{\text{d}\omega'}{2\pi}\mathcal{E}_{\text{s}}^*(\omega')\mathcal{E}_3(\omega' - \Omega)\text{e}^{-i\Omega T_1} \\ \times \int_{-\infty}^{\infty} \frac{\text{d}\omega_2}{2\pi}\frac{\text{d}\Delta}{2\pi}\mathcal{E}_2^*(\omega_2)\mathcal{E}_1(\omega_2 + \Delta)\text{e}^{i\Delta T_1} \\ \times \int_{-\infty}^{\infty} \text{d}t \int_{-\infty}^{t} \text{d}\tau_3 \text{e}^{-\gamma_a(t+\tau_3)+i\Omega t-i\Delta\tau_3}\sin\Big[\int_{\tau_3}^{t} \omega_{ac}(\tau)\text{d}\tau\Big] \end{aligned} \tag{66}$$

$$\begin{aligned} S_{\text{TR}-\text{ISRS}}(\Omega,\, T_1) = \\ -\mathcal{I}\frac{4}{\hbar^4}|\mathcal{E}_{\text{p}}|^2 \sum_{a,c} |\mu_{ag}|^2\alpha_{ac}^2 \int_{-\infty}^{\infty} \frac{\text{d}\omega'}{2\pi}\mathcal{E}_3^*(\omega')\mathcal{E}_3(\omega' - \Omega)\text{e}^{-i\Omega T_1} \\ \times \int_{-\infty}^{\infty} \frac{\text{d}\omega_2}{2\pi}\frac{\text{d}\Delta}{2\pi}\mathcal{E}_2^*(\omega_2)\mathcal{E}_2(\omega_2 + \Delta)\text{e}^{i\Delta T_1} \\ \times \int_{-\infty}^{\infty} \text{d}t \int_{-\infty}^{t} \text{d}\tau_3 \text{e}^{-\gamma_a(t+\tau_3)+i\Omega t-i\Delta\tau_3}\sin\Big[\int_{\tau_3}^{t} \omega_{ac}(\tau)\text{d}\tau\Big] \end{aligned} \tag{67}$$

We next discuss the semiclassical expressions of eqs 57, 61, 66, and 67. FSRS is distinct from the other techniques since the signal has only two rather than three frequency integrations. This explains why it has a better time resolution; the information on F_i and F_{ii} is less averaged. TR-ISRS and TG-ISRS are more closely related to TR-SPRS than to FSRS. Another notable point is that only the FR-SPRS signal can be recast as a modulus square of a transition amplitude. This implies that the spectra consist of purely absorptive peaks. FSRS, TG-ISRS, and TR-ISRS in contrast also contain dispersive features. The underlying physical reason is clear. The spontaneous signal is dissipative, and the system ends in a population state. Stimulated signals, on the other hand, contain diagrams that allow the system to be in a coherence state. The asymmetry between modes in the impulsive stimulated Raman signal arises because the signal is defined as a transmission of one field, whereas the dissipative signal will require measuring the transmission of all fields.[81] In FSRS, the asymmetry is caused by the frequency-dispersed detection of the probe pulse which occurs only at the ket; the bra interacts with all frequency components of the probe field.

Stimulated Raman techniques provide a glimpse at early events of nonadiabatic relaxation. For example, a series of carotenoids with different conjugation lengths (N) (neurosporene ($N = 9$), spheroidene ($N = 10$), lycopene ($N = 11$), and spirilloxanthin ($N = 13$)) was investigated by the pump-degenerate four-wave mixing TG-ISRS technique and revealed 100−320 fs S_2 lifetimes and involvement of a dark state for spheroidene.[272] By varying of solvent polarity, frequency shifts of C−C and C═C modes could be assigned to vibronic coupling due to involvement of a $1B_u^+$ state with the $1B_u^-$ state.[273] Excited state vibrational dynamics of all-trans biological polyenes is reviewed in ref 186. The close relation between TG-ISRS in heterodyne detection mode and TR-ISRS was demonstrated for two carotenoids, highlighting their complementary nature to FSRS.[236] The TG-ISRS technique was further applied for the retinal-protonated Schiff bases[274,275] and revealed coherent high-frequency vibrational dynamics, favoring a two-state relaxation model. TR-ISRS was applied to investigate photoinduced dynamics in photoexcited molecules,[235] allowing one to track the structural evolution in ultrafast photoisomerization reaction[276] and relaxation pathways of bacteriorhodopsin with high time resolution.[277] Excited state structural evolution and associated proton transfer dynamics was tracked by following low-frequency modes in GFP[278] on the basis of a recently developed TR-ISRS apparatus.[279] A subpicosecond Raman spectrometer was employed to study structural dynamics in heme proteins,[280] while time-resolved resonance Raman spectroscopy was used to explore reactive intermediates.[281] Vibrational dephasing was employed for the development of imaging techniques by time-resolved broadband coherent anti-Stokes Raman scattering microscopy.[282]

3.3.3. Comparison of Various SRS Signals. The SLE explains dispersive line shapes that appear in the spectra if the system dynamics time scale is fast relative to the dephasing time scale. In this limit, the stroboscopic snapshot picture is inaccurate, and coherences between vibrational modes have to be considered (see section 2.2.4). The standard analysis based on Hilbert space description cannot provide such a crisp picture and explanation. We discuss the Raman signals for the TSJ model, which is the simplest stochastic line shape model. The two vibrational states of the system are a and c with ω_{ac} being the vibrational frequency unperturbed by the bath. Similarly, the bath has two states which, adopting spin terminology, are denoted + for spin "up" and − for spin "down". The TSJ coupling to the vibrations is introduced by assuming that the vibrational frequency depends on the TSJ states: $\omega_+ \equiv \omega_{ac} + \delta$ for up and $\omega_- \equiv \omega_{ac} - \delta$ for down.

We simulated the Raman signals in the slow modulation limit (SML) using the signal expressions given in the Appendix, eqs 156−158. Short pulses provide high temporal resolution. Depending on the relation between the field and the matter spectral bandwidths, the pulse duration may be optimized to obtain both high temporal and spectral resolution. We assume temporally square pulses with corresponding spectral envelope: $\mathcal{E}_j(\omega) = \mathcal{E}_j \mathrm{sinc}\left(\frac{\omega - \omega_{j0}}{\sigma_j}\right)$, $j = 2,3$. Figure 15 depicts the Raman signals for short probe pulse $\mathcal{E}_3$ compared to δ^{-1} assuming a 5 fs probe pulse $\mathcal{E}_3$ and the splitting $\delta = 100\ \mathrm{cm}^{-1}$. The left column of Figure 15 depicts the snapshot dynamics of the FR-SPRS signal. The FR-SPRS spectra consist of two broad pulse envelopes centered around $\omega_\pm$. For small delay time T, the dominating peak is at ω_+, corresponding to the + state that exponentially decays with time. The − state appears as weak peak that grows as $1 - e^{-kT}$.

For comparison, the FSRS signal is depicted in the middle column of Figure 15. Since the probe pulse $\mathcal{E}_3$ is broad band, it does not affect the shape of the spectra. The two peaks corresponding to jump frequencies $\Omega \equiv \omega - \omega_2 = \omega_\pm$ are clearly visible and highlighted by red dashed lines. Depending on the time delay between the actinic pulse and the probe, the peak ω_+ decays and ω_- is enhanced. Note that the vibrational coherence ρ_{+-} survives the time scale of the stochastic jump process as $\gamma_a < k$ (slow modulation limit). At short times, the dominant contribution to the spectra arises from the + state $\Omega = \omega_+$. The line width is governed by the combined width imposed by the jump rate and dephasing $- k + \gamma_a$ and in this particular setting dominated by the jump rate k. At long delay times, the FSRS signal shows a single peak that corresponds to the − state $\Omega = \omega_-$, where the width is governed by the pure vibrational dephasing rate γ_a. Thus, the dephasing determines the system dynamics at long times.

The right column of Figure 15 shows the TG-ISRS signal using the same pulse envelope for $\mathcal{E}_s(\omega) = \mathcal{E}_3(\omega)$ and $\mathcal{E}_1(\omega) = \mathcal{E}_2(\omega)$, which effectively makes the TG-ISRS signal indistinguishable from the TR-ISRS technique. The right column of Figure 15 manifests dispersive line shapes that are caused by the heterodyne detection and the broken symmetry between bra and ket branches of the loop. Kukura demonstrated experimentally[111] that a fast modulation of the system frequency is dominated by dispersive line shapes for short delay times, whereas absorptive line shapes dominate for long delay times.[112] Similar to FSRS, TG-ISRS and TR-ISRS contain both absorptive and dispersive features. Therefore, all arguments given above for FSRS apply here as well. Furthermore, we note that in contrast to FSRS, TG-ISRS contains two frequency integrals which are not coupled to the Raman resonances $\Omega = \pm\omega_\pm$. In addition, the TG-ISRS has more freedom in tuning the pulses since it involves four pulses vs two pulses for TR-ISRS. Therefore, the resolution of the TG-ISRS and TR-ISRS is more strongly affected by the pulse envelopes compared to FSRS.

The TG-ISRS signal is very similar to FSRS provided that the pump pulse $\mathcal{E}_2$ is broader than the energy splitting of vibrational states δ. The effect of the pump pulse duration $\mathcal{E}_2$ is illustrated in Figure 16. For a long pump pulse compared to the energy splitting, the FR-SPRS yields two well-separated peaks with the widths σ_2 corresponding to the pulse bandwidth. For a shorter pump pulse, the peaks are broadened and eventually merge. In the case of TG-ISRS and TR-ISRS, the situation is the opposite, since the effective line shape is determined by the jump rate k and

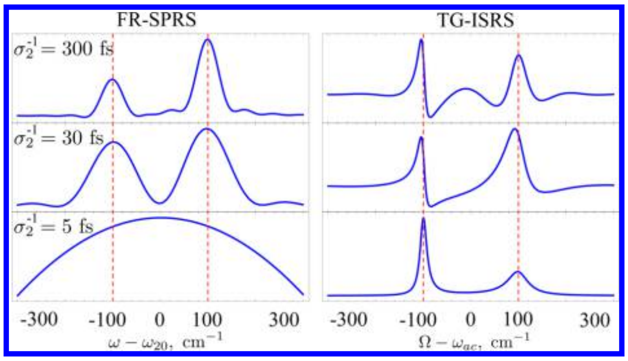

Figure 16. Effect of pump pulse duration σ_2 on the FR-SPRS signal (eq 156, left) and the TG-ISRS signal (eq 158, right). Remaining parameters are the same as in Figure 15. Reproduced with permission from ref 213. Copyright 2013 AIP Publishing LLC.

dephasing γ_a. The pulse envelope results in a background which may interfere with the spectra for long enough pulses. However, if the pump becomes shorter than the energy splitting, the background is uniform and the spectra contain background-free features. In this limit, the TG-ISRS and FSRS signals coincide for a specific configuration of the pulses. Thus, all three techniques yield essentially the same signal: $S_{\mathrm{FSRS}}(\Omega, T) \simeq S_{\mathrm{TG-ISRS}}(\Omega,T) \simeq S_{\mathrm{TR-ISRS}}(\Omega, T)$ provided that the bandwidths of the pump and probe pulse in TG-ISRS are the same as for the probe pulse in FSRS $\sigma_2 = \sigma_3$ and the narrow-band frequency of the pump in FSRS is equal to the central frequency of the probe $\omega_2 = \omega_{30}$.

4. RESONANT ELECTRONIC STATE DETECTION IN THE VISIBLE AND THE ULTRAVIOLET

The off-resonant techniques considered so far conserve the number of probe photons. The photon energy gets redistributed among the broad-band modes: $S^{(N)}$ vanishes, while $S^{(E)}$ is finite. When a pulse is resonant with a transition, actual photon absorption can take place. This renders $S^{(N)}$ finite, revealing new matter information. The resonant detection of electronic degrees of freedom offers an alternative to the vibrational spectroscopic techniques described in sections 2 and 3 for probing the nonadiabatic dynamics in the vicinity of CoIns. Representative methods include the TA technique with UV−vis pulses (section 4.1) and two-dimensional electronic spectroscopy (section 4.2).

4.1. Transient Absorption (TA)

TA is a widely used type of pump−probe spectroscopy.[23,24] It has been employed to identify the initial steps in the chemistry of vision,[18,283] photochemistry,[284] and DNA photodamage.[135] In conjunction with broad-band laser systems, it can be used to track the population dynamics[285] over a broad frequency range, making it a convenient tool for investigation of nonadiabatic dynamics in molecules.[286]

The corresponding diagrams for TA are shown in Figure 17. The system is prepared by an excitation process that terminates at t_0 from the ground state to an excited state population or coherence. After preparation, the system evolves freely in the excite state from t_0 until the interaction time τ with the probe pulse that is centered around T. During the probe pulse of finite length, photons can be absorbed (Figure 17a) or emitted (Figure 17b) into the signal mode. The TA signal is recorded in resonance with an excited electronic state and linear in the probe pulse intensity.[75] The TA technique is mainly sensitive to populations but can also be used to detect electronic coherences (given the energy gap is within the probe bandwidth).

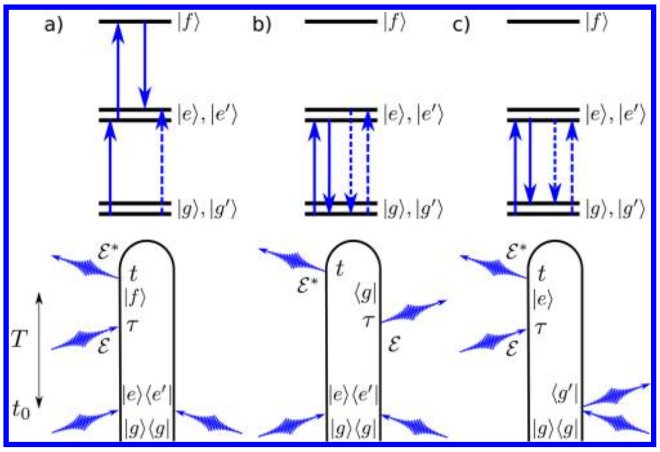

Figure 17. Loop diagrams (bottom row) and level schemes (top row) of the TA technique. Delay parameter T is shown next to the diagram: (a) Excited state absorption to a higher lying electronic state. (b) Excited state emission to the ground state. (c) Ground state bleach. The labels g, e, and f denote different electronic states, and a prime superscript denotes vibrational sublevels.

The TA signal can be described by the integrated photon number signal

$$S_N(T) = \frac{2}{\hbar^2}\mathcal{I}\int_{-\infty}^{\infty} \mathrm{d}t \int_{-\infty}^{t} \mathrm{d}\tau \mathcal{E}^*(t - T)\mathcal{E}(\tau - T) \times \langle \Psi_0 | U^\dagger(\tau, 0)\hat{\mu} U^\dagger(t, \tau)\hat{\mu}^\dagger U(t, 0)|\Psi_0\rangle \quad (68)$$

which results in net absorption (Figure 17a) or net stimulated emission (Figure 17b). The more detailed, frequency-dispersed TA signal

$$S_{\mathrm{FD}}(\omega, T) = \frac{2}{\hbar^2}\mathcal{I} i\mathcal{E}^*(\omega) \int_{-\infty}^{\infty} \mathrm{d}t e^{i\omega(t-T)} \int_{-\infty}^{t} \mathrm{d}\tau \mathcal{E}(\tau - T) \times \langle \Psi_0 | U^\dagger(t, 0)\hat{\mu} U(t, \tau)\hat{\mu}^\dagger U(\tau, 0)|\Psi_0\rangle \quad (69)$$

carries additional information, where resonances due to intervalence excitations are revealed along the detection axis. For impulsive excitation conditions, information about vibrational modes is revealed via Fourier transform along the delay time T. Note that the diagram of the TA technique closely resembles diagrams (i) and (ii) of the UV/IR signal (Figure 3 b) where the material quantity is described by the four-point matter correlation function. As we separated the preparation process from TA detection, eqs 68 and 69 are independent of the pump pulse.

The broad-band detection mode can track specific bands corresponding to different electronic transitions along the reaction coordinate and reveals the change in the energy gap toward a CoIn. However, monitoring the energy gap around the CoIn is experimentally challenging since it reaches deep into the near-IR region, which is outside the experimental capability of typical TA studies (see below for selected examples employing sophisticated spectral probe conditions). Moreover, in the vicinity of the CoIn the transition dipole moment typically decreases due to mixing of states with single-excitation and double-excitation character prohibiting direct observation of the passage of the CoIn by resonant transitions between electronic states. Figure 18b shows the recorded TA spectrum in the visible and near-IR spectral region of ultrafast isomerization of rhodopsin as the primary photochemical event in vision.[18] The

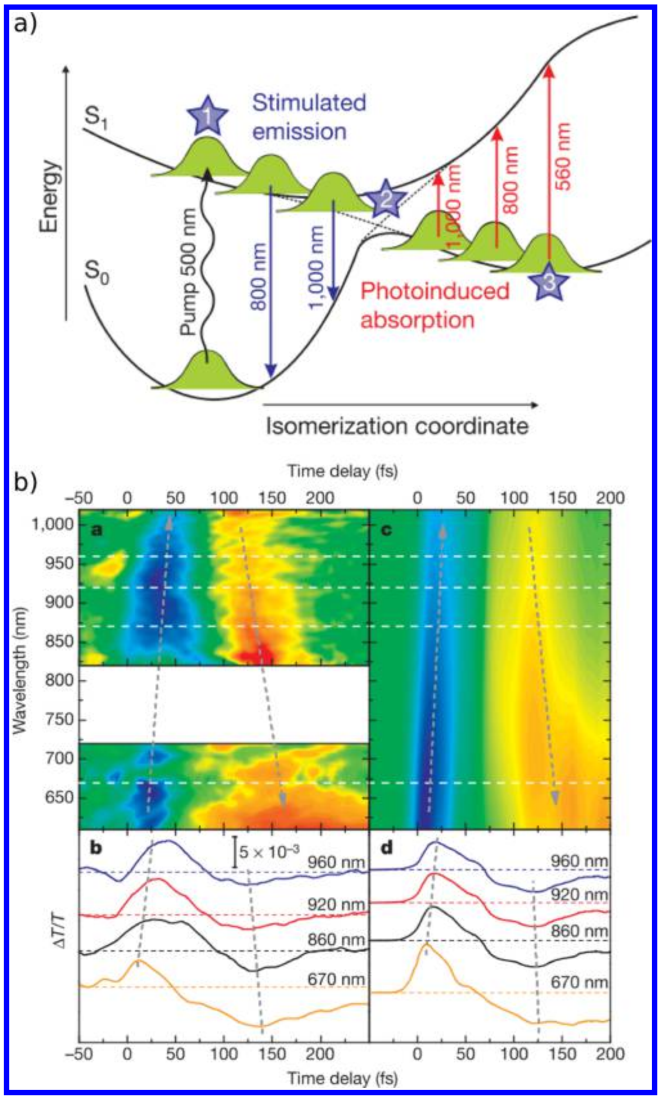

Figure 18. (a) Schematics of transient absorption (TA) detection of photoisomerization in rhodopsin. (b) TA spectrum (measured, left; simulated, right). Stimulated emission is shown in blue and absorption in red/yellow. Adapted with permission from ref 18. Copyright 2010 Nature Publishing Group.

TA spectrum initially shows a stimulated emission feature, which shifts to the red as the wavepacket approaches the CoIn. Once the molecule has passed the CoIn the stimulated emission band turns into an excited state absorption band of decreasing wavelength, indicating formation of the all-trans photoproduct within 150−250 fs. Notably, the TA signal does not follow exponential dynamics but increases abruptly around 150 fs, which was interpreted as the relevant time to pass the CoIn and enter the accessible probe window of the all-trans photoproduct. Additional insight on the isomerization reaction in rhodopsin has been obtained recently by het-TG spectroscopy[287] that allows for higher sensitivity due to background-free detection (cf. section 4.2). The data suggest that photoproduct formation occurs in a coherent fashion on an even faster, sub-50 fs time scale, and nuclear motions driving the isomerization reaction could be identified.

TA studies of ultrafast relaxation dynamics are very common; recent examples are refs 238 and 288−296, and femtosecond time-resolved pump−probe optical microscopy techniques are emerging[297,298] (for recent reviews see refs 298−301). Here, we denote special attention to studies that employed sophisticated spectral probe conditions. In particular, by extending the probe wavelength to the near IR ($\lambda_{\text{pr}} \approx 1900$ nm), the excited state dynamics of salinixanthin and xanthorhodopsin could be revealed by near-infrared-hyperspectral probing,[302,303] a strategy already successfully applied to the transient spectroscopy of short-lived, charge-separated states in the bacterial reaction center ($\lambda_{\text{pr}} \approx 1000$ nm).[304−307] Near-infrared-hyperspectral probing additionally provided insight into the ultrafast photochemistry of retinal proteins.[308] An alternative detection window arises from probing in the UV spectral region,[151,152,285,309−314] allowing access to the dynamics of important chromophores like aromatic amino acids in proteins and the DNA and RNA nucleobases.[315]

Focusing on the electronic degrees of freedom only, the TA technique provides per se low structural sensitivity by tracking the excited state populations (or coherences) over time. With the advent of ever-shorter optical pulses (sub-20 fs), impulsive excitation conditions could be realized that, to some extent, mitigate these deficiencies. The observation of superimposed coherent vibrational oscillations of excited states in TA signals has been reported for various molecular systems by Fourier transform along the delay time T.[152,285,312,316−319] The additional information allows one to extract structural insight into the ultrafast, nonadiabatic relaxation process.

A multitude of molecular systems, like, e.g., photochromic switches,[16,263,289,320] do not feature striking signatures of CoIns (i.e., low fluorescence, high photoactivity, femtosecond electronic kinetics) but are characterized by dynamics on the picosecond time scale together with high reaction quantum yields. Thus, the involvement of CoIns is only inferred indirectly, often by supporting theoretical calculations. The recently introduced coherent wavepacket evolution analysis[321,322] here provides access to CoIn-mediated relaxation dynamics, where molecules do not exhibit the impulsive signatures of a CoIn. The results support a picture where only a subset of vibrational modes forms the branching space of the CoIn. The underlying and well-known phenomena of phase changes[323−327] in impulsive broad-band TA signals has been recently readdressed.[328]

4.1.1. Transient Absorption of a Shaped Pulse; Linear Variant of FSRS.

In the following, we consider a hybrid variant of TA where the probe consists of a broad-band $\mathcal{E}_{\text{p}}$ and a narrow-band pulse $\mathcal{E}_1$ (Figure 19) and the molecule interacts once with each. The combination of broad-band $\mathcal{E}_{\text{p}}$ and narrow-band $\mathcal{E}_1$ is a special case of pulse shaping.[329−336] It can be viewed as a resonant TA technique with a hybrid probe pulse, where the first interaction with the probe comes from the narrow-band pulse and the second one comes from the broad-band pulse. We term this technique transient absorption linear hybrid detection (TALH). Different phase shapes allow one to enhance or suppress spectral features and manipulate line shapes. The formalism is general and can account for arbitrary pulse shapes that provide numerous control possibilities for the signals.

We consider the TA signal defined as the change in frequency-dispersed probe intensity (cf. eq 69) where the measurement is performed by TALH, i.e., a UV−vis pump and shaped probe (broad + narrow band) experiment. The actinic pulse $\mathcal{E}_{\text{a}}$ centered at τ_0 brings the molecule from the electronic ground state $|g\rangle$ to the electronic excited state a and c. Due to the broad bandwidth of $\mathcal{E}_{\text{a}}$, a superposition of vibrational levels a and c is generated and probed by a spectrally narrow $\mathcal{E}_1$ and a spectrally broad $\mathcal{E}_{\text{p}}$ probe pulse, both centered at $t_0 > \tau_0$. Probe interaction

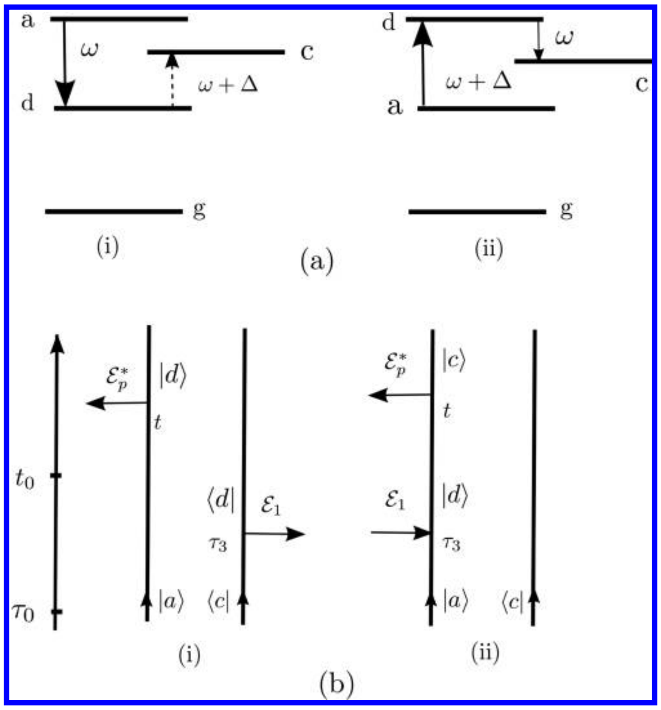

Figure 19. Level scheme (a) and ladder diagrams (b) for the TALH signal (eqs 70 and 71).

with the molecule can then stimulate either emission to a lower vibrational state or absorption to a higher vibrational state. Figure 19 represents the ladder diagrams that contribute to the signal (for diagram rules see ref 337). By expanding the time-ordered exponential to first order in $\mathcal{E}_1$ and $\mathcal{E}_{\rm p}$ and to second order in $\mathcal{E}_a$ and assuming the actinic pulses to be impulsive $\mathcal{E}_a(\tau) = \mathcal{E}_a\delta(\tau)$, we obtain[110]

$$S^{(i)}_{\rm TALH}(\omega;t_0,\tau_0) = \frac{2}{\hbar}\mathcal{I}\left[\left(-\frac{i}{\hbar}\right)\int_{-\infty}^{\infty}dt\int_0^{\infty}dt_3 e^{i\omega(t-t_0)} \times \langle V_{\rm L}\mathcal{G}(t_3)V_{\rm R}^{\dagger}\mathcal{G}(t-t_3-\tau_0)\rangle' \times \mathcal{E}_{\rm p}^*(\omega)\mathcal{E}_1(t-t_3-t_0)\right] \tag{70}$$

$$S^{(ii)}_{\rm TALH}(\omega;t_0,\tau_0) = \frac{2}{\hbar}\mathcal{I}\left[\left(\frac{i}{\hbar}\right)\int_{-\infty}^{\infty}dt\int_0^{\infty}dt_3 e^{i\omega(t-t_0)} \times \langle V_{\rm L}\mathcal{G}(t_3)V_{\rm L}^{\dagger}\mathcal{G}(t-t_3-\tau_0)\rangle' \times\mathcal{E}_{\rm p}{}^*(\omega)\mathcal{E}_1(t-t_3-t_0)\right] \tag{71}$$

where $\langle\cdots\rangle' \equiv \sum_{ac}\rho_{ac}\langle\langle I|\cdots|ac\rangle\rangle$. A nonstationary vibrational wavepacket in the excited state[338] is then described by $|\mathcal{E}_{\rm a}|^2V_{\rm R}V_{\rm L}^{\dagger}|gg\rangle\rangle = \rho_{ac}|ac\rangle\rangle$, where $\rho_{ac} = |\mathcal{E}_{\rm a}|^2\mu_{ga}\mu_{cg}$. By performing inverse Fourier transformation of the propagator and the electric field, performing time integrals and introducing a delay between preparation time τ_0 and probe pulse t_0, $T = t_0 - \tau_0$, eqs 70 and 71 yield

$$S^{(i)}_{\rm TALH}(\omega;T) = \frac{2}{\hbar}\mathcal{I}\left[\left(-\frac{i}{\hbar}\right)\int_{-\infty}^{\infty}\frac{d\Delta}{2\pi}e^{-i\Delta T}\mathcal{E}_{\rm p}^*(\omega) \times \mathcal{E}_1(\omega+\Delta)\tilde{\chi}^{(1)}_{{\rm TALH}(i)}(-\omega,\omega+\Delta)\right] \tag{72}$$

$$S^{(ii)}_{\rm TALH}(\omega;T) = \frac{2}{\hbar}\mathcal{I}\left[\left(\frac{i}{\hbar}\right)\int_{-\infty}^{\infty}\frac{d\Delta}{2\pi}e^{-i\Delta T}\mathcal{E}_{\rm p}^*(\omega) \times \mathcal{E}_1(\omega+\Delta)\tilde{\chi}^{(1)}_{{\rm TALH}(ii)}(-\omega,\omega+\Delta)\right] \tag{73}$$

where we introduced the generalized susceptibility $\tilde{\chi}_{{\rm TALH}(j)}{}^1(-\omega,\omega+\Delta)$, $j = i,ii$

$$\tilde{\chi}^{(1)}_{{\rm TALH}(i)}(-\omega,\omega+\Delta) = \langle V_{\rm L}\mathcal{G}(\omega)V_{\rm R}^{\dagger}\mathcal{G}(-\Delta)\rangle' \tag{74}$$

$$\tilde{\chi}^{(1)}_{{\rm TALH}(ii)}(-\omega,\omega+\Delta) = \langle V_{\rm L}\mathcal{G}(\omega)V_{\rm L}^{\dagger}\mathcal{G}(-\Delta)\rangle' \tag{75}$$

The idea of recasting the $(n + m)$-wave mixing signal in terms of an effective m-wave mixing has been extensively studied for FWM such as transient absorption by Champion[327,339] and termed "effective linear response approach". Here, we use this approach for the six-wave mixing FSRS signal. TALH with a visible pump and shaped probe (broad plus narrow band) can be regarded as a generalized linear response to the field $\mathcal{E}_1\mathcal{E}_{\rm p}$ from a nonstationary state ρ_{ac} prepared by the actinic pulse $\mathcal{E}_{\rm a}$. Note that $\tilde{\chi}^1_{\rm TALH}$ depends on two frequencies, which implies that the signal in eqs 72 and 73 is sensitive to the phase of the field. The choice of broad-band $\mathcal{E}_{\rm p}$ and narrow-band $\mathcal{E}_1$ is a particular choice of possible pulse shaping combinations.[329−335] The TALH signal carries information about the impulsively prepared nonstationary state $|ac\rangle\rangle$ of the molecule and can be seen as linear analogue of FSRS which is recorded in the time domain.

A closely related variant of TALH has been developed by Kukura and co-workers. Following impulsive excitation by a pump pulse $\mathcal{E}_{\rm a}$ the system is interrogated with a linear probe in the form of a broad-band white-light continuum of 300 fs nominal duration (spectral range ≈ 510−840 nm, 4.2 fs transform limit). The white light continuum probe here takes the place of the narrow- and broad-band probes of the TALH technique (cf. Figure 19), allowing one to record Raman spectra in the time domain.[340] By tuning the impulsive pump into electronic resonance, Raman spectra of the excited electronic state could be dissected.[341] The technique builds on recent advances in pulse generation, making sub-10 fs pump pulses and chirped white light continuum probes now routinely available.[342−346] The combination of the ultrashort pump pulse with the broad-band white light continuum probe reduces the experimental complexity and provides high sensitivity[347−349] while ensuring optimal effective temporal resolution. Correspondingly, by further augmenting the technique with an actinic pump pulse provided access to transient Raman spectra of short-lived intermediates (~200 fs)[350,351] that appear during excited state dynamics of, e.g., β-carotene or the retinal chromophore. The actinic pump−impulsive pump−white-light continuum probe setup provides ~11 fs temporal resolution and allows one to record vibrational coherences in the time domain over a large frequency bandwidth up to high-frequency modes (3000 cm^{-1}). Following the classification of section 3.2 the actinic pump−impulsive pump−white-light continuum probe technique employs a quadratic probe subsequent to the actinic excitation pulse and is thus conceptually closely related to the TR-ISRS and FSRS techniques (cf. section 3.3.2).

4.2. Two-Dimensional Electronic Spectroscopy (2DES)

Two-dimensional electronic spectroscopy (2DES) is, like TA, a nonlinear third-order technique that allows one to spread the information content of the nonlinear response in two frequency dimensions, thereby overcoming limitations of the TA technique. 2DES signals are recorded by varying the delay between two phase-stable ultrashort excitation pulses with interferometric precision (for diagrams see Figure 17). Subsequent Fourier transformation along the excitation delay time τ gives, in addition to the detection frequency axis of the frequency-dispersed TA signal, eq 69, the excitation frequency axis. The corresponding two-dimensional signals are parametrically dependent on the waiting time T, thereby reporting on spectral diffusion of homogeneous line width, interchromophore couplings, and energy transfer processes. Optical two-dimensional spectroscopy has been originally developed in the IR spectral region[352,353] and reached maturity in the visible[354] during the past decade. Extensive reviews cover technical developments and the underlying theoretical framework,[97,320,355−359] and these will not be covered here in detail. Exemplary applications are given in ref 360−368. Simulations suggest that vibrational coherence around a CoIn has an impact on the relaxation pathways and cross peaks in 2DES signals provide signatures of the CoIn.[369,370]

4.2.1. Two-Dimensional Electronic Spectroscopy in the UV (2DUV).

2DES in the UV spectral range (two-dimensional ultraviolet spectroscopy (2DUV))[314,372−381] appears promising for investigating prominent electronic absorption bands of a wide class of organic molecules (e.g., DNA, proteins, and (hetero)-aromatic compounds[315]) where striking nonadiabatic relaxation channels via CoIn appear. As such the ability to perform 2DUV measurements on relatively small organic molecules opens the possibility for direct comparison of experiments with simulated spectral signatures of photochemical relaxation dynamics. This approach provides a rigorous test for (ab initio) force fields and employed approximations.

A first step in this direction was taken in ref 371, where nonadiabatic ab initio molecular dynamics was employed to simulate the respective 2DUV signal of diphenylmethane (DPM). Due to the ability of 2DES to report on interchromophore couplings and energy transfer, DPM can be regarded as prototypical bichromophore in the UV spectral region. In DPM, the two aromatic phenyl moieties are separated by a bridging CH_2 group (cf. inlay in Figure 20b), making the molecule a promising candidate to investigate the ultrafast relaxation dynamics of electronically excited molecules. The developed microscopic algorithm combines nonlinear exciton propagation,[93,382] which allows one to account for arbitrary fluctuation dynamics (cf. section 2.2.2) with Tully's surface-hopping method[56,57,59] in order to take into account back-coupling between quantum (electronic) and classical (nuclear) degrees of freedom. As such, the method faithfully reproduces high-level results[383] for a model of two electronic states coupled to a harmonic coordinate and a classical heat bath. Phenomena like dynamic Stokes shift due to nuclear relaxation, spectral diffusion, and population transfer among electronic states are naturally included.

Diagrams of the quantum-classical feedback nonlinear exciton propagation (QF-NEP) for the rephasing signal $\mathbf{k}_I = \mathbf{k}_3 + \mathbf{k}_2 - \mathbf{k}_1$ are given in Figure 20a. The $\mathbf{k}_I$ signal can be expressed in compact form

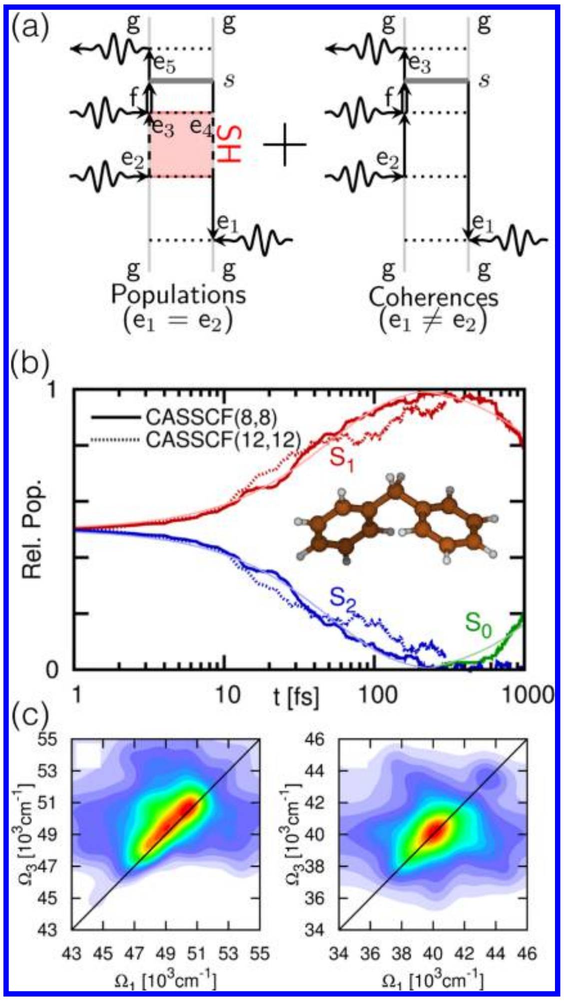

Figure 20. (a) Contributions of populations $e_1 = e_2$ and coherences $e_1 \neq e_2$ to the NEP ladder diagram arising from the contraction of excited state emission, ground state bleach, and excited state absorption contributions to the rephasing signal $\mathbf{k}_I = \mathbf{k}_3 + \mathbf{k}_2 - \mathbf{k}_1$. Solid arrows represent the forward (backward) propagation of single-exciton Green's functions, and double arrows describe the free evolution of biexciton Green's function. (b) Time evolution of adiabatic state populations for trajectories launched in S_1 and S_2: (solid lines) CASSCF(8,8) level of theory; (dotted lines) CASSCF(12,12) level of theory. (c) Absorptive 2D spectra for $t_2 = 0$ fs: (left) CASSCF(8,8) level of theory, (right) CASSCF(12,12) level of theory. Adapted with permission from ref 371. Copyright 2016 American Chemical Society.

$$
\begin{aligned}
&S^{\mathbf{k}_I}_{\nu_4\nu_3\nu_2\nu_1}(\tau_4, \tau_3, \tau_2, \tau_1) \\
&\quad = 2\left(\frac{i}{\hbar}\right)^4 \sum_{n_{1-4}} \sum_{m_{1-5}} \mu^{\nu_1}_{n_1}(\tau_1)\mu^{\nu_2}_{n_2}(\tau_2)\mu^{\nu_3}_{n_3}(\tau_3)\mu^{\nu_4}_{n_4}(\tau_4) \\
&\quad \times \int_{\tau_3}^{\tau_4} \mathrm{d}s G_{n_4m_5}(\tau_4, s)U_{m_5m_1m_4m_3}(s) \\
&\quad \times G_{m_4m_3n_3m_2}(s, \tau_3)G_{m_2n_2}(\tau_3, \tau_2)G^{*}_{m_1n_1}(s, \tau_1) \qquad (76)
\end{aligned}
$$

where τ_i are interaction times with laser pulses and $\mu^{\nu}_{n_i}(\tau_i)$ denote time-dependent transition dipole moments of exciton n_i generated by the pulse with polarization ν_i. The signal is given by Fourier transform of the nonlinear response function $S^{\mathbf{k}_I}_{\nu_4\nu_3\nu_2\nu_1}(t_3, t_2, t_1)$ over the delay times t_3 and t_1 with time intervals

DOI: 10.1021/acs.chemrev.7b00081
Chem. Rev. 2017, 117, 12165−12226

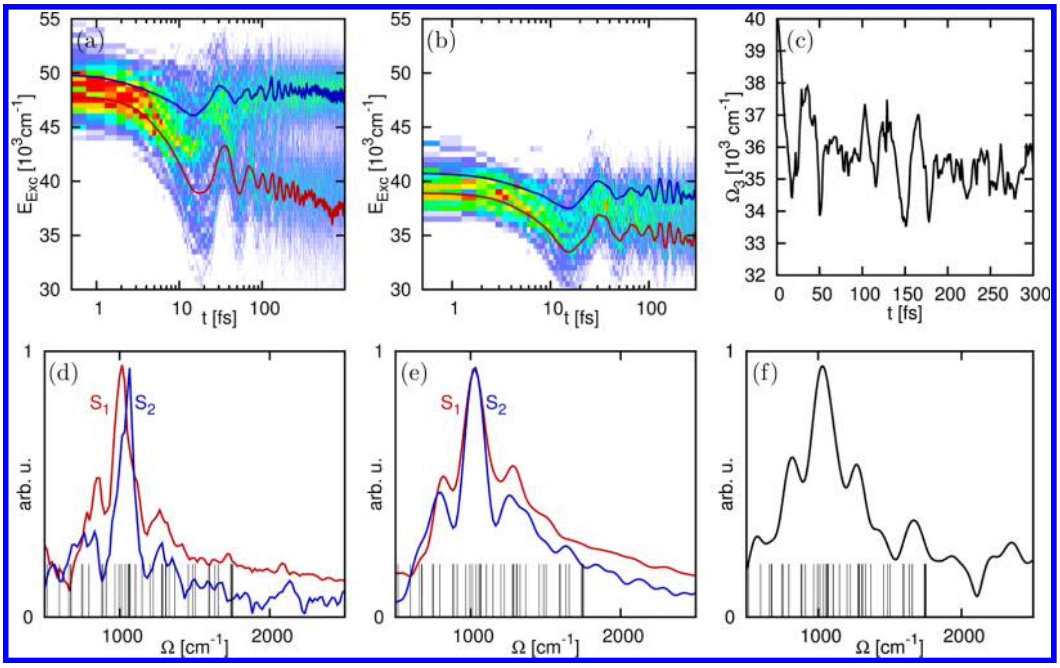

Figure 21. Distribution of excitation energies and average of S_1 (red) and S_2 (blue) excitation energies at the CASSCF(8,8) and CASSCF(12,12) level of theory (a and b, respectively). (c) Peak position along Ω_3 of absorptive 2D spectra (CASSCF(12,12), τ_l = 2 fs). (d) Fourier transform (FT) of the oscillatory component of a. (e) FT of panel b. (f) FT of panel c. Black sticks mark frequencies of vibrational modes of ground state DPM. Reproduced with permission from ref 371. Copyright 2016 American Chemical Society.

$t_1 = \tau_2 - \tau_1$, $t_2 = \tau_3 - \tau_2$, and $t_3 = \tau_4 - \tau_3$. The matter response can be read from the diagram (Figure 20a): excitation by pulse 2 creates a single exciton at time τ_2 that propagates forward until τ_3 (described by the single-exciton Green's function $G_{m_2n_2}(\tau_3,\tau_2)$). The interaction with the probe pulse at τ_3 generates a biexciton $G_{m_4m_3n_3m_2}(s,\tau_3)$; nonlinearities are accounted for due to the scattering interaction $U_{m_5m_1m_4m_3}(s)$ during $t_3 = \tau_4 - \tau_3$. Exciton scattering splits the biexciton into two single excitons, one propagating forward from s until detection time τ_4 (Green's function $G_{n_4m_5}(\tau_4,s)$) and the other propagating backward in time from s to the interaction time of the first laser pulse τ_1 (single-exciton retarded Green's function $G^*_{m_1n_1}(s,\tau_1)$).

The two diagrams given in Figure 20a account for the subpathway decomposition between population states ($m = n$) and interstate coherences ($m \neq n$) that arises from the choice of the reference Hamiltonian in the semiclassical treatment of quantum (electronic) and classical (nuclear) degrees of freedom.[107] This treatment was introduced for SOS methods,[383,384] but here it accounts for correlations of Hilbert-space wavefuntions propagating either on the bra or on the ket side of the diagram. Different approaches have been proposed employing either ground state, excited state, or mean-field reference Hamiltonians.[59,383,385,386] Coherence contributions to the signal ($m \neq n$) are modeled by trajectories subject to the fluctuations of the ground state reference Hamiltonian, while population contributions ($m = n$) are driven by the respective excited state reference Hamiltonian and experience a feedback force of the quantum region resulting in dynamic Stokes shift of the exciton energies during waiting time t_2.

The 2DUV signal of diphenylmethane subject to nonadiabatic relaxation has been calculated at the complete active space self-consistent field (CASSCF) level of theory where two different active spaces have been considered (CAS(8,8), CAS(12,12)). All 69 nuclear degrees of freedom are accounted for in an ab initio surface-hopping molecular dynamics. The CASSCF(8,8) level includes the π system of both phenyl rings but excludes the complete bonding and antibonding π orbitals, considered at the CASSCF(12,12) level. Due to restricted active space and lack of dynamic electron correlation, excitation energies are overestimated by >1 eV on the CASSCF(8,8) level. In contrast, the increased active space on the CASSCF(12,12) level allows for substantially improved accuracy (∼0.4 eV with respect to highest level CASPT2(12,12) multireference perturbation theory calculations). Notably, the simulated time evolution of state populations is nearly identical on both levels of theory (Figure 20b). Ensemble-averaged absorptive 2D spectra of DPM calculated on the CASSCF(8,8) and CASSCF(12,12) levels of theory (Figure 20c) were compared, both showing a slightly elliptic shape along the diagonal for shortest waiting times (t_2 < 10 fs). The elliptic shape is caused by the inhomogeneous excitation energy distribution of different initial conditions that is scrambled by ultrafast spectral diffusion, primarily imposed by high-frequency modes and substantially affecting the transition energies. Off-diagonal peaks are determined by the respective S_1/S_2 splitting, leading to an antidiagonal broadening of 2D spectra. The 2D spectrum simulated at the CASSCF(12,12) level (Figure 20c, right) shows a peak maximum located around $\Omega_1 = \Omega_3 \approx$ 40 000 cm^{-1} (unshifted value), in good agreement with the experimental absorption spectrum.[387]

Despite the large similarities of 2D signals calculated at the CASSCF(8,8) and CASSCF(12,12) levels for t_2 = 0 fs (apart from the constant shift imposed by excitation energies), markedly different behavior is revealed by analyzing the dynamics occurring during the t_2 time, as quantified by the time-dependent peak shift along Ω_3 (Figure 21) observed in the 2D spectra. For the signal calculated at the CASSCF(8,8) level, the peak shift is substantially larger than for the CASSCF(12,12) level, while oscillatory behavior can be similarly identified. Upon electronic excitation, ring-breathing modes of the aromatic system of DPM are excited, where the oscillation along these modes induces a periodic shift in energy gap of S_1 and S_2 with respect to the ground state S_0. Dissipation into other intramolecular vibrational modes proceeds rather slowly, which manifests in persistent oscillations. The oscillatory frequencies correspond to symmetric and asymmetric ring-breathing modes of DPM, which arise from combinations of ring-breathing modes of the single phenyl moieties. By Fourier transforming the time-dependent Ω_3 peak shifts or the oscillatory component of the energy gap fluctuations, characteristic frequencies of ring-breathing modes can be recovered, with dominant peaks around 1000−1100 cm^{-1} (Figure 21d and 21e) and ring distortion and CH_2−modes appearing as side bands at 800−850 and 1250−1300 cm^{-1}, respectively. Activated ring-breathing/distortion modes are thus predicted to have clear signatures in the 2D signals. Discrepancies between the different CASSCF levels can be assigned to the underlying shortcoming of the CASSCF(8,8) level for the description of excitation energies. During propagation, the excess energy is partially converted into kinetic energy and CASSCF(8,8) trajectories explore a larger region of the PES, while the CASSCF(12,12) trajectories retain a more compact distribution in phase space.

The simulations of ref 371 focused on excited state emission contributions to the 2D signals. An ab initio treatment of single-to-biexciton interband transitions is naturally included in the framework of QF-NEP but requires the assignment of biexcitons to its constituent single excitons. This can be performed by augmenting the protocol by static high-level electronic structure calculations[388,389] that reliably predict doubly excited states in order to characterize fluctuations of electronic anharmonicities, thereby allowing for quantitative comparison with state-of-the-art 2DUV experiments of organic compounds.

A closely related FWM technique to 2DES is het-TG spectroscopy.[390,391] het-TG provides, due to phase-sensitive detection in direction $\mathbf{k}_s = \mathbf{k}_3 + \mathbf{k}_2 - \mathbf{k}_1$, background-free signals that monitor the third-order response function in an integrated fashion over the ω_1 excitation frequency axis. As such, the absorptive part of the het-TG signal contains the same information as TA.[392,393] An intrinsic time domain technique, het-TG enables one to simultaneously measure vibrational and electronic population dynamics under impulsive excitation conditions (cf. section 4.1). The het-TG technique has been recently employed to study the isomerization reaction of retinal in the protein rhodopsin,[287] for the investigation of nonradiative decay of the S_2 excited state of β-carotene[394] and peridinin,[395,396] and to investigate carotenoid-to-bacteriochlorophyll energy transfer in the light-harvesting complex LH2.[397]

4.2.2. Phase-Modulated 2D Fluorescence (PM-Fl).

An alternative 2D technique relies on the detection of spontaneous emission induced by a sequence of four phase-controlled pulses and yields similar information about quantum pathways compared to 2DES. The phase-modulated 2D fluorescence (PM-Fl) technique[398−403] reveals comparable information as obtained from common third-order coherent techniques, like photon-echo or double-quantum coherence measurements.[404,405] The incoherent fluorescence detection in PM-Fl inherently provides background-free detection, offers higher sensitivity that can be used for single-molecule detection,[406] and provides advantages in scattering environments where phase matching is difficult. In PM-Fl, an additional ladder diagram contributes to the fourth-order PM-Fl signal that provides access to biexciton population states. Moreover, the signs of the interfering pathways vary. In an ideal PM-Fl experiment with infinite biexciton lifetimes (vanishing nonradiative decay), photon emission occurs from the biexciton population state via successive emission from bi- and single-exciton states, and the quantum yield reaches a limiting value of two. In this case, PM-Fl signals equal the respective third-order 2DES signals. Unavoidable nonradiative decay processes of biexciton states lead to differences in the PM-Fl signals and 2DES spectra that reveal additional information about the biexciton population dynamics and emission quantum yield. Especially for the system with pronounced photoluminescence properties (like self-assembled quantum dots investigated in refs 405 and 407), PM-Fl may serve as a promising alternative to third-order coherent techniques. In principle, spectrally resolved excited state absorption contributions then allow one to record different quantum pathways (i.e., excited state absorption and excited state emission/ground state bleach) independently. Alternative incoherent detection schemes, like two-dimensional photocurrent spectroscopy, have been reported as well that monitor the nonlinear photocurrent signal induced by a sequence of four laser pulses.[408,409]

5. X-RAY PROBES FOR VALENCE ELECTRONIC STATES

We now turn to signals that utilize X-ray pulses. Recently proposed Raman techniques with XUV/X-ray pulses inherently benefit from the broad pulse bandwidth and high temporal resolution down to the attoseconds time scale. The theoretical formalism and description of electronic probe techniques is closely related to the vibrational (IR or Raman) probe techniques presented in the previous sections. For example, the X-ray Raman scheme is conceptually related to a vibrational Raman scheme but differs in the choice of the intermediate states (Figure 2b). Instead of low-lying valence excited states, core excited states serve as an intermediate. An assessment of available X-ray pulses and requirements for nonlinear X-ray measurement was recently provided,[410] and perspectives of time-resolved X-ray spectroscopies have been discussed.[411] Time-resolved photoelectron spectroscopy (TRPES), which connects the neutral state with an ionized state by probing the kinetic energy of liberated photoelectrons, here poses a special case but can be regarded as a linear probe technique (see section 3.2) and is thus closely related to TA. However, the detection of photoelectrons instead of scatted photons is usually more sensitive. The resonances of core electrons in the soft X-ray are element specific. Addressing those resonances directly can provide indirect information about rearangement of valence electrons through their shift in the frequency domain. When those states are used to enhance Raman transitions their exact resonance frequency becomes immaterial and the energy splittings between valence becomes accessible.

We note that the formalism of section 3 applies to both optical and X-ray signals. X-ray signals allow one to probe valence excitations rather than vibrations. First experiments that rely on a table-top water window high-harmonic source (cf. section 5.4.2) and employ X-ray pulses as probe in TA have emerged very recently.[15,412] Furthermore, both the initial preparation and/or the preparation process can then be the product of an X-ray scattering, photoionization, or Auger process (as recently discussed in refs 137 and 413), in addition to an X-ray Raman process. The signals obtained by a Raman probe then detect both the amplitude and the phase of the coherent superpositions of singly or doubly ionized states. These are signatures of many-body effects in the photoionization and Auger processes. In this review, as in our previous work, we provide a systematic description of a series of X-ray Raman signals. Using the present terminology, in our earlier work,[213] we presented $S_{\mathrm{QH}}^{(\mathrm{fd})}$, S_{Q12}^{N}, and some S_{QH}^{N} signals. The signals studied in ref 110 are $S_{\mathrm{QH}}^{(\mathrm{fd})}$ and $S_{\mathrm{LH}}^{(\mathrm{fd})}$. Finally, in recent work,[205] we investigated the S_{QH}^{N} signal.

5.1. X-ray Hybrid Stimulated Raman Detection: Attosecond Stimulated X-ray Raman Spectroscopy (ASRS)

Attosecond X-ray pulses provide a novel means for probing the strongly coupled electron−nuclear dynamics occurring in the vicinity of CoIns. The ASRS technique, proposed in ref 414 and schematically depicted in Figure 22a, appears promising by transferring concepts of the FSRS technique[76,219] to the X-ray spectral domain for element-sensitive probing of electronic properties. Following the classification terminology introduced in section 3.2, the ASRS signal is frequency dispersed, employs a quadratic hybrid probe ($S_{\mathrm{QH}}^{(\mathrm{fd})}$), and involves resonant core to valence transitions. The narrow-band pulse allows one to clearly resolve the transition peaks and the quadratic hybrid signal is independent of the phases of the narrow-band and broad-band pulses. In general, the $S_{\mathrm{QH}}^{(\mathrm{fd})}$ carries information about coherences, but a background arises due to contributions from populations. In ASRS, temporal and spectral properties of femto- and attosecond pulses (vs pico- and femtosecond in FSRS, cf. section 3.3) are combined. In particular, a first UV pulse $\boldsymbol{k}_1$, referred to as the actinic pump, initiates an excited state process like a ring-opening reaction, and after a time delay T, the system interacts with two X-ray pulses $\boldsymbol{k}_2$ and $\boldsymbol{k}_3$. The X-ray Raman process is triggered by a ∼50 fs Raman pump $\boldsymbol{k}_2$ that is resonant with core transitions at frequency ω_2 and narrow band with respect to the attosecond probe $\boldsymbol{k}_3$ (∼100 as) with red shifted ω_3. As determined by the system dynamics under investigation, the Raman pump $\boldsymbol{k}_2$ is insufficient to induce an electronic Raman transition on its own and is narrow band compared to the lifetime broadening of electronic core-to-valence transitions (with typical orders fwhm ≈ 0.06 eV for 30 fs pump and 0.13 eV lifetime broadening of O 1s core hole transitions[415]). In ASRS, the attosecond pulse is employed as a sharp time mark and ruler to measure the time delay T to the actinic pump. The broad-band spectrum of the attosecond probe $\boldsymbol{k}_3$ (for 100 attosecond pulse durations ≈ 10−20 eV) offers an extremely broad detection window, covering the entire valence state evolution regardless of changing intervalence transition moments or vanishing energy gap during the valence state relaxation dynamics. If the carrier frequency falls in the X-ray regime, element-specific changes in structure can be tracked by tuning the Raman excitation frequency to atoms that are involved in bond breaking and formation.

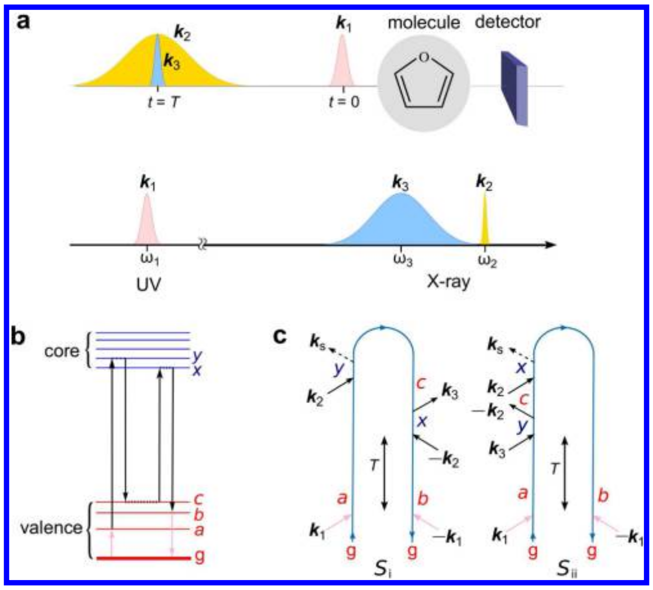

Figure 22. Physical picture of the attosecond stimulated X-ray Raman spectroscopy (ASRS) experiment: (a) Pulse sequence in the time and frequency domain (top and bottom, respectively). UV actinic pump pulse $\boldsymbol{k}_1$ initiates the reaction, and after time delay T, the time-coincident narrow femtosecond pump $\boldsymbol{k}_2$ and broad attosecond probe X-ray pulses $\boldsymbol{k}_3$ interact with the molecule to generate the ASRS signal. (b) Energy level diagram and transition process involved in ASRS detection; state variables are according to eqs 78 and 79; *a*, *b*, and *c* denote valence excited states (including the ground state g); *x* and *y* denote core excited states. (c) Two loop diagrams that contribute to the signal (eq 77). Both diagrams show a wave function evolution pathway along $b \leftarrow x \leftarrow c \leftarrow y \leftarrow a$ but vary in the interaction with the Raman sequence in either the bra or the ket side of the loop. Reproduced with permission from ref 414. Copyright 2016 AIP Publishing, https://creativecommons.org/licenses/by/3.0/CCBY3.0.

Assuming a monochromatic Raman pump $\mathcal{E}_2(\omega)=\delta(\omega-\omega_2)$, the ASRS signal is given by[69]

$$S(\omega-\omega_2,\omega_2,T) = S_i(\omega-\omega_2,\omega_2,T)+S_{ii}(\omega-\omega_2,\omega_2,T) \tag{77}$$

$$\begin{aligned} S_i(\omega-\omega_2,\omega_2,T) &= -\mathcal{I}\sum_{abcxy}\{\rho_{ab}(T)V_{bx}V_{xc}^{*}V_{cy}V_{ya}^{*}\mathcal{E}_3(\omega)\mathcal{E}_3(\omega-\omega_{ab})\} \\ &/\{[\omega_2-\omega_{xb}-i(\gamma_x-\gamma_b)][\omega_2-\omega_{ya}+i(\gamma_y-\gamma_a)] \\ &\times[\omega-\omega_2-\omega_{ac}+i\gamma_{ac}]\} \end{aligned} \tag{78}$$

$$\begin{aligned} S_{ii}(\omega-\omega_2,\omega_2,T) &= \mathcal{I}\sum_{abcxy}\{\rho_{ab}(T)V_{bx}V_{xc}^{*}V_{cy}V_{ya}^{*}\mathcal{E}_3(\omega)\mathcal{E}_3(\omega-\omega_{ab})\} \\ &/\{[\omega-\omega_{xb}+i\gamma_{xb}][\omega-\omega_{yb}+i\gamma_{yb}] \\ &\times[\omega-\omega_2-\omega_{cb}+i\gamma_{cb}]\} \end{aligned} \tag{79}$$

The two contributing terms S_{i} and S_{ii} can be read off diagrams (*i*) and (*ii*) in Figure 22c. A central assumption in eqs 77−79 is that the electronic Hamiltonian does not change considerably during the fast interaction with the Raman probe (cf. section 2.2.2), thereby neglecting attosecond dynamics, which is justified by a X-ray Raman process occurring within the core lifetime (∼5 fs).[416]

During the delay time T, the molecule evolves in the excited state, eventually described by a CoIn-induced superposition of valence states described by the density matrix $\rho_{ab}(T)=c_a c_b^{*}$. The ASRS technique provides sensitivity to monitor the geometrical and electronic structure evolution of the system evolving toward and via the CoIn to discriminate reactant, product, and CoIn. In ref 414 the signal was simulated on the basis of on-the-fly trajectory simulations and spectroscopic quantities, i.e., transition moments between valence and core-to-valence excited states obtained at the CASSCF level of theory. The appearing absorptive and dispersive peaks that mathematically arise from single and multiresonances (double and triple) (cf. denomintors in eqs 78 and 79) map out valence and core resonance information, respectively.

The ASRS signal provides a direct probe of the populated state character and reveals the energy shift of constituent electronic states in the ring opening of photoexcited furan with respect to core excitations, Figure 23. Due to the broad bandwidth of the attosecond Raman probe, the technique is able to capture the entire state evolution, irrespective of the changes in intervalence transition moments and the vanishing energy gap during the valence state relaxation dynamics. The T evolution of the signal revealed that minor perturbations in chemical structure can be tracked as noticeable variations in electronic structure due to the breakdown of the Born−Oppenheimer approximation. The ASRS technique thus provides the temporal resolutions for monitoring sudden changes in electronic structure and state population to the point of detecting the passage of a CoIn. In contrast, the combination with the narrow-band pulse in the Raman sequence provides high spectral resolution just as in the case of FSRS (cf. section 3.3). We note that spectral and temporal resolution in ASRS are not conjugate variables, which allows for improved resolution compared to detection sequences based on X-ray absorption.

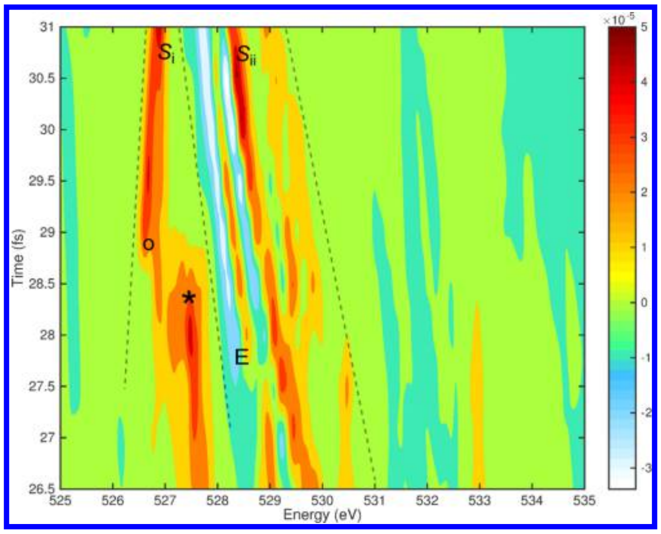

Figure 23. ASRS signal of the ring-opening reaction of photoexcited furan given as a two-dimensional plot of the simulated ASRS signals averaged over 15 trajectories during the period 26.5−31.0 fs. Signals feature two evident regions which mainly arise from the S_i and S_{ii} channels, respectively (dashes are added to guide eyes). Three peak features are labeled as "o", "*" (absorptive peaks), and "E" (dispersive peak). Reproduced with permission from ref 414. Copyright 2016 AIP Publishing, https://creativecommons.org/licenses/by/3.0/CCBY3.0.

From eqs 77−79, we note that the contributions from electronic coherences $\rho_{ab}(T)$ that are recorded in ASRS are imposed by interstate derivative couplings. Nevertheless, these coherence signal contributions are scrambled by population contributions to the signal. Phase-sensitive detection here provides means to further clarify the signals (cf. section 5.2). Optical detection is often hampered by the vanishing energy gap of valence electronic states, intervalence transition moments, and the limited bandwidth of optical probe techniques (cf. Figure 18). The probed core-to-valence transitions in ASRS provide a high density of states, which helps to characterize regions of the PES close to the conical intersection seam. By combining femtosecond−attosecond pump−probe pulses for X-ray Raman detection without the necessity for phase control, broad-band signals are recorded in a single shot, making ASRS a promising tool for nonlinear X-ray spectroscopy.

5.2. Linear off-Resonant X-ray Raman

Off-resonant Raman detection is capable of fast, impulsive measurements. Resonant Raman methods like ASRS provide a tool for studying additional dynamics, which is interesting in its own right, but its analysis is more complicated. The linear detection mode is only sensitive to the coherences but not populations. If a wavepacket reaches a CoIn, it branches into two electronic states creating an electronic coherence ρ_{ge}. A proposed technique to exclusively probe this coherence in a background-free way is TRUECARS.[215] Here, the linear part of an off-resonant Raman process is measured as a frequency-dispersed signal (Figure 24c). A combination of femtosecond pump and attosecond probe is used for background-free measurements of the electronic coherence. Using broad-band X-ray pulses allows one to cover a wide range of energies and track the varying energy gap beginning from the direct vicinity of the CoIn. When resonant, this process is formally identical to TA. However, in the off-resonant regime, the signal consists solely of the parametric redistribution of the photons in the probe pulse. The energy is redistributed between the red and the blue components of the pulse spectrum. There is no net absorption of photons. It therefore probes only electronic coherences created by the CoIn, making it a background-free technique. The technique can also be viewed as the second half of a CARS process, but instead of the first two pulses creating the coherence it is created by the material. The CoIn takes over the function of the CARS pump pulses.

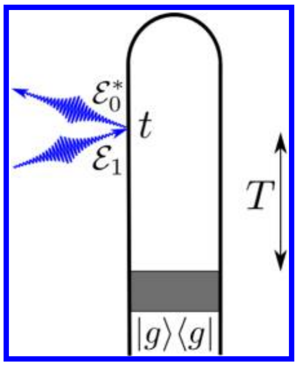

Figure 24. Diagram of the TRUECARS technique: Probe is off-resonant, and there is no net absorption of photons, but rather they are redistributed between different modes (cf. diagram of Figure 17, which is resonant).

The frequency-dispersed signal reads

$$S_{\mathrm{FD}}(\omega, T) = 2\mathcal{I} \int_{-\infty}^{+\infty} \mathrm{d}t\, e^{i\omega(t-T)} \mathcal{E}_0^*(\omega)\mathcal{E}_1(t-T) \times \langle \psi(t)|\hat{\alpha}|\psi(t)\rangle \tag{80}$$

where α is the frequency-dependent polarizability between the contributing electronic valence states, $\mathcal{E}_0$ is the envelope of the attosecond broad-band pulse, and $\mathcal{E}_1$ is the envelope of the femtosecond narrow-band pulse (see Figure 25b). Note that the probe scheme is formally similar to TALH (section 4.1.1), which works with a resonant probe instead.

A typical signal for a harmonic model made of two displaced parabolic potentials is shown in Figure 25c. The signal is absent within the first 20 fs since the wavepacket is on a single electronic

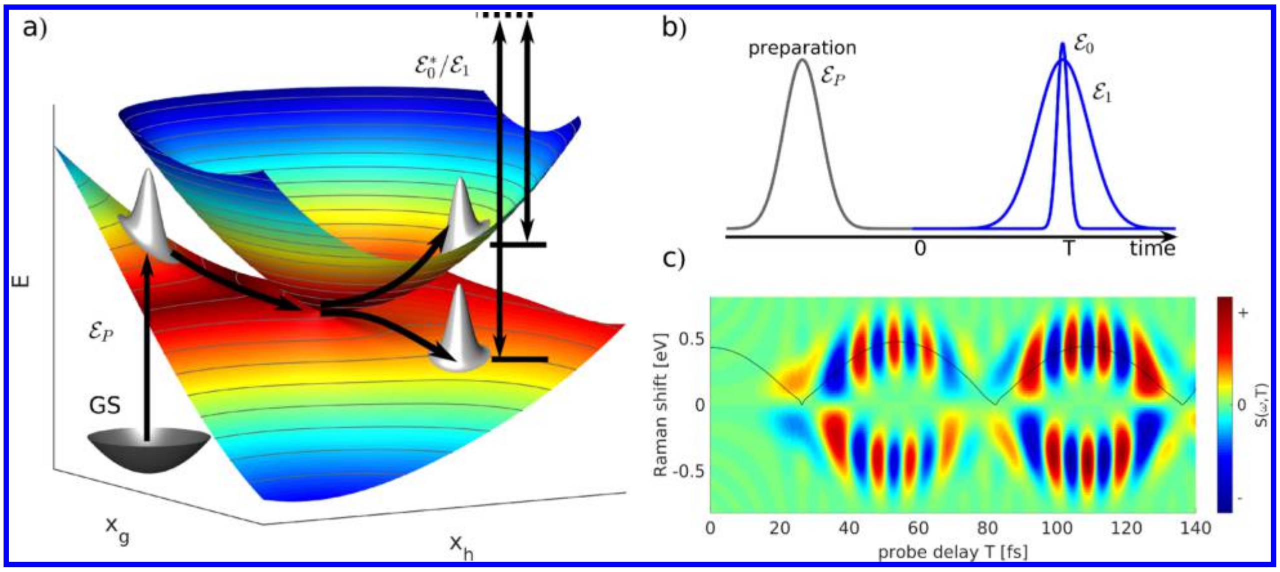

Figure 25. (a) Schematics of the TRUECARS process: A pump pulse $\mathcal{E}_P$ excites the molecule and launches the nuclear dynamics. When the nuclear wavepacket hits a CoIn and the population branches into two electronic states, an electronic coherence is created which is then probed by $\mathcal{E}_0$ and $\mathcal{E}_1$. (b) Pulse sequence. (c) TRUECARS signal for a one-dimensional systems. Reproduced with permission from ref 215. Copyright 2015 American Physical Society.

surface. Once it hits the level crossing, i.e., the nonadiabatic coupling, a coherence is created and the signal turns on. As it leaves the coupling region, the energy gap between the two curves increases, which can be directly read off from the Raman shift and the period of the oscillation pattern in T. In contrast to the quadratic Raman probe signals, the temporal and spectral resolution are not independent but are a conjugate Fourier pair. Since it is a linear probe the signal is proportional to $\mathcal{E}_0\mathcal{E}_1$, and thus, phase-stable pulses are required. The method time stamps the CoIn and may also give information about its geometry. The signal decays as the wavepackets on different surfaces drift apart, i.e., as the overlap $\langle \psi_g | \psi_e \rangle$ vanishes. The major influence of this decay is the gradient difference between the two electronic surfaces.

Simulations of linear off-resonant signals are straightforward. Since the signal is based on a one-time correlation function formed by the polarizability, only the time evolution of $\psi(t)$ in the excited valence has to be obtained with a suitable method (e.g., AIMS, MCTDH, or FFT on a numerical grid).

5.3. Time-Resolved Photoelectron Spectroscopy

Photoelectron spectroscopy[417] probes the kinetic energy of liberated photoelectrons, rather than photons, and can be understood as a generalization of the photoelectric effect.[418] It has long been utilized to identify the internal energy levels of molecules and solid-state systems. The signal is usually the kinetic-energy-dependent electron count, which yields the ionization potential of a specific molecular energy level. In TRPES[419] a pump pulse initiates the dynamics, which is then probed by a UV/XUV/X-ray probe pulse, liberating valence or lower-lying electrons from the sample. TRPES can be used to follow vibrational wavepacket motion[420] like in a typical pump−probe experiment. As such, it can also in principle be used to obtain signatures of CoIns[421] and follow the population dynamics. TRPES has been used to follow the population dynamics of nonradiative decay in $(NO)_2$,[422] in adenine and its nucleotides,[423,424] in thymine,[150] and in various nucleotides.[425]

The TRPES signal is linear in the probe intensity (Figure 26) and can be used to probe a CoIn through either population contributions or the created electronic coherences like in TRUECARS. However, in TRPES both contributions will appear on top of each other and it is therefore not a background-free detection method for the coherences as TRUECARS is. To detect CoIns and the created electronic coherences, both states must have access to a common ion state (see Figure 27) and the probe−pulse must be broad band with respect to the electronic energy gap.

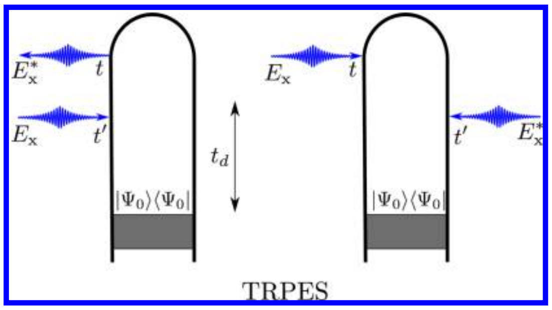

Figure 26. Loop diagrams for the TRPES signal: Field ionizes the molecule into the ion state $|I\rangle$ and a free-electron state $|\mathbf{p}\rangle$.

A simulated signal is shown in Figure 28. The underlying model is two-dimensional with a CoIn.[426] The wavepacket reaches the CoIn ≈ 10 fs after initial exciation. The temporal oscillations due to the coherence can be seen after 13 fs. The 200 as pulse resolves the oscillation pattern. This has, in principle been observed experimentally for an avoided crossing in NO,[427] where two closely lying dissociation channels contribute to a long-lived oscillation pattern on the picosecond time scale. Quantum beating created by a CoIn has been reported for pyrazine.[428]

The signal[426] can be read from the diagrams in Figure 26 and is derived from the integrated change of the electron number

$$S_e(\epsilon_{\mathbf{p}}, t_d) = \int dt \int dt' \tilde{E}_x^*(t)\tilde{E}_x(t') e^{-i(\epsilon_{\mathbf{p}}-\omega_x)(t-t')} \times \langle \hat{\mu}(t)\hat{\mu}^\dagger(t')\rangle_0 \qquad (81)$$

DOI: 10.1021/acs.chemrev.7b00081
Chem. Rev. 2017, 117, 12165−12226

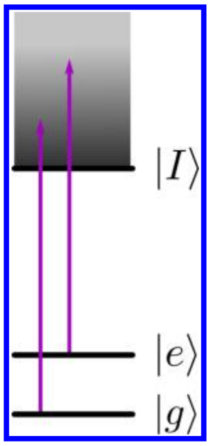

Figure 27. Energy-level diagram for TRPES: To detect electronic coherences of the molecule, both neutral states $|g\rangle$ and $|e\rangle$ must be ionized into the same ion state $|I\rangle$. Otherwise, only populations are detected.

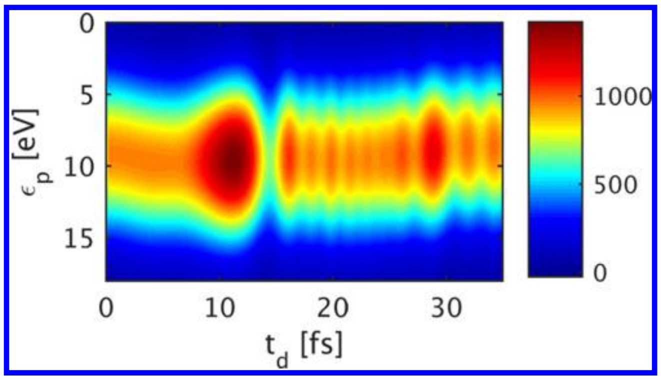

Figure 28. Simulated TRPES signal (eq 81, fwhm 200 as, $\omega_x = 20$ eV). Reproduced with permission from ref 426. Copyright 2016 American Chemical Society.

where t_d is the delay time, ω_x, the carrier frequency of the probe $\tilde{E}_x$ is the envelope of the probe field, ε_p is photoelectron kinetic energy, and $\hat{\mu}$ is the transition dipole between the neutral species and the cation. A derivation of the signal in Liouville space can be found in ref 413. From Figure 26 and inspection of the correlation function in eq 81 it becomes clear that this signal involves the time evolution of the nuclear wavepacket in the neutral molecule state as well as the time evolution on the ionic states. Since TRPES can be considered resonant, the nuclear time evolution in the excited state during the probe pulse has to be considered. A simulation of the signal according to eq 81 is exact but requires the evaluation of a two-time correlation function. Its computational effort thus scales quadratically with the investigated time span.

If the probe pulse is short with respect to the nuclear motion, the signal expression can be simplified, making it more suitable for semiclassical simulation techniques like, e.g., AIMS[429,430] or FSSH. This approximation is the quasi-static Fermi golden rule (FGR)[426]

$$S_{\mathrm{qs}}(\varepsilon_{\mathbf{p}}, t_{\mathrm{d}}) = S_{\mathrm{qs}}^{\mathrm{pop}}(\varepsilon_{\mathbf{p}}, t_{\mathrm{d}}) + S_{\mathrm{qs}}^{\mathrm{coh}}(\varepsilon_{\mathbf{p}}, t_{\mathrm{d}}) \tag{82}$$

where the signal can be written as a sum of the population and coherence contributions. The population term

$$S_{\mathrm{qs}}^{\mathrm{pop}}(\varepsilon_{\mathbf{p}}, t_{d}) = \sum_{a\alpha} \rho_{aa}(t_{\mathrm{d}}) \times |\mu_{\alpha a}(t_{\mathrm{d}})\tilde{E}_x(\varepsilon_{\mathbf{p}} - \omega_x + \mathcal{E}_\alpha(t_{\mathrm{d}}) - \mathcal{E}_a(t_{\mathrm{d}}))|^2 \tag{83}$$

depends on the electronic state populations ρ_{aa} of the neutral molecule, the transition dipole moments $\mu_{a\alpha}$ to the ionic states α, and the probe intensity. The coherence term

$$S_{\mathrm{qs}}^{\mathrm{coh}}(\varepsilon_{\mathbf{p}}, t_{d}) = \sum_{a\neq b,\alpha} \rho_{ab}(t_{\mathrm{d}})\langle\phi_{\alpha b}(t_{\mathrm{d}})|\phi_{\alpha a}(t_{\mathrm{d}})\rangle\mu_{\alpha b}(t_{\mathrm{d}})\mu_{\alpha a}^{*}(t_{\mathrm{d}}) \times \tilde{E}_x^{*}(\varepsilon_{\mathbf{p}} - \omega_x + \mathcal{E}_\alpha(t_{\mathrm{d}}) - \mathcal{E}_b(t_{\mathrm{d}})) \times \tilde{E}_x(\varepsilon_{\mathbf{p}} - \omega_x + \mathcal{E}_\alpha(t_{\mathrm{d}}) - \mathcal{E}_a(t_{\mathrm{d}})) \tag{84}$$

involves the electronic coherences ρ_{ab} between the neutral states, the nuclear overlap integral, the instantaneous eigenvalues of the electronic states $\mathcal{E}_{a/b/\alpha}$, and the probe field $\tilde{E}_{\mathrm{x}}^{*}\tilde{E}_x$, thus making it sensitive to the phase of the probe field. For details see ref 426. The transition dipole moments between the neutral and the ionic states can be approximated by the norm of the so-called Dyson orbitals.[429−431]

In a typical TRPES experiment, the photoelectrons are collected in a single direction, giving a signal depending only on photoelectron and probe delay. However, additional information in the angular distribution of the ejected photoelectrons can be utilized to monitor the possible change of orbital character as a molecule passes through a CoIn. The photoelectron angular distribution is usually well described by the shape of the orbital from which the electron originates (Dyson orbitals). The variation in spatial and temporal photoelectron current shape can be tracked with time-resolved photoelectron angular distributions, as demonstrated experimentally for the CS_2 molecule.[432]

As TRPES is linear in the probe field it is subject to the Fourier limit. A time resolution sufficient to resolve the dynamics of the electronic coherence will thus result in a loss of frequency resolution, which prevents identification of the neutral states involved in the dynamics. The time resolution of TRPES may be enhanced by an IR streaking field acting on the liberated photoelectrons.[433] This allows to time stamp the release time of the ejected photoelectrons and to use the phase relation between electrons in different momentum states originating from different electronic states. This adds a second, independent control knob to the scheme that allows partial recovery of the time resolution. The streaking field spreads out the photoelectrons across the kinetic-energy spectrum. Moreover, it allows one to couple photoelectrons which originate from different neutral states. These photoelectrons still carry the phase of their respective molecular state. A streaked photoelectron spectrum provides signatures of coherences without requiring attosecond ionization pulses.

5.4. Other Methods

Here, we briefly summarize other spectroscopic methods that have been used to keep track of nonadiabatic dynamics in molecules.

5.4.1. Auger Electron Spectroscopy. Time-resolved Auger electron spectroscopy has been used to monitor the dynamics around the CoIn in thymine.[137,139] Collecting secondary electrons released upon a core excitation (the Auger effect[434,435]) allows for element-specific measurements. For a theoretical description of time-resolved Auger electron spectroscopy, see ref 413. In contrast to TRPES where the transition moments are given by the Dyson orbitals, which is an effective one-electron property, the Auger decay is described by the Coulomb interaction. This requires calculation of two-electron integrals.

5.4.2. Time-Resolved High Harmonic Spectroscopy.

HHG[436,437] has been widely used to generate XUV pulses and as a starting point for the generation of attosecond pulses. In the HHG process, a strong femtosecond IR laser field tunnel ionizes an atomic gas. The electron then recollides with the parent ion, resulting in a broad comb of odd multiples of the fundamental driving laser frequency. Its extension to molecules is called time-resolved high-harmonic spectroscopy.[438,439] A molecule, which has been excited by a UV pump pulse is interrogated with a strong femtosecond IR laser field (after a delay), yielding information on different reaction channels through the generated harmonics. The signal is generated by recombination of the accelerated electron with the remaining ion. The method is similar to TRPES but is less sensitive to Franck−Condon (FC) factors. Tunnel ionization and high-harmonic generation are highly nonlinear processes. It may not be easily described with perturbation theory and is beyond the scope of this review. This method has been applied to the nonadiabtic dynamics in benzene[38] and NO_2.[37]

6. SUMMARY AND CONCLUSIONS

We presented a comprehensive overview of ultrafast state-of-the-art coherent multidimensional spectroscopic techniques and how they can be used to probe strongly coupled electron−nuclear dynamics in molecules, their theoretical description, and how the signals can be simulated by means of ab initio methods. In section 2.1, we introduced the loop diagrammatic formalism, which provides a theoretical framework for the description of transient IR signals. The presented formalism can be readily adapted to off-resonant Raman signals.

Four major protocols for the simulation of nonlinear signals are presented in section 2.2. The first employs a direct propagation of the wave function, which is the most accurate protocol but numerically expensive, since it requires a quantum description of the vibrational dynamics and is only feasible if the vibrational dynamics can be reduced to a few (effective) modes. The second protocol, sum over states, requires an expansion of the matter correlation function in system eigenstates. It is applicable if eigenvalues can be directly determined or can be reduced to a small number of contributing eigenvalues. In the above two protocols, bath modes must be explicitly included (or totally neglected). The third protocol separates primary and bath degrees of freedom. The primary vibrational modes of interest are modulated by bath modes, making this approach especially tractable for semiclassical methods. In contrast to the above three methods, which operate on the wave function in Hilbert space, the fourth protocol is based on the SLE and operates on the density matrix in Liouville space. It allows for a low-cost inclusion of bath modes and can handle complex line shapes.

Section 2.4 presents different variants of transient IR probe techniques. The most direct technique, UV/IR, tracks the frequency change of vibrational marker bands. The signal is linear in the probe, and the temporal resolution of direct IR detection is limited by the pulse bandwidth and ultimately by the carrier frequency. This limitation can be overcome by Raman probes. The T-2DIR technique can be considered an extension of conventional 2DIR to include transient, excited state dynamics. It delivers additional information about intermode couplings and spectral diffusion caused by environment fluctuations. 2DEV is a hybrid configuration that correlates electronic excitations with the vibrational modes and follows their time evolution.

The various vibrational probe techniques presented in section 3 rely on different configurations of an off-resonant stimulated Raman probe sequence that treat the actinic excitation and probe pulses as a six-wave mixing processes. All considered signals provide spectrally and temporally resolved information about vibrational bands. Using UV−vis rather than IR pulses allows one to lift some restrictions on pulse duration and bandwidth. The simplest spontaneous technique, FR-SPRS, is a homodyne-detected signal that provides purely absorptive peaks since the signal can be recast as the magnitude of a transition amplitude. The FSRS signal, in contrast, is emitted along the direction of the probe pulse (self-phase matched) and is heterodyne detected as Raman gain/loss on top of the broad-band probe spectrum. The FSRS technique employs a hybrid broad-band/narrow-band probe pulse pair, which lifts some restrictions of the Fourier uncertainty $\Delta\omega\Delta t > 1$. It provides a better signal-to-noise ratio and spectral resolution than FR-SPRS. TR-ISRS uses two temporally separated probe pulses and derives its frequency resolution from scanning a second time interval rather than from frequency-dispersed detection. TG-ISRS uses a noncollinear configuration and three probe pulses. Like TR-ISRS it derives its frequency resolution from two time intervals. The four-pulse scheme allows a higher degree of control. The computation of all of these vibrational probes requires simulating the nonadiabatic excited state dynamics and the transient excited state dipole moments (for IR detection) or the transient excited state polarizabilities (for Raman detection). Vibrational frequencies are sensitive to conformational changes and fine details of PESs, making them an excellent probe for CoIns. Even though the distribution of time and frequency resolution over independent variables allows one to remove the Fourier uncertainty restriction from the detection process, the time resolution in vibrational spectroscopy is ultimately limited by the carrier frequency of the employed probe pulses.

Specifically probing the electronic states allows one to push the time resolution into the attosecond regime. Several techniques that address the electronic degrees of freedom by means of resonant optical probe pulses are reviewed in section 4. The simplest and most common example is resonant TA, which monitors excited state populations and coherences. It has per se lower structural sensitivity than vibrational probes but allows for a direct observation of the excited state dynamics. The realization of impulsive excitation conditions mitigates this deficiency to some extent by revealing coherent vibrational oscillations that appear superimposed in TA signals. TALH is an extension to TA that yields information about vibrational modes and can be seen as linear analogue of FSRS but recorded in the time domain.

2DES is currently the most sophisticated technique that spreads the information content of the third-order nonlinear response in two frequency dimensions, thereby overcoming limitations of the TA technique (section 4.2). The respective two-dimensional signals allow one to correlate the excitation and detection frequency and thus monitor spectral diffusion, interchromophore couplings, energy transfer processes, and electronic coherences. In particular, 2DES in the UV spectral regime (2DUV) appears promising to investigate prominent electronic absorption bands of organic molecules, such as DNA, proteins, and (hetero-) aromatic compounds, where striking nonadiabatic relaxation channels via CoIns appear. Emerging

2D-UV/vis measurements open the possibility for direct comparison of experiments with simulated spectral signatures of photochemical relaxation dynamics, thereby providing a rigorous test for ab initio force fields and other employed approximations. het-TG spectroscopy is closely related to 2DES and monitors the third-order response function in an integrated fashion over the ω_1 excitation frequency axis. The absorptive part of the het-TG signal contains identical information as TA. Alternative incoherent detection schemes like PM-Fl and two-dimensional photocurrent spectroscopy yield similar information compared to 2DES. In the fourth-order PM-Fl technique, an additional ladder diagram contains information on biexciton population states. Incoherent fluorescence provides background-free detection and offers higher sensitivity that can be extended to single-molecule detection.

Several techniques that address the electronic degrees of freedom by means of X-ray pulses rather than optical pulses are presented in section 5. X-ray pulses offer a better time resolution than optical pulses. The two considered Raman methods, ASRS and TRUECARS, make use of excitations from core electrons into the valence space. Core electrons are highly localized and element specific, adding an additional spatial control to the technique. X-ray Raman techniques are formally analogous to their UV−vis counter parts: the electronic valence states are investigated rather than vibrational states, and intermediate states are now core excited states rather than valence states. The calculation of core excited states poses a major challenge to the simulation of such signals (for a review see ref 440). By combining femtosecond−attosecond pulses, ASRS transfers the concept of a frequency-dispersed quadratic hybrid probe ($S_{\text{QH}}^{(\text{fd})}$) of the FSRS technique to the X-ray spectral domain. This allows for element-sensitive probing of electronic properties without the requirement of phase control. It provides information about electronic populations as well as coherences. In contrast, the TRUECARS technique is off-resonant and sensitive to the electronic coherences created in the vicinity of a CoIn. It is background free with respect to electronic populations.

TRPES is formally similar to TA but with the major differences being that it detects photoelectrons rather than photons and that the signal is purely absorptive (no-stimulated emission like in TA). Photoelectron detection is highly sensitive and allows for high temporal resolution. TRPES can detect the population and coherences of different electronic states. As a linear method, it is subject to the Fourier limit, which may be partially lifted by adding an IR streaking field. Angular resolved photoelectron spectroscopy (ARPES)[428,432,441] and chiral photoelectron spectroscopy[442] are interesting new frontiers that were not reviewed here.

Before turning to open questions in the field we want to briefly pause and recapture the information content obtained by state of the art nonlinear techniques on the nonadiabatic relaxation of selected molecular systems. We focus on discussing the light-induced relaxation dynamics of pyrimidine DNA and RNA nucleobases thymine and uracil which is, due to the inherent UV photoprotection properties, perhaps one of the most important examples of a CoIn. A wealth of information has been obtained recently by TA with probing in the visible and UV spectral region,[151,152,443] UV-IR,[153] 2DUV,[141] time-resolved Auger electron spectroscopy,[137,138] TRPES,[140,150,424] and transient NEXAFS,[139] augmented by in-depth theoretical studies (see, e.g., refs 103, 113, 144, 150, and 158 and ref 136 for a recent review).

From these in part complementary methods a picture emerges that involves participation of two distinct conical intersection in the ultrafast nonadiabatic relaxation process. In the gas phase, transient NEXAFS spectroscopy at the oxygen edge (∼520−550 eV)[139] has been employed to identify a new, slightly delayed appearing resonance (60 fs) that was assigned to an oxygen 1s → 2p transition arising from the participating, long-lived $n_O\pi^*$ state (10 ps). Participation of the direct relaxation channel, including trapping in a $\pi\pi^*$ state minimum, could nevertheless not be ruled out. Complementary ultrafast X-ray Auger probing allowed to dissect nuclear and electronic relaxation dynamics and suggests short-lived population of the $\pi\pi^*$ minimum (200 fs), characterized by an extended C(4)−O(8) bond.[137,138] These findings overhaul assignments in pioneering TRPES studies[150] where barrier crossing to the minimal energy $\pi\pi^*$/gs CoIn was attributed to the slower, picosecond decay. In the currently emerging picture, an indirect $\pi\pi^* \rightarrow n_O\pi^*$ channel leads to formation of an optical dark $n_O\pi^*$ state that is discussed as precursor of triplet formation.[158] In parallel, the direct $\pi\pi^*$ → gs channel leads to ultrafast repopulation of the electronic ground state (cf. Figure 29). We note that alternative assignments were suggested on the basis of TRPES data where population of the $n_O\pi^*$ state serves as a doorway to ground state repopulation.[424]

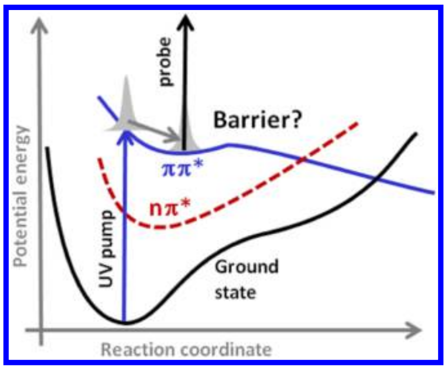

Figure 29. UV excitation and molecular relaxation scheme of pyrimidine DNA and RNA nucleobases thymine and uracil in a potential energy representation. Radiationless electronic relaxation pathways from the photoexcited $\pi\pi^*$ state into to the $n_O\pi^*$ and the ground state are facilitated by CoIn. Adapted with permission from ref 138. Copyright 2016 American Chemical Society.

In aqueous solution, the participation of different relaxation channels and interconnection to long-lived triplet states is a matter of ongoing debate.[140,141,151,152] In polar solvents, state ordering upon vertical excitation is reversed, with the $\pi\pi^*$ state becoming the first excited state, followed by the $n_O\pi^*$ state as the second excited state.[136,444] Here participation of the $\pi\pi^*$ → gs channel has been inferred from TA with UV spectral probes,[152,443] demonstrating ultrafast (∼1 ps) ground state recovery upon photoexcitation. Ground state vibrational cooling of uracil and thymine could be observed by a continuous UV probe extending down to 250 nm, which provides strong evidence of the ultrafast $\pi\pi^*$ → gs decay.[151] We note that the derived 1−2 ps cooling time scale[151] is a matter of some debate.[141] The sustained but weak contribution of the $\pi\pi^* \rightarrow n_O\pi^*$ channel, albeit reversed state ordering, was assigned from a long-lived (>10 ps) component upon probing the excited state absorption signal at ∼320 nm.[151,443]

This assignment was recently challenged by a TRPES study performed on an aqueous solution liquid jet setup that found no contribution of a long-lived $n_O\pi^*$ state.[140] The findings are in stark contrast to TA[151,152,443] and UV/IR[153] experiments that demonstrate formation of long-lived transient states (potentially coupled to the triplet manifold), indicating a primary sensitivity of the TRPES technique toward the initially populated $\pi\pi^*$ state. Chemical modification at the C6 and C5 position of uracil demonstrated that methyl substitution on uracil in water in general inhibits the $\pi\pi^* \to n_O\pi^*$ channel, thereby promoting the direct $\pi\pi^* \to$ gs decay channel.[151] Recently employed sub-10 fs UV probe pulses[152] allowed to realize impulsive excitation in TA giving access to vibrational modes in ground and excited states. The shortest time constant (<100 fs) was assigned to the relaxation through CoIn from the first excited S_2 ($\pi\pi^*$) state to the S_1 ($n_O\pi^*$) state ($\pi\pi^* \to n_O\pi^*$ channel), while the second ultrafast time constant (~1 ps) was assigned to relaxation from the relaxed $\pi\pi^*$ state to the S_0 ground state ($\pi\pi^* \to$ gs channel). The results indicated a large homogeneous width of pyrimidine nucleobases in aqueous solution, larger than structural features of the employed laser spectrum (~50 meV). Vibrational modes at 1380 and 1100 cm^{-1} were assigned to dynamics in excited states where the acquired vibrational phase relaxation time (50 fs) is controlled by the electronic decay of the S_2 ($\pi\pi^*$) state. A vibrational mode at 1247 cm^{-1} was assigned to the electronic ground state on the basis of the longer dephasing time scale.

A recent report of TA, 2DES, and het-TG signals recorded with sub-10 fs pulses in the UV suggested a different relaxation mechanism being operational for all DNA bases.[141] Here fast relaxation (500−700 fs) occurs from the excited state $\pi\pi^*$ to a "dark" state that is subsequently depopulation to the ground state within 1−2 ps. The authors conclude that the dark state can be associated with the $n\pi^*$ electronic state, which is connected to the excited and ground states via two distinct CoIns ($\pi\pi^* \to n_O\pi^* \to$ gs). Notably, the reported 1247 and 1380 cm^{-1} modes[152] could be confirmed by het-TG spectroscopy together with an additional 1685 cm^{-1} mode.[141] The pronounced homogeneous broadening was revealed in the 2D spectra, suggesting very strong system−bath interaction in these compounds, in agreement with the conclusions of ref 152.

Summarizing the emerging picture, participation of two distinct CoIn in the ultrafast nonadiabatic relaxation process of pyrimidine DNA and RNA nucleobases thymine and uracil is suggested by recent experiments employing probes in the UV spectral region with highest temporal resolution.[141,152] Nevertheless, the involvement and sequence of participating CoIns is under debate. One suggestion favors sequential excited state deactivation via an intermediate state ($\pi\pi^* \to n_O\pi^* \to$ gs).[141] This view is challenged by the bifurcation scenario ($n_O\pi^* \leftarrow \pi\pi^* \to$ gs)[152] that resembles the gas-phase deactivation mechanism (cf. Figure 29), albeit reversed state ordering at the FC geometry. Notably, in the direct $\pi\pi^* \to$ gs and sequential $\pi\pi^* \to n_O\pi^* \to$ gs proposal the involvement of CoIn is inferred indirectly from the ultrashort excited state lifetime (decay of population) and concomitant ground state bleach recovery within ~1 ps, i.e., direct participation and characterization of the CoIn has eluded observation. For the direct $\pi\pi^* \to$ gs pathway, the involved CoIn is predicted to be of ethylenic twist character.[113,136,144] Here, besides emerging nonlinear X-ray probes,[15,412] vibronic detection of C═C and C═O modes (cf. section 3) upon UV excitation is expected to provide access to structural information as reporter of ring out-of-plane distortions during the relaxation process. A very recent FSRS study on 2′-deoxyguanosine 5′-monophosphate with UV excitation[445] reported dynamic distortions in excited states and an extraordinary broad transient line width of modes. Together with in-depth modeling of frequency evolution in excited states[113] such information appears particularly promising for characterization of deactivation pathways.

In more general terms, the involvement of CoIns is typically inferred from ultrashort excited state lifetimes (sometimes in conjunction with ground state recovery) together with modeling of static minimum energy crossing seam CoIn structures. The concept of the CoIn here has proven tremendous predictive power for the qualitative understanding of reaction mechanisms, but quantitative modeling of nonadiabatic dynamics together with associated nonlinear signals is scarce. Beyond phenomenological assignments, to date only a few time-resolved experimental probings of a CoIn have been reported. Most reported experiments have indirect circumstantial evidence of their presence by probing the fast dynamics of a vibrational wave packet passing through a conical intersection[18,446] or via the product branching ratio.[447] Ultrafast TRPES can locate the CoIn with a resolution of a few tens of femtoseconds.[428,441] Recent examples that are sensitive directly to the change in electronic structure include high harmonic generation study of NO_2[37] and time-resolved Auger and NEXAFS probes of thymine.[137,139] In principle, fast nonradiative relaxation between electronic states can also be described within an adiabatic, perturbative framework.[448] In such a picture the quasi-continuous density of vibrational states together with interstate FC integrals mediate relaxation dynamics, and no primary subset of modes exist that direct the nonradiative relaxation due to to strong vibronic nonadiabatic coupling. The linear−vibronic coupling model,[5] which due to the nuclear dependence of coupling parameters accounts for the formation of CoIn, here provides a rigorous framework to disentangle nonadiabatic effects in linear[449] and nonlinear signals[450,451] beyond often employed phenomenological assignments of nonadiabaticity. Dissecting vibronic effects in nonlinear signals has recently attracted attention.[72,74,366,397] Such analysis provides guidance for assignment of nonadiabatic relaxation phenomena beyond commonly employed experimental indications for the involvement of a CoIn that rely, e.g., on nonexponential kinetics and oscillatory dynamics.[18,286,287] The advent of broad-band pulses, i.e., impulsive excitation conditions, further provides access to excited state vibrational modes, frequency shifts, and dephasing time scales that allow one to quantify CoIn involvement.[152,347,349,351] Together with advanced Raman probes[111,266,274,276] and emerging X-ray probes of electronic state character,[15] these techniques are expected to enhance our understanding of nonadiabatic relaxation phenomena and associated reactive CoIn structures in the not so distant future.

7. OUTLOOK

In the following, we summarize open questions and future challenges for ultrafast spectroscopy of nonadiabatic relaxation. One question is the detection of more universal classes of CoIns and their manifestation in dynamics and spectroscopic observables. The concept of CoIn as a mechanism to strongly couple electronic and vibrational degrees of freedom can be generalized to nonconventional CoIns (e.g., imposed by multiple states or electric fields, see below), which call for more advanced spectroscopic techniques. These might help improve the understanding of general characteristics of CoIns. Technical challenges arise in particular in the design and implementation of modern X-ray detection techniques. Novel X-ray techniques provide great potential for improved detection due to their higher temporal resolution and their elemental specificity. Entangled photons and nonclassical states of light provide novel control parameters for optical signals and can improve the resolution and overcome typical limitations of classical light spectroscopy. However, their implementation is a challenge for broad-band pulse sources. Established transient one-dimensional probes for CoIns are more common. Multidimensional probes give deeper insights by monitoring couplings between different modes.

CoIns between more than two electronic states, like three-state CoIns, have long been proposed[143,452] in highly symmetric molecules as an additional photophysical relaxation mechanism. More recent theoretical investigations have predicted them in a variety of molecules (e.g., methyl cation,[452] ethyl radical,[453] allyl radical,[454] pyrazolyl,[455] cytosine,[456,457] uracil and andenine,[458] malonic acid,[459] and diphenyl methyl radical[460]) and demonstrate that three-state CoIns are more common than initially believed. Four-state CoIns have been reported as well.[461] In contrast to standard two-state CoIns, the degeneracy of three states at a singular point requires five constraints which leads to a five-dimensional branching space. Accordingly, three-state CoIns arise in molecules with at least four atoms. Investigations on three-state CoIns are so far purely theoretical; their relevance in the excited state relaxation dynamics and how they can be observed is an exciting open issue.

Considering the electric field as an additional degree of freedom for control, light-induced conical intersection (LiCi)[462] has been proposed as a way to create a CoIn in diatomic molecules in which only avoided crossings usually exist due to the strict noncrossing rule for PESs of the same symmetry. In a LiCi, two electronic states are coupled by a strong laser field, thereby generating an avoided crossing in the dressed states picture. Taking into account the molecular rotation with respect to the polarization of the field axis as an additional degree of freedom yields a point of degeneracy if the dipole and polarization vector becomes orthogonal, i.e., a LiCi is created. In contrast to naturally occurring CoIns, LiCis can be controlled by changing the frequency, intensity, and temporal envelope of the coupling laser field. This allows on-demand activation and control of their position in the nuclear subspace. This has been experimentally demonstrated for cyclohexadiene,[11] where the outcome of a photochemical reaction was influenced, and in in the strong field dissociation of H_2^+.[463] It has been shown that LiCis are subject to a geometric phase effects, and thus, a Berry phase (see below) is predicted to arise in diatomic systems.[464]

In a similar way as a LiCi can be created by a classical laser field, quantized light fields in optical cavities can create nonadiabatic couplings in molecules. A CoIn or avoided crossing between two electronic states in the dressed state basis is created when a molecule is coupled resonantly to the vacuum field of a cavity.[48,465] These artificially created CoIns may be studied by means of ultrafast spectroscopy in greater detail.

A sign change of a real adiabatic electronic state is induced if one encircles the point of a CoIn in a closed loop. This *geometric phase effect*, or *Berry phase*,[466] depends solely on the CoIn topology, is independent of many molecular details, but has so far eluded direct observation in molecular systems (for a review see ref 467). The observation of a Berry phase in a molecular system would manifest as a clear signature of the CoIn. The direct experimental observation of the $\pm\pi$ phase around CoIn remains an open challenge. Distinct signatures in emission spectra have been proposed as a proof of the acquired π phase.[468] A spectroscopic observation of the geometric phase through the spatial localization of eigenfunctions[469,470] caused by the nonadiabatic coupling might be another strategy. A general route to the direct observation may be provided by linear probes which are particularly sensitive to the phase of the electronic coherences, e.g., TRUECARS,[215] TRPES[426] with attosecond pulses, or streaked TRPES measurements.[433] The conditions for the observability of the Berry phase are also discussed in refs 471−473. An experimental measurement of the Berry phase might pose a unique and unambiguous proof for the existence of a CoIn.

Hamm et al.[474] proposed vibrational (as opposed to electronic) CoIns as potential mechanisms of ultrafast vibrational relaxation. Vibrational CoIns arise by partitioning the vibrations into high-frequency (fast) and low-frequency (slow) modes, in analogy to conventional (electronic) CoIns where (slow) vibrational degrees of freedom are coupled to the (fast) electronic degrees of freedom. Theoretical studies predict vibrational CoIns for OH stretch[475,476] and CH stretch[477] modes. Recently, vibrational lifetimes of the Zundel cation $H_5O_2^+$ selectively prepared in acetonitrile were reported to be in the sub-100 fs range,[478] much shorter than those of neat water and similar to lifetimes of electronic excited states, where pronounced non-Born-Oppenheimer effects appear.[441,479] An experimental scheme to unambiguously detect vibrational CoIns has yet to be realized.

The multidimensional extension of transient vibrational probe schemes (like transient IR and FSRS) that follow the frequency change of a marker band as one-dimensional probes provides access to anharmonicities and intermode couplings in excited states that are influenced by the coupling in the vicinity of a CoIn.[174,480] 2D-FSRS with fifth- or seventh-order pulse sequences are expected to carry this type of information.[481−483] Here, an impulsive (off-resonant) pump couples low-frequency modes with high-frequency (spectator) modes. Since low-frequency modes are expected to contribute to the coupling and tuning modes of the CoIn,[484] this type of scheme may yield additional direct information about the CoIn. Replacing the impulsive pump pulse by two resonant IR interactions yields another detection scheme, which might give access to anharmonicities and intermode couplings of spectator modes.

2D-FSRS is known to suffer from competing cascading processes,[481,485−490] which complicates its measurement. Cascading is a many-body phenomenon that occurs when the polarization induced on one molecule serves as a source for interactions with another molecule in the sample. The result is a signal given by a product of lower order molecular polarizations rather than the desired higher order process. The phase matching of each of these lower order processes together creates the same phase matching as for the direct higher order process, posing a challenge for their separation from the desired higher order signals. For example, fifth-order pulse sequences seek to measure $P^{(5)}$, the single-molecule fifth-order polarization, but inevitably measure the product of third-order polarizations $P^{(3)}P^{(3)}$, which lacks the desired information on anharmonicities and intermode couplings. Besides appearing in the same phase-matching direction and with the same dependence on external field amplitudes, the fact that the cascading signal scales quadratically in the molecular density (since it is a two-molecule effect) leads it to overwhelm the direct higher order signals of interest and ratios as unfavorable as 50:1 have been reported in liquid CS_2.[491] Historically, cascading has been selected against using the $\pi/2$ phase shift generated by the extra emission event in cascading versus a direct nonlinear process[107,336,491−494] (polarization-based techniques have also been pursued[495]). A quantum electrodynamic derivation of cascading viewed as photon exchange demonstrates how this phase shift originates in geometric effects and is not simply $\pi/2$ in cases of a few molecules or nontrivial geometries.[496,497] Moreover, the derivation reveals that cascading signals should increase in magnitude with the frequency of the cascading photon due to the larger density of electromagnetic field states. Thus, cascading can be expected to pose a greater challenge in higher frequency X-ray experiments. Future research should consider cascading processes in samples embedded in optical cavities.[498] Optical cavities only allow certain modes. In macroscopic samples, where the cascading mode is well defined by the phase-matching condition, this should allow the suppression of cascading when the cascading mode is not one of the cavity modes. In few-molecule samples, in which the cascading takes place in all available vacuum modes, optical cavities could force the cascading into the cavity modes, allowing precise control of the cascading process.

Ultrafast experiments are most commonly carried out with pulses with simple temporal and spectral shapes (e.g., Gaussian). However, shaped pulses (see refs 499 and 500 for reviews) allows for quantum control in the vicinity of CoIn[501,502] and may provide an opportunity to enhance nonlinear spectra. Subcycle control of coupled electron−nuclear dynamics at a conical intersection has been proposed.[503] The spectro-temporal shape of optical laser pulses and polarization[504] can be controlled. Novel developments allow subcycle waveform control,[505,506] which may be used for shaping of XUV pulses. Pulse shaping has been demonstrated to enhance, e.g., Raman signals[507,508] and CARS microscopy.[509] Electromagentic-induced transparency has been proposed for the decongestion of molecular spectra.[510]

The current feasibility of X-ray Raman experiments is limited by existing pulse sources (for a detailed discussion see ref 410). Thus far, a resonant Raman process has been demonstrated in atoms.[511] Nonlinear coherent probes require, e.g., phase-stable multicolor attosecond or femtosecond pulses. Phase-locked pulses generated from seeded FELs have been reported[512,513] and will allow for implementation of linear or hybrid Raman probes. Apart from FEL sources, a possible pathway to produce soft X-ray broad−narrow pulse pairs can be to utilize the HHG process: A single harmonic is selected to serve as narrow-band pulse, while the full comb may be used to produce a broad-band attosecond pulse. This scheme might deliver stable pulses for, e.g., ASRS or TRUECARS detection.

FEL facilities produce high intensity, hard X-ray pulses. These allow one to perform time-resolved diffraction in the gas phase, thereby probing the structural dynamics of molecules.[14,514−517] X-ray scattering from nonstationary states contains not only elastic but also inelastic contributions which can be attributed to electronic coherences.[518] Following the strategy presented in section 5.2 the creation of electronic coherence in the vicinity of CoIns may be used to extract unique signatures from time-dependent diffraction experiments. One striking advantage of this approach is that the diffraction patterns directly encode spatial information and thus can potentially reveal the location of the created coherence.

Multidimensional XUV/X-ray coherent probes may reveal nonadiabatic dynamics in the vicinity of CoIns (for a review of multidimensional X-ray probes see ref 519). The element selectivity may allow one to narrow down the location of a CoIn in a molecule. One example could be the X-ray double-quantum coherence technique,[520] which correlates different core transitions and their anharmoninicities caused by rearrangement of the valence electrons. An upcoming high repetition rate upgrade of the SLAC facility (LCLS-II) should make multidimensional X-ray Raman measurements feasible.[521]

Noncollinear wave mixing of XUV and IR pulses from a table-top light source has been reported for atoms.[522,523] Transient grating, which combines XUV and optical pulses from a FEL source, has been reported by Bencivenga et al.[524,525] These recent developments[526] demonstrate the feasibility of noncollinear wave mixing in the XUV/X-ray regime and provide the foundation for multidimensional probes of nonadiabatic relaxation with unique information content.

The present formalism for employing nonlinear optical signals toward the study of of nonadiabatic processes is not limited to classical laser fields. Quantum light opens up new avenues for spectroscopy by utilizing parameters of the quantum state of light as novel control knobs and through the variation of photon statistics by coupling to matter. To account for quantum field effects, the general formalism in this review has to be modified by explicit evaluation of multipoint correlation functions of the electric field for a given state of light. Laser light corresponds to a coherent state of the field, i.e., the eigenstates of the photon annihilation operator, and is generally considered as "classical". All field correlation functions may be factorized up to field commutators (non-normally ordered corrections can be neglected in this case) into products of field amplitudes—classical functions that are used in the present review. The more general formalism that describes various nonlinear optical signals studied by quantum light is summarized in a recent review.[527]

One of the notable examples of state of light other than coherent state, which is widely used in quantum optics, is entangled light. Entangled photon pairs have an advantage over laser light in spectroscopy applications, as they are not subjected to the classical Fourier limitations on the joint temporal and spectral resolution, discussed in section 2.3. Going from the laser light to the single-photon level requires a different set of detection tools. Photon coincidence signals, also known as biphoton signals,[528−531] provide an additional tool for nonlinear spectroscopy. In a typical setup, a pair of entangled photons denoted as E_s and E_r generated by parametric down conversion (PDC) are separated on a beam splitter. One photon E_s is transmitted through the molecular sample and then detected in coincidence with E_r. In order to use it as a spectroscopic tool, a frequency filter can be placed in front of one of the detectors which measures the spectrum. This type of signal shows a number of interesting features: First, coincidence detection improves the signal-to-noise ratio.[532] Second, the two detectors may operate in very different spectral regions and at different spatial locations.[530] For example, to measure the spectroscopic properties of a sample in the vacuum ultraviolet (VUV) range, it is not necessary to set a spectrometer in a vacuum chamber and control it under the vacuum condition. Instead, using a VUV and a visible entangled-photon pair, only the latter should be resolved by a spectrometer. Another advantage is for IR spectroscopy; the power of the light source must often be very low to prevent possible damage of a sample, but an IR photodetector is usually noisy. Photon coincidence measurements can overcome the noise. IR signals can be measured with more sensitive detectors in the visible regime.

Entangled photon pairs together with coincidence detection and ultrafast upconversion techniques can be employed for Raman studies of ultrafast nonadiabatic dynamics. A new proposed technique interferometric femtosecond stimulated

Raman spectroscopy (IFSRS)[533] combines quantum entangled light with interferometric detection in order to enhance the resolution and selectivity of Raman signals. The measurement uses a pair of entangled photons: one (signal) photon interacts with the molecule and acts as the broad-band probe ($\mathcal{E}_2$ in Figure 12), while the other (idler) does not interact with the molecule and provides a reference for the coincidence measurement between the two arms. Using photon counting IFSRS can separately measure the gain and the loss contributions to the Raman signal.[534] Classical FSRS signals only report their sum (i.e., the net gain or loss). In IFSRS, the probe pulse $\mathcal{E}_2$ belongs to a pair of entangled beams generated in degenerate type-II PDC. The polarizing beam splitter then separates the orthogonally polarized photons. The horizontally polarized beam $\mathcal{E}_2$ propagates in the one arm of the interferometer and interacts with the molecule. The vertically polarized beam propagates freely in the other arm and serves as a reference. Apart from the different detection windows, there is another important distinction between IFSRS and the classical FSRS signals. In the latter, both the gain and the loss contributions contain red- and blue-shifted features relative to the narrow pump frequency. The FSRS signal contains both Stokes and anti-Stokes components, and FSRS can only distinguish between red and blue contributions. The interferometric signal, in contrast, can separately measure the gain (two photons in the s arm) and loss contributions (no photons).

APPENDIX

Time-Gated Signals

We present the time-gated signals corresponding to the frequency-gated expressions given in the main text. The UV/IR signal can be read from diagrams similar to eqs 23 and 24 by introducing the τ-dispersed signal in time domain as an analogue to eq 22 and is given by

$$S_{\mathrm{IR}}(t, T) = \mathcal{I}\int_{-\infty}^{t} \mathrm{d}\tau \mathcal{E}_2^*(t-T)\mathcal{E}_2(\tau-T)\tilde{S}_{\mathrm{IR}}(t, T; \tau) \tag{85}$$

where $\tilde{S}_{\mathrm{IR}}(t,T;\tau) = \tilde{S}_{\mathrm{IR}}^{(i)}(t,T;\tau) + \tilde{S}_{\mathrm{IR}}^{(ii)}(t,T;\tau)$ and the individual terms are given by

$$\tilde{S}_{\mathrm{IR}}^{(i)}(t, T; \tau) = \frac{2}{\hbar}\int_{-\infty}^{t}\mathrm{d}\tau_1\int_{-\infty}^{\tau}\mathrm{d}\tau_5\mathcal{E}_1^*(\tau_5)\mathcal{E}_1(\tau_1) \times \langle V_e G^\dagger(\tau, \tau_5)V_n^\dagger G^\dagger(t, \tau)V_n G(t, \tau_1)V_e^\dagger\rangle \tag{86}$$

$$\tilde{S}_{\mathrm{IR}}^{(ii)}(t, T; \tau) = \frac{2}{\hbar}\int_{-\infty}^{t}\mathrm{d}\tau_1\int_{-\infty}^{\tau}\mathrm{d}\tau_5\mathcal{E}_1(\tau_5)\mathcal{E}_1^*(\tau_1) \times \langle V_e G^\dagger(t, \tau_1)V_n G(t, \tau)V_n^\dagger G(\tau, \tau_5)V_e^\dagger\rangle \tag{87}$$

where $\tilde{S}(t,T;\tau)$ is the signal at time t resulting from interaction with $\mathcal{E}_2$ at time $\tau - T$. The signal is obtained by integration over τ.

The corresponding SRS signal reads

$$\tilde{S}_{\mathrm{SRS}}^{(i)}(t, T; \tau) = \frac{2}{\hbar}\int_{-\infty}^{t}\mathrm{d}\tau_1\int_{-\infty}^{\tau_3}\mathrm{d}\tau_5\mathcal{E}_1^*(\tau_5)\mathcal{E}_1(\tau_1) \times \mathcal{E}_3(t-T)\mathcal{E}_3^*(\tau-T)\langle V_e G^\dagger(\tau, \tau_5)\alpha_n G^\dagger(t, \tau)\alpha_n G(t, \tau_1)V_e^\dagger\rangle \tag{88}$$

$$\tilde{S}_{\mathrm{SRS}}^{(ii)}(t, T; \tau) = \frac{2}{\hbar}\int_{-\infty}^{t}\mathrm{d}\tau_1\int_{-\infty}^{\tau_3}\mathrm{d}\tau_5\mathcal{E}_1(\tau_5)\mathcal{E}_1^*(\tau_1) \times \mathcal{E}_3(t-T)\mathcal{E}_3^*(\tau-T)\langle V_e G^\dagger(t, \tau_1)\alpha_n G(t, \tau)\alpha_n G(\tau, \tau_5)V_e^\dagger\rangle \tag{89}$$

Equations 88 and 89 are analogues of eqs 49 and 50.

The time domain UV/IR signals eqs 86 and 87 can be recast using SOS expansion

$$\tilde{S}_{\mathrm{IR}}^{(i)}(t, T; \tau) = \frac{2}{\hbar}\theta(\tau)\theta(t)\sum_{a,a',d}\mu_{ga'}\mu_{ag}^*\mu_{a'd}^*\mu_{ad} \times \mathcal{E}_1^*(\omega_{a'} + i\gamma_{a'})\mathcal{E}_1(\omega_a - i\gamma_a)\mathrm{e}^{-(i\omega_{ad}+\gamma_{ad})t+(i\omega_{a'd}+\gamma_d-\gamma_{a'})\tau} \tag{90}$$

$$\tilde{S}_{\mathrm{IR}}^{(ii)}(t, T; \tau) = -\frac{2}{\hbar}\theta(\tau)\theta(t)\sum_{a,a',c}\mu_{ga'}\mu_{ag}^*\mu_{a'c}^*\mu_{ca} \times \mathcal{E}_1^*(\omega_{a'} + i\gamma_{a'})\mathcal{E}_1(\omega_a - i\gamma_a)e^{-(i\omega_{a'c}+\gamma_{a'c})t+(i\omega_{ac}+\gamma_c-\gamma_a)\tau} \tag{91}$$

that are analogues to eqs 27 and 28.

Frequency-Domain UV/IR Signal Expression

In eqs 23 and 24, the matter correlation function is given in the time domain. Alternatively, one can read the signal (eq 22) from the diagrams when both field and matter correlation functions are given in the frequency domain

$$S_{\mathrm{IR}}^{(i)}(\omega, T) = \mathcal{I}\frac{4\pi}{\hbar}\int_{-\infty}^{\infty}\frac{\mathrm{d}\omega'}{2\pi}\frac{\mathrm{d}\omega_1}{2\pi}\frac{\mathrm{d}\omega_1'}{2\pi} \times \mathcal{E}_2^*(\omega)\mathcal{E}_2(\omega')\mathcal{E}_1^*(\omega_1)\mathcal{E}_1(\omega_1')\delta(\omega - \omega' + \omega_1 - \omega_1') \times \langle V_e G^\dagger(\omega_g + \omega_1)V_n^\dagger G^\dagger(\omega_g + \omega_1 - \omega')V_n G(\omega_g + \omega_1')V_e^\dagger\rangle \tag{92}$$

$$S_{\mathrm{IR}}^{(ii)}(\omega, T) = \mathcal{I}\frac{4\pi}{\hbar}\int_{-\infty}^{\infty}\frac{\mathrm{d}\omega'}{2\pi}\frac{\mathrm{d}\omega_1}{2\pi}\frac{\mathrm{d}\omega_1'}{2} \times \mathcal{E}_2^*(\omega)\mathcal{E}_2(\omega')\mathcal{E}_1^*(\omega_1)\mathcal{E}_1(\omega_1')\delta(\omega - \omega' + \omega_1 - \omega_1') \times \langle V_e G^\dagger(\omega_g + \omega_1)V_n G(\omega_g + \omega' + \omega_1')V_n^\dagger G(\omega_g + \omega_1')V_e^\dagger\rangle \tag{93}$$

Here, $G(\omega) = h^{-1}/[\omega - H/\hbar + i\epsilon]$ and $\delta(\omega - \omega' + \omega_1 - \omega_1')$ represents the energy conservation that follows from time-translation symmetry of all four field–matter interactions. One can separate the preparation pulse $\mathcal{E}_1$ and break the $\delta -$ function as follows

$$\delta(\omega - \omega' + \omega_1 - \omega_1') = \int_{-\infty}^{\infty}\mathrm{d}\Delta\delta(\omega - \omega' + \Delta)\delta(\omega_1 - \omega_1' - \Delta) \tag{94}$$

where Δ defines the spectral bandwidth of the incoming pulse which translates into the spectral bandwidth of the relevant matter degrees of freedom. Equations 92 and 93 then yield

$$S_{\mathrm{IR}}^{(i)}(\omega, T) = \mathcal{I}\frac{2}{\hbar}\int_{-\infty}^{\infty}\mathrm{d}\Delta\mathrm{d}\omega_1\mathcal{E}_2^*(\omega)\mathcal{E}_2(\omega + \Delta)\mathcal{E}_1^*(\omega_1) \times \mathcal{E}_1(\omega_1 - \Delta) \times\langle V_e G^\dagger(\omega_g + \omega_1)V_n^\dagger G^\dagger(\omega_g + \omega_1 - \omega - \Delta)V_n \times G(\omega_g + \omega_1 - \Delta)V_e^\dagger\rangle \tag{95}$$

$$S_{\mathrm{IR}}^{(ii)}(\omega, T) = \mathcal{I}\frac{2}{\hbar}\int_{-\infty}^{\infty} \mathrm{d}\Delta \mathrm{d}\omega_1 \mathcal{E}_2^*(\omega)\mathcal{E}_2(\omega + \Delta)\mathcal{E}_1^*(\omega_1) \\ \times \mathcal{E}_1(\omega_1 - \Delta) \\ \times \langle V_e G^\dagger(\omega_g + \omega_1)V_n G(\omega_g + \omega + \omega_1)V_n^\dagger \\ \times G(\omega_g + \omega_1 - \Delta)V_e^\dagger\rangle \tag{96}$$

Spontaneous Signals

The spontaneous photon-counting signal is defined as an integrated number of photon registered by the detector

$$S(\bar{t}, \varpi) \\ = \int_{-\infty}^{\infty} \mathrm{d}t \sum_{s,s'} \langle \hat{E}_{sR}^{(\mathrm{tf})\dagger}(\bar{t}, \varpi; r_\mathrm{D}, t)\hat{E}_{s'L}^{(\mathrm{tf})}(\bar{t}, \varpi; r_\mathrm{D}, t)\rangle \tag{97}$$

where the angular brackets denote $\langle ...\rangle \equiv \mathrm{Tr}[\rho(t)...]$. The density operator $\rho(t)$ is defined in the joint field–matter space of the entire system. Note that eq 97 represents the observable homodyne-detected signal and is always positive since it can be recast as a modulus square of an amplitude (cf. eq 58). For clarity, we hereafter omit the position dependence in the fields assuming that propagation between r_G and r_D is included in the spectral gate function F_f. In the case when detection is represented by a consecutive time gate F_t with central time $\bar{t}$ and frequency gate F_f with central frequency ϖ, the corresponding time- and frequency-resolved electric field reads

$$E^{(\mathrm{tf})}(\bar{t}, \varpi; r_D, t) = \int_{-\infty}^{\infty} \mathrm{d}t' F_f(t - t', \varpi)F_t(t', \bar{t})\hat{E}(r_G, t') \tag{98}$$

where the positive frequency part of the electric field operator is given by

$$\hat{\mathbf{E}}(t, \mathbf{r}) = \sum_{\mathbf{k}_s,\mu}\left(\frac{2\pi\hbar\omega_s}{\Omega}\right)^{1/2} \epsilon^{(\mu)}(\mathbf{k}_s)\hat{a}_{\mathbf{k}_s}\mathrm{e}^{-i\omega_s t + i\mathbf{k}_s\cdot\mathbf{r}} \tag{99}$$

and $\epsilon^\mu(\mathbf{k})$ is the unit electric polarization vector of mode $(\mathbf{k}_s,\mu)$, μ being the index of polarization, $\omega_s = c|\mathbf{k}_s|$, c is speed of light, and Ω is quantization volume. Similarly, one can apply the frequency gate first and obtain frequency- and time-gated field E^{ft}. Introducing the detector's Wigner spectrogram

$$W_\mathrm{D}(\bar{t}, \varpi; t', \omega') \\ = \int_{-\infty}^{\infty} \frac{\mathrm{d}\omega}{2\pi}\left|F_f(\omega, \varpi)\right|^2 W_t(\bar{t}; t', \omega' - \omega) \tag{100}$$

which is given by

$$W_t(\bar{t}; t', \omega) = \int_{-\infty}^{\infty} \mathrm{d}\tau F_t^*(t' + \tau/2, \bar{t})F_t(t' - \tau/2, \bar{t})\mathrm{e}^{i\omega\tau} \tag{101}$$

The detector spectrogram W_D is an ordinary function of the gating time and frequency parameters which are characterized by standard deviations of the time and frequency gating σ_T and σ_ω, respectively. The structure of W_D guarantees that these always satisfy the Fourier uncertainty $\sigma_\omega\sigma_T \geq 1$. Combining eqs 98–101, we can recast eq 97 in the form

$$S(\bar{t}, \varpi) = \int_{-\infty}^{\infty} \mathrm{d}t' \frac{\mathrm{d}\omega'}{2\pi} W_\mathrm{D}(\bar{t}, \varpi; t', \omega')W_\mathrm{B}(t', \omega') \tag{102}$$

The signal is given by the spectral and temporal overlap of a bare signal and a detector spectrogram. The bare signal contains all of the relevant information about the molecules. In order to maintain the book-keeping of all interactions and develop a perturbative expansion for signals we adopt superoperator notation. With each ordinary operator O, we associate a pair of superoperators[337] "left" $\hat{O}_L = OX$, "right" $\hat{O}_R X = XO$, and the combination $\hat{O}_- = \hat{O}_L - \hat{O}_R$. The bare spectrogram W_B in the gated photon counting signal, eq 102, is given in terms of superoperators as

$$W_\mathrm{B}(t', \omega') = \frac{\mathcal{D}^2(\omega')}{\hbar^2}\int_{-\infty}^{\infty} \mathrm{d}\tau \mathrm{e}^{-i\omega'\tau}\mathcal{E}_2^*(t' + \tau)\mathcal{E}_2(t') \\ \times \langle \mathcal{T}\alpha_{nR}(t' + \tau)\alpha_{nL}(t')\mathrm{e}^{-i/\hbar\int_{-\infty}^{t'}\hat{H}_-'(T)\mathrm{d}T}\rangle \tag{103}$$

The Hamiltonian superoperator in the interaction picture under the rotating-wave approximation is given by

$$\hat{H}'_q(t) = \int \mathrm{d}\mathbf{r}\hat{\mathbf{E}}_q^\dagger(t, \mathbf{r})\hat{\mathbf{V}}_q(t, \mathbf{r}) + H.\,c,\ q = L, R \tag{104}$$

where $\mathbf{V}(t,\mathbf{r}) = \sum_\alpha \mathbf{V}^\alpha(t)\delta(\mathbf{r} - \mathbf{r}_\alpha)$ is a matter operator representing the lowering (exciton annihilation) part of the dipole coupling and α runs over molecules in the sample located at $\mathbf{r}_\alpha$. The operator $\mathcal{T}$ maintains positive time ordering of superoperators and is a key book-keeping device. It is defined as follows

$$\mathcal{T}\hat{E}_q(t_1)\hat{E}_{q'}(t_2) = \theta(t_1 - t_2)\hat{E}_q(t_1)\hat{E}_{q'}(t_2) \\ + \theta(t_2 - t_1)\hat{E}_{q'}(t_2)\hat{E}_q(t_1) \tag{105}$$

where $\theta(t)$ is the Heaviside step function. In the absence of the frequency gate $F_f(\omega,\varpi) = 1$ and taking the limit of the narrow time gating $W_\mathrm{D}(t',\omega';\bar{t},\varpi) = \delta(t' - \bar{t})$ the signal, eq 102, reads

$$S(\bar{t}) = |T_{fi}(\bar{t})|^2 \tag{106}$$

where

$$T_{fi}(t) = \frac{\mathcal{D}(\omega_{fi})}{\hbar}\mathcal{E}_2(t)\langle\mathcal{T}\alpha(t)\mathrm{e}^{-i/\hbar\int_{-\infty}^{t}H'(T)\mathrm{d}T}\rangle \tag{107}$$

is a transition amplitude. Similarly, in the absence of time gate $F_t(t',\bar{t}) = 1$ and taking the limit of narrow frequency gate $W_\mathrm{D}(t',\omega';\bar{t},\varpi) = \delta(\omega' - \varpi)$, the signal (eq 102) reads

$$S(\varpi) = |T_{fi}(\varpi)|^2 \tag{108}$$

where $T_{fi}(\omega) = \int_{-\infty}^{\infty}\mathrm{d}t\mathrm{e}^{i\omega t}T_{fi}(t)$. Therefore, in the pure time or frequency detection the signal is given by the modulus square of the transition amplitude as expected.[78] In this review, we use eqs 108 for FR-SPRS, but the results can be extended by using eqs 102 and 103.

Frequency-Resolved Spontaneous Raman Signal (FR-SPRS)

We read the bare signal (see eq 102) of the diagrams in Figure 30 as

$$W_\mathrm{B}^{(i)}(t', \omega', T) = -i\hbar\int_0^\infty \mathrm{d}\tau\mathrm{e}^{i\omega'\tau}\int_{-\infty}^{t'}\mathrm{d}\tau_1\int_{-\infty}^{t'-\tau}\mathrm{d}\tau_5 \\ \times \mathcal{D}^2(\varpi)\mathcal{E}_2^*(t' - \tau - T)\mathcal{E}_2(t' - T)\mathcal{E}_\mathrm{p}^*(\tau_5)\mathcal{E}_\mathrm{p}(\tau_1) \\ \times F_i(t' - \tau - \tau_5, \tau, t' - \tau_1) \tag{109}$$

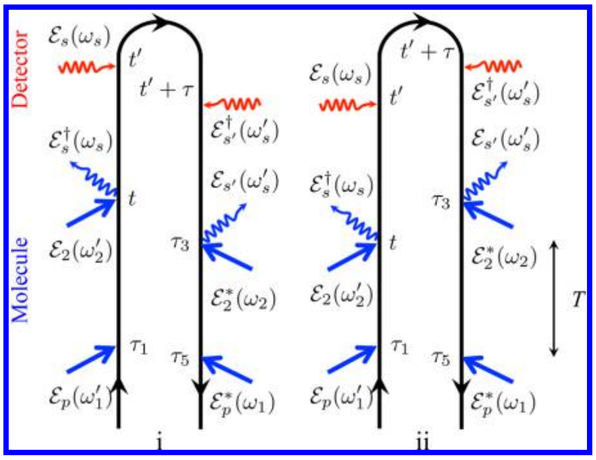

Figure 30. Loop diagrams for the time and frequency SPRS signal including interactions with the detector. Time-translational invariance yields $\omega'_1 + \omega'_2 - \omega_s + \omega_s - \omega_s{}' + \omega_s{}' - \omega_2 - \omega_1$.

$$W_{\mathrm{B}}^{(ii)}(t', \omega', T) = i\hbar \int_0^\infty \mathrm{d}\tau \mathrm{e}^{-i\omega'\tau} \int_{-\infty}^{t'} \mathrm{d}\tau_1 \int_{-\infty}^{t'+\tau} \mathrm{d}\tau_5 \times \mathcal{D}^2(\bar{\varpi})\mathcal{E}_2^*(t' + \tau - T)\mathcal{E}_2(t' - T)\mathcal{E}_{\mathrm{p}}^*(\tau_5)\mathcal{E}_{\mathrm{p}}(\tau_1) \times F_{ii}(t' + \tau - \tau_5, \tau, t' - \tau_1) \tag{110}$$

The bare signal, eqs 109 and 110, can be alternatively recast in the frequency domain

$$W_{\mathrm{B}}^{(i)}(t', \omega', T) = -i\hbar \int_{-\infty}^{\infty} \frac{\mathrm{d}\omega_1}{2\pi}\frac{\mathrm{d}\omega_1'}{2\pi}\frac{\mathrm{d}\omega_2}{2\pi}\frac{\mathrm{d}\omega_2{}'}{2\pi}\mathcal{D}^2(\bar{\varpi}) \times \mathcal{E}_2^*(\omega_2)\mathcal{E}_2(\omega_2{}')\mathcal{E}_{\mathrm{p}}^*(\omega_1)\mathcal{E}_{\mathrm{p}}(\omega_1')\mathrm{e}^{i(\omega_2-\omega_2{}'+\omega_1-\omega_1')t'} \times F_i(\omega_1, \omega_1 + \omega_2 - \omega', \omega_1')\mathrm{e}^{i(\omega_2{}'-\omega_2)T} \tag{111}$$

$$W_{\mathrm{B}}^{(ii)}(t', \omega', T) = i\hbar \int_{-\infty}^{\infty} \frac{\mathrm{d}\omega_1}{2\pi}\frac{\mathrm{d}\omega_1'}{2\pi}\frac{\mathrm{d}\omega_2}{2\pi}\frac{\mathrm{d}\omega_2{}'}{2\pi}\mathcal{D}^2(\bar{\varpi}) \times \mathcal{E}_2^*(\omega_2)\mathcal{E}_2(\omega_2{}')\mathcal{E}_{\mathrm{p}}^*(\omega_1)\mathcal{E}_{\mathrm{p}}(\omega_1')\mathrm{e}^{i(\omega_2-\omega_2{}'+\omega_1-\omega_1')t'} \times F_{ii}(\omega_1, \omega_1 + \omega_2 - \omega', \omega_1')\mathrm{e}^{i(\omega_2{}'-\omega_2)T} \tag{112}$$

To draw a full analogy with the stimulated signals, we assume no time gate. In this case, the detector spectrogram $W_{\mathrm{D}}(\bar{t}, \bar{\varpi}; t', \omega') = |F_f(\omega'; \bar{\varpi})|^2$. The time-translational invariance yields

$$\int_{-\infty}^{\infty} \mathrm{d}t' \mathrm{e}^{i(\omega_2-\omega_2{}'+\omega_1-\omega_1')t'} = 2\pi\delta(\omega_2 - \omega_2{}' + \omega_1 - \omega_1') \tag{113}$$

which yields the signal $S_{\mathrm{FR-SPRS}}(\bar{\varpi},T) = S^{(i)}_{\mathrm{FR-SPRS}}(\bar{\varpi},T) + S^{(ii)}_{\mathrm{FR-SPRS}}(\bar{\varpi},T)$

$$S^{(i)}_{\mathrm{FR-SPRS}}(\bar{\varpi}, T) = -i\hbar \int_{-\infty}^{\infty} \frac{\mathrm{d}\omega_1}{2\pi}\frac{\mathrm{d}\omega_1'}{2\pi}\frac{\mathrm{d}\omega_2}{2\pi}\frac{\mathrm{d}\omega'}{2\pi}\mathcal{D}^2(\bar{\varpi}) \times |F_f(\omega'; \bar{\varpi})|^2\mathcal{E}_2^*(\omega_2)\mathcal{E}_2(\omega_1 - \omega_1' + \omega_2)\mathcal{E}_{\mathrm{p}}^*(\omega_1)\mathcal{E}_{\mathrm{p}}(\omega_1') \times F_i(\omega_1, \omega_1 + \omega_2 - \omega', \omega_1')\mathrm{e}^{i(\omega_1-\omega_1')T} \tag{114}$$

$$S^{(ii)}_{\mathrm{FR-SPRS}}(\bar{\varpi}, T) = i\hbar \int_{-\infty}^{\infty} \frac{\mathrm{d}\omega_1}{2\pi}\frac{\mathrm{d}\omega_1'}{2\pi}\frac{\mathrm{d}\omega_2}{2\pi}\frac{\mathrm{d}\omega'}{2\pi}\mathcal{D}^2(\bar{\varpi}) \times |F_f(\omega'; \bar{\varpi})|^2\mathcal{E}_2^*(\omega_2)\mathcal{E}_2(\omega_1 - \omega_1' + \omega_2)\mathcal{E}_{\mathrm{p}}^*(\omega_1)\mathcal{E}_{\mathrm{p}}(\omega_1') \times F_{ii}(\omega_1, \omega_1 + \omega_2 - \omega', \omega_1')\mathrm{e}^{i(\omega_1-\omega_1')T} \tag{115}$$

For an ideal frequency gate, eqs 114 and 115 become eq 56.

Mapping of off-Resonant Interactions to Effective Polarizabilities

The purpose of this section is to simplify the 4-point correlation function of dipole operators that appears in resonant quadratic hybrid Raman signals into a 2-point correlation function of polarizability operators. This contrasts with the approach in the main text, in which the polarizability operator was directly incorporated into the interaction Hamiltonian. Though both approaches are appropriate for off-resonant interactions, the following derivation also reveals a broad line width limit that is useful. The signal can be read directly from diagrams with the same topology as in Figure 8b (we do not incorporate the actinic pump here but rather consider only the broad–narrow hybrid probe impinging on an arbitrarily-prepared state) and reads

$$S^{(\mathrm{fd})}_{\mathrm{HSXRS}}(\omega_s, \omega_1) = \mathcal{R}\Big[\mathcal{E}^*(\omega_s) \int \mathrm{d}t \mathrm{e}^{i\omega_s t} \int_{-\infty}^{t} \mathrm{d}t' \mathcal{E}_1 \mathrm{e}^{-i\omega_1 t'} \times \Big(\int_{-\infty}^{t'} \mathrm{d}t'' \int_{-\infty}^{t''} \mathrm{d}t''' \langle \hat{V}(t)\hat{V}^\dagger(t')\hat{V}(t'')\hat{V}^\dagger(t''')\rangle_0 \times \mathcal{E}(t''')\mathcal{E}_1^*\mathrm{e}^{i\omega_1 t''} + \int_{-\infty}^{t} \mathrm{d}t'' \int_{-\infty}^{t''} \mathrm{d}t''' \mathcal{E}(t'') \times \mathcal{E}_1^*\mathrm{e}^{i\omega_1 t'''} \langle \hat{V}(t''')\hat{V}^\dagger(t'')\hat{V}(t)\hat{V}^\dagger(t')\rangle_0\Big)\Big] \tag{116}$$

where $\mathcal{E}_1$, ω_1 are the amplitude and frequency of the narrow-band pulse, $\mathcal{E}(t)$ is the temporal envelope of the broad-band pulse, and $\langle ... \rangle_0$ indicates expectation value over nuclear and electronic degrees of freedom of the initial wave function $|\Psi(t_0)\rangle$. We note that this expression refers to an experiment in which all four interactions happen within the same hybrid pulse. An alternative experiment involves a more complex probe composed of a temporally well-separated pair of hybrid pulses. In this case, the two interactions with broad-band components happen with different pulses, and the integral over t' can be taken to ∞. This probe will then also contain information on the dynamics subsequent to the first hybrid pulse and does not merely probe the dynamics of the initialized state $|\Psi(t_0)\rangle$ alone. We now make the substitutions $t' - t''' = \tau'$, $t - t' = \tau$ and explicitly write the time propagators $U(t - t')$ (which propagate both nuclear and electronic degrees of freedom but are field free). For brevity, we only explicitly write the first term of eq 116 with the second term following similarly

$$S_1(\mathrm{fd})(\omega_s, \omega_1) = \mathcal{R}\Big[\mathcal{E}^*(\omega_s)\mathcal{E}_1 \int \mathrm{d}t\mathrm{d}\tau\mathrm{d}\tau' \theta(t - t_0)\theta(\tau)\theta(\tau') \times \mathrm{e}^{i(\omega_s-\omega_1)(t-T)}\mathrm{e}^{i\omega_1\tau} \int \mathrm{d}t''' \mathcal{E}(t''')\mathcal{E}_1^*\mathrm{e}^{i\omega_1(t'''+\tau'-T)}\theta(t''' - t_0) \times \langle \Psi(t_0)|\hat{U}^\dagger(t - t_0)\hat{V}\hat{U}(\tau)\hat{V}^\dagger\hat{U}(t - \tau - t''' - \tau')\hat{V} \times \hat{U}(\tau')\hat{V}^\dagger\hat{U}(t''' - t_0)|\Psi(t_0)\rangle\Big] \tag{117}$$

We can define the Green's function $i\theta(t)\hat{U}(t) \equiv G(t)$ and it's Fourier transform $G(\omega)$. Making this substitution we obtain

$$\begin{aligned} &S_1^{(\mathrm{fd})}(\omega_s, \omega_1) \\ &= \mathcal{R}\Bigg[\frac{i}{(2\pi)^3}\mathcal{E}^*(\omega_s)\mathcal{E}_1 \int \mathrm{d}t\mathrm{d}\tau\mathrm{d}\tau' \mathrm{e}^{i(\omega_s-\omega_1)(t-T)}\mathrm{e}^{i\omega_1\tau} \\ &\times \int \mathrm{d}t'''\mathcal{E}(t''')\mathrm{e}^{i\omega_1(t'''+\tau'-T)} \int \mathrm{d}\omega\mathrm{d}\omega'\mathrm{d}\omega'''\mathcal{E}_1^* \\ &\times \mathrm{e}^{-i\omega\tau}\mathrm{e}^{-i\omega'\tau'}\mathrm{e}^{-i\omega''(t-\tau-t'''-\tau')} \\ &\times \langle\Psi(t_0)|\hat{G}^\dagger(t-t_0)\hat{V}\hat{G}(\omega) \\ &\times \hat{V}^\dagger\hat{G}(\omega'')\hat{V}\hat{G}(\omega')\hat{V}^\dagger\hat{G}(t'''-t_0)|\Psi(t_0)\rangle\Bigg] \end{aligned} \tag{118}$$

We may now integrate over dτ, dτ', dω, and dω' to give

$$\begin{aligned} &S_1^{(\mathrm{fd})}(\omega_s, \omega_1) \\ &= \mathcal{R}\Bigg[\frac{i}{2\pi}\mathcal{E}^*(\omega_s)|\mathcal{E}_1|^2 \\ &\times \int \mathrm{d}t\mathrm{e}^{i(\omega_s-\omega_1)(t-T)} \int \mathrm{d}t'''\mathcal{E}(t''')\mathrm{e}^{i\omega_1(t'''-T)} \\ &\times \int \mathrm{d}\omega'''\mathrm{e}^{-i\omega''(t-t''')} \\ &\times \langle\Psi(t_0)|\hat{G}_\mathrm{v}^\dagger(t-t_0)\hat{V}\hat{G}_\mathrm{c}(\omega_1+\omega'')\hat{V}^\dagger\hat{G}_\mathrm{v}(\omega'') \\ &\times \hat{V}\hat{G}_\mathrm{c}(\omega_1+\omega'')\hat{V}^\dagger\hat{G}_\mathrm{v}(t'''-t_0)|\Psi(t_0)\rangle\Bigg] \end{aligned} \tag{119}$$

Here, we used the fact that in the case of an X-ray Raman experiment, the dipole operators only connect core and valence electronic states. Assuming the initial wave function $|\Psi(t_0)\rangle$ has no core excitations, we can denote propagation in the valence or core states with G_v and G_c respectively. In the case of sufficiently off-resonant excitation or broad core excitation line width so that $\hat{G}_\mathrm{c}(\omega_1+\omega') \approx \hat{G}_\mathrm{c}(\omega_1)$ for all valence excitation frequencies ω', we can return to a fully time domain expression

$$\begin{aligned} &S_1^{(\mathrm{fd})}(\omega_s, \omega_1) \\ &= \mathcal{R}\Bigg[\frac{i}{2\pi}\mathcal{E}^*(\omega_s)|\mathcal{E}_1|^2 \int \mathrm{d}t\mathrm{e}^{i(\omega_s-\omega_1)(t-T)} \int \mathrm{d}t'\tilde{\mathcal{E}}(t') \\ &\times \mathrm{e}^{i(\omega_1-\omega_0)(t'-T)}\langle\Psi(t_0)|\hat{G}_\mathrm{v}^\dagger(t-t_0)\hat{\alpha}^{(\mathrm{h})}(\omega_1) \\ &\times \hat{G}_\mathrm{v}(t-t')\hat{\alpha}^{(\mathrm{h})}(\omega_1)\hat{G}_\mathrm{v}(t'-t_0)|\Psi(t_0)\rangle\Bigg] \end{aligned} \tag{120}$$

where we substituted the effective polarizability due to Raman excitation to the core states $\hat{\alpha}^\mathrm{h}(\omega) = \hat{V}\ \hat{G}_\mathrm{c}(\omega)\hat{V}^\dagger$ (the h superscript, standing for "hybrid", serves to distinguish from other definitions of the effective polarizability used in the text and highlights that the simplification is only possible because of the trivial time dependence of the narrow-band pulse component). We also relabeled $t''' \to t'$ and substituted the temporal envelope of the broad-band X-ray pulse with the product of profile and carrier frequency $\mathcal{E}(t) \to \tilde{\mathcal{E}}(t)\mathrm{e}^{-i\omega_0 t}$. This last simplification is not technically necessary but faciliates computation since only differences of X-ray frequencies are then necessary with respect to choosing the time discretization. Note that this step is not necessary for the spectral envelope since the other exponential factor already comes with a difference frequency. This can be rewritten in the more compact form

$$\begin{aligned} &S_1^{(\mathrm{fd})}(\omega_s, \omega_1) \\ &= \mathcal{R}\Bigg[\frac{1}{2\pi}\mathcal{E}^*(\omega_s)|\mathcal{E}_1|^2 \int \mathrm{d}t\mathrm{e}^{i(\omega_s-\omega_1)(t-T)} \int_{t_0}^{t} \mathrm{d}t' \\ &\times \tilde{\mathcal{E}}(t')\mathrm{e}^{i(\omega_1-\omega_0)(t'-T)}\langle\hat{\alpha}(\omega_1, t)\hat{\alpha}(\omega_1, t')\rangle_0\Bigg] \end{aligned} \tag{121}$$

where we added time dependence to $\hat{\alpha}^\mathrm{h}$ in the usual way for interaction-picture operators $\hat{O}(t) = \hat{U}^\dagger(t)\hat{O}\hat{U}(t)$. We also explicitly put the lower limit of the dt' integral as t_0, even though this is redundant since the temporal profile of the probe $\mathcal{E}(t)$ is assumed not to overlap with the preparation process, so as to facilitate simulation. The total hybrid stimulated X-ray Raman signal is then

$$\begin{aligned} &S_1^{(\mathrm{fd})}(\omega_s, \omega_1) \\ &= \mathcal{R}\Bigg[\frac{1}{2\pi}\mathcal{E}^*(\omega_s)|\mathcal{E}_1|^2 \int \mathrm{d}t\mathrm{e}^{i(\omega_s-\omega_1)(t-T)} \int_{t_0}^{t} \mathrm{d}t' \\ &\times \tilde{\mathcal{E}}(t')\mathrm{e}^{i(\omega_1-\omega_0)(t'-T)}\langle\hat{\alpha}^{(\mathrm{h})}(\omega_1, t)\hat{\alpha}^{(\mathrm{h})}(\omega_1, t')\rangle_0 \\ &- \mathrm{e}^{-i(\omega_1-\omega_0)(t'-T)}\langle\hat{\alpha}^{(\mathrm{h})\dagger}(\omega_1, t')\hat{\alpha}^{(\mathrm{h})}(\omega_1, t)\rangle_0\Bigg] \end{aligned} \tag{122}$$

Stimulated Signals

Stimulated (heterodyne-detected) optical signals are defined as the energy change of the electromagnetic field

$$S = \int_{-\infty}^{\infty} \frac{\mathrm{d}}{\mathrm{d}t}\langle a^\dagger(t)a(t)\rangle\mathrm{d}t \tag{123}$$

where $a(a^\dagger)$ is the annihilation (creation) operator for the field $\mathcal{E}$. The radiation−matter interaction Hamiltonian in the rotating wave approximation is

$$H'(t) = V(t)\mathcal{E}^\dagger(t) + H.\ c. \tag{124}$$

where $V(t) + V^\dagger(t)$ is a Heisenberg dipole operator and the electric field operator $E(t) = \mathcal{E}(t) + \mathcal{E}^\dagger(t)$. Both are separated into positive (nondagger) and negative (dagger) frequency components (lowering and raising photon operators, respectively).

The Heisenberg equation of motion for the field operator $E(t)$ then gives for the above integrated signal

$$\begin{aligned} S &= \frac{2}{\hbar}\int_{-\infty}^{\infty} \mathrm{d}t'\mathcal{I}\langle V(t')\mathcal{E}^\dagger(t')\rangle \\ &= \frac{2}{\hbar}\int_{-\infty}^{\infty} \frac{\mathrm{d}\omega'}{2\pi}\mathcal{I}\langle V(\omega')\mathcal{E}^\dagger(\omega')\rangle \end{aligned} \tag{125}$$

where $\mathcal{I}$ denotes the imaginary part. The angular brackets denote $\langle ...\rangle = \mathrm{Tr}[\rho(t)...]$ with the density operator $\rho(t)$ defined in the joint field−matter space of the entire system. In practice the temporal or spectral range of the integrations in eq 125 is restricted by the response function of the detector. For a classical optical pulse one can replace the electric field operator by the expectation value $\langle\mathcal{E}\rangle = \mathcal{E}$. If the detector contains a narrow time gate with nearly δ function response $\delta(t'-t)$, eq 125 yields

$$S_t(t; \Gamma) = \frac{2}{\hbar}\mathcal{I}\mathcal{E}^*(t)P(t) \tag{126}$$

where $P(t) = \langle V(t)\rangle$ is polarization and Γ denotes a set of parameters that characterize the various laser pulses. Similarly, if the detector consists of a spectrometer with narrow frequency response $\delta(\omega'-\omega)$, we obtain the frequency-gated signal

$$S_f(\omega;\,\Gamma) = \frac{2}{\hbar}\mathcal{I}\mathcal{E}^*(\omega)P(\omega) \tag{127}$$

where $P(\omega) = \int_{-\infty}^{\infty}\mathrm{d}tP(t)\mathrm{e}^{i\omega t}$. Note that the two signals in eqs 126 and 127 carry different information and are not related by a simple Fourier transform. A Wigner spectrogram representation[77−79] was used in ref 80 for the integrated pump−probe signals (eq 97). Here we use loop diagrams to describe the more detailed time- or frequency-gated signals, eqs 126 and 127, respectively. We can also recast the signals, eqs 126 and 127, in the superoperator notation for arbitrary field operator

$$S_t(t;\,\Gamma) = \frac{2}{\hbar}\mathcal{I}\langle\mathcal{E}_\mathrm{L}^\dagger(t)V_\mathrm{L}(t)\mathrm{e}^{-i/\hbar\int_{-\infty}^{\infty}\hat{H}_-'(T)\mathrm{d}T}\rangle \tag{128}$$

where Γ denotes a set of parameters that characterize the various laser pulses. Similarly, if the detector consists of a spectrometer with narrow frequency response $\delta(\omega' - \omega)$, we obtain the frequency-gated signal

$$S_f(\omega;\,\Gamma) = \frac{2}{\hbar}\mathcal{I}\int_{-\infty}^{\infty}\mathrm{d}t\mathrm{e}^{i\omega t}\langle\mathcal{E}_\mathrm{L}^\dagger(\omega)V_\mathrm{L}(t)\mathrm{e}^{-i/\hbar\int_{-\infty}^{\infty}\hat{H}_-'(T)\mathrm{d}T}\rangle \tag{129}$$

This expression is our starting point for computing the three stimulated signals TG-ISRS, TR-ISRS, and FSRS.

FSRS

We read the signal off the diagrams given in Figure 12

$$\begin{aligned} S_\mathrm{FSRS}&(\omega,\,T) \\ &= \mathcal{I}\int_{-\infty}^{\infty}\frac{\mathrm{d}\Delta}{2\pi}\mathcal{E}_3^*(\omega)\mathcal{E}_3(\omega+\Delta)\tilde{S}_\mathrm{FSRS}(\omega,\,T;\,\Delta) \end{aligned} \tag{130}$$

where $\tilde{S}_\mathrm{FSRS}(\omega,T;\,\Delta) = \tilde{S}^{(i)}_\mathrm{FSRS}(\omega,T;\,\Delta) + \tilde{S}^{(ii)}_\mathrm{FSRS}(\omega,T;\,\Delta)$ and

$$\begin{aligned} \tilde{S}^{(i)}_\mathrm{FSRS}(\omega,\,T;\,\Delta) &= \frac{2}{\hbar}\int_{-\infty}^{\infty}\mathrm{d}t\int_{-\infty}^{t}\mathrm{d}\tau_1\int_{-\infty}^{t}\mathrm{d}\tau_3\int_{-\infty}^{\tau_3}\mathrm{d}\tau_5 \\ &\times \mathcal{E}_2^*(\tau_3)\mathcal{E}_2(t)\mathcal{E}_\mathrm{p}^*(\tau_5)\mathcal{E}_\mathrm{p}(\tau_1)\mathrm{e}^{i\omega(t-\tau_3)-i\Delta(\tau_3-T)} \\ &\times F_i(\tau_3-\tau_5,\,t-\tau_3,\,t-\tau_1) \end{aligned} \tag{131}$$

$$\begin{aligned} \tilde{S}^{(ii)}_\mathrm{FSRS}(\omega,\,T;\,\Delta) &= \frac{2}{\hbar}\int_{-\infty}^{\infty}\mathrm{d}t\int_{-\infty}^{t}\mathrm{d}\tau_1\int_{-\infty}^{t}\mathrm{d}\tau_3\int_{-\infty}^{\tau_3}\mathrm{d}\tau_5 \\ &\times \mathcal{E}_2^*(\tau_3)\mathcal{E}_2(t)\mathcal{E}_\mathrm{p}(\tau_5)\mathcal{E}_\mathrm{p}^*(\tau_1)\mathrm{e}^{i\omega(t-\tau_3)-i\Delta(\tau_3-T)} \\ &\times F_{ii}(t-\tau_1,\,t-\tau_3,\,\tau_3-\tau_5) \end{aligned} \tag{132}$$

We can recast eqs 131 and 132 using frequency domain matter correlation functions

$$\begin{aligned} \tilde{S}^{(i)}_\mathrm{FSRS}(\omega,\,T;\,\Delta) &= \mathcal{I}\frac{2}{\hbar}\int_{-\infty}^{\infty}\frac{\mathrm{d}\omega_1}{2\pi}\frac{\mathrm{d}\omega_1'}{2\pi}\frac{\mathrm{d}\omega_2}{2\pi} \\ &\times \mathcal{E}_2^*(\omega_2)\mathcal{E}_2(\omega_2+\Delta+\omega_1'-\omega_1)\mathcal{E}_\mathrm{p}^*(\omega_1)\mathcal{E}_\mathrm{p}(\omega_1')\mathrm{e}^{i(\omega_1-\omega_1')T} \\ &\times F_i(\omega_1,\,\omega_1+\omega_2-\omega-\Delta,\,\omega_1') \end{aligned} \tag{133}$$

$$\begin{aligned} \tilde{S}^{(ii)}_\mathrm{FSRS}(\omega,\,T;\,\Delta) &= \mathcal{I}\frac{2}{\hbar}\int_{-\infty}^{\infty}\frac{\mathrm{d}\omega_1}{2\pi}\frac{\mathrm{d}\omega_1'}{2\pi}\frac{\mathrm{d}\omega_2}{2\pi} \\ &\times \mathcal{E}_2^*(\omega_2)\mathcal{E}_2(\omega_2+\Delta+\omega_1'-\omega_1)\mathcal{E}_\mathrm{p}^*(\omega_1)\mathcal{E}_\mathrm{p}(\omega_1')\mathrm{e}^{i(\omega_1-\omega_1')T} \\ &\times F_{ii}(\omega_1,\,\omega+\Delta-\omega_2+\omega_1',\,\omega_1') \end{aligned} \tag{134}$$

Assuming that pulse 2 is a narrow band (picosecond) and set $\mathcal{E}_2(t-T) = \mathcal{E}_2\mathrm{e}^{-i\omega_2(t-T)}$ the FSRS signal for the Raman shift $\Omega = \omega - \omega_2$ then reads

$$\begin{aligned} S_\mathrm{FSRS}(\Omega,\,T) &= \mathcal{I}\int_{-\infty}^{\infty}\frac{\mathrm{d}\Delta}{2\pi}\mathcal{E}_3^*(\Omega+\omega_2)\mathcal{E}_3(\Omega+\omega_2+\Delta) \\ &\times \tilde{S}_\mathrm{FSRS}(\Omega,\,T;\,\Delta) \end{aligned} \tag{135}$$

$$\begin{aligned} \tilde{S}^{(i)}_\mathrm{FSRS}(\Omega,\,T;\,\Delta) &= \frac{2}{\hbar}\int_{-\infty}^{\infty}\mathrm{d}t\int_{-\infty}^{t}\mathrm{d}\tau_1\int_{-\infty}^{t}\mathrm{d}\tau_3\int_{-\infty}^{\tau_3}\mathrm{d}\tau_5 \\ &\times |\mathcal{E}_2|^2\mathcal{E}_\mathrm{p}^*(\tau_5)\mathcal{E}_\mathrm{p}(\tau_1)\mathrm{e}^{i\Omega(t-\tau_3)-i\Delta(\tau_3-T)} \\ &\times F_i(\tau_3-\tau_5,\,t-\tau_3,\,t-\tau_1) \end{aligned} \tag{136}$$

$$\begin{aligned} \tilde{S}^{(ii)}_\mathrm{FSRS}(\Omega,\,T;\,\Delta) &= \frac{2}{\hbar}\int_{-\infty}^{\infty}\mathrm{d}t\int_{-\infty}^{t}\mathrm{d}\tau_1\int_{-\infty}^{t}\mathrm{d}\tau_3\int_{-\infty}^{\tau_3}\mathrm{d}\tau_5 \\ &\times |\mathcal{E}_2|^2\mathcal{E}_\mathrm{p}(\tau_5)\mathcal{E}_\mathrm{p}^*(\tau_1)\mathrm{e}^{i\Omega(t-\tau_3)-i\Delta(\tau_3-T)} \\ &\times F_{ii}(t-\tau_1,\,t-\tau_3,\,\tau_3-\tau_5) \end{aligned} \tag{137}$$

We can recast eqs 135−137 using frequency domain matter correlation functions and obtain eq 60.

TG-ISRS and TR-ISRS

We read the TG-ISRS signal off the diagrams in Figure 13b

$$\begin{aligned} \tilde{S}^{(i)}_\mathrm{TG-ISRS}(\Omega,\,T_1) &= \frac{2}{\hbar}\int_{-\infty}^{\infty}\mathrm{d}t\int_{-\infty}^{t}\mathrm{d}\tau_1\int_{-\infty}^{t}\mathrm{d}\tau_3\int_{-\infty}^{\tau_3}\mathrm{d}\tau_5 \\ &\times \mathcal{E}_\mathrm{p}^*(\tau_5)\mathcal{E}_\mathrm{p}(\tau_1)\mathcal{E}_2^*(\tau_3-T)\mathcal{E}_1(\tau_3-T)\mathrm{e}^{i\Omega(t-T_1)} \\ &\times F_i(\tau_3-\tau_5,\,t-\tau_3,\,t-\tau_1) \end{aligned} \tag{138}$$

$$\begin{aligned} \tilde{S}^{(ii)}_\mathrm{TG-ISRS}(\Omega,\,T_1) &= \frac{2}{\hbar}\int_{-\infty}^{\infty}\mathrm{d}t\int_{-\infty}^{t}\mathrm{d}\tau_1\int_{-\infty}^{t}\mathrm{d}\tau_3\int_{-\infty}^{\tau_3}\mathrm{d}\tau_5 \\ &\times \mathcal{E}_\mathrm{p}^*(\tau_1)\mathcal{E}_\mathrm{p}(\tau_5)\mathcal{E}_2^*(\tau_3-T)\mathcal{E}_1(\tau_3-T)\mathrm{e}^{i\Omega(t-T_1)} \\ &\times F_{ii}(t-\tau_1,\,t-\tau_3,\,\tau_3-\tau_5) \end{aligned} \tag{139}$$

One can alternatively express the signals in eqs 138 and 139 via the frequency domain correlation function of matter and obtain eq 63.

Similarly, we read TR-ISRS off the diagrams in Figure 14b

$$\begin{aligned} \tilde{S}^{(i)}_\mathrm{TR-ISRS}(\Omega,\,T_1) &= \frac{2}{\hbar}\int_{-\infty}^{\infty}\mathrm{d}t\int_{-\infty}^{t}\mathrm{d}\tau_1\int_{-\infty}^{t}\mathrm{d}\tau_3\int_{-\infty}^{\tau_3}\mathrm{d}\tau_5 \\ &\times \mathcal{E}_\mathrm{p}^*(\tau_5)\mathcal{E}_\mathrm{p}(\tau_1)|\mathcal{E}_2(\tau_3-T)|^2e^{i\Omega(t-T_1)} \\ &\times F_i(\tau_3-\tau_5,\,t-\tau_3,\,t-\tau_1) \end{aligned} \tag{140}$$

$$\begin{aligned} \tilde{S}^{(ii)}_\mathrm{TR-ISRS}(\Omega,\,T_1) &= \frac{2}{\hbar}\int_{-\infty}^{\infty}\mathrm{d}t\int_{-\infty}^{t}\mathrm{d}\tau_1\int_{-\infty}^{t}\mathrm{d}\tau_3\int_{-\infty}^{\tau_3}\mathrm{d}\tau_5 \\ &\times \mathcal{E}_\mathrm{p}^*(\tau_1)\mathcal{E}_\mathrm{p}(\tau_5)|\mathcal{E}_2(\tau_3-T)|^2e^{i\Omega(t-T_1)} \\ &\times F_{ii}(t-\tau_1,\,t-\tau_3,\,\tau_3-\tau_5) \end{aligned} \tag{141}$$

Similarly, one can recast eqs 140 and 141 in the frequency domain and obtain eq 65.

Stochastic Liouville Equation (SLE) Based Signals

Two-State Jump Model

The Liouville operator $\hat{\mathcal{L}}$ in SLE (30) is diagonal in the vibrational Liouville space and is thus given by four 2 × 2 diagonal blocks in spin space[535]

$$[\hat{\mathcal{L}}]_{\nu\nu's,\nu_1\nu_1's'} = \delta_{\nu\nu_1}\delta_{\nu'\nu_1'}[\hat{L}_S]_{s,s'} + \delta_{\nu\nu 1}\delta_{\nu'\nu_1'}\delta_{ss'}[\hat{\mathcal{L}}_S]_{\nu\nu's,\nu\nu's} \tag{142}$$

where $\hat{L}_S = -K$ describes the kinetics given by the rate equation

$$\frac{\mathrm{d}}{\mathrm{d}t}\rho_{aa}^{(s)}(t) = -\sum_{s'} K_{ss'}\rho_{aa}^{(s')}(t) \tag{143}$$

where $\rho_{aa}^{s}(t)$ is the population of the sth bath state. The solution of eq 143 is given by

$$\rho_{aa}^{(s)}(t) = \sum_{s'} U_{ss'} \exp[-K^{\mathrm{diag}}t]_{s's'}U_{s's}^{-1}\rho_{aa}^{(s)}(0) \tag{144}$$

where U is the transformation matrix and eigenvectors are organized as rows. This matrix satisfies left-eigen equation $\sum_p U_{sp}K_{ps'} = K_{s's'}^{\mathrm{diag}}U_{ss'}$ as the rate matrix K is not necessarily Hermitian. $\rho_{aa}^{s}(0)$ represents the population of the initial bath state.

The coherent part $\hat{\mathcal{L}}_S = -(i/\hbar)[H_S, ...]$, which describes the vibrational dynamics, vanishes for the $|aa\rangle\rangle$ and $|cc\rangle\rangle$ blocks, $[\hat{\mathcal{L}}_S]_{aa,aa} = [\hat{\mathcal{L}}_S]_{cc,cc} = 0$. The remaining blocks of $\hat{\mathcal{L}}_S$ read

$$[\hat{\mathcal{L}}_S]_{ac,ac} = i\begin{pmatrix} \omega_{ca}^{(1)} & 0 & ... & 0 \\ 0 & \omega_{ca}^{(2)} & ... & 0 \\ ... & ... & ... & ... \\ 0 & 0 & ... & \omega_{ca}^{(N)} \end{pmatrix} \tag{145}$$

The two Liouville space Green's functions are thus given by

$$\begin{aligned} \mathcal{G}_{aa,aa}(t) &= -\frac{i}{\hbar}\theta(t)\exp[[\hat{L}_S]t] \\ &= -\frac{i}{\hbar}\theta(t)\mathbf{U}\exp[[\hat{L}_S]^{\mathrm{diag}}t]\mathbf{U}^{-1} \end{aligned} \tag{146}$$

$$\begin{aligned} \mathcal{G}_{ac,ac}(t) &= -\frac{i}{\hbar}\theta(t)\exp[([\hat{L}_S] + [\hat{\mathcal{L}}_S]_{ac,ac})t] \\ &= -\frac{i}{\hbar}\theta(t)\mathbf{V}\exp[[\hat{\mathcal{L}}]_{ac,ac}^{\mathrm{diag}}t]\mathbf{V}^{-1} \end{aligned} \tag{147}$$

where $\mathbf{U}$ and $\mathbf{V}$ are transformation matrices, which diagonalize the matrices in the exponents. For two-state jump kinetics the expressions become 2 × 2 matrices

$$[\hat{L}_S] = \begin{pmatrix} -k_d & k_u \\ k_d & -k_u \end{pmatrix} \tag{148}$$

$\mathcal{L}_S$ reads

$$[\hat{\mathcal{L}}_S]_{ac,ac} = -i\begin{pmatrix} \omega_{ac} + \delta & 0 \\ 0 & \omega_{ac} - \delta \end{pmatrix} \tag{149}$$

where δ describes the magnitude of the jump whereas ω_{ac} is the vibrational frequency unperturbed by the bath. The two Liouville space Green's functions $\mathcal{G}(t) = -(i/\hbar)\theta(t)\mathrm{e}^{\hat{\mathcal{L}}t}$ relevant to the Raman signal as the solution of eq 30 are given by[535]

$$\mathcal{G}_{aa,aa}(t) = (-i/\hbar)\theta(t)\left[\hat{1} + \frac{1 - \mathrm{e}^{-(k_u+k_d)t}}{k_d + k_u}\begin{pmatrix} -k_d & k_u \\ k_d & -k_u \end{pmatrix}\right] \tag{150}$$

$$\begin{aligned} \mathcal{G}_{ac,ac}(t) &= (-i/\hbar)\theta(t) \\ &\times \left[\left(\frac{\eta_2}{\eta_2 - \eta_1}\hat{1} - \frac{1}{\eta_2 - \eta_1}\hat{\mathcal{L}}_{ac,\mathrm{ac}}\right)\mathrm{e}^{\eta_1 t} \right. \\ &\left. + \left(\frac{\eta_1}{\eta_1 - \eta_2}\hat{1} - \frac{1}{\eta_1 - \eta_2}\hat{\mathcal{L}}_{ac,ac}\right)\mathrm{e}^{\eta_2 t}\right] \end{aligned} \tag{151}$$

where $\hat{1}$ is unit 2 × 2 matrix and

$$\begin{aligned} \eta_{1,2} &= -\frac{k_d + k_u}{2} - i\omega_{ac} \\ &\pm \sqrt{\frac{(k_d + k_u)^2}{4} - \delta^2 + i\delta(k_d - k_u)} \end{aligned}$$

FSRS for General Multistage Jump and Arbitrary Temperature

The time domain FSRS signal on the Stokes side ($\omega < \omega_0$) is given by

$$\begin{aligned} &S_{\mathrm{FSRS}}(\omega, T) \\ &= \mathcal{I}\int_{-\infty}^{\infty}\frac{\mathrm{d}\Delta}{2\pi}\mathcal{E}_{\mathrm{p}}^{*}(\omega)\mathcal{E}_{\mathrm{p}}(\omega + \Delta)\tilde{S}_{\mathrm{FSRS}}^{(i)}(\omega, T; \Delta) \end{aligned} \tag{152}$$

where $\tilde{S}^{i}{}_{\mathrm{FSRS}}(\omega,T;\Delta)$ can be recast in Liouville space as follows

$$\begin{aligned} \tilde{S}_{\mathrm{FSRS}}^{(i)}(\omega, T; \Delta) = &\frac{2}{\hbar}\int_{-\infty}^{\infty}\mathrm{d}t\int_{-\infty}^{t}\mathrm{d}\tau_3|\mathcal{E}_1|^2|\mathcal{E}_a|^2\mathrm{e}^{-i\Delta(\tau_3 - T)} \\ &\times e^{i(\omega-\omega_1)(t-\tau_3)}\mathcal{F}(t - \tau_3, \tau_3) \end{aligned} \tag{153}$$

by using the Green's functions in eqs 146 and 147. The matter correlation function $\mathcal{F}(t_1, t_2)$ is given by

$$\begin{aligned} \mathcal{F}(t_1, t_2) &= -\frac{i}{\hbar}\sum_{a,c}\alpha_{ac}^2|V_{ag}|^2\langle\langle I|\mathcal{G}_{ac,ac}(t_1)\mathcal{G}_{aa,aa}(t_2)|\rho_0\rangle\rangle_S \\ &= -\left(\frac{i}{\hbar}\right)^3\sum_{a,c}\alpha_{ac}^2|V_{ag}|^2\theta(t_1)\theta(t_2)e^{-\gamma_a(t_1+2t_2)} \\ &\times (1, 1, ..., 1)\mathbf{V}\exp[[\hat{\mathcal{L}}]_{ac,\mathrm{ac}}^{\mathrm{diag}}t_1]\mathbf{V}^{-1} \\ &\times \mathbf{U}\exp[[\hat{L}_S]^{\mathrm{diag}}t_2]\mathbf{U}^{-1}\begin{pmatrix} 1 \\ 0 \\ ... \\ 0 \end{pmatrix} \end{aligned} \tag{154}$$

Here, the initial state is the direct product

$$|\rho_0\rangle\rangle_S = |aa\rangle\rangle\begin{pmatrix} 1 \\ 0 \\ ... \\ 0 \end{pmatrix} \tag{155}$$

and we traced over the final state $\langle\langle\mathbf{1}| = (1,1,...,1)$ Tr where Tr $= \langle\langle aa| + \langle\langle cc|$. Vibrational dephasing terms have been added; $\mathrm{e}^{-\gamma_a t}$ is added to $\mathcal{G}_{ac,ac}$ and $\mathrm{e}^{-2\gamma_a t}$ to $\mathcal{G}_{aa,aa}$. The effect of the inhomogeneous broadening can be included on top of the existent model. It can be done by separating the dynamics of the collective coordinate into two components. The first one (nonperturbative) is to account for the nonadiabatic frequency change. The correction to that motion can be perturbatively expanded using cumulant expansion. We incorporated this level of theory in one of our earlier papers.[76]

Closed Expressions for the Raman Signals in the SML

The FR-SPRS signal in the SML is given by

$$S^{(\mathrm{SML})}_{\mathrm{FR-SPRS}}(\omega, T) = \frac{\mathcal{D}^2(\omega)}{\hbar^2}|\mathcal{E}_{\mathrm{p}}|^2 \sum_{a,c} \alpha_{ac}^2 |\mu_{ag}|^2 \mathrm{e}^{-2\gamma_a T}$$
$$\times (|\mathcal{E}_2(\omega - \omega_-)|^2[1 - \mathrm{e}^{-kT}] + |\mathcal{E}_2(\omega - \omega_+)|^{2\mathrm{e}^{-kT}}) \tag{156}$$

The FSRS signal for the TSJ model in the SML reads

$$S^{(\mathrm{SML})}_{\mathrm{FSRS}}(\Omega, T) = \frac{1}{\hbar^4}|\mathcal{E}_{\mathrm{p}}|^2|\mathcal{E}_2|^2|\mathcal{E}_3(\Omega + \omega_2)|^2 \sum_{a,c} \alpha_{ac}^2|\mu_{ag}|^2$$
$$\times \mathrm{e}^{-2\gamma_a T}\left(\frac{\gamma_a(1 - \mathrm{e}^{-kT})}{(\Omega - \omega_-)^2 + \gamma_a^2} + \frac{(\gamma_a + k)\mathrm{e}^{-kT}}{(\Omega - \omega_+)^2 + (\gamma_a + k)^2} + \frac{k}{2\delta}\mathrm{e}^{-kT}\left[\frac{\Omega - \omega_-}{(\Omega - \omega_-)^2 + \gamma_a^2} - \frac{\Omega - \omega_+}{(\Omega - \omega_+)^2 + (\gamma_a + k)^2}\right]\right) - [\omega_\pm \leftrightarrow -\omega_\mp] \tag{157}$$

where $\Omega = \omega - \omega_2$ and the last line corresponds to the signal above with the exchanged up and down states which accounts for the anti-Stokes Raman transitions (e.g., Stokes transition $\Omega - \omega_+$ becomes anti-Stokes $\Omega + \omega_-$, etc.).

The TG-ISRS signal in the SML yields

$$S^{(\mathrm{SML})}_{\mathrm{TG-ISRS}}(\Omega, T) = \frac{1}{\hbar^4}|\mathcal{E}_{\mathrm{p}}|^2 \sum_{a,c} \alpha_{ac}^2|\mu_{ag}|^2$$
$$\times \int_{-\infty}^{\infty} \frac{\mathrm{d}\omega'}{2\pi}\mathcal{E}_{\mathrm{s}}(\omega')\mathcal{E}_3(\omega' - \Omega)$$
$$\times \int_{-\infty}^{\infty} \frac{\mathrm{d}\omega_2}{2\pi}\mathcal{E}_2(\omega_2)\mathcal{E}_1(\omega_2 + \Omega)$$
$$\times \mathrm{e}^{-2\gamma_a T}\left(\frac{\gamma_a(1 - \mathrm{e}^{-kT})}{(\Omega - \omega_-)^2 + \gamma_a^2} + \frac{(\gamma_a + k)\mathrm{e}^{-kT}}{(\Omega - \omega_+)^2 + (\gamma_a + k)^2} + \frac{k}{2\delta}\mathrm{e}^{-kT}\left[\frac{\Omega - \omega_-}{(\Omega - \omega_-)^2 + \gamma_a^2} - \frac{\Omega - \omega_+}{(\Omega - \omega_+)^2 + (\gamma_a + k)^2}\right]\right) - [\omega_\pm \leftrightarrow -\omega_\mp] \tag{158}$$

The TR-ISRS is given by eq 158 by simply replacing $\mathcal{E}_{\mathrm{s}} \to \mathcal{E}_3$ and $\mathcal{E}_1 \to \mathcal{E}_2$.

ASSOCIATED CONTENT

Special Issue Paper

This paper is an additional review for *Chem. Rev.* **2017**, *117*, issue 16, "Ultrafast Processes in Chemistry".

AUTHOR INFORMATION

Corresponding Authors

*E-mail: mkowalew@uci.edu.
*E-mail: fingerhut@mbi-berlin.de.
*E-mail: dorfmank@lps.ecnu.edu.cn.
*E-mail: smukamel@uci.edu.

ORCID

Markus Kowalewski: 0000-0002-2288-2548
Shaul Mukamel: 0000-0002-6015-3135

Author Contributions

‡M.K. and B.P.F.: These authors contributed equally to this manuscript.

Notes

The authors declare no competing financial interest.

Biographies

Markus Kowalewski received his Master's degree in Chemistry from the Ludwig-Maximilians-University (LMU), Munich, in 2007. During his Master's and Ph.D. studies, he was working in the field of cold molecules, their quantum dynamical treatment, and on optimal control theory. In 2012 he finished his Ph.D. thesis in theoretical chemistry at the LMU under the supervision of Prof. Dr. Regina de Vivie-Riedle. For this thesis "Quantum Dynamics of Isolated Molecular Systems" he received an award from the Dr. Klaus Römer Foundation. He then took a postdoctoral position at the Centre of Interdisciplinary Mathematics (CIM) of the University of Uppsala, where he worked on numerical methods for quantum dynamics. In 2014 he joined Shaul Mukamel's group at the University of California, Irvine (UCI) to work on novel spectroscopic methods for the identification of conical intersections and later launched theoretical research on molecules in optical cavities. He was awarded a Feodor Lynen Research Fellowship of the Alexander von Humboldt Foundation to conduct his research in Irvine.

Benjamin P. Fingerhut, born in Germany, studied chemistry at the LMU, Munich, Germany, where he received his Ph.D. in Theoretical Physical Chemistry under the supervision of Prof. Dr. Regina de Vivie-Riedle in 2011. He joined the group of Prof. Shaul Mukamel at University of California, Irvine (UCI) as a postdoctoral fellow in September 2011, supported by a Feodor Lynen Research Fellowship of the Alexander von Humboldt Foundation. In 2014 he moved to the Max Born Institute for Nonlinear Optics and Short Pulse Spectroscopy (MBI), Berlin, Germany, where he is currently heading the junior research group Biomolecular Dynamics, supported by an Emmy Noether Early Career Grant of the German Research Foundation (DFG). He is a recipient of the 2016 Robin Hochstrasser Young Investigator Award. His research involves the development of state of the art spectroscopic simulation techniques and their application to the real-time determination of ultrafast structural dynamics of molecular and biomolecular systems. The group combines analytical and computational approaches for novel simulation protocols suited to investigate excited state nonadiabatic dynamics as well as vibrational dynamics of spacio-selective probes like phosphate groups. A major topic is fluctuation-induced decoherence dynamics in aqueous and biological environments.

Konstantin E. Dorfman was born in Russia. He completed his B.S. degree in Physics from Nizhny Novgorod State University, Russia, in 2006. In 2009 he completed his Ph.D. degree at Texas A&M University, where he investigated many-body fluctuations of Bose−Einstein Condensate. From 2010 to 2012 as a joint postdoctoral fellow at Princeton University and Texas A&M University he investigated fundamental light−matter interactions in classical/quantum optical devices, quantum heat engines, and photosynthetic light harvesting. From 2012 to 2015 he was a postdoctoral research scholar at the University of California, Irvine, where he investigated multidimensional nonlinear optical spectroscopy that utilizes quantum states of light, light range from THz to X-ray. From 2016 to 2017 as a staff scientist in Singapore Agency for Science, Technology and Research (AastSTAR) he worked on various aspecbiots of X-ray photonics. He is now a professor of physics at State Key Laboratory of Precision Spectroscopy, East China Normal University, Shanghai. His scientific interests include atomic, molecular, optical, and chemical physics, energy and charge transport processes, quantum optics and electronics, X-ray optics, relativistic and Terahertz physics, statistical mechanics, many-body theory, quantum photovoltaics, and semiconductor physics.

Kochise Bennett, born and raised in Indiana, completed his B.S. degree in Physics from UCLA in 2009. In 2016, under the guidance of Professor Shaul Mukamel, he completed his M.S. degree in Physics with concentration in Chemical and Materials Physics from UC Irvine. His masters thesis “Effects of Electronic Coherence in Ultrafast Spectroscopy” discusses transient Raman and photoelectron spectroscopies and how they may be used to observe and track nonadiabatic molecular dynamics through the associated, internally generated electronic coherences. Under the advisement of Professor Shaul Mukamel, he completed his Ph.D. degree in Physics with concentration in Chemical and Materials Physics from UC Irvine in 2017. His doctoral thesis “Quantum-Field Effects in Ultrafast Nonlinear X-ray and Optical Spectroscopy of Molecules” analyzed light scattering and cascading, a many-body effect in hyper-Raman and *n*-wave mixing experiments, from a quantum-field perspective. This work also discussed modifying chemical reactivity using optical cavities and presented a series of techniques that can be deployed to simulate any parameter regime, from weak to ultrastrong coupling. Since graduating, he has worked as a postdoctoral scholar for Professor Shaul Mukamel, studying single-molecule diffraction and ghost imaging.

Shaul Mukamel is a Distinguished Professor of Chemistry and of Physics and Astronomy at UC Irvine and a member of the National Academy of Science. He received his Ph.D. degree from Tel Aviv University and served on the faculty at Rice University, the Weizmann Institute, and the University of Rochester. His research focuses on the design of ultrafast multidimensional coherent optical spectroscopies in molecules which span from the infrared to the X-ray spectral regimes and are used for probing and controlling electronic and vibrational molecular dynamics in the condensed phase. His theoretical and computational work shows how to employ these techniques to study energy and electron transfer in photosynthetic complexes, excitons in semiconductor nanostructures, and the secondary structure of proteins. His recent effort includes attosecond X-ray spectroscopy, utilizing the quantum nature of optical fields and photon entanglement to achieve temporal and spectral resolutions not possible with classical light, and nonlinear spectroscopy of nonadiabatic dynamics at concial intersections of molecules dressed by photons in microcavities. He is the author of over 900 publications and the textbook *Principles of Nonlinear Optical Spectroscopy* (1995), which paved the way for the field of multidimensional spectroscopy. His recent awards include the Ahmed Zewail ACS Award in Ultrafast Science and Technology, the Coblentz Society ABB Sponsored Bomem-Michelson Award, the William F. Meggers Award of OSA, and senior Humboldt and FRIAS fellowships.

ACKNOWLEDGMENTS

The support of the National Science Foundation (grant CHE-1663822) is gratefully acknowledged as well as support of the Chemical Sciences, Geosciences, and Biosciences division, Office of Basic Energy Sciences, Office of Science, U.S. Department of Energy through award No. DE-FG02-04ER15571. K.B. and computational resources were supported by the DOE grant. K.D. gratefully acknowledges support from the Zijiang Endowed Young Scholar Fund. M.K. and B.P.F. gratefully acknowledge support from the Alexander von Humboldt foundation through the Feodor Lynen program. B.P.F. acknowledges support through the German Research Foundation (DFG) within the Emmy Noether Programme (Grant No. FI 2034/1-1). We wish to thank Professor Wolfgang Domcke for useful discussions.

ACRONYMS

2DES	two-dimensional electronic spectroscopy
2DEV	two-dimensional electronic−vibrational spectroscopy
2DVE	two-dimensional vibrational-electronic spectroscopy
2DUV	two-dimensional ultraviolet spectroscopy
2D-UVvis	two-dimensional UV−vis
AIMS	ab initio multiple spawning
ASRS	attosecond stimulated Raman spectroscopy
CARS	coherent anti-Stokes Raman spectroscopy
CASSCF	complete active space self-consistent field
Chl	chlorophyll
CoIn	conical intersection
CW	continuous wave
DNA	deoxyribonucleic acid
DPM	diphenylmethane
FEL	free electron laser
FC	Franck−Condon
FDIR	frequency dispersed infrared detection
FGR	Fermi golden rule
FR-SPRS	frequency-resolved spontaneous Raman signal
FSRS	femtosecond stimulated Raman spectroscopy
FSSH	fewest switching surface hopping
fwhm	full width at half-maximum
FWM	four wave mixing
HHG	high harmonic generation
IR	infrared
IFSRS	interferometric femtosecond stimulated Raman spectroscopy
LiCi	light-induced conical intersection
MCTDH	multiconfiguration time-dependent Hartree
NEXAFS	near-edge X-ray absorption fine structure
PDC	parametric downconversion
PES	potential energy surface
PS	photoelectron spectroscopy
PM-Fl	phase-modulated 2D fluorescence
QF-NEP	quantum-classical feedback nonlinear exciton propagation
RNA	ribonucleic acid
SLE	stochastic Liouville equation
SML	slow modulation limit
SOS	sum over states
SRS	stimulated Raman spectroscopy
TALH	transient absorption linear hybrid detection
TG-ISRS	transient grating impulsive stimulated Raman spectroscopy
TR-ISRS	time-resolved impulsive stimulated Raman spectroscopy
T-2DIR	transient two-dimensional infrared spectroscopy
TA	transient absorption
het-TG	heterodyne transient grating
TRPES	time-resolved photoelectron spectroscopy

TRUECARS	transient redistribution of ultrafast electronic coherences in attosecond Raman signals
TSJ	two-state jump
TL	transform limit
UV/IR	UV−vis pump IR probe
UV	ultraviolet
VIS	visual
VUV	vacuum ultraviolet
XUV	extreme ultraviolet

REFERENCES

(1) Hund, F. Zur Deutung der Molekelspektren. I. *Eur. Phys. J. A* **1927**, *40*, 742−764.

(2) von Neumann, J.; Wigner, E. Über Merkwürdige Diskrete Eigenwerte. *Phys. Z.* **1929**, *30*, 467.

(3) Teller, E. The Crossing of Potential Surfaces. *J. Phys. Chem.* **1937**, *41*, 109−116.

(4) Robb, M. A. In This Molecule There Must Be a Conical Intersection. *Adv. Phys. Org. Chem.* **2014**, *48*, 189−228.

(5) Domcke, W.; Yarkony, D. R.; Köppel, H. *Conical Intersections*; World Scientific: Singapore, 2011; Vol. *17*.

(6) Born, M.; Oppenheimer, R. Zur Quantentheorie der Molekeln. *Ann. Phys.* **1927**, *389*, 457−484.

(7) Hoffmann, R.; Woodward, R. B. Selection Rules For Concerted Cycloaddition Reactions. *J. Am. Chem. Soc.* **1965**, *87*, 2046−2048.

(8) Pullen, S.; Walker, L. A.; Donovan, B.; Sension, R. J. Femtosecond Transient Absorption Study of the Ring-Opening Reaction of 1,3-Cyclohexadiene. *Chem. Phys. Lett.* **1995**, *242*, 415−420.

(9) Lochbrunner, S.; Fuss, W.; Schmid, W. E.; Kompa, K.-L. Electronic Relaxation and Ground-State Dynamics of 1,3-Cyclohexadiene and cis-Hexatriene in Ethanol. *J. Phys. Chem. A* **1998**, *102*, 9334−9344.

(10) Geppert, D.; Seyfarth, L.; de Vivie-Riedle, R. Laser Control Schemes For Molecular Switches. *Appl. Phys. B: Lasers Opt.* **2004**, *79*, 987−992.

(11) Kim, J.; Tao, H.; White, J. L.; Petrović, V. S.; Martinez, T. J.; Bucksbaum, P. H. Control of 1,3-Cyclohexadiene Photoisomerization Using Light-induced Conical Intersections. *J. Phys. Chem. A* **2012**, *116*, 2758−2763.

(12) Tamura, H.; Nanbu, S.; Ishida, T.; Nakamura, H. ab initio Nonadiabatic Quantum Dynamics of Cyclohexadiene/Hexatriene Ultrafast Photoisomerization. *J. Chem. Phys.* **2006**, *124*, 084313.

(13) Deb, S.; Weber, P. M. The Ultrafast Pathway of Photon-Induced Electrocyclic Ring-Opening Reactions: The Case of 1,3-Cyclohexadiene. *Annu. Rev. Phys. Chem.* **2011**, *62*, 19−39.

(14) Minitti, M. P.; Budarz, J. M.; Kirrander, A.; Robinson, J. S.; Ratner, D.; Lane, T. J.; Zhu, D.; Glownia, J. M.; Kozina, M.; Lemke, H. T.; et al. Imaging Molecular Motion: Femtosecond X-Ray Scattering of an Electrocyclic Chemical Reaction. *Phys. Rev. Lett.* **2015**, *114*, 255501.

(15) Attar, A. R.; Bhattacherjee, A.; Pemmaraju, C. D.; Schnorr, K.; Closser, K. D.; Prendergast, D.; Leone, S. R. Femtosecond X-Ray Spectroscopy of an Electrocyclic Ring-Opening Reaction. *Science* **2017**, *356*, 54−59.

(16) *Molecular Switches*; Feringa, B. L., Browne, W. R., Eds.; Wiley-VCH Verlag GmbH: Weinheim, FRG, 2001.

(17) Tapavicza, E.; Meyer, A. M.; Furche, F. Unravelling the Details of Vitamin D Photosynthesis by Non-adiabatic Molecular Dynamics Simulations. *Phys. Chem. Chem. Phys.* **2011**, *13*, 20986−20998.

(18) Polli, D.; Altoe, P.; Weingart, O.; Spillane, K. M.; Manzoni, C.; Brida, D.; Tomasello, G.; Orlandi, G.; Kukura, P.; Mathies, R. A.; et al. Conical Intersection Dynamics of the Primary Photoisomerization Event in Vision. *Nature* **2010**, *467*, 440−443.

(19) Schreier, W. J.; Gilch, P.; Zinth, W. Early Events of DNA Photodamage. *Annu. Rev. Phys. Chem.* **2015**, *66*, 497−519.

(20) Barlev, A.; Sen, D. Catalytic DNAs That Harness Violet Light To Repair Thymine Dimers in a DNA Substrate. *J. Am. Chem. Soc.* **2013**, *135*, 2596−2603.

(21) Liu, Z.; Tan, C.; Guo, X.; Kao, Y.-T.; Li, J.; Wang, L.; Sancar, A.; Zhong, D. Dynamics and Mechanism of Cyclobutane Pyrimidine Dimer Repair by DNA Photolyase. *Proc. Natl. Acad. Sci. U. S. A.* **2011**, *108*, 14831−14836.

(22) Markwick, P. R. L.; Doltsinis, N. L. Ultrafast Repair of Irradiated DNA: Nonadiabatic ab initio Simulations of the Guanine-Cytosine Photocycle. *J. Chem. Phys.* **2007**, *126*, 175102.

(23) Zewail, A. H. Laser Femtochemistry. *Science* **1988**, *242*, 1645−1653.

(24) Rose, T. S.; Rosker, M. J.; Zewail, A. H. Femtosecond Real-Time Probing of Reactions. IV. the Reactions of Alkali Halides. *J. Chem. Phys.* **1989**, *91*, 7415−7436.

(25) Zewail, A. H. Femtochemistry: Atomic-Scale Dynamics of the Chemical Bond. *J. Phys. Chem. A* **2000**, *104*, 5660−5694.

(26) Engel, V.; Metiu, H. A Quantum Mechanical Study of Predissociation Dynamics of NaI Excited by a Femtosecond Laser Pulse. *J. Chem. Phys.* **1989**, *90*, 6116−6128.

(27) Engel, V.; Metiu, H. TwoPhoton Excitation of NaI with Femtosecond Laser Pulses. *J. Chem. Phys.* **1989**, *91*, 1596−1602.

(28) Landau, L. Zur Theorie Der Energieübertragung. II. *Phys. Z. Sowjetunion* **1932**, *2*, 46−51.

(29) Zener, C. Non-adiabatic Crossing of Energy Levels. *Proc. R. Soc. London, Ser. A* **1932**, *137*, 696−702.

(30) Krausz, F.; Ivanov, M. Attosecond Physics. *Rev. Mod. Phys.* **2009**, *81*, 163−234.

(31) Popmintchev, T.; Chen, M.-C.; Arpin, P.; Murnane, M. M.; Kapteyn, H. C. The Attosecond Nonlinear Optics of Bright Coherent X-Ray Generation. *Nat. Photonics* **2010**, *4*, 822−832.

(32) Zhao, K.; Zhang, Q.; Chini, M.; Wu, Y.; Wang, X.; Chang, Z. Tailoring a 67 Attosecond Pulse Through Advantageous Phase-Mismatch. *Opt. Lett.* **2012**, *37*, 3891−3893.

(33) Teichmann, S. M.; Silva, F.; Cousin, S. L.; Hemmer, M.; Biegert, J. 0.5-keV Soft X-Ray Attosecond Continua. *Nat. Commun.* **2016**, *7*, 11493.

(34) Harmand, M.; Coffee, R.; Bionta, M. R.; Chollet, M.; French, D.; Zhu, D.; Fritz, D. M.; Lemke, H. T.; Medvedev, N.; Ziaja, B.; et al. Achieving Few-Femtosecond Time-Sorting at Hard X-Ray Free-Electron Lasers. *Nat. Photonics* **2013**, *7*, 215−218.

(35) Ding, Y.; Huang, Z.; Ratner, D.; Bucksbaum, P.; Merdji, H. Generation of Attosecond X-Ray Pulses with a Multicycle Two-Color Enhanced Self-Amplified Spontaneous Emission Scheme. *Phys. Rev. Spec. Top.–Accel. Beams* **2009**, *12*, 060703.

(36) Helml, W.; Maier, A. R.; Schweinberger, W.; Grguraš, I.; Radcliffe, P.; Doumy, G.; Roedig, C.; Gagnon, J.; Messerschmidt, M.; Schorb, S.; et al. Measuring the Temporal Structure of Few-Femtosecond Free-Electron Laser X-Ray Pulses Directly in the Time Domain. *Nat. Photonics* **2014**, *8*, 950−957.

(37) Worner, H. J.; Bertrand, J. B.; Fabre, B.; Higuet, J.; Ruf, H.; Dubrouil, A.; Patchkovskii, S.; Spanner, M.; Mairesse, Y.; Blanchet, V.; et al. Conical Intersection Dynamics in NO2 Probed by Homodyne High-Harmonic Spectroscopy. *Science* **2011**, *334*, 208−212.

(38) Patchkovskii, S.; Schuurman, M. S. Short-Time Dynamics at a Conical Intersection in High-Harmonic Spectroscopy. *J. Phys. Chem. A* **2014**, *118*, 12069−12079.

(39) Torres, R.; Siegel, T.; Brugnera, L.; Procino, I.; Underwood, J. G.; Altucci, C.; Velotta, R.; Springate, E.; Froud, C.; Turcu, I. C. E.; et al. Extension of High Harmonic Spectroscopy in Molecules by a 1300 nm Laser Field. *Opt. Express* **2010**, *18*, 3174−3180.

(40) Zaïr, A.; Siegel, T.; Sukiasyan, S.; Risoud, F.; Brugnera, L.; Hutchison, C.; Diveki, Z.; Auguste, T.; Tisch, J. W. G.; Salières, P.; et al. Molecular Internal Dynamics Studied by Quantum Path Interferences in High Order Harmonic Generation. *Chem. Phys.* **2013**, *414*, 184−191.

(41) Carpenter, B. K.; Harvey, J. N.; Orr-Ewing, A. J. The Study of Reactive Intermediates in Condensed Phases. *J. Am. Chem. Soc.* **2016**, *138*, 4695−4705.

(42) Domcke, W.; Yarkony, D. R. Role of Conical Intersections in Molecular Spectroscopy and Photoinduced Chemical Dynamics. *Annu. Rev. Phys. Chem.* **2012**, *63*, 325−352.

(43) Sølling, T. I.; Kuhlman, T. S.; Stephansen, A. B.; Klein, L. B.; Møller, K. B. The Non-Ergodic Nature of Internal Conversion. *ChemPhysChem* **2014**, *15*, 249−259.

(44) Domcke, W.; Stock, G. Theory of Ultrafast Nonadiabatic Excited-State Processes and Their Spectroscopic Detection in Real Time. *Adv. Chem. Phys.* **1997**, *100*, 1−169.

(45) Szabo, A.; Ostlund, N. S. *Modern Quantum Chemistry*; Dover Publications: New York, 1996.

(46) Marques, M.; Maitra, N.; Nogueira, F.; Gross, E.; Rubio, A. *Fundamentals of Time-Dependent Density Functional Theory*; Lecture Notes in Physics; Springer: Berlin, Heidelberg, 2012.

(47) Hofmann, A.; de Vivie-Riedle, R. Adiabatic Approach For Ultrafast Quantum Dynamics Mediated by Simultaneously Active Conical Intersections. *Chem. Phys. Lett.* **2001**, *346*, 299−304.

(48) Kowalewski, M.; Bennett, K.; Mukamel, S. Non-Adiabatic Dynamics of Molecules in Optical Cavities. *J. Chem. Phys.* **2016**, *144*, 054309.

(49) Mead, C. A.; Truhlar, D. G. Conditions for the Definition of a Strictly Diabatic Electronic Basis for Molecular Systems. *J. Chem. Phys.* **1982**, *77*, 6090−6098.

(50) Köppel, H.; Domcke, W.; Cederbaum, L. S. Multimode Molecular Dynamics Beyond the Born-Oppenheimer Approximation. *Adv. Chem. Phys.* **1984**, *57*, 59−246.

(51) Simah, D.; Hartke, B.; Werner, H.-J. Photodissociation Dynamics of H_2S on New Coupled Ab Initio Potential Energy Surfaces. *J. Chem. Phys.* **1999**, *111*, 4523−4534.

(52) Li, S. L.; Truhlar, D. G.; Schmidt, M. W.; Gordon, M. S. Model Space Diabatization for Quantum Photochemistry. *J. Chem. Phys.* **2015**, *142*, 064106.

(53) Cave, R. J.; Stanton, J. F. A Simple Quasi-Diabatization Scheme Suitable for Spectroscopic Problems Based on One-Electron Properties of Interacting States. *J. Chem. Phys.* **2016**, *144*, 054110.

(54) An, H.; Baeck, K. K. A Practical and Efficient Diabatization That Combines Lorentz and Laplace Functions to Approximate Non-adiabatic Coupling Terms. *J. Chem. Phys.* **2015**, *143*, 194102.

(55) Hoyer, C. E.; Parker, K.; Gagliardi, L.; Truhlar, D. G. The DQ and DQ Electronic Structure Diabatization Methods: Validation for General Applications. *J. Chem. Phys.* **2016**, *144*, 194101.

(56) Tully, J. C. Molecular Dynamics with Electronic Transitions. *J. Chem. Phys.* **1990**, *93*, 1061.

(57) Hammes-Schiffer, S.; Tully, J. C. Proton Transfer in Solution: Molecular Dynamics with Quantum Transitions. *J. Chem. Phys.* **1994**, *101*, 4657−4667.

(58) Malhado, J. P.; Bearpark, M.; Hynes, J. Non-Adiabatic Dynamics Close To Conical Intersections and the Surface Hopping Perspective. *Front. Chem.* **2014**, *2*, 97.

(59) Subotnik, J. E.; Jain, A.; Landry, B.; Petit, A.; Ouyang, W.; Bellonzi, N. Understanding the Surface Hopping View of Electronic Transitions and Decoherence. *Annu. Rev. Phys. Chem.* **2016**, *67*, 387−417.

(60) Martens, C. C. Surface Hopping by Consensus. *J. Phys. Chem. Lett.* **2016**, *7*, 2610−2615.

(61) Ben-Nun, M.; Quenneville, J.; Martínez, T. J. ab initio Multiple Spawning: Photochemistry From First Principles Quantum Molecular Dynamics. *J. Phys. Chem. A* **2000**, *104*, 5161−5175.

(62) Thallmair, S.; Roos, M. K.; de Vivie-Riedle, R. Design of Specially Adapted Reactive Coordinates To Economically Compute Potential and Kinetic Energy Operators Including Geometry Relaxation. *J. Chem. Phys.* **2016**, *144*, 234104.

(63) Kowalewski, M.; Mikosch, J.; Wester, R.; de Vivie-Riedle, R. Nucleophilic Substitution Dynamics: Comparing Wave Packet Calculations with Experiment. *J. Phys. Chem. A* **2014**, *118*, 4661−4669.

(64) Tannor, D. J. *Introduction To Quantum Mechanics: a Time-Dependent Perspective*; University Science Books: United States, 2006.

(65) Marquardt, R.; Quack, M. In *Handbook of High-Resolution Spectroscopy*; Quack, M., Merkt, F., Eds.; John Wiley & Sons, Ltd.: New York, 2011; pp 511.

(66) Meyer, H.-D. Studying Molecular Quantum Dynamics with the Multiconfiguration Time-Dependent Hartree Method. *WIREs Comput. Mol. Sci.* **2012**, *2*, 351−374.

(67) Biggs, J. D.; Zhang, Y.; Healion, D.; Mukamel, S. Two-Dimensional Stimulated Resonance Raman Spectroscopy of Molecules with Broadband X-Ray Pulses. *J. Chem. Phys.* **2012**, *136*, 174117.

(68) Mukamel, S.; Healion, D.; Zhang, Y.; Biggs, J. D. Multidimensional Attosecond Resonant X-Ray Spectroscopy of Molecules: Lessons From the Optical Regime. *Annu. Rev. Phys. Chem.* **2013**, *64*, 101.

(69) Zhang, Y.; Biggs, J. D.; Hua, W.; Dorfman, K. E.; Mukamel, S. Three-Dimensional Attosecond Resonant Stimulated X-Ray Raman Spectroscopy of Electronic Excitations in Core-Ionized Glycine. *Phys. Chem. Chem. Phys.* **2014**, *16*, 24323−24331.

(70) Gelin, M. F.; Egorova, D.; Domcke, W. Efficient Calculation of Time- and Frequency-Resolved Four-Wave-Mixing Signals. *Acc. Chem. Res.* **2009**, *42*, 1290−1298.

(71) Rao, B. J.; Gelin, M. F.; Domcke, W. Resonant Femtosecond Stimulated Raman Spectra: Theory and Simulations. *J. Phys. Chem. A* **2016**, *120*, 3286−3295.

(72) Krčmář, J.; Gelin, M. F.; Egorova, D.; Domcke, W. Signatures of Conical Intersections in Two-Dimensional Electronic Spectra. *J. Phys. B: At., Mol. Opt. Phys.* **2014**, *47*, 124019.

(73) Krčmář, J.; Gelin, M. F.; Domcke, W. Simulation of Femtosecond Two-Dimensional Electronic Spectra of Conical Intersections. *J. Chem. Phys.* **2015**, *143*, 074308.

(74) Sala, M.; Egorova, D. Two-Dimensional Photon-Echo Spectroscopy at a Conical Intersection: a Two-Mode Pyrazine Model with Dissipation. *Chem. Phys.* **2016**, *481*, 206−217.

(75) Dorfman, K. E.; Bennett, K.; Mukamel, S. Detecting Electronic Coherence by Multidimensional Broadband Stimulated X-Ray Raman Signals. *Phys. Rev. A: At., Mol., Opt. Phys.* **2015**, *92*, 023826.

(76) Dorfman, K. E.; Fingerhut, B. P.; Mukamel, S. Broadband Infrared and Raman Probes of Excited-State Vibrational Molecular Dynamics: Simulation Protocols Based on Loop Diagrams. *Phys. Chem. Chem. Phys.* **2013**, *15*, 12348−12359.

(77) Stolz, H. Time-Resolved Light Scattering From Excitons. *Springer Tracts in Modern Physics 130*; Springer-Verlag: Berlin, 1994.

(78) Dorfman, K. E.; Mukamel, S. Nonlinear Spectroscopy with Time- and Frequency-Gated Photon Counting: a Superoperator Diagrammatic Approach. *Phys. Rev. A: At., Mol., Opt. Phys.* **2012**, *86*, 013810.

(79) Dorfman, K. E.; Mukamel, S. Photon Coincidence Counting in Parametric Down-Conversion: Interference of Field-Matter Quantum Pathways. *Phys. Rev. A: At., Mol., Opt. Phys.* **2012**, *86*, 023805.

(80) Polli, D.; Brida, D.; Mukamel, S.; Lanzani, G.; Cerullo, G. Effective Temporal Resolution in Pump-Probe Spectroscopy with Strongly Chirped Pulses. *Phys. Rev. A: At., Mol., Opt. Phys.* **2010**, *82*, 053809.

(81) Rahav, S.; Mukamel, S. *Adv. At., Mol., Opt. Phys.* **2010**, *59*, 223.

(82) Kosloff, R. Propagation Methods For Quantum Molecular Dynamics. *Annu. Rev. Phys. Chem.* **1994**, *45*, 145−178.

(83) Chen, X.; Batista, V. S. Matching-Pursuit/Split-Operator-Fourier-Transform Simulations of Excited-State Nonadiabatic Quantum Dynamics in Pyrazine. *J. Chem. Phys.* **2006**, *125*, 124313.

(84) Leforestier, C.; Bisseling, R. H.; Cerjan, C.; Feit, M. D.; Friesner, R.; Guldberg, A.; Hammerich, A.; Jolicard, G.; Karrlein, W.; Meyer, H.-D.; et al. A Comparison of Different Propagation Schemes For the Time Dependent Propagation Schrödinger Equation. *J. Comput. Phys.* **1991**, *94*, 59−80.

(85) Wu, Y.; Batista, V. S. Quantum Tunneling Dynamics in Multidimensional Systems: a Matching-Pursuit Description. *J. Chem. Phys.* **2004**, *121*, 1676−1680.

(86) Beck, M. The Multiconfiguration Time-Dependent Hartree (MCTDH) Method: a Highly Efficient Algorithm For Propagating Wavepackets. *Phys. Rep.* **2000**, *324*, 1−105.

(87) Lasorne, B.; Bearpark, M. J.; Robb, M. A.; Worth, G. A. Direct Quantum Dynamics Using Variational Multi-Configuration Gaussian Wavepackets. *Chem. Phys. Lett.* **2006**, *432*, 604−609.

(88) Burghardt, I.; Giri, K.; Worth, G. A. Multimode Quantum Dynamics Using Gaussian Wavepackets: the Gaussian-Based Multi-configuration Time-Dependent Hartree (G-MCTDH) Method Applied to the Absorption Spectrum of Pyrazine. *J. Chem. Phys.* **2008**, *129*, 174104.

(89) Richings, G. W.; Polyak, I.; Spinlove, K. E.; Worth, G. A.; Burghardt, I.; Lasorne, B. Quantum Dynamics Simulations Using Gaussian Wavepackets: the vMCG Method. *Int. Rev. Phys. Chem.* **2015**, *34*, 269−308.

(90) Martínez, T. J.; Ben-Nun, M.; Levine, R. D. Multi-Electronic-State Molecular Dynamics: a Wave Function Approach with Applications. *J. Phys. Chem.* **1996**, *100*, 7884−7895.

(91) Ben-Nun, M.; Martínez, T. J. Nonadiabatic Molecular Dynamics: Validation of the Multiple Spawning Method For a Multidimensional Problem. *J. Chem. Phys.* **1998**, *108*, 7244.

(92) Yang, S.; Coe, J. D.; Kaduk, B.; Martínez, T. J. An "Optimal" Spawning Algorithm For Adaptive Basis Set Expansion in Nonadiabatic Dynamics. *J. Chem. Phys.* **2009**, *130*, 134113.

(93) Falvo, C.; Palmieri, B.; Mukamel, S. Coherent Infrared Multidimensional Spectra of the OH Stretching Band in Liquid Water Simulated by Direct Nonlinear Exciton Propagation. *J. Chem. Phys.* **2009**, *130*, 184501.

(94) Kowalewski, M.; Mukamel, S. Stimulated Raman Signals at Conical Intersections: ab initio Surface Hopping Simulation Protocol with Direct Propagation of the Nuclear Wave Function. *J. Chem. Phys.* **2015**, *143*, 044117.

(95) Torii, H. Effects of Intermolecular Vibrational Coupling and Liquid Dynamics on the Polarized Raman and Two-Dimensional Infrared Spectral Profiles of Liquid N,N-Dimethylformamide Analyzed with a Time-Domain Computational Method. *J. Phys. Chem. A* **2006**, *110*, 4822−4832.

(96) Jansen, T. l. C.; Knoester, J. Nonadiabatic Effects in the Two-Dimensional Infrared Spectra of Peptides: Application to Alanine Dipeptide. *J. Phys. Chem. B* **2006**, *110*, 22910−22916.

(97) Abramavicius, D.; Palmieri, B.; Voronine, D. V.; Šanda, F.; Mukamel, S. Coherent Multidimensional Optical Spectroscopy of Excitons in Molecular Aggregates; Quasiparticle Versus Supermolecule Perspectives. *Chem. Rev.* **2009**, *109*, 2350−2408.

(98) Kwac, K.; Cho, M. Molecular Dynamics Simulation Study of N-Methylacetamide in Water. I. Amide I Mode Frequency Fluctuation. *J. Chem. Phys.* **2003**, *119*, 2247−2255.

(99) Hayashi, T.; la Cour Jansen, T.; Zhuang, W.; Mukamel, S. Collective Solvent Coordinates for the Infrared Spectrum of HOD in D2O Based on an ab initio Electrostatic Map. *J. Phys. Chem. A* **2005**, *109*, 64−82.

(100) Fingerhut, B. P.; Costard, R.; Elsaesser, T. Predominance of Short Range Coulomb Forces in Phosphate-Water Interactions−a Theoretical Analysis. *J. Chem. Phys.* **2016**, *145*, 115101.

(101) Barbatti, M.; Shepard, R.; Lischka, H. In *Conical Intersections: Theory, Computation and Experiment*; Domcke, W., Yarkony, D. R., Koppel, H., Eds.; World Scientific: Singapore, 2011; p 415.

(102) Reiher, M.; Neugebauer, J. A Mode-Selective Quantum Chemical Method For Tracking Molecular Vibrations Applied to Functionalized Carbon Nanotubes. *J. Chem. Phys.* **2003**, *118*, 1634−1641.

(103) Fingerhut, B. P.; Dorfman, K. E.; Mukamel, S. Monitoring Nonadiabatic Dynamics of the RNA Base Uracil by UV Pump-IR Probe Spectroscopy. *J. Phys. Chem. Lett.* **2013**, *4*, 1933−1942.

(104) Kubo, R. In *Fluctuations, Relaxation and Resonance in Magnetic Systems*; Haar, D. t., Ed.; Oliver and Boyd: Edingburgh, 1962; p 23.

(105) Kubo, R. Stochastic Liouville Equations. *J. Math. Phys.* **1963**, *4*, 174−183.

(106) Anderson, P. W. A Mathematical Model For the Narrowing of Spectral Lines by Exchange or Motion. *J. Phys. Soc. Jpn.* **1954**, *9*, 316−339.

(107) Mukamel, S. *Principles of Nonlinear Optics and Spectroscopy*; Oxford University Press: Oxford, UK, 1995.

(108) Biggs, J. D.; Voll, J. A.; Mukamel, S. Coherent Nonlinear Optical Studies of Elementary Processes in Biological Complexes: Diagrammatic Techniques Based on the Wave Function Versus the Density Matrix. *Philos. Trans. R. Soc., A* **2012**, *370*, 3709−3727.

(109) Ando, H.; Fingerhut, B. P.; Dorfman, K. E.; Biggs, J. D.; Mukamel, S. Femtosecond Stimulated Raman Spectroscopy of the Cyclobutane Thymine Dimer Repair Mechanism: a Computational Study. *J. Am. Chem. Soc.* **2014**, *136*, 14801−14810.

(110) Agarwalla, B. K.; Ando, H.; Dorfman, K. E.; Mukamel, S. Stochastic Liouville Equations For Femtosecond Stimulated Raman Spectroscopy. *J. Chem. Phys.* **2015**, *142*, 024115.

(111) Kukura, P.; McCamant, D. W.; Yoon, S.; Wandschneider, D. B.; Mathies, R. A. Structural Observation of the Primary Isomerization in Vision with Femtosecond-Stimulated Raman. *Science* **2005**, *310*, 1006−1009.

(112) Mukamel, S.; Biggs, J. D. Communication: Comment on the Effective Temporal and Spectral Resolution of Impulsive Stimulated Raman Signals. *J. Chem. Phys.* **2011**, *134*, 161101.

(113) Fingerhut, B. P.; Dorfman, K. E.; Mukamel, S. Probing the Conical Intersection Dynamics of the RNA Base Uracil by UV-Pump Stimulated-Raman-Probe Signals; ab initio Simulations. *J. Chem. Theory Comput.* **2014**, *10*, 1172−1188.

(114) Dietze, D. R.; Mathies, R. A. Femtosecond Stimulated Raman Spectroscopy. *ChemPhysChem* **2016**, *17*, 1224−1251.

(115) Mukamel, S. Partially-Time-Ordered Schwinger-Keldysh Loop Expansion of Coherent Nonlinear Optical Susceptibilities. *Phys. Rev. A: At., Mol., Opt. Phys.* **2008**, *77*, 023801.

(116) Schreier, W. J.; Schrader, T. E.; Koller, F. O.; Gilch, P.; Crespo-Hernández, C. E.; Swaminathan, V. N.; Carell, T.; Zinth, W.; Kohler, B. Thymine Dimerization in DNA is an Ultrafast Photoreaction. *Science* **2007**, *315*, 625−629.

(117) Doorley, G.; McGovern, D.; George, M.; Towrie, M.; Parker, A.; Kelly, J.; Quinn, S. Picosecond Transient Infrared Study of the Ultrafast Deactivation Processes of Electronically Excited B-DNA and Z-DNA Forms of [Poly(Dg-Dc)]2. *Angew. Chem., Int. Ed.* **2009**, *48*, 123−127.

(118) Haiser, K.; Fingerhut, B. P.; Heil, K.; Glas, A.; Herzog, T. T.; Pilles, B. M.; Schreier, W. J.; Zinth, W.; de Vivie-Riedle, R.; Carell, T. Mechanism of UV-Induced Formation of Dewar Lesions in DNA. *Angew. Chem., Int. Ed.* **2012**, *51*, 408−411.

(119) Doorley, G. W.; Wojdyla, M.; Watson, G. W.; Towrie, M.; Parker, A. W.; Kelly, J. M.; Quinn, S. J. Tracking DNA Excited States by Picosecond-Time-Resolved Infrared Spectroscopy: Signature Band For a Charge-Transfer Excited State in Stacked Adenine-Thymine Systems. *J. Phys. Chem. Lett.* **2013**, *4*, 2739−2744.

(120) Zhang, Y.; Improta, R.; Kohler, B. Mode-Specific Vibrational Relaxation of Photoexcited Guanosine 5′-Monophosphate and Its acid Form: a Femtosecond Broadband mid-IR Transient Absorption and Theoretical Study. *Phys. Chem. Chem. Phys.* **2014**, *16*, 1487−1499.

(121) Roberts, G. M.; Marroux, H. J. B.; Grubb, M. P.; Ashfold, M. N. R.; Orr-Ewing, A. J. On the Participation of Photoinduced N-H Bond Fission in Aqueous Adenine at 266 and 220 nm: a Combined Ultrafast Transient Electronic and Vibrational Absorption Spectroscopy Study. *J. Phys. Chem. A* **2014**, *118*, 11211−11225.

(122) Bucher, D. B.; Schlueter, A.; Carell, T.; Zinth, W. Watson-Crick Base Pairing Controls Excited-State Decay in Natural DNA. *Angew. Chem., Int. Ed.* **2014**, *53*, 11366−11369.

(123) Bucher, D. B.; Pilles, B. M.; Carell, T.; Zinth, W. Charge Separation and Charge Delocalization Identified in Long-Living States of Photoexcited DNA. *Proc. Natl. Acad. Sci. U. S. A.* **2014**, *111*, 4369−4374.

(124) Ni, G. X.; Wang, L.; Goldflam, M. D.; Wagner, M.; Fei, Z.; McLeod, A. S.; Liu, M. K.; Keilmann, F.; Oezyilmaz, B.; Neto, A. H. C.; et al. Ultrafast Optical Switching of Infrared Plasmon Polaritons in High-Mobility Graphene. *Nat. Photonics* **2016**, *10*, 244.

(125) Koyama, D.; Orr-Ewing, A. J. Photochemical Reaction Dynamics of 2,2′-Dithiobis(Benzothiazole): Direct Observation of the Addition Product of an Aromatic Thiyl Radical To an alkene with Time-Resolved Vibrational and Electronic Absorption Spectroscopy. *Phys. Chem. Chem. Phys.* **2016**, *18*, 12115−12127.

(126) Zhang, Y.; de La Harpe, K.; Beckstead, A. A.; Martínez-Fernández, L.; Improta, R.; Kohler, B. Excited-State Dynamics of DNA Duplexes with Different H-Bonding Motifs. *J. Phys. Chem. Lett.* **2016**, *7*, 950−954.

(127) Stensitzki, T.; Yang, Y.; Muders, V.; Schlesinger, R.; Heberle, J.; Heyne, K. Femtosecond Infrared Spectroscopy of Channelrhodopsin-1 Chromophore Isomerization. *Struct. Dyn.* **2016**, *3*, 043208.

(128) Anfinrud, P. A.; Han, C.; Hochstrasser, R. M. Direct Observations of Ligand Dynamics in Hemoglobin by Subpicosecond Infrared Spectroscopy. *Proc. Natl. Acad. Sci. U. S. A.* **1989**, *86*, 8387−8391.

(129) Lim, M.; Jackson, T. A.; Anfinrud, P. A. Binding of Co to Myoglobin From a Heme Pocket Docking Site To Form Nearly Linear Fe-C-O. *Science* **1995**, *269*, 962−966.

(130) Heyne, K.; Mohammed, O.; Usman, A.; Dreyer, J.; Nibbering, E.; Cusanovich, M. Structural Evolution of the Chromophore in the Primary Stages of Trans/Cis isomerization in Photoactive Yellow Protein. *J. Am. Chem. Soc.* **2005**, *127*, 18100−18106.

(131) Mohammed, O. F.; Pines, D.; Dreyer, J.; Pines, E.; Nibbering, E. T. J. Sequential Proton Transfer Through Water Bridges in Acid-Base Reactions. *Science* **2005**, *310*, 83−86.

(132) Mohammed, O. F.; Adamczyk, K.; Banerji, N.; Dreyer, J.; Lang, B.; Nibbering, E. T. J.; Vauthey, E. Direct Femtosecond Observation of Tight and Loose Ion Pairs Upon Photoinduced Bimolecular Electron Transfer. *Angew. Chem., Int. Ed.* **2008**, *47*, 9044−9048.

(133) Adamczyk, K.; Prémont-Schwarz, M.; Pines, D.; Pines, E.; Nibbering, E. T. J. Real-Time Observation of Carbonic Acid Formation in Aqueous Solution. *Science* **2009**, *326*, 1690−1694.

(134) Schreier, W. J.; Kubon, J.; Regner, N.; Haiser, K.; Schrader, T. E.; Zinth, W.; Clivio, P.; Gilch, P. Thymine Dimerization in DNA Model Systems: Cyclobutane Photolesion is Predominantly Formed Via the Singlet Channel. *J. Am. Chem. Soc.* **2009**, *131*, 5038−5039.

(135) Fingerhut, B. P.; Herzog, T. T.; Ryseck, G.; Haiser, K.; Graupner, F. F.; Heil, K.; Gilch, P.; Schreier, W. J.; Carell, T.; de Vivie-Riedle, R.; et al. Dynamics of Ultraviolet-Unduced DNA Lesions: Dewar Formation Guided by Pre-Tension Induced by the Backbone. *New J. Phys.* **2012**, *14*, 065006.

(136) Improta, R.; Santoro, F.; Blancafort, L. Quantum Mechanical Studies on the Photophysics and the Photochemistry of Nucleic Acids and Nucleobases. *Chem. Rev.* **2016**, *116*, 3540−3593.

(137) McFarland, B. K.; Farrell, J. P.; Miyabe, S.; Tarantelli, F.; Aguilar, A.; Berrah, N.; Bostedt, C.; Bozek, J. D.; Bucksbaum, P. H.; Castagna, J. C.; et al. Ultrafast X-Ray Auger Probing of Photoexcited Molecular Dynamics. *Nat. Commun.* **2014**, *5*, 4235.

(138) Gessner, O.; Gühr, M. Monitoring Ultrafast Chemical Dynamics by Time-Domain X-Ray Photo- and Auger-Electron Spectroscopy. *Acc. Chem. Res.* **2016**, *49*, 138−145.

(139) Wolf, T.; Myhre, R. H.; Coriani, S.; Koch, H.; Battistoni, A.; Berrah, N.; Bucksbaum, P. H.; Coffee, R.; Coslovich, G.; Cryan, J. P. et al. Transient NEXAFS Spectroscopy at the Oxygen Edge: Pinning Down $\pi\pi^*/n\pi^*$ Internal Conversion. *International Conference on Ultrafast Phenomena*; 2016; p UF1A.3.

(140) Buchner, F.; Nakayama, A.; Yamazaki, S.; Ritze, H.-H.; Lübcke, A. Excited-State Relaxation of Hydrated Thymine and Thymidine Measured by Liquid-Jet Photoelectron Spectroscopy: Experiment and Simulation. *J. Am. Chem. Soc.* **2015**, *137*, 2931−2938.

(141) Prokhorenko, V. I.; Picchiotti, A.; Pola, M.; Dijkstra, A. G.; Miller, R. J. D. New Insights Into the Photophysics of DNA Nucleobases. *J. Phys. Chem. Lett.* **2016**, *7*, 4445−4450.

(142) Sobolewski, A. L.; Domcke, W. The Chemical Physics of the Photostability of Life. *Europhys. News* **2006**, *37*, 20−23.

(143) Matsika, S.; Krause, P. Nonadiabatic Events and Conical Intersections. *Annu. Rev. Phys. Chem.* **2011**, *62*, 621−643.

(144) Perun, S.; Sobolewski, A. L.; Domcke, W. Conical Intersections in Thymine. *J. Phys. Chem. A* **2006**, *110*, 13238−13244.

(145) Delchev, V. B.; Sobolewski, A. L.; Domcke, W. Comparison of the Non-Radiative Decay Mechanisms of 4-Pyrimidinone and Uracil: an ab initio Study. *Phys. Chem. Chem. Phys.* **2010**, *12*, 5007−5015.

(146) Cadet, J.; Mouret, S.; Ravanat, J.-L.; Douki, T. Photoinduced Damage To Cellular DNA: Direct and Photosensitized Reactions†. *Photochem. Photobiol.* **2012**, *88*, 1048−1065.

(147) Kaindl, R. A.; Wurm, M.; Reimann, K.; Hamm, P.; Weiner, A. M.; Woerner, M. Generation, Shaping, and Characterization of Intense Femtosecond Pulses Tunable From 3 To 20 μm. *J. Opt. Soc. Am. B* **2000**, *17*, 2086−2094.

(148) Fuji, T.; Suzuki, T. Generation of Sub-Two-Cycle Mid-Infrared Pulses by Four-Wave Mixing Through Filamentation in Air. *Opt. Lett.* **2007**, *32*, 3330−3332.

(149) Brida, D.; Manzoni, C.; Cirmi, G.; Marangoni, M.; Bonora, S.; Villoresi, P.; De Silvestri, S.; Cerullo, G. Few-Optical-Cycle Pulses Tunable From the Visible To the Mid-Infrared by Optical Parametric Amplifiers. *J. Opt.* **2010**, *12*, 013001.

(150) Hudock, H. R.; Levine, B. G.; Thompson, A. L.; Satzger, H.; Townsend, D.; Gador, N.; Ullrich, S.; Stolow, A.; Martínez, T. J. ab initio Molecular Dynamics and Time-Resolved Photoelectron Spectroscopy of Electronically Excited Uracil and Thymine. *J. Phys. Chem. A* **2007**, *111*, 8500−8508.

(151) Hua, X.; Hua, L.; Liu, X. The Methyl- and Aza-Substituent Effects on Nonradiative Decay Mechanisms of Uracil in Water: a Transient Absorption Study in the UV Region. *Phys. Chem. Chem. Phys.* **2016**, *18*, 13904−13911.

(152) Xue, B.; Yabushita, A.; Kobayashi, T. Ultrafast Dynamics of Uracil and Thymine Studied Using a Sub-10 fs Deep Ultraviolet Laser. *Phys. Chem. Chem. Phys.* **2016**, *18*, 17044−17053.

(153) Manna, A.; Park, S.; Lee, T.; Lim, M. Photoexcitation Dynamics of Thymine in Acetonitrile and an Ionic Liquid Probed by Time-Resolved Infrared Spectroscopy. *Bull. Korean Chem. Soc.* **2016**, *37*, 1064−1070.

(154) González, L.; Escudero, D.; Serrano-Andrés, L. Progress and Challenges in the Calculation of Electronic Excited States. *ChemPhysChem* **2012**, *13*, 28−51.

(155) Fingerhut, B. P.; Oesterling, S.; Haiser, K.; Heil, K.; Glas, A.; Schreier, W. J.; Zinth, W.; Carell, T.; de Vivie-Riedle, R. ONIOM Approach for Non-adiabatic on-the-fly Molecular Dynamics Demonstrated For the Backbone Controlled Dewar Valence Isomerization. *J. Chem. Phys.* **2012**, *136*, 204307.

(156) DeFusco, A.; Ivanic, J.; Schmidt, M. W.; Gordon, M. S. Solvent-induced Shifts in Electronic Spectra of Uracil. *J. Phys. Chem. A* **2011**, *115*, 4574−4582.

(157) Climent, T.; González-Luque, R.; Merchán, M.; Serrano-Andrés, L. On the Intrinsic Population of the Lowest Triplet State of Uracil. *Chem. Phys. Lett.* **2007**, *441*, 327−331.

(158) Etinski, M.; Fleig, T.; Marian, C. M. Intersystem Crossing and Characterization of Dark States in the Pyrimidine Nucleobases Uracil, Thymine, and 1-Methylthymine. *J. Phys. Chem. A* **2009**, *113*, 11809−11816.

(159) Hamm, P.; Zanni, M. *Concepts and Methods of 2D Infrared Spectroscopy*, 1st ed.; Cambridge University Press: Cambridge, 2011.

(160) Bredenbeck, J.; Helbing, J.; Behrendt, R.; Renner, C.; Moroder, L.; Wachtveitl, J.; Hamm, P. Transient 2D-IR Spectroscopy: Snapshots of the Nonequilibrium Ensemble During the Picosecond Conformational Transition of a Small Peptide. *J. Phys. Chem. B* **2003**, *107*, 8654−8660.

(161) Bredenbeck, J.; Helbing, J.; Sieg, A.; Schrader, T.; Zinth, W.; Renner, C.; Behrendt, R.; Moroder, L.; Wachtveitl, J.; Hamm, P. Picosecond Conformational Transition and Equilibration of a Cyclic Peptide. *Proc. Natl. Acad. Sci. U. S. A.* **2003**, *100*, 6452−6457.

(162) Bredenbeck, J.; Helbing, J.; Hamm, P. Labeling Vibrations by Light: Ultrafast Transient 2D-IR Spectroscopy Tracks Vibrational Modes During Photoinduced Charge Transfer. *J. Am. Chem. Soc.* **2004**, *126*, 990−991.

(163) Bredenbeck, J.; Helbing, J.; Hamm, P. Solvation Beyond the Linear Response Regime. *Phys. Rev. Lett.* **2005**, *95*, 083201.

(164) Kolano, C.; Helbing, J.; Kozinski, M.; Sander, W.; Hamm, P. Watching Hydrogen-Bond Dynamics in a [bgr]-Turn by Transient Two-Dimensional Infrared Spectroscopy. *Nature* **2006**, *444*, 469−472.

(165) Bredenbeck, J.; Helbing, J.; Kolano, C.; Hamm, P. Ultrafast 2D-IR Spectroscopy of Transient Species. *ChemPhysChem* **2007**, *8*, 1747−1756.

(166) Hunt, N. T. Transient 2D-IR Spectroscopy of Inorganic Excited States. *Dalton Trans.* **2014**, *43*, 17578−17589.

(167) Delor, M.; Sazanovich, I. V.; Towrie, M.; Weinstein, J. A. Probing and Exploiting the Interplay Between Nuclear and Electronic Motion in Charge Transfer Processes. *Acc. Chem. Res.* **2015**, *48*, 1131−1139.

(168) Kiefer, L. M.; King, J. T.; Kubarych, K. J. Equilibrium Excited State Dynamics of a Photoactivated Catalyst Measured with Ultrafast Transient 2DIR. *J. Phys. Chem. A* **2014**, *118*, 9853−9860.

(169) Xiong, W.; Laaser, J. E.; Paoprasert, P.; Franking, R. A.; Hamers, R. J.; Gopalan, P.; Zanni, M. T. Transient 2D IR Spectroscopy of Charge Injection in Dye-Sensitized Nanocrystalline Thin Films. *J. Am. Chem. Soc.* **2009**, *131*, 18040−18041.

(170) Lynch, M. S.; Slenkamp, K. M.; Cheng, M.; Khalil, M. Coherent Fifth-order Visible-Infrared Spectroscopies: Ultrafast Nonequilibrium Vibrational Dynamics in Solution. *J. Phys. Chem. A* **2012**, *116*, 7023−7032.

(171) Lynch, M. S.; Slenkamp, K. M.; Khalil, M. Communication: Probing Non-Equilibrium Vibrational Relaxation Pathways of Highly Excited C≡N Stretching Modes Following Ultrafast Back-Electron Transfer. *J. Chem. Phys.* **2012**, *136*, 241101.

(172) Delor, M.; Sazanovich, I. V.; Towrie, M.; Spall, S. J.; Keane, T.; Blake, A. J.; Wilson, C.; Meijer, A. J. H. M.; Weinstein, J. A. Dynamics of Ground and Excited State Vibrational Relaxation and Energy Transfer in Transition Metal Carbonyls. *J. Phys. Chem. B* **2014**, *118*, 11781−11791.

(173) Di Donato, M.; Ragnoni, E.; Lapini, A.; Kardaś, T. M.; Ratajska-Gadomska, B.; Foggi, P.; Righini, R. Identification of the Excited-State C═C and C═O Modes of Trans-*β*-apo-8′-Carotenal with Transient 2D-IR-Exsy and Femtosecond Stimulated Raman Spectroscopy. *J. Phys. Chem. Lett.* **2015**, *6*, 1592−1598.

(174) Oliver, T. A. A.; Lewis, N. H. C.; Fleming, G. R. Correlating the Motion of Electrons and Nuclei with Two-Dimensional Electronic-Vibrational Spectroscopy. *Proc. Natl. Acad. Sci. U. S. A.* **2014**, *111*, 10061−10066.

(175) Gallagher Faeder, S. M.; Jonas, D. M. Two-Dimensional Electronic Correlation and Relaxation Spectra: Theory and Model Calculations. *J. Phys. Chem. A* **1999**, *103*, 10489−10505.

(176) Shim, S.-H.; Strasfeld, D. B.; Ling, Y. L.; Zanni, M. T. Automated 2D IR Spectroscopy Using a Mid-IR Pulse Shaper and Application of This Technology To the Human Islet Amyloid Polypeptide. *Proc. Natl. Acad. Sci. U. S. A.* **2007**, *104*, 14197−14202.

(177) Shim, S.-H.; Zanni, M. T. How To Turn Your Pump-Probe instrument into a Multidimensional Spectrometer: 2D IR and Vis Spectroscopiesvia Pulse Shaping. *Phys. Chem. Chem. Phys.* **2009**, *11*, 748−761.

(178) Myers, J. A.; Lewis, K. L. M.; Tekavec, P. F.; Ogilvie, J. P. Two-Color Two-Dimensional Fourier Transform Electronic Spectroscopy with a Pulse-Shaper. *Opt. Express* **2008**, *16*, 17420−17428.

(179) Gaynor, J. D.; Courtney, T. L.; Balasubramanian, M.; Khalil, M. Fourier Transform Two-Dimensional Electronic-Vibrational Spectroscopy Using an Octave-Spanning Mid-IR Probe. *Opt. Lett.* **2016**, *41*, 2895−2898.

(180) Courtney, T. L.; Fox, Z. W.; Slenkamp, K. M.; Khalil, M. Two-Dimensional Vibrational-Electronic Spectroscopy. *J. Chem. Phys.* **2015**, *143*, 154201.

(181) Lewis, N. H. C.; Dong, H.; Oliver, T. A. A.; Fleming, G. R. A Method For the Direct Measurement of Electronic Site Populations in a Molecular Aggregate Using Two-Dimensional Electronic-Vibrational Spectroscopy. *J. Chem. Phys.* **2015**, *143*, 124203.

(182) Dong, H.; Lewis, N. H. C.; Oliver, T. A. A.; Fleming, G. R. Determining the Static Electronic and Vibrational Energy Correlations Via Two-Dimensional Electronic-Vibrational Spectroscopy. *J. Chem. Phys.* **2015**, *142*, 174201.

(183) Terenziani, F.; Painelli, A. Two-Dimensional Electronic-Vibrational Spectra: Modeling Correlated Electronic and Nuclear Motion. *Phys. Chem. Chem. Phys.* **2015**, *17*, 13074−13081.

(184) Cho, M. Triply Resonant Infrared-Infrared-Visible Sum Frequency Generation: Three-Dimensional Vibronic Spectroscopy For the Investigation of Vibrational and Vibronic Couplings. *J. Chem. Phys.* **2000**, *112*, 9002−9014.

(185) Oliver, T. A. A.; Fleming, G. R. Following Coupled Electronic-Nuclear Motion Through Conical Intersections in the Ultrafast Relaxation of *β*-apo-8′-Carotenal. *J. Phys. Chem. B* **2015**, *119*, 11428−11441.

(186) Buckup, T.; Motzkus, M. Multidimensional Time-Resolved Spectroscopy of Vibrational Coherence in Biopolyenes. *Annu. Rev. Phys. Chem.* **2014**, *65*, 39−57.

(187) Lewis, N. H. C.; Gruenke, N. L.; Oliver, T. A. A.; Ballottari, M.; Bassi, R.; Fleming, G. R. Observation of Electronic Excitation Transfer Through Light Harvesting Complex II Using Two-Dimensional Electronic−Vibrational Spectroscopy. *J. Phys. Chem. Lett.* **2016**, *7*, 4197−4206.

(188) Stahl, A. D.; Di Donato, M.; van Stokkum, I.; van Grondelle, R.; Groot, M. L. A Femtosecond Visible/Visible and Visible/Mid-Infrared Transient Absorption Study of the Light Harvesting Complex II. *Biophys. J.* **2009**, *97*, 3215−3223.

(189) Schlau-Cohen, G. S.; Calhoun, T. R.; Ginsberg, N. S.; Read, E. L.; Ballottari, M.; Bassi, R.; van Grondelle, R.; Fleming, G. R. Pathways of Energy Flow in LHCII From Two-Dimensional Electronic Spectroscopy. *J. Phys. Chem. B* **2009**, *113*, 15352−15363.

(190) Petersen, P. B.; Tokmakoff, A. Source For Ultrafast Continuum Infrared and Terahertz Radiation. *Opt. Lett.* **2010**, *35*, 1962−1964.

(191) Nomura, Y.; Shirai, H.; Ishii, K.; Tsurumachi, N.; Voronin, A. A.; Zheltikov, A. M.; Fuji, T. Phase-Stable Sub-Cycle Mid-Infrared Conical Emission From Filamentation in Gases. *Opt. Express* **2012**, *20*, 24741−24747.

(192) Cheng, M.; Reynolds, A.; Widgren, H.; Khalil, M. Generation of Tunable Octave-Spanning Mid-Infrared Pulses by Filamentation in Gas Media. *Opt. Lett.* **2012**, *37*, 1787−1789.

(193) de Marco, L.; Ramasesha, K.; Tokmakoff, A. Experimental Evidence of Fermi Resonances in Isotopically Dilute Water From Ultrafast Broadband IR Spectroscopy. *J. Phys. Chem. B* **2013**, *117*, 15319−15327.

(194) Suchowski, H.; Krogen, P. R.; Huang, S.-W.; Kärtner, F. X.; Moses, J. Octave-Spanning Coherent Mid-IR Generation Via Adiabatic Difference Frequency Conversion. *Opt. Express* **2013**, *21*, 28892−28901.

(195) Petersen, C. R.; Møller, U.; Kubat, I.; Zhou, B.; Dupont, S.; Ramsay, J.; Benson, T.; Sujecki, S.; Abdel-Moneim, N.; Tang, Z.; et al. Mid-Infrared Supercontinuum Covering the 1.4−13.3 μm Molecular Fingerprint Region Using Ultra-High NA Chalcogenide Step-Index Fibre. *Nat. Photonics* **2014**, *8*, 830−834.

(196) Fuji, T.; Shirai, H.; Nomura, Y. Ultrabroadband Mid-Infrared Spectroscopy with Four-Wave Difference Frequency Generation. *J. Opt.* **2015**, *17*, 094004.

(197) Pires, H.; Baudisch, M.; Sanchez, D.; Hemmer, M.; Biegert, J. Ultrashort Pulse Generation in the Mid-IR. *Prog. Quantum Electron.* **2015**, *43*, 1−30.

(198) Balasubramanian, M.; Courtney, T. L.; Gaynor, J. D.; Khalil, M. Compression of Tunable Broadband Mid-IR Pulses with a Deformable Mirror Pulse Shaper. *J. Opt. Soc. Am. B* **2016**, *33*, 2033−2037.

(199) Szyc, Ł.; Yang, M.; Elsaesser, T. Ultrafast Energy Exchange Via Water-Phosphate Interactions in Hydrated DNA. *J. Phys. Chem. B* **2010**, *114*, 7951−7957.

(200) Costard, R.; Tyborski, T.; Fingerhut, B. P.; Elsaesser, T. Ultrafast Phosphate Hydration Dynamics in Bulk H2O. *J. Chem. Phys.* **2015**, *142*, 212406.

(201) Siebert, T.; Guchhait, B.; Liu, Y.; Fingerhut, B. P.; Elsaesser, T. Range, Magnitude, and Ultrafast Dynamics of Electric Fields at the Hydrated DNA Surface. *J. Phys. Chem. Lett.* **2016**, *7*, 3131−3136.

(202) Junginger, F.; Sell, A.; Schubert, O.; Mayer, B.; Brida, D.; Marangoni, M.; Cerullo, G.; Leitenstorfer, A.; Huber, R. Single-Cycle Multiterahertz Transients with Peak Fields above 10 MV/cm. *Opt. Lett.* **2010**, *35*, 2645−2647.

(203) Somma, C.; Folpini, G.; Gupta, J.; Reimann, K.; Woerner, M.; Elsaesser, T. Ultra-Broadband Terahertz Pulses Generated in the Organic Crystal DSTSMS. *Opt. Lett.* **2015**, *40*, 3404−3407.

(204) Towrie, M.; Doorley, G. W.; George, M. W.; Parker, A. W.; Quinn, S. J.; Kelly, J. M. Ps-TRIR Covers all the Bases - Recent Advances in the Use of Transient IR For the Detection of Short-Lived Species in Nucleic Acids. *Analyst* **2009**, *134*, 1265−1273.

(205) Batignani, G.; Fumero, G.; Mukamel, S.; Scopigno, T. Energy Flow Between Spectral Components in 2D Broadband Stimulated Raman Spectroscopy. *Phys. Chem. Chem. Phys.* **2015**, *17*, 10454−10461.

(206) Ideguchi, T.; Holzner, S.; Bernhardt, B.; Guelachvili, G.; Picqué, N.; Hänsch, T. W. Coherent Raman Spectro-Imaging with Laser Frequency Combs. *Nature* **2013**, *502*, 355−358.

(207) Bostedt, C.; Bozek, J. D.; Bucksbaum, P. H.; Coffee, R. N.; Hastings, J. B.; Huang, Z.; Lee, R. W.; Schorb, S.; Corlett, J. N.; Denes, P.; et al. Ultra-Fast and Ultra-Intense X-Ray Sciences: First Results From the Linac Coherent Light Source Free-Electron Laser. *J. Phys. B: At., Mol. Opt. Phys.* **2013**, *46*, 164003.

(208) Katayama, T.; Anniyev, T.; Beye, M.; Coffee, R.; Dell'Angela, M.; Föhlisch, A.; Gladh, J.; Kaya, S.; Krupin, O.; Nilsson, A.; et al. Ultrafast Soft X-Ray Emission Spectroscopy of Surface Adsorbates Using an X-Ray Free Electron Laser. *J. Electron Spectrosc. Relat. Phenom.* **2013**, *187*, 9−14.

(209) Lemke, H. T.; Bressler, C.; Chen, L. X.; Fritz, D. M.; Gaffney, K. J.; Galler, A.; Gawelda, W.; Haldrup, K.; Hartsock, R. W.; Ihee, H.; et al. Femtosecond X-Ray Absorption Spectroscopy at a Hard X-Ray Free Electron Laser: Application To Spin Crossover Dynamics. *J. Phys. Chem. A* **2013**, *117*, 735−740.

(210) Bennett, K.; Biggs, J. D.; Zhang, Y.; Dorfman, K. E.; Mukamel, S. Time-, Frequency-, and Wavevector-Resolved X-Ray Diffraction From Single Molecules. *J. Chem. Phys.* **2014**, *140*, 204311.

(211) Biggs, J. D.; Bennett, K.; Zhang, Y.; Mukamel, S. Multidimensional Scattering of Attosecond X-Ray Pulses Detected by Photon-Coincidence. *J. Phys. B: At., Mol. Opt. Phys.* **2014**, *47*, 124037−124044.

(212) Dorfman, K. E.; Bennett, K.; Zhang, Y.; Mukamel, S. Nonlinear Light Scattering in Molecules Triggered by an Impulsive X-Ray Raman Process. *Phys. Rev. A: At., Mol., Opt. Phys.* **2013**, *87*, 053826.

(213) Dorfman, K. E.; Fingerhut, B. P.; Mukamel, S. Time-Resolved Broadband Raman Spectroscopies: a Unified Six-Wave-Mixing Representation. *J. Chem. Phys.* **2013**, *139*, 124113.

(214) Batignani, G.; Pontecorvo, E.; Giovannetti, G.; Ferrante, C.; Fumero, G.; Scopigno, T. Electronic Resonances in Broadband Stimulated Raman Spectroscopy. *Sci. Rep.* **2016**, *6*, 18445.

(215) Kowalewski, M.; Bennett, K.; Dorfman, K. E.; Mukamel, S. Catching Conical Intersections in the Act: Monitoring Transient Electronic Coherences by Attosecond Stimulated X-Ray Raman Signals. *Phys. Rev. Lett.* **2015**, *115*, 193003.

(216) Colarusso, P.; Zhang, K.; Guo, B.; Bernath, P. F. The Infrared Spectra of Uracil, Thymine, and Adenine in the Gas Phase. *Chem. Phys. Lett.* **1997**, *269*, 39−48.

(217) Nist Standard Reference Database 69: NIST Chemistry Webbook. 1964; [online] http://webbook.nist.gov/cgi/cbook.cgi?ID/74-84-0.

(218) Nist Standard Reference Database 69: NIST Chemistry Webbook. 1964; [online] http://webbook.nist.gov/cgi/cbook.cgi?ID/74-85-1.

(219) Kukura, P.; McCamant, D. W.; Mathies, R. A. Femtosecond Stimulated Raman Spectroscopy. *Annu. Rev. Phys. Chem.* **2007**, *58*, 461−488.

(220) Valley, D. T.; Hoffman, D. P.; Mathies, R. A. Reactive and Unreactive Pathways in a Photochemical Ring Opening Reaction From 2D Femtosecond Stimulated Raman. *Phys. Chem. Chem. Phys.* **2015**, *17*, 9231−9240.

(221) Zinth, W.; Nuss, M.; Kaiser, W. A New Raman Technique of Superior Spectral Resolution. *Chem. Phys. Lett.* **1982**, *88*, 257−261.

(222) Zinth, W.; Nuss, M.; Kaiser, W. Narrowing of Spectral Lines Beyond the Natural or Dephasing Line Width. *Opt. Commun.* **1983**, *44*, 262−266.

(223) Hamaguchi, H.; Gustafson, T. L. Ultrafast Time-Resolved Spontaneous and Coherent Raman Spectroscopy: the Structure and Dynamics of Photogenerated Transient Species. *Annu. Rev. Phys. Chem.* **1994**, *45*, 593−622.

(224) Fujino, T.; Tahara, T. Picosecond Time-Resolved Raman Study of Trans-azobenzene. *J. Phys. Chem. A* **2000**, *104*, 4203−4210.

(225) Kim, J. E.; McCamant, D. W.; Zhu, L.; Mathies, R. A. Resonance Raman Structural Evidence That the Cis-To-Trans Isomerization in Rhodopsin Occurs in Femtoseconds. *J. Phys. Chem. B* **2001**, *105*, 1240−1249.

(226) Rhinehart, J. M.; Mehlenbacher, R. D.; McCamant, D. Probing the Charge Transfer Reaction Coordinate of 4-(Dimethylamino)-Benzonitrile with Femtosecond Stimulated Raman Spectroscopy. *J. Phys. Chem. B* **2010**, *114*, 14646−14656.

(227) McCamant, D. W. Re-Evaluation of Rhodopsin's Relaxation Kinetics Determined From Femtosecond Stimulated Raman Lineshapes. *J. Phys. Chem. B* **2011**, *115*, 9299−9305.

(228) Kuramochi, H.; Takeuchi, S.; Tahara, T. Ultrafast Structural Evolution of Photoactive Yellow Protein Chromophore Revealed by Ultraviolet Resonance Femtosecond Stimulated Raman Spectroscopy. *J. Phys. Chem. Lett.* **2012**, *3*, 2025−2029.

(229) Kovalenko, S. A.; Dobryakov, A. L.; Pollak, E.; Ernsting, N. P. Communication: Optical Cooling of Trans-Stilbene. *J. Chem. Phys.* **2013**, *139*, 011101.

(230) Pontecorvo, E.; Ferrante, C.; Elles, C. G.; Scopigno, T. Spectrally Tailored Narrowband Pulses For Femtosecond Stimulated Raman Spectroscopy in the Range 330−750 nm. *Opt. Express* **2013**, *21*, 6866−6872.

(231) Knoester, J.; Mukamel, S. Transient Gratings, Four-Wave Mixing and Polariton Effects in Nonlinear Optics. *Phys. Rep.* **1991**, *205*, 1−58.

(232) Hogemann, C.; Pauchard, M.; Vauthey, E. Picosecond Transient Grating Spectroscopy: the Nature of the Diffracted Spectrum. *Rev. Sci. Instrum.* **1996**, *67*, 3449−3453.

(233) Goodno, G. D.; Dadusc, G.; Miller, R. J. D. Ultrafast Heterodyne-Detected Transient-Grating Spectroscopy Using Diffractive Optics. *J. Opt. Soc. Am. B* **1998**, *15*, 1791−1794.

(234) Xu, Q.-H.; Ma, Y.-Z.; Fleming, G. R. Heterodyne Detected Transient Grating Spectroscopy in Resonant and Non-Resonant Systems Using a Simplified Diffractive Optics Method. *Chem. Phys. Lett.* **2001**, *338*, 254−262.

(235) Fujiyoshi, S.; Takeuchi, S.; Tahara, T. Time-Resolved Impulsive Stimulated Raman Scattering From Excited-State Polyatomic Molecules in Solution. *J. Phys. Chem. A* **2003**, *107*, 494−500.

(236) Kraack, J. P.; Wand, A.; Buckup, T.; Motzkus, M.; Ruhman, S. Mapping Multidimensional Excited State Dynamics in Real Time Using Pump-Impulsive-Vibrational-Spectroscopy and Pump-Degenerate-Four-Wave-Mixing. *Phys. Chem. Chem. Phys.* **2013**, *15*, 14487−14501.

(237) Fumero, G.; Batignani, G.; Dorfman, K. E.; Mukamel, S.; Scopigno, T. On the Resolution Limit of Femtosecond Stimulated Raman Spectroscopy: Modelling Fifth-order Signals with Overlapping Pulses. *ChemPhysChem* **2015**, *16*, 3438−3443.

(238) Quick, M.; Kasper, M.-A.; Richter, C.; Mahrwald, R.; Dobryakov, A. L.; Kovalenko, S. A.; Ernsting, N. P. *β*-Carotene Revisited by Transient Absorption and Stimulated Raman Spectroscopy. *ChemPhysChem* **2015**, *16*, 3824−3835.

(239) Yoshizawa, M.; Hattori, Y.; Kobayashi, T. Femtosecond Time-Resolved Resonance Raman Gain Spectroscopy in Polydiacetylene. *Phys. Rev. B: Condens. Matter Mater. Phys.* **1994**, *49*, 13259−13262.

(240) McCamant, D. W.; Kukura, P.; Mathies, R. A. Femtosecond Time-Resolved Stimulated Raman Spectroscopy: Application to the Ultrafast Internal Conversion in *β*-Carotene. *J. Phys. Chem. A* **2003**, *107*, 8208−8214.

(241) Frontiera, R. R.; Fang, C.; Dasgupta, J.; Mathies, R. A. Probing Structural Evolution along Multidimensional Reaction Coordinates with Femtosecond Stimulated Raman Spectroscopy. *Phys. Chem. Chem. Phys.* **2012**, *14*, 405−414.

(242) Prince, R. C.; Frontiera, R. R.; Potma, E. O. Stimulated Raman Scattering: From Bulk To Nano. *Chem. Rev.* **2017**, *117*, 5070−5094.

(243) Kardaś, T. M.; Ratajska-Gadomska, B.; Lapini, A.; Ragnoni, E.; Righini, R.; di Donato, M.; Foggi, P.; Gadomski, W. Dynamics of the Time-Resolved Stimulated Raman Scattering Spectrum in Presence of Transient Vibronic Inversion of Population on the Example of Optically Excited Trans-*β*-apo-8′-Carotenal. *J. Chem. Phys.* **2014**, *140*, 204312.

(244) Takaya, T.; Iwata, K. Relaxation Mechanism of *β*-Carotene from S2 (1Bu$^+$) State to S1 (2Ag$^-$) State: Femtosecond Time-Resolved Near-

IR Absorption and Stimulated Resonance Raman Studies in 900−1550 nm Region. *J. Phys. Chem. A* **2014**, *118*, 4071−4078.

(245) Quick, M.; Dobryakov, A. L.; Kovalenko, S. A.; Ernsting, N. P. Resonance Femtosecond-Stimulated Raman Spectroscopy without Actinic Excitation Showing Low-Frequency Vibrational Activity in the S2 State of all-Trans β-Carotene. *J. Phys. Chem. Lett.* **2015**, *6*, 1216−1220.

(246) Redeckas, K.; Voiciuk, V.; Vengris, M. Investigation of the S1/ICT Equilibrium in Fucoxanthin by Ultrafast Pump-Dump-Probe and Femtosecond Stimulated Raman Scattering Spectroscopy. *Photosynth. Res.* **2016**, *128*, 169−181.

(247) Ruchira Silva, W.; Frontiera, R. R. Excited State Structural Evolution During Charge-Transfer Reactions in Betaine-30. *Phys. Chem. Chem. Phys.* **2016**, *18*, 20290−20297.

(248) Weigel, A.; Dobryakov, A.; Klaumünzer, B.; Sajadi, M.; Saalfrank, P.; Ernsting, N. P. Femtosecond Stimulated Raman Spectroscopy of Flavin after Optical Excitation. *J. Phys. Chem. B* **2011**, *115*, 3656−3680.

(249) Ferrante, C.; Pontecorvo, E.; Cerullo, G.; Vos, M. H.; Scopigno, T. Direct Observation of Subpicosecond Vibrational Dynamics in Photoexcited Myoglobin. *Nat. Chem.* **2016**, *8*, 1137−1143.

(250) Fang, C.; Frontiera, R. R.; Tran, R.; Mathies, R. A. Mapping Gfp Structure Evolution During Proton Transfer with Femtosecond Raman Spectroscopy. *Nature* **2009**, *462*, 200−204.

(251) Liu, W.; Han, F.; Smith, C.; Fang, C. Ultrafast Conformational Dynamics of Pyranine During Excited State Proton Transfer in Aqueous Solution Revealed by Femtosecond Stimulated Raman Spectroscopy. *J. Phys. Chem. B* **2012**, *116*, 10535−10550.

(252) Han, F.; Liu, W.; Fang, C. Excited-State Proton Transfer of Photoexcited Pyranine in Water Observed by Femtosecond Stimulated Raman Spectroscopy. *Chem. Phys.* **2013**, *422*, 204−219.

(253) Liu, W.; Wang, Y.; Tang, L.; Oscar, B. G.; Zhu, L.; Fang, C. Panoramic Portrait of Primary Molecular Events Preceding Excited State Proton Transfer in Water. *Chem. Sci.* **2016**, *7*, 5484−5494.

(254) Creelman, M.; Kumauchi, M.; Hoff, W. D.; Mathies, R. A. Chromophore Dynamics in the Pyp Photocycle From Femtosecond Stimulated Raman Spectroscopy. *J. Phys. Chem. B* **2014**, *118*, 659−667.

(255) Han, F.; Liu, W.; Zhu, L.; Wang, Y.; Fang, C. Initial Hydrogen-Bonding Dynamics of Photoexcited Coumarin in Solution with Femtosecond Stimulated Raman Spectroscopy. *J. Mater. Chem. C* **2016**, *4*, 2954−2963.

(256) Yoon, S.; Kukura, P.; Stuart, C. M.; Mathies, R. A. Direct Observation of the Ultrafast Intersystem Crossing in Tris(2,2′-Bipyridine)Ruthenium(II) Using Femtosecond Stimulated Raman Spectroscopy. *Mol. Phys.* **2006**, *104*, 1275−1282.

(257) Frontiera, R. R.; Dasgupta, J.; Mathies, R. A. Probing Interfacial Electron Transfer in Coumarin 343 Sensitized TiO_2 Nanoparticles with Femtosecond Stimulated Raman. *J. Am. Chem. Soc.* **2009**, *131*, 15630−15632.

(258) Rhinehart, J. M.; Challa, J. R.; McCamant, D. W. Multimode Charge-Transfer Dynamics of 4-(Dimethylamino)Benzonitrile Probed with Ultraviolet Femtosecond Stimulated Raman Spectroscopy. *J. Phys. Chem. B* **2012**, *116*, 10522−10534.

(259) Magnanelli, T. J.; Bragg, A. E. Time-Resolved Raman Spectroscopy of Polaron Pair Formation in Poly(3-Hexylthiophene) Aggregates. *J. Phys. Chem. Lett.* **2015**, *6*, 438−445.

(260) Hoffman, D. P.; Leblebici, S. Y.; Schwartzberg, A. M.; Mathies, R. A. Exciton Mobility in Organic Photovoltaic Heterojunctions From Femtosecond Stimulated Raman. *J. Phys. Chem. Lett.* **2015**, *6*, 2919−2923.

(261) Zhou, J.; Yu, W.; Bragg, A. E. Structural Relaxation of Photoexcited Quaterthiophenes Probed with Vibrational Specificity. *J. Phys. Chem. Lett.* **2015**, *6*, 3496−3502.

(262) Hoffman, D. P.; Mathies, R. A. Photoexcited Structural Dynamics of an Azobenzene Analog 4-Nitro-4′-Dimethylamino-Azobenzene From Femtosecond Stimulated Raman. *Phys. Chem. Chem. Phys.* **2012**, *14*, 6298−6306.

(263) Pontecorvo, E.; Ferrante, C.; Elles, C. G.; Scopigno, T. Structural Rearrangement Accompanying the Ultrafast Electrocyclization Reaction of a Photochromic Molecular Switch. *J. Phys. Chem. B* **2014**, *118*, 6915−6921.

(264) Frobel, S.; Buschhaus, L.; Villnow, T.; Weingart, O.; Gilch, P. The Photoformation of a Phthalide: a Ketene Intermediate Traced by FSRS. *Phys. Chem. Chem. Phys.* **2015**, *17*, 376−386.

(265) Nelson, T.; Bjorgaard, J.; Greenfield, M.; Bolme, C.; Brown, K.; McGrane, S.; Scharff, R. J.; Tretiak, S. Ultrafast Photodissociation Dynamics of Nitromethane. *J. Phys. Chem. A* **2016**, *120*, 519−526.

(266) Hoffman, D. P.; Ellis, S. R.; Mathies, R. A. Characterization of a Conical Intersection in a Charge-Transfer Dimer with Two-Dimensional Time-Resolved Stimulated Raman Spectroscopy. *J. Phys. Chem. A* **2014**, *118*, 4955−4965.

(267) Hoffman, D. P.; Mathies, R. A. Femtosecond Stimulated Raman Exposes the Role of Vibrational Coherence in Condensed-Phase Photoreactivity. *Acc. Chem. Res.* **2016**, *49*, 616−625.

(268) Frontiera, R. R.; Henry, A.-I.; Gruenke, N. L.; Van Duyne, R. P. Surface-Enhanced Femtosecond Stimulated Raman Spectroscopy. *J. Phys. Chem. Lett.* **2011**, *2*, 1199−1203.

(269) Molesky, B. P.; Guo, Z.; Moran, A. M. Femtosecond Stimulated Raman Spectroscopy by Six-Wave Mixing. *J. Chem. Phys.* **2015**, *142*, 212405.

(270) Dhar, L.; Rogers, J. A.; Nelson, K. A. Time-Resolved Vibrational Spectroscopy in the Impulsive Limit. *Chem. Rev.* **1994**, *94*, 157−193.

(271) Voehringer, P.; Scherer, N. F. Transient Grating Optical Heterodyne Detected Impulsive Stimulated Raman Scattering in Simple Liquids. *J. Phys. Chem.* **1995**, *99*, 2684−2695.

(272) Marek, M. S.; Buckup, T.; Southall, J.; Cogdell, R. J.; Motzkus, M. Highlighting Short-Lived Excited Electronic States with Pump-Degenerate-Four-Wave-Mixing. *J. Chem. Phys.* **2013**, *139*, 074202.

(273) Miki, T.; Buckup, T.; Krause, M. S.; Southall, J.; Cogdell, R. J.; Motzkus, M. Vibronic Coupling in the Excited-States of Carotenoids. *Phys. Chem. Chem. Phys.* **2016**, *18*, 11443−11453.

(274) Kraack, J. P.; Buckup, T.; Motzkus, M. Coherent High-Frequency Vibrational Dynamics in the Excited Electronic State of all-Trans Retinal Derivatives. *J. Phys. Chem. Lett.* **2013**, *4*, 383−387.

(275) Kraack, J. P.; Buckup, T.; Motzkus, M. Evidence For the Two-State-Two-Mode Model in Retinal Protonated Schiff-Bases From Pump Degenerate Four-Wave-Mixing Experiments. *Phys. Chem. Chem. Phys.* **2012**, *14*, 13979−13988.

(276) Takeuchi, S.; Ruhman, S.; Tsuneda, T.; Chiba, M.; Taketsugu, T.; Tahara, T. Spectroscopic Tracking of Structural Evolution in Ultrafast Stilbene Photoisomerization. *Science* **2008**, *322*, 1073−1077.

(277) Kahan, A.; Nahmias, O.; Friedman, N.; Sheves, M.; Ruhman, S. Following Photoinduced Dynamics in Bacteriorhodopsin with 7-fs Impulsive Vibrational Spectroscopy. *J. Am. Chem. Soc.* **2007**, *129*, 537−546.

(278) Fujisawa, T.; Kuramochi, H.; Hosoi, H.; Takeuchi, S.; Tahara, T. Role of Coherent Low-Frequency Motion in Excited-State Proton Transfer of Green Fluorescent Protein Studied by Time-Resolved Impulsive Stimulated Raman Spectroscopy. *J. Am. Chem. Soc.* **2016**, *138*, 3942−3945.

(279) Kuramochi, H.; Takeuchi, S.; Tahara, T. Femtosecond Time-Resolved Impulsive Stimulated Raman Spectroscopy Using Sub-7-fs Pulses: Apparatus and Applications. *Rev. Sci. Instrum.* **2016**, *87*, 043107.

(280) Kruglik, S. G.; Lambry, J.-C.; Martin, J.-L.; Vos, M. H.; Negrerie, M. Sub-Picosecond Raman Spectrometer For Time-Resolved Studies of Structural Dynamics in Heme Proteins. *J. Raman Spectrosc.* **2011**, *42*, 265−275.

(281) Sahoo, S. K.; Umapathy, S.; Parker, A. W. Time-Resolved Resonance Raman Spectroscopy: Exploring Reactive Intermediates. *Appl. Spectrosc.* **2011**, *65*, 1087−1115.

(282) Lee, Y. J.; Cicerone, M. T. Vibrational Dephasing Time Imaging by Time-Resolved Broadband Coherent Anti-Stokes Raman Scattering Microscopy. *Appl. Phys. Lett.* **2008**, *92*, 041108.

(283) Gai, F.; Hasson, K. C.; McDonald, J. C.; Anfinrud, P. A. Chemical Dynamics in Proteins: the Photoisomerization of Retinal in Bacteriorhodopsin. *Science* **1998**, *279*, 1886−1891.

(284) Mundt, R.; Villnow, T.; Ziegenbein, C. T.; Gilch, P.; Marian, C.; Rai-Constapel, V. Thioxanthone in Apolar Solvents: Ultrafast Internal

Conversion Precedes Fast Intersystem Crossing. *Phys. Chem. Chem. Phys.* **2016**, *18*, 6637−6647.

(285) Riedle, E.; Bradler, M.; Wenninger, M.; Sailer, C. F.; Pugliesi, I. Electronic Transient Spectroscopy From the Deep UV To the NIR: Unambiguous Disentanglement of Complex Processes. *Faraday Discuss.* **2013**, *163*, 139−158.

(286) Riedle, E.; Roos, M. K.; Thallmair, S.; Sailer, C. F.; Krebs, N.; Fingerhut, B. P.; de Vivie-Riedle, R. Ultrafast Photochemistry with Two Product Channels: Wavepacket Motion Through Two Distinct Conical Intersections. *Chem. Phys. Lett.* **2017**, *683*, 128.

(287) Johnson, P. J. M.; Halpin, A.; Morizumi, T.; Prokhorenko, V. I.; Ernst, O. P.; Miller, R. J. D. Local Vibrational Coherences Drive the Primary Photochemistry of Vision. *Nat. Chem.* **2015**, *7*, 980−986.

(288) Krauter, C. M.; Mohring, J.; Buckup, T.; Pernpointner, M.; Motzkus, M. Ultrafast Branching in the Excited State of Coumarin and Umbelliferone. *Phys. Chem. Chem. Phys.* **2013**, *15*, 17846−17861.

(289) Buckup, T.; Sarter, C.; Volpp, H.-R.; Jäschke, A.; Motzkus, M. Ultrafast Time-Resolved Spectroscopy of Diarylethene-Based Photoswitchable Deoxyuridine Nucleosides. *J. Phys. Chem. Lett.* **2015**, *6*, 4717−4721.

(290) Johnson, P. J. M.; Halpin, A.; Morizumi, T.; Brown, L. S.; Prokhorenko, V. I.; Ernst, O. P.; Dwayne Miller, R. J. The Photocycle and Ultrafast Vibrational Dynamics of Bacteriorhodopsin in Lipid Nanodiscs. *Phys. Chem. Chem. Phys.* **2014**, *16*, 21310−21320.

(291) Balevicius, V.; Pour, A. G.; Savolainen, J.; Lincoln, C. N.; Lukes, V.; Riedle, E.; Valkunas, L.; Abramavicius, D.; Hauer, J. Vibronic Energy Relaxation Approach Highlighting Deactivation Pathways in Carotenoids. *Phys. Chem. Chem. Phys.* **2015**, *17*, 19491−19499.

(292) Iyer, E. S. S.; Gdor, I.; Eliash, T.; Sheves, M.; Ruhman, S. Efficient Femtosecond Energy Transfer From Carotenoid To Retinal in Gloeobacter Rhodopsin-Salinixanthin Complex. *J. Phys. Chem. B* **2015**, *119*, 2345−2349.

(293) Rozin, R.; Wand, A.; Jung, K.-H.; Ruhman, S.; Sheves, M. pH Dependence of anabaena Sensory Rhodopsin: Retinal Isomer Composition, Rate of Dark Adaptation, and Photochemistry. *J. Phys. Chem. B* **2014**, *118*, 8995−9006.

(294) Chen, J.; Kohler, B. Base Stacking in adenosine Dimers Revealed by Femtosecond Transient absorption Spectroscopy. *J. Am. Chem. Soc.* **2014**, *136*, 6362−6372.

(295) Kahan, A.; Wand, A.; Ruhman, S.; Zilberg, S.; Haas, Y. Solvent Tuning of a Conical Intersection: Direct Experimental Verification of a Theoretical Prediction. *J. Phys. Chem. A* **2011**, *115*, 10854−10861.

(296) Guo, Z.; Giokas, P. G.; Cheshire, T. P.; Williams, O. F.; Dirkes, D. J.; You, W.; Moran, A. M. Ultrafast Spectroscopic Signatures of Coherent Electron-Transfer Mechanisms in a Transition Metal Complex. *J. Phys. Chem. A* **2016**, *120*, 5773−5790.

(297) Polli, D.; Grancini, G.; Clark, J.; Celebrano, M.; Virgili, T.; Cerullo, G.; Lanzani, G. Nanoscale Imaging of the Interface Dynamics in Polymer Blends by Femtosecond Pump-Probe Confocal Microscopy. *Adv. Mater.* **2010**, *22*, 3048−3051.

(298) Schnedermann, C.; Lim, J. M.; Wende, T.; Duarte, A. S.; Ni, L.; Gu, Q.; Sadhanala, A.; Rao, A.; Kukura, P. Sub-10 fs Time-Resolved Vibronic Optical Microscopy. *J. Phys. Chem. Lett.* **2016**, *7*, 4854−4859.

(299) Grumstrup, E. M.; Gabriel, M. M.; Cating, E. E. M.; van Goethem, E. M.; Papanikolas, J. M. Pump-Probe Microscopy: Visualization and Spectroscopy of Ultrafast Dynamics at the Nanoscale. *Chem. Phys.* **2015**, *458*, 30−40.

(300) Davydova, D.; de la Cadena, A.; Akimov, D.; Dietzek, B. Transient Absorption Microscopy: Advances in Chemical Imaging of Photoinduced Dynamics. *Laser Photonic Rev.* **2016**, *10*, 62−81.

(301) Fischer, M. C.; Wilson, J. W.; Robles, F. E.; Warren, W. S. Invited Review article: Pump-Probe Microscopy. *Rev. Sci. Instrum.* **2016**, *87*, 031101.

(302) Gdor, I.; Zhu, J.; Loevsky, B.; Smolensky, E.; Friedman, N.; Sheves, M.; Ruhman, S. Investigating Excited State Dynamics of Salinixanthin and Xanthorhodopsin in the Near-Infrared. *Phys. Chem. Chem. Phys.* **2011**, *13*, 3782−3787.

(303) Loevsky, B.; Wand, A.; Bismuth, O.; Friedman, N.; Sheves, M.; Ruhman, S. A New Spectral Window on Retinal Protein Photochemistry. *J. Am. Chem. Soc.* **2011**, *133*, 1626−1629.

(304) Holzapfel, W.; Finkele, U.; Kaiser, W.; Oesterhelt, D.; Scheer, H.; Stilz, H. U.; Zinth, W. Initial Electron-Transfer in the Reaction Center From Rhodobacter Sphaeroides. *Proc. Natl. Acad. Sci. U. S. A.* **1990**, *87*, 5168−5172.

(305) Zinth, W.; Wachtveitl, J. The First Picoseconds in Bacterial Photosynthesis−Ultrafast Electron Transfer For the Efficient Conversion of Light Energy. *ChemPhysChem* **2005**, *6*, 871−880.

(306) Zhu, J.; van Stokkum, I. H.; Paparelli, L.; Jones, M. R.; Groot, M. L. Early Bacteriopheophytin Reduction in Charge Separation in Reaction Centers of Rhodobacter Sphaeroides. *Biophys. J.* **2013**, *104*, 2493−2502.

(307) Dominguez, P. N.; Himmelstoss, M.; Michelmann, J.; Lehner, F. T.; Gardiner, A. T.; Cogdell, R. J.; Zinth, W. Primary Reactions in Photosynthetic Reaction Centers of Rhodobacter Sphaeroides - Time Constants of the Initial Electron Transfer. *Chem. Phys. Lett.* **2014**, *601*, 103−109.

(308) Wand, A.; Loevsky, B.; Friedman, N.; Sheves, M.; Ruhman, S. Probing Ultrafast Photochemistry of Retinal Proteins in the Near-IR: Bacteriorhodopsin and anabaena Sensory Rhodopsin vs Retinal Protonated Schiff Base in Solution. *J. Phys. Chem. B* **2013**, *117*, 4670−4679.

(309) Schenkl, S.; van Mourik, F.; Friedman, N.; Sheves, M.; Schlesinger, R.; Haacke, S.; Chergui, M. Insights into Excited-State and Isomerization Dynamics of Bacteriorhodopsin From Ultrafast Transient UV Absorption. *Proc. Natl. Acad. Sci. U. S. A.* **2006**, *103*, 4101−4106.

(310) Kobayashi, T.; Kida, Y. Ultrafast Spectroscopy with Sub-10 fs Deep-Ultraviolet Pulses. *Phys. Chem. Chem. Phys.* **2012**, *14*, 6200−6210.

(311) Fingerhut, B. P. Sailer, C. F.; Ammer, J.; Riedle, E.; de Vivie-Riedle, R. Buildup and Decay of the Optical Absorption in the Ultrafast Photo-Generation and Reaction of Benzhydryl Cations in Solution. *J. Phys. Chem. A* **2012**, *116*, 11064−11074.

(312) Sailer, C. F.; Krebs, N.; Fingerhut, B. P.; de Vivie-Riedle, R.; Riedle, E. Wavepacket Splitting in the First 100 fs Determines the Products From the Bond Cleavage of Diphenylmethylchloride. *EPJ Web Conf.* **2013**, *41*, 05042.

(313) Ajdarzadeh, A.; Consani, C.; Bräm, O.; Tortschanoff, A.; Cannizzo, A.; Chergui, M. Ultraviolet Transient Absorption, Transient Grating and Photon Echo Studies of Aqueous Tryptophan. *Chem. Phys.* **2013**, *422*, 47−52.

(314) West, B. A.; Molesky, B. P.; Giokas, P. G.; Moran, A. M. Uncovering Molecular Relaxation Processes with Nonlinear Spectroscopies in the Deep UV. *Chem. Phys.* **2013**, *423*, 92−104.

(315) Cannizzo, A. Ultrafast UV Spectroscopy: From a Local To a Global View of Dynamical Processes in Macromolecules. *Phys. Chem. Chem. Phys.* **2012**, *14*, 11205−11223.

(316) Fingerhut, B. P.; Geppert, D.; de Vivie-Riedle, R. Ultrafast Dissociation Pathways of Diphenylmethyl Chloride To Generate Reactive Carbo Cations. *Chem. Phys.* **2008**, *343*, 329−339.

(317) Bishop, M. M.; Roscioli, J. D.; Ghosh, S.; Mueller, J. J.; Shepherd, N. C.; Beck, W. F. Vibrationally Coherent Preparation of the Transition State For Photoisomerization of the Cyanine Dye Cy5 in Water. *J. Phys. Chem. B* **2015**, *119*, 6905−6915.

(318) Cheminal, A.; Leonard, J.; Kim, S.-Y.; Jung, K.-H.; Kandori, H.; Haacke, S. 100 fs Photo-isomerization with Vibrational Coherences but Low Quantum Yield in anabaena Sensory Rhodopsin. *Phys. Chem. Chem. Phys.* **2015**, *17*, 25429−25439.

(319) Gueye, M.; Nillon, J.; Crégut, O.; Léonard, J. Broadband UV-Vis Vibrational Coherence Spectrometer Based on a Hollow Fiber Compressor. *Rev. Sci. Instrum.* **2016**, *87*, 093109.

(320) Nuernberger, P.; Ruetzel, S.; Brixner, T. Multidimensional Electronic Spectroscopy of Photochemical Reactions. *Angew. Chem., Int. Ed.* **2015**, *54*, 11368−11386.

(321) Brazard, J.; Bizimana, L. A.; Gellen, T.; Carbery, W. P.; Turner, D. B. Experimental Detection of Branching at a Conical Intersection in a Highly Fluorescent Molecule. *J. Phys. Chem. Lett.* **2016**, *7*, 14−19.

(322) Jumper, C. C.; Arpin, P. C.; Turner, D. B.; McClure, S. D.; Rafiq, S.; Dean, J. C.; Cina, J. A.; Kovac, P. A.; Mirkovic, T.; Scholes, G. D. Broad-Band Pump-Probe Spectroscopy Quantifies Ultrafast Solvation Dynamics of Proteins and Molecules. *J. Phys. Chem. Lett.* **2016**, *7*, 4722−4731.

(323) Fragnito, H.; Bigot, J.-Y.; Becker, P.; Shank, C. Evolution of the Vibronic Absorption Spectrum in a Molecule Following Impulsive Excitation with a 6 fs Optical Pulse. *Chem. Phys. Lett.* **1989**, *160*, 101−104.

(324) Wang, Q.; Schoenlein, R.; Peteanu, L.; Mathies, R.; Shank, C. Vibrationally Coherent Photochemistry in the Femtosecond Primary Event of Vision. *Science* **1994**, *266*, 422−424.

(325) Zhu, L.; Sage, J.; Champion, P. Observation of Coherent Reaction Dynamics in Heme Proteins. *Science* **1994**, *266*, 629−632.

(326) Rosca, F.; Kumar, A. T. N.; Ye, X.; Sjodin, T.; Demidov, A. A.; Champion, P. M. Investigations of Coherent Vibrational Oscillations in Myoglobin. *J. Phys. Chem. A* **2000**, *104*, 4280−4290.

(327) Kumar, A. T. N.; Rosca, F.; Widom, A.; Champion, P. M. Investigations of Amplitude and Phase Excitation Profiles in Femtosecond Coherence Spectroscopy. *J. Chem. Phys.* **2001**, *114*, 701−724.

(328) Cina, J. A.; Kovac, P. A.; Jumper, C. C.; Dean, J. C.; Scholes, G. D. Ultrafast Transient absorption Revisited: Phase-Flips, Spectral Fingers, and Other Dynamical Features. *J. Chem. Phys.* **2016**, *144*, 175102.

(329) Meshulach, D.; Silberberg, Y. Coherent Quantum Control of Two-Photon Transitions by a Femtosecond Laser Pulse. *Nature* **1998**, *396*, 239−242.

(330) Dudovich, N.; Oron, D.; Silberberg, Y. Single-Pulse Coherently Controlled Nonlinear Raman Spectroscopy and Microscopy. *Nature* **2002**, *418*, 512−514.

(331) Silberberg, Y. Quantum Coherent Control For Nonlinear Spectroscopy and Microscopy. *Annu. Rev. Phys. Chem.* **2009**, *60*, 277−292.

(332) Lozovoy, V. V.; Pastirk, I.; Walowicz, K. A.; Dantus, M. Multiphoton Intrapulse Interference. II. Control of Two- and Three-Photon Laser Induced Fluorescence with Shaped Pulses. *J. Chem. Phys.* **2003**, *118*, 3187−3196.

(333) Lozovoy, V. V.; Pastirk, I.; Dantus, M. Multiphoton Intrapulse Interference.IV.Ultrashort Laser Pulse Spectral Phase Characterization and Compensation. *Opt. Lett.* **2004**, *29*, 775−777.

(334) Konar, A.; Shah, J. D.; Lozovoy, V. V.; Dantus, M. Optical Response of Fluorescent Molecules Studied by Synthetic Femtosecond Laser Pulses. *J. Phys. Chem. Lett.* **2012**, *3*, 1329−1335.

(335) Konar, A.; Lozovoy, V. V.; Dantus, M. Solvation Stokes-Shift Dynamics Studied by Chirped Femtosecond Laser Pulses. *J. Phys. Chem. Lett.* **2012**, *3*, 2458−2464.

(336) Frostig, H.; Bayer, T.; Dudovich, N.; Eldar, Y. C.; Silberberg, Y. Single-Beam Spectrally Controlled Two-Dimensional Raman Spectroscopy. *Nat. Photonics* **2015**, *9*, 339−343.

(337) Harbola, U.; Mukamel, S. Superoperator Nonequilibrium Green's Function Theory of Many-Body Systems; Applications To Charge Transfer and Transport in Open Junctions. *Phys. Rep.* **2008**, *465*, 191−222.

(338) Lee, S.-Y.; Zhang, D.; McCamant, D. W.; Kukura, P.; Mathies, R. A. Theory of Femtosecond Stimulated Raman Spectroscopy. *J. Chem. Phys.* **2004**, *121*, 3632−3642.

(339) Kumar, A. T. N.; Rosca, F.; Widom, A.; Champion, P. M. Investigations of Ultrafast Nuclear Response Induced by Resonant and Nonresonant Laser Pulses. *J. Chem. Phys.* **2001**, *114*, 6795−6815.

(340) Liebel, M.; Kukura, P. Broad-Band Impulsive Vibrational Spectroscopy of Excited Electronic States in the Time Domain. *J. Phys. Chem. Lett.* **2013**, *4*, 1358−1364.

(341) Liebel, M.; Schnedermann, C.; Wende, T.; Kukura, P. Principles and Applications of Broadband Impulsive Vibrational Spectroscopy. *J. Phys. Chem. A* **2015**, *119*, 9506−9517.

(342) Wilhelm, T.; Piel, J.; Riedle, E. Sub-20-fs Pulses Tunable Across the Visible From a Blue-Pumped Single-Pass Noncollinear Parametric Converter. *Opt. Lett.* **1997**, *22*, 1494−1496.

(343) Riedle, E.; Beutter, M.; Lochbrunner, S.; Piel, J.; Schenkl, S. Spörlein, S.; Zinth, W. Generation of 10 to 50 fs Pulses Tunable Through all of the Visible and the NIR. *Appl. Phys. B: Lasers Opt.* **2000**, *71*, 457−465.

(344) Cerullo, G.; de Silvestri, S. Ultrafast Optical Parametric Amplifiers. *Rev. Sci. Instrum.* **2003**, *74*, 1−18.

(345) Bradler, M.; Baum, P.; Riedle, E. Femtosecond Continuum Generation in Bulk Laser Host Materials with Sub-μJ Pump Pulses. *Appl. Phys. B: Lasers Opt.* **2009**, *97*, 561.

(346) Liebel, M.; Schnedermann, C.; Kukura, P. Sub-10-fs Pulses Tunable From 480 to 980 nm From a NOPA Pumped by an Yb:KGW Source. *Opt. Lett.* **2014**, *39*, 4112−4115.

(347) Musser, A. J.; Liebel, M.; Schnedermann, C.; Wende, T.; Kehoe, T. B.; Rao, A.; Kukura, P. Evidence For Conical Intersection Dynamics Mediating Ultrafast Singlet Exciton Fission. *Nat. Phys.* **2015**, *11*, 352−357.

(348) Schnedermann, C.; Liebel, M.; Kukura, P. Mode-Specificity of Vibrationally Coherent Internal Conversion in Rhodopsin During the Primary Visual Event. *J. Am. Chem. Soc.* **2015**, *137*, 2886−2891.

(349) Schnedermann, C.; Muders, V.; Ehrenberg, D.; Schlesinger, R.; Kukura, P.; Heberle, J. Vibronic Dynamics of the Ultrafast all-Trans to 13-Cis Photoisomerization of Retinal in Channelrhodopsin-1. *J. Am. Chem. Soc.* **2016**, *138*, 4757−4762.

(350) Liebel, M.; Schnedermann, C.; Bassolino, G.; Taylor, G.; Watts, A.; Kukura, P. Direct Observation of the Coherent Nuclear Response after the Absorption of a Photon. *Phys. Rev. Lett.* **2014**, *112*, 238301.

(351) Liebel, M.; Schnedermann, C.; Kukura, P. Vibrationally Coherent Crossing and Coupling of Electronic States During Internal Conversion in β-Carotene. *Phys. Rev. Lett.* **2014**, *112*, 198302.

(352) Hamm, P.; Lim, M.; Hochstrasser, R. M. Structure of the Amide I Band of Peptides Measured by Femtosecond Nonlinear-Infrared Spectroscopy. *J. Phys. Chem. B* **1998**, *102*, 6123−6138.

(353) Hochstrasser, R. M. Two-Dimensional Spectroscopy at Infrared and Optical Frequencies. *Proc. Natl. Acad. Sci. U. S. A.* **2007**, *104*, 14190−14196.

(354) Brixner, T.; Stenger, J.; Vaswani, H. M.; Cho, M.; Blankenship, R. E.; Fleming, G. R. Two-Dimensional Spectroscopy of Electronic Couplings in Photosynthesis. *Nature* **2005**, *434*, 625−628.

(355) Cho, M. Coherent Two-Dimensional Optical Spectroscopy. *Chem. Rev.* **2008**, *108*, 1331−1418.

(356) Cheng, Y.-C.; Fleming, G. R. Dynamics of Light Harvesting in Photosynthesis. *Annu. Rev. Phys. Chem.* **2009**, *60*, 241−262.

(357) Fuller, F. D.; Ogilvie, J. P. Experimental Implementations of Two-Dimensional Fourier Transform Electronic Spectroscopy. *Annu. Rev. Phys. Chem.* **2015**, *66*, 667−690.

(358) Chenu, A.; Scholes, G. D. Coherence in Energy Transfer and Photosynthesis. *Annu. Rev. Phys. Chem.* **2015**, *66*, 69−96.

(359) Nardin, G. Multidimensional Coherent Optical Spectroscopy of Semiconductor Nanostructures: a Review. *Semicond. Sci. Technol.* **2016**, *31*, 023001.

(360) Dean, J. C.; Rafiq, S.; Oblinsky, D. G.; Cassette, E. Jumper, C. C.; Scholes, G. D. Broadband Transient Absorption and Two-Dimensional Electronic Spectroscopy of Methylene Blue. *J. Phys. Chem. A* **2015**, *119*, 9098−9108.

(361) Rafiq, S.; Dean, J. C.; Scholes, G. D. Observing Vibrational Wavepackets During an Ultrafast Electron Transfer Reaction. *J. Phys. Chem. A* **2015**, *119*, 11837−11846.

(362) Lim, J.; Paleček, D.; Caycedo-Soler, F.; Lincoln, C. N.; Prior, J.; von Berlepsch, H.; Huelga, S. F.; Plenio, M. B.; Zigmantas, D.; Hauer, J. Vibronic Origin of Long-Lived Coherence in an Artificial Molecular Light Harvester. *Nat. Commun.* **2015**, *6*, 7755.

(363) Guo, Z.; Giokas, P. G.; Cheshire, T. P.; Williams, O. F.; Dirkes, D. J.; You, W.; Moran, A. M. Communication: Uncovering Correlated Vibrational Cooling and Electron Transfer Dynamics with Multidimensional Spectroscopy. *J. Chem. Phys.* **2016**, *145*, 101101.

(364) Dean, J. C.; Oblinsky, D. G.; Rafiq, S.; Scholes, G. D. Methylene Blue Exciton States Steer Nonradiative Relaxation: Ultrafast Spectroscopy of Methylene Blue Dimer. *J. Phys. Chem. B* **2016**, *120*, 440−454.

(365) Tempelaar, R.; Halpin, A.; Johnson, P. J. M.; Cai, J.; Murphy, R. S.; Knoester, J.; Miller, R. J. D.; Jansen, T. L. C. Laser-Limited Signatures of Quantum Coherence. *J. Phys. Chem. A* **2016**, *120*, 3042−3048.

(366) Bakulin, A. A.; Morgan, S. E.; Kehoe, T. B.; Wilson, M. W. B.; Chin, A. W.; Zigmantas, D.; Egorova, D.; Rao, A. Real-Time Observation of Multiexcitonic States in Ultrafast Singlet Fission Using Coherent 2D Electronic Spectroscopy. *Nat. Chem.* **2016**, *8*, 16−23.

(367) Gellen, T. A.; Bizimana, L. A.; Carbery, W. P.; Breen, I.; Turner, D. B. Ultrabroadband Two-Quantum Two-Dimensional Electronic Spectroscopy. *J. Chem. Phys.* **2016**, *145*, 064201.

(368) Dostál, J.; Pšenčík, J.; Zigmantas, D. in Situ Mapping of the Energy Flow Through the Entire Photosynthetic Apparatus. *Nat. Chem.* **2016**, *8*, 705−710.

(369) Duan, H.-G.; Miller, R. J. D.; Thorwart, M. Impact of Vibrational Coherence on the Quantum Yield at a Conical Intersection. *J. Phys. Chem. Lett.* **2016**, *7*, 3491−3496.

(370) Duan, H.-G.; Thorwart, M. Quantum Mechanical Wave Packet Dynamics at a Conical Intersection with Strong Vibrational Dissipation. *J. Phys. Chem. Lett.* **2016**, *7*, 382−386.

(371) Richter, M.; Fingerhut, B. P. Simulation of Multi-Dimensional Signals in the Optical Domain: Quantum-Classical Feedback in Nonlinear Exciton Propagation. *J. Chem. Theory Comput.* **2016**, *12*, 3284.

(372) Tseng, C.; Matsika, S.; Weinacht, T. C. Two-Dimensional Ultrafast Fourier Transform Spectroscopy in the Deep Ultraviolet. *Opt. Express* **2009**, *17*, 18788−18793.

(373) Selig, U.; Schleussner, C.-F.; Foerster, M.; Langhojer, F.; Nuernberger, P.; Brixner, T. Coherent Two-Dimensional Ultraviolet Spectroscopy in Fully Noncollinear Geometry. *Opt. Lett.* **2010**, *35*, 4178−4180.

(374) West, B. A.; Womick, J. M.; Moran, A. M. Probing Ultrafast Dynamics in Adenine with Mid-UV Four-Wave Mixing Spectroscopies. *J. Phys. Chem. A* **2011**, *115*, 8630−8637.

(375) Brida, D.; Manzoni, C.; Cerullo, G. Phase-Locked Pulses For Two-Dimensional Spectroscopy by a Birefringent Delay Line. *Opt. Lett.* **2012**, *37*, 3027−3029.

(376) Auböck, G.; Consani, C.; van Mourik, F.; Chergui, M. Ultrabroadband Femtosecond Two-Dimensional Ultraviolet Transient Absorption. *Opt. Lett.* **2012**, *37*, 2337−2339.

(377) Consani, C. Auböck, G.; van Mourik, F.; Chergui, M. Ultrafast Tryptophan-To-Heme Electron Transfer in Myoglobins Revealed by UV 2D Spectroscopy. *Science* **2013**, *339*, 1586−1589.

(378) Krebs, N.; Pugliesi, I.; Hauer, J.; Riedle, E. Two-Dimensional Fourier Transform Spectroscopy in the Ultraviolet with Sub-20 fs Pump Pulses and 250−720 nm Supercontinuum Probe. *New J. Phys.* **2013**, *15*, 085016.

(379) Prokhorenko, V.; Picchiotti, A.; Maneshi, S.; Miller, D. Broadband Electronic Two- Dimensional Spectroscopy in the Deep UV. *19th International Conference on Ultrafast Phenomena*; 2014; p 09.Wed.A.4.

(380) Borrego-Varillas, R.; Oriana, A.; Ganzer, L.; Trifonov, A.; Buchvarov, I.; Manzoni, C.; Cerullo, G. Two-Dimensional Electronic Spectroscopy in the Ultraviolet by a Birefringent Delay Line. *Opt. Express* **2016**, *24*, 28491−28499.

(381) Jiang, J.; Mukamel, S. Two-Dimensional Ultraviolet (2DUV) Spectroscopic Tools For Identifying Fibrillation Propensity of Protein Residue Sequences. *Angew. Chem., Int. Ed.* **2010**, *49*, 9666−9669.

(382) Falvo, C.; Sanda, F.; Mukamel, S. In *Ultrafast Infrared Vibrational Spectroscopy*; Fayer, M. D., Ed.; Taylor & Francis: Milton Park, Oxfordshire, 2013; pp 405−435.

(383) Tempelaar, R.; van der Vegte, C. P.; Knoester, J.; Jansen, T. L. C. Surface Hopping Modeling of Two-Dimensional Spectra. *J. Chem. Phys.* **2013**, *138*, 164106.

(384) Abramavicius, D.; Voronine, D. V.; Mukamel, S. Unravelling Coherent Dynamics and Energy Dissipation in Photosynthetic Complexes by 2D Spectroscopy. *Biophys. J.* **2008**, *94*, 3613−3619.

(385) van der Vegte, C. P.; Dijkstra, A. G.; Knoester, J.; Jansen, T. L. C. Calculating Two-Dimensional Spectra with the Mixed Quantum-Classical Ehrenfest Method. *J. Phys. Chem. A* **2013**, *117*, 5970−5980.

(386) Petit, A. S.; Subotnik, J. E. Appraisal of Surface Hopping as a Tool For Modeling Condensed Phase Linear Absorption Spectra. *J. Chem. Theory Comput.* **2015**, *11*, 4328−4341.

(387) Kortüm, G.; Dreesen, G. Über die Konstitutionsabhängigkeit der Schwingungsstruktur im Absorptionsspektrum von Aromatischen Kohlenwasserstoffen. *Chem. Ber.* **1951**, *84*, 182−203.

(388) Nenov, A.; Giussani, A.; Fingerhut, B. P.; Rivalta, I.; Dumont, E.; Mukamel, S.; Garavelli, M. Spectral Lineshapes in Nonlinear Electronic Spectroscopy. *Phys. Chem. Chem. Phys.* **2015**, *17*, 30925−30936.

(389) Nenov, A.; Giussani, A.; Segarra-Martí, J.; Jaiswal, V. K.; Rivalta, I.; Cerullo, G.; Mukamel, S.; Garavelli, M. Modeling the High-Energy Electronic State Manifold of adenine: Calibration For Nonlinear Electronic Spectroscopy. *J. Chem. Phys.* **2015**, *142*, 212443.

(390) Maznev, A. A.; Nelson, K. A.; Rogers, J. A. Optical Heterodyne Detection of Laser-induced Gratings. *Opt. Lett.* **1998**, *23*, 1319−1321.

(391) Goodno, G. D.; Dadusc, G.; Miller, R. J. D. Ultrafast Heterodyne-Detected Transient-Grating Spectroscopy Using Diffractive Optics. *J. Opt. Soc. Am. B* **1998**, *15*, 1791−1794.

(392) Jonas, D. M. Two-Dimensional Femtosecond Spectroscopy. *Annu. Rev. Phys. Chem.* **2003**, *54*, 425−463.

(393) Lincoln, C. N.; Hayden, J.; Pour, A. G.; Perlík, V.; Šanda, F.; Hauer, J. A Quantitative Study of Coherent Vibrational Dynamics Probed by Heterodyned Transient Grating Spectroscopy. *Vib. Spectrosc.* **2016**, *85*, 167−174.

(394) Ghosh, S.; Bishop, M. M.; Roscioli, J. D.; Mueller, J. J.; Shepherd, N. C.; LaFountain, A. M.; Frank, H. A.; Beck, W. F. Femtosecond Heterodyne Transient-Grating Studies of Nonradiative Decay of the S2 (11Bu+) State of *β*-Carotene: Contributions from Dark Intermediates and Double-Quantum Coherences. *J. Phys. Chem. B* **2015**, *119*, 14905−14924.

(395) Ghosh, S.; Roscioli, J. D.; Bishop, M. M.; Gurchiek, J. K.; LaFountain, A. M.; Frank, H. A.; Beck, W. F. Torsional Dynamics and Intramolecular Charge Transfer in the S2 ($1^1B_u^+$) Excited State of Peridinin: a Mechanism For Enhanced Mid-Visible Light Harvesting. *J. Phys. Chem. Lett.* **2016**, *7*, 3621−3626.

(396) Ghosh, S.; Bishop, M. M.; Roscioli, J. D.; LaFountain, A. M.; Frank, H. A.; Beck, W. F. Femtosecond Heterodyne Transient Grating Studies of Nonradiative Deactivation of the S2 ($1^1B_u^+$) State of Peridinin: Detection and Spectroscopic Assignment of an Intermediate in the Decay Pathway. *J. Phys. Chem. B* **2016**, *120*, 3601−3614.

(397) Perlík, V.; Seibt, J.; Cranston, L. J.; Cogdell, R. J.; Lincoln, C. N.; Savolainen, J.; Šanda, F.; Mančal, T.; Hauer, J. Vibronic Coupling Explains the Ultrafast Carotenoid-to-Bacteriochlorophyll Energy Transfer in Natural and Artificial Light Harvesters. *J. Chem. Phys.* **2015**, *142*, 212434.

(398) Tekavec, P. F.; Lott, G. A.; Marcus, A. H. Fluorescence-Detected Two-Dimensional Electronic Coherence Spectroscopy by Acousto-Optic Phase Modulation. *J. Chem. Phys.* **2007**, *127*, 214307.

(399) Lott, G. A.; Perdomo-Ortiz, A.; Utterback, J. K.; Widom, J. R.; Aspuru-Guzik, A.; Marcus, A. H. Conformation of Self-assembled Porphyrin Dimers in Liposome Vesicles by Phase-Modulation 2D Fluorescence Spectroscopy. *Proc. Natl. Acad. Sci. U. S. A.* **2011**, *108*, 16521−16526.

(400) Perdomo-Ortiz, A.; Widom, J. R.; Lott, G. A.; Aspuru-Guzik, A.; Marcus, A. H. Conformation and Electronic Population Transfer in Membrane-Supported Self-assembled Porphyrin Dimers by 2D Fluorescence Spectroscopy. *J. Phys. Chem. B* **2012**, *116*, 10757−10770.

(401) Widom, J. R.; Johnson, N. P.; von Hippel, P. H.; Marcus, A. H. Solution Conformation of 2-Aminopurine Dinucleotide Determined by Ultraviolet Two-Dimensional Fluorescence Spectroscopy. *New J. Phys.* **2013**, *15*, 025028.

(402) Widom, J. R.; Lee, W.; Perdomo-Ortiz, A.; Rappoport, D.; Molinski, T. F.; Aspuru-Guzik, A.; Marcus, A. H. Temperature-Dependent Conformations of a Membrane Supported Zinc Porphyrin Tweezer by 2D Fluorescence Spectroscopy. *J. Phys. Chem. A* **2013**, *117*, 6171−6184.

(403) De, A. K.; Monahan, D.; Dawlaty, J. M.; Fleming, G. R. Two-Dimensional Fluorescence-Detected Coherent Spectroscopy with

Absolute Phasing by Confocal Imaging of a Dynamic Grating and 27-Step Phase-Cycling. *J. Chem. Phys.* **2014**, *140*, 194201.

(404) Mukamel, S.; Richter, M. Multidimensional Phase-Sensitive Single-Molecule Spectroscopy with Time-and-Frequency-Gated Fluorescence Detection. *Phys. Rev. A: At., Mol., Opt. Phys.* **2011**, *83*, 013815.

(405) Fingerhut, B. P.; Richter, M.; Luo, J.-W.; Zunger, A.; Mukamel, S. Dissecting Biexciton Wave Functions of Self-assembled Quantum Dots by Double-Quantum-Coherence Optical Spectroscopy. *Phys. Rev. B: Condens. Matter Mater. Phys.* **2012**, *86*, 235303.

(406) Brinks, D.; Stefani, F. D.; Kulzer, F.; Hildner, R.; Taminiau, T. H.; Avlasevich, Y.; Mullen, K.; van Hulst, N. F. Visualizing and Controlling Vibrational Wave Packets of Single Molecules. *Nature* **2010**, *465*, 905−908.

(407) Fingerhut, B. P.; Richter, M.; Luo, J.-W.; Zunger, A.; Mukamel, S. 2D Optical Photon Echo Spectroscopy of a Self-assembled Quantum Dot. *Ann. Phys.* **2013**, *525*, 31−42.

(408) Rahav, S.; Mukamel, S. Multidimensional Optical Spectroscopy of a Single Molecule in a Current-Carrying State. *J. Chem. Phys.* **2010**, *133*, 244106.

(409) Karki, K. J.; Widom, J. R.; Seibt, J.; Moody, I.; Lonergan, M. C.; Pullerits, T.; Marcus, A. H. Coherent Two-Dimensional Photocurrent Spectroscopy in a PbS Quantum Dot Photocell. *Nat. Commun.* **2014**, *5*, 5869.

(410) Kimberg, V.; Sanchez-Gonzalez, A.; Mercadier, L.; Weninger, C.; Lutman, A.; Ratner, D.; Coffee, R. N.; Bucher, M.; Mucke, M.; Agaker, M.; et al. Stimulated X-Ray Raman Scattering - a Critical Assessment of the Building Block of Nonlinear X-Ray Spectroscopy. *Faraday Discuss.* **2016**, *194*, 305−324.

(411) Chergui, M. Time-Resolved X-Ray Spectroscopies of Chemical Systems: New Perspectives. *Struct. Dyn.* **2016**, *3*, 031001.

(412) Pertot, Y.; Schmidt, C.; Matthews, M.; Chauvet, A.; Huppert, M.; Svoboda, V.; von Conta, A.; Tehlar, A.; Baykusheva, D.; Wolf, J.-P.; et al. Time-resolved X-Ray Absorption Spectroscopy with a Water Window High-Harmonic Source. *Science* **2017**, *355*, 264−267.

(413) Bennett, K.; Kowalewski, M.; Mukamel, S. Probing Electronic and Vibrational Dynamics in Molecules by Time-Resolved Photoelectron, Auger-Electron, and X-Ray Photon Scattering Spectroscopy. *Faraday Discuss.* **2015**, *177*, 405−428.

(414) Hua, W.; Oesterling, S.; Biggs, J. D.; Zhang, Y.; Ando, H.; de Vivie-Riedle, R.; Fingerhut, B. P.; Mukamel, S. Monitoring Conical Intersections in the Ring Opening of Furan by Attosecond Stimulated X-Ray Raman Spectroscopy. *Struct. Dyn.* **2016**, *3*, 023601.

(415) Zschornack, G. H. *Handbook of X-Ray Data*, 1st ed.; Springer: Berlin, 2007.

(416) Tashiro, M.; Ehara, M.; Fukuzawa, H.; Ueda, K.; Buth, C.; Kryzhevoi, N. V.; Cederbaum, L. S. Molecular Double Core Hole Electron Spectroscopy For Chemical Analysis. *J. Chem. Phys.* **2010**, *132*, 184302.

(417) Carlson, T. A. Photoelectron Spectroscopy. *Annu. Rev. Phys. Chem.* **1975**, *26*, 211−234.

(418) Einstein, A. Über einen die Erzeugung und Verwandlung des Lichtes Betreffenden Heuristischen Gesichtspunkt. *Ann. Phys.* **1905**, *322*, 132−148.

(419) Stolow, A.; Bragg, A. E.; Neumark, D. M. Femtosecond Time-Resolved Photoelectron Spectroscopy. *Chem. Rev.* **2004**, *104*, 1719−1758.

(420) Assion, A.; Geisler, M.; Helbing, J.; Seyfried, V.; Baumert, T. Femtosecond Pump-Probe Photoelectron Spectroscopy: Mapping of Vibrational Wave-Packet Motion. *Phys. Rev. A: At., Mol., Opt. Phys.* **1996**, *54*, R4605−R4608.

(421) Seel, M.; Domcke, W. Femtosecond Time-Resolved Ionization Spectroscopy of Ultrafast Internal-Conversion Dynamics in Polyatomic Molecules: Theory and Computational Studies. *J. Chem. Phys.* **1991**, *95*, 7806−7822.

(422) Blanchet, V.; Stolow, A. Nonadiabatic Dynamics in Polyatomic Systems Studied by Femtosecond Time-Resolved Photoelectron Spectroscopy. *J. Chem. Phys.* **1998**, *108*, 4371−4374.

(423) Chatterley, A. S.; West, C. W.; Roberts, G. M.; Stavros, V. G.; Verlet, J. R. R. Mapping the Ultrafast Dynamics of Adenine onto Its Nucleotide and Oligonucleotides by Time-Resolved Photoelectron Imaging. *J. Phys. Chem. Lett.* **2014**, *5*, 843−848.

(424) Ullrich, S.; Schultz, T.; Zgierski, M. Z.; Stolow, A. Electronic Relaxation Dynamics in DNA and RNA Bases Studied by Time-Resolved Photoelectron Spectroscopy. *Phys. Chem. Chem. Phys.* **2004**, *6*, 2796−2801.

(425) Chatterley, A. S.; West, C. W.; Stavros, V. G.; Verlet, J. R. R. Time-Resolved Photoelectron Imaging of the isolated Deprotonated Nucleotides. *Chem. Sci.* **2014**, *5*, 3963−3975.

(426) Bennett, K.; Kowalewski, M.; Mukamel, S. Nonadiabatic Dynamics May Be Probed Through Electronic Coherence in Time-Resolved Photoelectron Spectroscopy. *J. Chem. Theory Comput.* **2016**, *12*, 740.

(427) Trabs, P.; Buchner, F.; Ghotbi, M.; Lübcke, A.; Ritze, H.-H.; Vrakking, M. J. J.; Rouzée, A. Time-, Angle- and Kinetic-Energy-Resolved Photoelectron Spectroscopy of Highly Excited States of NO. *J. Phys. B: At., Mol. Opt. Phys.* **2014**, *47*, 124016.

(428) Suzuki, Y.-I.; Fuji, T.; Horio, T.; Suzuki, T. Time-Resolved Photoelectron Imaging of Ultrafast S2→S1 internal Conversion Through Conical Intersection in Pyrazine. *J. Chem. Phys.* **2010**, *132*, 174302.

(429) Thompson, A. L.; Martínez, T. J. Time-Resolved Photoelectron Spectroscopy From First Principles: Excited State Dynamics of Benzene. *Faraday Discuss.* **2011**, *150*, 293−311.

(430) Mori, T.; Glover, W. J.; Schuurman, M. S.; Martinez, T. J. Role of Rydberg States in the Photochemical Dynamics of Ethylene. *J. Phys. Chem. A* **2012**, *116*, 2808−2818.

(431) Oana, C. M.; Krylov, A. I. Cross Sections and Photoelectron Angular Distributions in Photodetachment From Negative Ions Using Equation-of-Motion Coupled-Cluster Dyson Orbitals. *J. Chem. Phys.* **2009**, *131*, 124114.

(432) Wang, K.; McKoy, V.; Hockett, P.; Schuurman, M. S. Time-Resolved Photoelectron Spectra of CS_2: Dynamics at Conical Intersections. *Phys. Rev. Lett.* **2014**, *112*, 113007.

(433) Kowalewski, M.; Bennett, K.; Rouxel, J. R.; Mukamel, S. Monitoring Nonadiabatic Electron-Nuclear Dynamics in Molecules by Attosecond Streaking of Photoelectrons. *Phys. Rev. Lett.* **2016**, *117*, 043201.

(434) Meitner, L. Über Die Entstehung Der β-Strahl-Spektren Radioaktiver Substanzen. *Eur. Phys. J. A* **1922**, *9*, 131−144.

(435) Burhop, E. *The Auger Effect and Other Radiationless Transitions*; Cambridge University Press: Cambridge, 2014.

(436) Lewenstein, M. Ph,; Yu,; L'Huillier, A.; Corkum, P. B. Theory of High-Harmonic Generation by Low-Frequency Laser Fields. *Phys. Rev. A: At., Mol., Opt. Phys.* **1994**, *49*, 2117−2132.

(437) Christov, I. P.; Murnane, M. M.; Kapteyn, H. C. High-Harmonic Generation of Attosecond Pulses in the "Single-Cycle" Regime. *Phys. Rev. Lett.* **1997**, *78*, 1251−1254.

(438) Tehlar, A.; Wörner, H. J. Time-Resolved High-Harmonic Spectroscopy of the Photodissociation of CH_3I and CF_3I. *Mol. Phys.* **2013**, *111*, 2057−2067.

(439) Smirnova, O.; Mairesse, Y.; Patchkovskii, S.; Dudovich, N.; Villeneuve, D.; Corkum, P.; Ivanov, M. Y. High Harmonic Interferometry of Multi-Electron Dynamics in Molecules. *Nature* **2009**, *460*, 972−977.

(440) Zhang, Y.; Hua, W.; Bennett, K.; Mukamel, S. In *Density-Functional Methods for Excited States*; Ferré, N., Filatov, M., Huix-Rotllant, M., Eds.; Topics in Current Chemistry; Springer International Publishing: New York, 2016; Vol. *368*; pp 273−345.

(441) Horio, T.; Fuji, T.; Suzuki, Y.-I.; Suzuki, T. Probing Ultrafast Internal Conversion Through Conical Intersection Via Time-Energy Map of Photoelectron Angular Anisotropy. *J. Am. Chem. Soc.* **2009**, *131*, 10392−10393.

(442) Lux, C.; Wollenhaupt, M.; Bolze, T.; Liang, Q.; Köhler, J.; Sarpe, C.; Baumert, T. Circular Dichroism in the Photoelectron Angular Distributions of Camphor and Fenchone From Multiphoton Ionization with Femtosecond Laser Pulses. *Angew. Chem., Int. Ed.* **2012**, *51*, 5001−5005.

(443) Hare, P. M.; Crespo-Hernández, C. E.; Kohler, B. Internal Conversion to the Electronic Ground State Occurs via Two Distinct Pathways for Pyrimidine Bases in Aqueous Solution. *Proc. Natl. Acad. Sci. U. S. A.* **2007**, *104*, 435−440.

(444) Etinski, M. Marian, C. M. Ab initio Investigation of the Methylation and Hydration Effects on the Electronic Spectra of Uracil and Thymine. *Phys. Chem. Chem. Phys.* **2010**, *12*, 4915−4923.

(445) Lee, J.; Challa, J. R.; McCamant, D. W. Ultraviolet Light Makes dGMP Floppy: Femtosecond Stimulated Raman Spectroscopy of 2′-Deoxyguanosine 5′-Monophosphate. *J. Phys. Chem. B* **2017**, *121*, 4722−4732.

(446) Kitney-Hayes, K. A.; Ferro, A. A.; Tiwari, V.; Jonas, D. M. Two-dimensional Fourier Transform Electronic Spectroscopy at a Conical Intersection. *J. Chem. Phys.* **2014**, *140*, 124312.

(447) Lim, J. S.; Kim, S. K. Experimental Probing of Conical Intersection Dynamics in the Photodissociation of Thioanisole. *Nat. Chem.* **2010**, *2*, 627−632.

(448) Jortner, J. Spiers Memorial Lecture On Dynamics From Isolated Molecules to Biomolecules. *Faraday Discuss.* **1997**, *108*, 1−22.

(449) Domcke, W. Köppel, H.; Cederbaum, L. Spectroscopic Effects of Conical Intersections of Molecular Potential Energy Surfaces. *Mol. Phys.* **1981**, *43*, 851−875.

(450) Meyer, H. Köppel, H. Time Evolution of Fluorescence and Strong Nonadiabatic Effects. *J. Chem. Phys.* **1984**, *81*, 2605−2619.

(451) Stock, G.; Domcke, W. Model Studies on the Time-Resolved Measurement of Excited-State Vibrational Dynamics and Vibronic Coupling. *Chem. Phys.* **1988**, *124*, 227−238.

(452) Katriel, J.; Davidson, E. R. The Non-Crossing Rule: Triply Degenerate Ground-State Geometries of CH_4^+. *Chem. Phys. Lett.* **1980**, *76*, 259−262.

(453) Matsika, S.; Yarkony, D. R. Accidental Conical Intersections of Three States of the Same Symmetry. I. Location and Relevance. *J. Chem. Phys.* **2002**, *117*, 6907−6910.

(454) Matsika, S.; Yarkony, D. R. Beyond Two-State Conical Intersections. Three-State Conical Intersections in Low Symmetry Molecules: the Allyl Radical. *J. Am. Chem. Soc.* **2003**, *125*, 10672−10676.

(455) Matsika, S.; Yarkony, D. R. Conical Intersections of Three Electronic States Affect the Ground State of Radical Species with Little or No Symmetry: Pyrazolyl. *J. Am. Chem. Soc.* **2003**, *125*, 12428−12429.

(456) Kistler, K. A.; Matsika, S. Three-State Conical Intersections in Cytosine and Pyrimidinone Bases. *J. Chem. Phys.* **2008**, *128*, 215102.

(457) González-Vázquez, J.; González, L. A Time-Dependent Picture of the Ultrafast Deactivation of Keto-Cytosine Including Three-State Conical Intersections. *ChemPhysChem* **2010**, *11*, 3617−3624.

(458) Matsika, S. Three-State Conical Intersections in Nucleic Acid Bases. *J. Phys. Chem. A* **2005**, *109*, 7538−7545.

(459) Coe, J. D.; Ong, M. T.; Levine, B. G.; Martínez, T. J. On the Extent and Connectivity of Conical Intersection Seams and the Effects of Three-State Intersections. *J. Phys. Chem. A* **2008**, *112*, 12559−12567.

(460) Thallmair, S.; Roos, M. K.; de Vivie-Riedle, R. Molecular Features in Complex Environment: Cooperative Team Players During Excited State Bond Cleavage. *Struct. Dyn.* **2016**, *3*, 043205.

(461) Corral, I.; González, L. Four-State Conical Intersections: the Nonradiative Deactivation Funnel Connected To O-O Homolysis in Benzene Endoperoxide. *Chem. Phys. Lett.* **2010**, *499*, 21−25.

(462) Demekhin, P. V.; Cederbaum, L. S. Light-induced Conical Intersections in Polyatomic Molecules: General Theory, Strategies of Exploitation, and Application. *J. Chem. Phys.* **2013**, *139*, 154314.

(463) Natan, A.; Ware, M. R.; Prabhudesai, V. S.; Lev, U.; Bruner, B. D.; Heber, O.; Bucksbaum, P. H. Observation of Quantum Interferences via Light-induced Conical Intersections in Diatomic Molecules. *Phys. Rev. Lett.* **2016**, *116*, 143004.

(464) Halász, G. J.; Vibók, A.; Šindelka, M.; Moiseyev, N.; Cederbaum, L. S. Conical Intersections Induced by Light: Berry Phase and Wavepacket Dynamics. *J. Phys. B: At., Mol. Opt. Phys.* **2011**, *44*, 175102.

(465) Galego, J.; Garcia-Vidal, F. J.; Feist, J. Cavity-induced Modifications of Molecular Structure in the Strong-Coupling Regime. *Phys. Rev. X* **2015**, *5*, 041022.

(466) Berry, M. V. Quantal Phase Factors Accompanying Adiabatic Changes. *Proc. R. Soc. London, Ser. A* **1984**, *392*, 45−57.

(467) Xiao, D.; Chang, M.-C.; Niu, Q. Berry Phase Effects on Electronic Properties. *Rev. Mod. Phys.* **2010**, *82*, 1959−2007.

(468) Englman, R. Spectroscopic Detectability of the Molecular Aharonov-Bohm Effect. *J. Chem. Phys.* **2016**, *144*, 024103.

(469) Joubert-Doriol, L.; Ryabinkin, I. G.; Izmaylov, A. F. Geometric Phase Effects in Low-Energy Dynamics Near Conical Intersections: A Study of the Multidimensional Linear Vibronic Coupling Model. *J. Chem. Phys.* **2013**, *139*, 234103.

(470) Ryabinkin, I. G.; Izmaylov, A. F. Geometric Phase Effects in Dynamics Near Conical Intersections: Symmetry Breaking and Spatial Localization. *Phys. Rev. Lett.* **2013**, *111*, 220406.

(471) Englman, R. Analysis of a Two Dimensional Molecular Berry Phase System. *Chem. Phys. Lett.* **2015**, *635*, 224−227.

(472) Larson, J. Absence of Vacuum Induced Berry Phases without the Rotating Wave Approximation in Cavity QED. *Phys. Rev. Lett.* **2012**, *108*, 033601.

(473) Min, S. K.; Abedi, A.; Kim, K. S.; Gross, E. K. U. Is the Molecular Berry Phase an Artifact of the Born-Oppenheimer Approximation? *Phys. Rev. Lett.* **2014**, *113*, 263004.

(474) Hamm, P.; Stock, G. Vibrational Conical Intersections as a Mechanism of Ultrafast Vibrational Relaxation. *Phys. Rev. Lett.* **2012**, *109*, 173201.

(475) Hamm, P.; Stock, G. Nonadiabatic Vibrational Dynamics in the $HCO_2^-\cdot H_2O$ Complex. *J. Chem. Phys.* **2015**, *143*, 134308.

(476) Hamm, P.; Stock, G. Vibrational Conical Intersections in the Water Dimer. *Mol. Phys.* **2013**, *111*, 2046−2056.

(477) Dawadi, M. B.; Perry, D. S. Communication: Conical Intersections Between Vibrationally adiabatic Surfaces in Methanol. *J. Chem. Phys.* **2014**, *140*, 161101.

(478) Dahms, F.; Costard, R.; Pines, E.; Fingerhut, B. P.; Nibbering, E. T. J.; Elsaesser, T. The Hydrated Excess Proton in the Zundel Cation $H_5O_2^+$: the Role of Ultrafast Solvent Fluctuations. *Angew. Chem., Int. Ed.* **2016**, *55*, 10600−10605.

(479) Raab, A.; Worth, G. A.; Meyer, H.-D.; Cederbaum, L. S. Molecular Dynamics of Pyrazine after Excitation To the S2 Electronic State Using a Realistic 24-Mode Model Hamiltonian. *J. Chem. Phys.* **1999**, *110*, 936−946.

(480) Lewis, N. H. C.; Fleming, G. R. Two-Dimensional Electronic-Vibrational Spectroscopy of Chlorophyll a and b. *J. Phys. Chem. Lett.* **2016**, *7*, 831−837.

(481) Mehlenbacher, R. D.; Lyons, B.; Wilson, K. C.; Du, Y.; McCamant, D. W. Theoretical Analysis of Anharmonic Coupling and Cascading Raman Signals Observed with Femtosecond Stimulated Raman Spectroscopy. *J. Chem. Phys.* **2009**, *131*, 244512.

(482) Wilson, K. C.; Lyons, B.; Mehlenbacher, R.; Sabatini, R.; McCamant, D. W. Two-Dimensional Femtosecond Stimulated Raman Spectroscopy: Observation of Cascading Raman Signals in Acetonitrile. *J. Chem. Phys.* **2009**, *131*, 214502.

(483) Wende, T.; Liebel, M.; Schnedermann, C.; Pethick, R. J.; Kukura, P. Population-Controlled Impulsive Vibrational Spectroscopy: Background- and Baseline-Free Raman Spectroscopy of Excited Electronic States. *J. Phys. Chem. A* **2014**, *118*, 9976−9984.

(484) Sun, Y.; Benabbas, A.; Zeng, W.; Kleingardner, J. G.; Bren, K. L.; Champion, P. M. Investigations of Heme Distortion, Low-Frequency Vibrational Excitations, and Electron Transfer in Cytochrome C. *Proc. Natl. Acad. Sci. U. S. A.* **2014**, *111*, 6570−6575.

(485) Tokmakoff, A.; Fleming, G. Two-Dimensional Raman Spectroscopy of the Intermolecular Modes of Liquid CS_2. *J. Chem. Phys.* **1997**, *106*, 2569.

(486) Cho, M.; Blank, D. A.; Sung, J.; Park, K.; Hahn, S.; Fleming, G. R. Intrinsic Cascading Contributions to the Fifth-and Seventh-order Electronically Off-Resonant Raman Spectroscopies. *J. Chem. Phys.* **2000**, *112*, 2082−2094.

(487) Lozovoy, V. V.; Pastirk, I.; Comstock, M. G.; Dantus, M. Cascaded Free-induction Decay Four-Wave Mixing. *Chem. Phys.* **2001**, *266*, 205−212.

(488) Kaufman, L. J.; Heo, J.; Ziegler, L. D.; Fleming, G. R. Heterodyne-Detected Fifth-order Nonresonant Raman Scattering From Room Temperature CS_2. *Phys. Rev. Lett.* **2002**, *88*, 207402.

(489) Kubarych, K. J.; Milne, C. J.; Miller, R. D. Fifth-order Two-Dimensional Raman Spectroscopy: a New Direct Probe of the Liquid State. *Int. Rev. Phys. Chem.* **2003**, *22*, 497−532.

(490) Dunlap, B.; Wilson, K.; McCamant, D. Recent Advances in Two Dimensional Femtosecond Stimulated Raman Spectroscopy (2D-FSRS). *Frontiers in Optics 2012/Laser Science XXVIII* **2012**, LM3I.3.

(491) Blank, D. A.; Kaufman, L. J.; Fleming, G. R. Fifth-order Two-Dimensional Raman Spectra of CS_2 are Dominated by Third-order Cascades. *J. Chem. Phys.* **1999**, *111*, 3105−3114.

(492) Boyd, R. W. *Nonlinear Optics*; Academic Press Inc.: San Diego, CA, 1992.

(493) Golonzka, O. Demirdöven, N.; Khalil, M.; Tokmakoff, A. Separation of Cascaded and Direct Fifth-order Raman Signals Using Phase-Sensitive Intrinsic Heterodyne Detection. *J. Chem. Phys.* **2000**, *113*, 9893−9896.

(494) Zhao, B.; Sun, Z.; Lee, S. Quantum Theory of Time-Resolved Femtosecond Stimulated Raman Spectroscopy: Direct Versus Cascade Processes and Application to $CDCl_3$. *J. Chem. Phys.* **2011**, *134*, 024307.

(495) Gelin, M. F.; Domcke, W. Simple Recipes For Separating Excited-State Absorption and Cascading Signals by Polarization-Sensitive Measurements. *J. Phys. Chem. A* **2013**, *117*, 11509.

(496) Bennett, K.; Mukamel, S. Cascading and Local-Field Effects in Non-Linear Optics Revisited: a Quantum-Field Picture Based on Exchange of Photons. *J. Chem. Phys.* **2014**, *140*, 044313.

(497) Bennett, K.; Chernyak, V.; Mukamel, S. Discriminating cascading processes in nonlinear optics: A QED analysis based on their molecular and geometric origin. *Phys. Rev. A: At., Mol., Opt. Phys.* **2017**, *95*, 033840.

(498) Zhang, Z.; Bennett, K.; Chernyak, V.; Mukamel, S. Utilizing Microcavities to Suppress Third-Order Cascades in Fifth-Order Raman Spectra. *J. Phys. Chem. Lett.* **2017**.

(499) Weiner, A. M. Ultrafast Optical Pulse Shaping: a Tutorial Review. *Opt. Commun.* **2011**, *284*, 3669−3692.

(500) Manzoni, C.; Mücke, O. D.; Cirmi, G.; Fang, S.; Moses, J.; Huang, S.-W.; Hong, K.-H.; Cerullo, G.; Kärtner, F. X. Coherent Pulse Synthesis: Towards Sub-Cycle Optical Waveforms. *Laser Photonics Rev.* **2015**, *9*, 129−171.

(501) von den Hoff, P.; Thallmair, S.; Kowalewski, M.; Siemering, R.; de Vivie-Riedle, R. Optimal Control Theory - Closing the Gap Between Theory and Experiment. *Phys. Chem. Chem. Phys.* **2012**, *14*, 14460.

(502) Gordon, R. J.; Seideman, T. In *Advances in Multi-Photon Processes and Spectroscopy*; Lin, S. H., et al., Eds.; World Scientific Publishing Co.: Singapore, 2016; pp 1−54.

(503) Richter, M.; Bouakline, F.; González-Vázquez, J.; Martínez-Fernández, L.; Corral, I.; Patchkovskii, S.; Morales, F.; Ivanov, M.; Martín, F.; Smirnova, O. Sub-Laser-Cycle Control of Coupled Electron-Nuclear Dynamics at a Conical Intersection. *New J. Phys.* **2015**, *17*, 113023.

(504) Brixner, T.; Krampert, G.; Pfeifer, T.; Selle, R.; Gerber, G.; Wollenhaupt, M.; Graefe, O.; Horn, C.; Liese, D.; Baumert, T. Quantum Control by Ultrafast Polarization Shaping. *Phys. Rev. Lett.* **2004**, *92*, 208301.

(505) Schweinberger, W.; Sommer, A.; Bothschafter, E.; Li, J.; Krausz, F.; Kienberger, R.; Schultze, M. Waveform-Controlled Near-Single-Cycle Milli-Joule Laser Pulses Generate Sub-10 nm Extreme Ultraviolet Continua. *Opt. Lett.* **2012**, *37*, 3573−3575.

(506) Huang, S.-W.; Cirmi, G.; Moses, J.; Hong, K.-H.; Bhardwaj, S.; Birge, J. R.; Chen, L.-J.; Li, E.; Eggleton, B. J.; Cerullo, G.; et al. High-Energy Pulse Synthesis with Sub-Cycle Waveform Control For Strong-Field Physics. *Nat. Photonics* **2011**, *5*, 475−479.

(507) Glenn, R.; Dantus, M. Single Broadband Phase-Shaped Pulse Stimulated Raman Spectroscopy For Standoff Trace Explosive Detection. *J. Phys. Chem. Lett.* **2016**, *7*, 117−125.

(508) Levitt, J. M.; Katz, O.; Silberberg, Y. Frequency-Encoded Multiplexed Cars Microscopy by Rapid Pulse Shaping. *J. Mod. Opt.* **2014**, *61*, 872−876.

(509) Rehbinder, J.; Brückner, L.; Wipfler, A.; Buckup, T.; Motzkus, M. Multimodal Nonlinear Optical Microscopy with Shaped 10 fs Pulses. *Opt. Express* **2014**, *22*, 28790−28797.

(510) Eilam, A.; Shapiro, E. A.; Shapiro, M. Electromagnetically Induced Transparency Spectroscopy. *J. Chem. Phys.* **2012**, *136*, 064201.

(511) Weninger, C.; Purvis, M.; Ryan, D.; London, R. A.; Bozek, J. D.; Bostedt, C.; Graf, A.; Brown, G.; Rocca, J. J.; Rohringer, N. Stimulated Electronic X-Ray Raman Scattering. *Phys. Rev. Lett.* **2013**, *111*, 233902.

(512) Prince, K. C.; Allaria, E.; Callegari, C.; Cucini, R.; de Ninno, G.; di Mitri, S.; Diviacco, B.; Ferrari, E.; Finetti, P.; Gauthier, D.; et al. Coherent Control with a Short-Wavelength Free-Electron Laser. *Nat. Photonics* **2016**, *10*, 176−179.

(513) Gauthier, D.; Ribič, P. c. v. R.; De Ninno, G.; Allaria, E.; Cinquegrana, P.; Danailov, M. B.; Demidovich, A.; Ferrari, E.; Giannessi, L. Generation of Phase-Locked Pulses From a Seeded Free-Electron Laser. *Phys. Rev. Lett.* **2016**, *116*, 024801.

(514) Miller, R. J. D. Mapping atomic Motions with Ultrabright Electrons: the Chemists' Gedanken Experiment Enters the Lab Frame. *Annu. Rev. Phys. Chem.* **2014**, *65*, 583−604.

(515) Manz, S.; Casandruc, A.; Zhang, D.; Zhong, Y.; Loch, R. A.; Marx, A.; Hasegawa, T.; Liu, L. C.; Bayesteh, S.; Delsim-Hashemi, H.; et al. Mapping Atomic Motions with Ultrabright Electrons: Towards Fundamental Limits in Space-Time Resolution. *Faraday Discuss.* **2015**, *177*, 467−491.

(516) Baum, P.; Zewail, A. H. 4D Attosecond Imaging with Free Electrons: Diffraction Methods and Potential Applications. *Chem. Phys.* **2009**, *366*, 2−8.

(517) Pande, K.; Hutchison, C. D. M.; Groenhof, G.; Aquila, A.; Robinson, J. S.; Tenboer, J.; Basu, S.; Boutet, S.; DePonte, D. P.; Liang, M.; et al. Femtosecond Structural Dynamics Drives the trans/cis Isomerization in Photoactive Yellow Protein. *Science* **2016**, *352*, 725−729.

(518) Kowalewski, M.; Bennett, K.; Mukamel, S. Monitoring Nonadiabatic Avoided Crossing Dynamics in Molecules by Ultrafast X-ray Diffraction. *Struct. Dyn.* **2017**, *4*, 054101.

(519) Bennett, K.; Zhang, Y.; Kowalewski, M.; Hua, W.; Mukamel, S. Multidimensional Resonant Nonlinear Spectroscopy with Coherent Broadband X-Ray Pulses. *Phys. Scr.* **2016**, *T169*, 014002.

(520) Hua, W.; Bennett, K.; Zhang, Y.; Luo, Y.; Mukamel, S. Study of Double Core Hole Excitations in Molecules by X-Ray Double-Quantum-Coherence Signals: a Multi-Configuration Simulation. *Chem. Sci.* **2016**, *7*, 5922−5933.

(521) New Science Opportunities Enabled by LCLS-II X-Ray Lasers. *SLAC Report SLAC-R-1053*, 2015; https://goo.gl/1heOeB, Accessed: Jan 31, 2017.

(522) Cao, W.; Warrick, E. R.; Fidler, A.; Neumark, D. M.; Leone, S. R. Noncollinear Wave Mixing of Attosecond XUV and Few-Cycle Optical Laser Pulses in Gas-Phase atoms: Toward Multidimensional Spectroscopy Involving XUV Excitations. *Phys. Rev. A: At., Mol., Opt. Phys.* **2016**, *94*, 053846.

(523) Ding, T.; Ott, C.; Kaldun, A.; Blättermann, A.; Meyer, K.; Stooss, V.; Rebholz, M.; Birk, P.; Hartmann, M.; Brown, A.; et al. Time-Resolved Four-Wave-Mixing Spectroscopy for Inner-Valence Transitions. *Opt. Lett.* **2016**, *41*, 709−712.

(524) Bencivenga, F.; Cucini, R.; Capotondi, F.; Battistoni, A.; Mincigrucci, R.; Giangrisostomi, E.; Gessini, A.; Manfredda, M.; Nikolov, I. P.; Pedersoli, E.; et al. Four-Wave Mixing Experiments with Extreme Ultraviolet Transient Gratings. *Nature* **2015**, *520*, 205−208.

(525) Bencivenga, F.; Calvi, A.; Capotondi, F.; Cucini, R.; Mincigrucci, R.; Simoncig, A.; Manfredda, M.; Pedersoli, E.; Principi, E.; Dallari, F.; et al. Four-Wave-Mixing Experiments with Seeded Free Electron Lasers. *Faraday Discuss.* **2016**, *194*, 283−303.

(526) Hartmann, N.; Glownia, J. M. X-Ray Photonics: Attosecond Coherent Control at FELs. *Nat. Photonics* **2016**, *10*, 148−150.

(527) Dorfman, K. E.; Schlawin, F.; Mukamel, S. Nonlinear Optical Signals and Spectroscopy with Quantum Light. *Rev. Mod. Phys.* **2016**, *88*, 045008.

(528) Scarcelli, G.; Valencia, A.; Gompers, S.; Shih, Y. Remote Spectral Measurement Using Entangled Photons. *Appl. Phys. Lett.* **2003**, *83*, 5560−5562.

(529) Yabushita, A.; Kobayashi, T. Spectroscopy by Frequency-Entangled Photon Pairs. *Phys. Rev. A: At., Mol., Opt. Phys.* **2004**, *69*, 013806.

(530) Kalachev, A.; Kalashnikov, D.; Kalinkin, A.; Mitrofanova, T.; Shkalikov, A.; Samartsev, V. Biphoton Spectroscopy of YAG:Er^{3+} Crystal. *Laser Phys. Lett.* **2007**, *4*, 722−725.

(531) Slattery, O.; Ma, L.; Kuo, P.; Kim, Y.-S.; Tang, X. Frequency Correlated Biphoton Spectroscopy Using Tunable Upconversion Detector. *Laser Phys. Lett.* **2013**, *10*, 075201.

(532) Kalashnikov, D. A.; Pan, Z.; Kuznetsov, A. I.; Krivitsky, L. A. Quantum Spectroscopy of Plasmonic Nanostructures. *Phys. Rev. X* **2014**, *4*, 011049.

(533) Dorfman, K. E.; Schlawin, F.; Mukamel, S. Stimulated Raman Spectroscopy with Entangled Light: Enhanced Resolution and Pathway Selection. *J. Phys. Chem. Lett.* **2014**, *5*, 2843−2849.

(534) Harbola, U.; Umapathy, S.; Mukamel, S. Loss and Gain Signals in Broadband Stimulated-Raman Spectra: Theoretical Analysis. *Phys. Rev. A: At., Mol., Opt. Phys.* **2013**, *88*, 011801.

(535) Sanda, F.; Mukamel, S. Stochastic Simulation of Chemical Exchange in Two Dimensional Infrared Spectroscopy. *J. Chem. Phys.* **2006**, *125*, 014507.